Towards a new insight of the carbon transport in the global ocean

Florian Ricour

To cite this version:

Florian Ricour. Towards a new insight of the carbon transport in the global ocean. Ocean, Atmosphere. Sorbonne Université; Université de Liège, 2023. English. NNT : 2023SORUS191 . tel-04200208

HAL Id: tel-04200208
https://theses.hal.science/tel-04200208

Submitted on 8 Sep 2023

University of Liège
Sorbonne University

Towards a new insight of the carbon transport in the global ocean

Florian Ricour

Dissertation presented in fulfillment for the degree of Doctor of Sciences

Supervisors

Hervé Claustre, director
Marilaure Grégoire, director
Alexander Barth, co-director

Jury Members

Pr. Stephanie Henson	University of Southampton	Reviewer
Dr. Margaret Estapa	University of Maine	Reviewer
Dr. Griet Neukermans	University of Ghent	Examiner
Dr. Ivona Cetinić	Morgan State University	Examiner
Pr. Lars Stemmann	Sorbonne University	Jury President
Dr. Lionel Guidi	Sorbonne University	Guest
Dr. Hervé Claustre	Sorbonne University	PhD Director
Pr. Marilaure Grégoire	University of Liège	PhD Director
Dr. Alexander Barth	University of Liège	PhD Co-director

May 2023

Foreword

As of 2022, it has now become obvious to the general public that the Earth's climate is changing. Massive flood events, repeated heatwaves, never-ending droughts, disappearing glaciers, biodiversity collapse, … Reports on weather anomalies were already published in the 1960's, the Intergovernmental Panel on Climate Change (IPCC) was created in 1988, the Kyoto Protocol was adopted in 1997, An Inconvenient Truth was released in 2006, the Paris Agreement was signed in 2015 and still, what has really changed?

As I am writing this part, the COP27 (sponsored by Coca-Cola, no joke) is taking place with an acknowledged record number of fossil fuel lobbyists, bloody stadiums with outside air conditioning are about to be used in the desert for a month and it seems like 'leaders' of the Free World have been having hearing issues. See for yourself:

"I am drowning" said Pakistan

"I'm sorry, what?" said the Free World

"I am starving" said Ethiopia

"Can't hear you, louder please!" said the Free World

"We are suffocating" said India

"Aaaah okay. Yes you're absolutely right, let's save the banks one more time" said the Free World

Although I am not an activist (yet?) or a politician (I am too honest to be elected), rest assured that there is no fake news in this work. I hope you will enjoy it.

Acknowledgements

I would like to thank the members of the jury for taking the time to read and evaluate this three and a half year work. I look forward to discussing it during the defense.

Merci aux membres du comité de thèse pour leur temps et leurs retours sur l'évolution du projet.

Cette thèse a été particulière à bien des égards, avec son lot de points positifs et négatifs mais surtout avec son lot de rebondissements qui m'ont permis d'affûter mes connaissances, ma résilience et je l'espère ma tolérance. Pour cela, je tiens à remercier chaleureusement toutes les personnes y ayant contribué de près ou de loin.

Merci à Hervé, Lionel et Jean-Olivier pour leur accueil au Laboratoire de Villefranche-sur-Mer et pour leur disponibilité ainsi que pour leurs conseils avisés, tant scientifiques que personnels.

Merci à Alex, Charles et Arthur pour leur aide et leur gentillesse.

Merci également aux personnes que j'ai pu côtoyer à COMPLEX comme chez OMTAB depuis mon passage en stage en 2018 et les multiples allers-retours Belgique-France.

Merci à Antoine Mangin de m'avoir prêté un bureau dans les locaux d'ACRI sur Grasse l'été dernier pendant que mon appartement servait d'Airbnb estival pour le plus grand bonheur du portefeuille de mon proprio.

Un grand merci à mes colocs de bureau: Ophélie, Laetitia et Thelma pour votre soutien et votre bonne humeur sans faille (contrairement à moi).

Merci à AMP (elle se reconnaitra), Chloé et Anaïs pour les pauses midi sur le ponton. AMP, merci d'avoir accepté de vivre virtuellement avec moi afin que la sécu daigne enfin me donner une carte vitale !

Ne me demandez pas des noms de restos ou de bars sur la côte d'Azur, je n'en ai aucune idée. Par contre, je connais pas mal les routes du coin. Merci à tous ceux qui ont partagé (ou subi) des kilomètres à mes côtés, surtout en montée (le plat pays, qui est le mien): Flavien, Ophé, Lucas, Thelma, Laeti et Satoshi.

Un grand merci à Marine et Alice pour leur bienveillance. Marine, je te souhaite le meilleur pour tes projets futurs mais fais attention à qui tu donnes tes clés quand même.

Merci également à Alex qui a été un excellent roommate pendant les confinements, couvre-feux et ordonnances en tout genre. See you in London !

Merci aux Liégeois(es) (Thomas, Florent, Flop, Nico, Evgeny et Lucie) et en particulier Hadrien qui a accepté de m'avoir comme coloc pendant plusieurs mois (et qui y a survécu).

Merci aux Montois (Mathieu, Chris, Flo, Ju & Ju) pour votre soutien à distance, un mariage en 3 actes et pour vos visites sur Nice. Petite dédicace à Ju K qui, à force d'avoir joué avec le diable en subissant l'enfer des pourcentages, va littéralement en devenir un. Vivement 2024 pour casser la baraque !

Un très grand merci à ma famille nucléaire qui ne comprend toujours pas mon job mais qui fait semblant quand je lui explique, c'est le principal. C'est vrai que la défense tombe mal au niveau timing donc on se voit à la Ducasse :-)

Enfin, un grand merci à une personne toute particulière qui en a probablement marre que je parle de la Belgique mais qui à présent est parfaite bilingue, mission accomplie?

Summary

Towards a new insight of the carbon transport in the global ocean

The ocean is known to play a key role in the carbon cycle. Without it, atmospheric CO_2 levels would be much higher than they are today thanks to the presence of carbon pumps that maintain a gradient of dissolved inorganic carbon (DIC) between the surface and the deep ocean. The biological carbon pump (BCP) is primarily responsible for this gradient. It consists in a series of ocean processes through which inorganic carbon is fixed as organic matter by photosynthesis in sunlit surface waters and then transported to the ocean interior and possibly the sediment where it will be sequestered from the atmosphere for millions of years. The BCP was long thought as solely the gravitational settling of particulate organic carbon (POC). However, a new paradigm for the BCP has recently been defined in which physically and biologically mediated particle injection pumps have been added to the original definition. Physically mediated particle injection pumps provide a pathway to better understand the transport of dissolved organic carbon (DOC) whereas biologically mediated particle injection pumps focus on the transport of POC by vertically migrating animals, either daily or seasonally. Therefore, a better understanding of these processes could help bridge the gap between carbon leaving the surface and carbon demand in the ocean interior. To address this new paradigm, this work will benefit from the advent of recent sensors that equip a new generation of Biogeochemical-Argo floats (BGC-Argo). The first part focuses on the development of an embedded zooplankton classification model for the Underwater Vision Profiler 6 (UVP6) under strict technical and energy constraints. The second part studies particle and carbon fluxes in the Labrador Sea using BGC-Argo floats equipped for the first time with the UVP6 and an optical sediment trap (OST), providing two independent measurements of sinking particles. The last part consists in revisiting the BCP using a new framework called CONVERSE for Continuous Vertical Sequestration. With this new approach, we re-evaluate the total carbon sequestered from the atmosphere ($\geq$ 100 years) by the BCP and its transport pathways on the entire water column, in contrast to the carbon sequestration typically assumed below a fixed reference depth.

Keywords Carbon pumps – Underwater Vision Profiler 6 – BGC-Argo floats – Machine learning

Résumé

Vers une meilleure compréhension du transport du carbone dans l’océan global

L’océan est connu pour jouer un rôle clé dans le cycle du carbone. Sans lui, les niveaux de CO_2 atmosphérique seraient bien plus élevés qu’aujourd’hui grâce à la présence de pompes à carbone qui maintiennent un gradient de carbone inorganique dissous (DIC) entre la surface et le fond de l’océan. La pompe à carbone biologique (BCP) est principalement responsable de ce gradient. Elle consiste en une série de processus océaniques au cours desquels le carbone inorganique est converti en matière organique via la photosynthèse dans les eaux de surface, puis transporté vers l’intérieur de l’océan et éventuellement les sédiments où il sera séquestré par rapport à l’atmosphère pour des millions d’années. La BCP était longtemps considérée comme étant uniquement la déposition gravitationnelle de carbone organique particulaire (POC). Cependant, un nouveau paradigme pour la BCP a récemment été défini dans lequel des pompes d’origine physique et biologique d’injection de particules ont été ajoutées à la définition originale. Les pompes physiques d’injection de particules fournissent un moyen de mieux comprendre le transport de carbone organique dissous (DOC), tandis que les pompes biologique d’injection de particules se concentrent sur le transport de POC par des animaux migrant verticalement, quotidiennement ou saisonnièrement. Par conséquent, une meilleure compréhension de ces processus pourrait aider à combler l’écart entre le carbone quittant la surface et la demande de carbone dans l’océan profond. Pour aborder ce nouveau paradigme, ce travail bénéficiera de l’arrivée de capteurs récents équipant une nouvelle génération de flotteurs Biogéochimiques-Argo (BGC-Argo). La première partie se concentre sur le développement d’un modèle embarqué de classification de zooplancton pour l’Underwater Vision Profiler 6 (UVP6) avec des contraintes techniques et énergétiques strictes. La deuxième partie étudie les flux de particules et de carbone dans la mer du Labrador en utilisant des flotteurs BGC-Argo équipés pour la première fois de l’UVP6 et d’un piège à sédiments optique (OST), fournissant deux mesures indépendantes des particules. La dernière partie consiste à revisiter la BCP en utilisant un nouveau cadre appelé CONVERSE qui fait référence à la séquestration verticale continue du carbone dans la colonne d’eau. Avec cette nouvelle approche, nous réévaluons le carbone total séquestré par rapport à l’atmosphère ($\geq$ 100 ans) par la BCP et ses voies de transport sur toute la colonne d’eau, par opposition à la séquestration de carbone généralement supposée en-dessous d’une profondeur de référence fixe.

Mots clés Pompes à carbone – Underwater Vision Profiler 6 – Flotteurs BGC-Argo – Machine learning

Table of contents

List of Figures

List of Tables

1 Introduction

1.1 The global carbon cycle

The global carbon cycle (Figure 1.1) consists of a series of exchanges of carbon in various organic and inorganic forms among four major reservoirs: the lithosphere, the hydrosphere, the atmosphere and the biosphere. These exchanges occur at different time scales, such that the carbon cycle can be roughly divided into a slow and a fast component. The former operates on geological time scales where carbon is hidden from the surface for millions of years (e.g. in hydrocarbon deposits such as petroleum or natural gas) before a part of it is released through volcanic activity while the latter operates on shorter time scales, from minutes to years (e.g. photosynthesis, air-sea fluxes) up to decades and millenia (e.g. ocean ventilation, changing ocean buffering capacity) (Bertrand and Legendre 2021; Canadell et al. 2021).

99% of the Earth's carbon is stored in rocks, holding about 100,000 times as much carbon as the atmosphere while the ocean contains about 60 times as much carbon as the atmosphere (Sarmiento 2006; Bertrand and Legendre 2021; DeVries 2022) with roughly 37,000 Pg (i.e. 1 Pg $= 10^{15}$ g $=$ 1 Gt) of dissolved inorganic carbon (DIC) and 700 Pg of dissolved organic carbon (DOC) (Friedlingstein et al. 2022).

The global carbon cycle had been at close equilibrium for millions of years before the industrial revolution started in the 18th century. Since then, human have been burning fossil fuels at an unprecedented rate, releasing huge amounts of carbon dioxide (CO_2) in the atmosphere that should have been discharged slowly through the slow carbon cycle (Bertrand and Legendre 2021). These emissions, resulting from the burning of fossil fuels but also from land use change (e.g. deforestation, land management), have been estimated around 700 Pg C since 1750 (Canadell et al. 2021).

Thankfully, more than half of this anthropogenic CO_2 has been absorbed by terrestrial ecosystems and by the ocean (Friedlingstein et al. 2022), forming major carbon sinks.

1.2 How is the ocean a CO_2 sink?

The ocean is known to play a key role in the fast carbon cycle due to its size and rapid exchange of CO_2 with the atmosphere, controlling atmospheric CO_2 levels on time scales of decades to millennia (Sarmiento 2006; DeVries 2022). Currently, the ocean absorbs ~2.5 Pg C year^{-1},

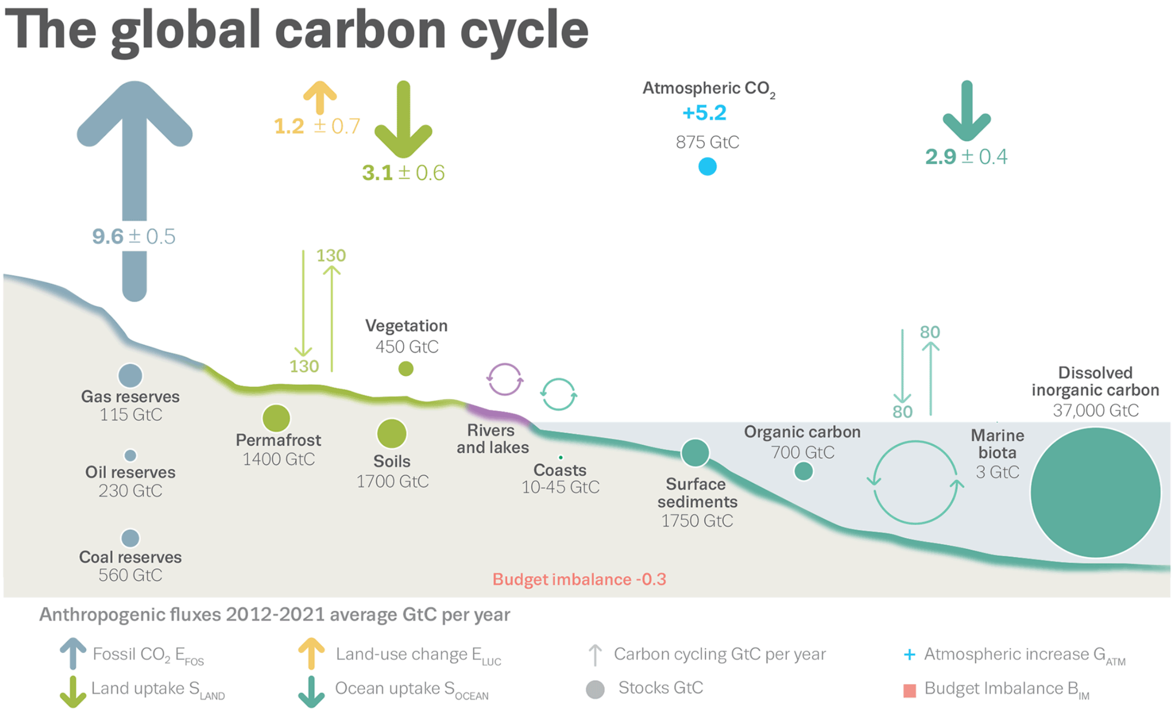

Figure 1.1: Illustration of the global carbon cycle (numbers represent a global average for the decade 2012-2021). Arrows and circles depict, respectively, carbon fluxes in Pg C year^{-1} and carbon content in Pg C. Figure taken from Friedlingstein et al. (2022).

which represents about 25% of annual anthropogenic CO_2 emissions (Canadell et al. 2021; Friedlingstein et al. 2022). In order to understand how the ocean absorbs the latter, one must take a look at seawater carbonate chemistry.

1.2.1 Inorganic carbonate chemistry

The intensity of the exchange of CO_2 at the air-sea interface is driven by the difference between the partial pressure of CO_2 in the atmosphere (pCO_2^{atm}) and in the surface ocean ($pCO_2^{surface}$).

$$\Delta pCO_2 = pCO_2^{surface} - pCO_2^{atm} \tag{1.1}$$

When $\Delta pCO_2 > 0$, surface waters are supersaturated in CO_2 resulting in a net flux of CO_2 from the ocean to the atmosphere. On the contrary, surface waters are undersaturated with a net CO_2 flux in the opposite direction (Sarmiento 2006).

When a molecule of $CO_{2\ (gas)}$ dissolves in seawater, it first gets hydrated to form $CO_{2\ (aq)}$ then it reacts with water to form carbonic acid (H_2CO_3).

$$CO_{2\ (gas)} + H_2O \rightleftharpoons CO_{2\ (aq)} + H_2O \rightleftharpoons H_2CO_3 \tag{1.2}$$

H_2CO_3 is a strong acid that quickly dissociates in two steps to form bicarbonate (HCO_3^-) and carbonate (CO_3^{2-}) where each reaction releases one free proton (H^+).

$$H_2CO_3 \rightleftarrows H^+ + HCO_3^- \tag{1.3}$$

$$HCO_3^- \rightleftarrows H^+ + CO_3^{2-} \tag{1.4}$$

The abundance of each carbonate species is governed by the equilibrium between those three relationships (Sarmiento 2006). According to Gattuso and Hansson (2011), at a typical surface pH of 8.2, the relative abundances of CO_2 (encompassing $CO_{2\ (aq)}$ and H_2CO_3 because it is difficult to distinguish them analytically), HCO_3^- and CO_3^{2-} are, respectively, 0.5%, 89% and 10.5%. For convenience, the sum of all dissolved carbonate species will be hereafter referred to as DIC

$$DIC = [CO_2] + [HCO_3^-] + [CO_3^{2-}] \tag{1.5}$$

where brackets denote concentrations.

1.2.2 Distribution of DIC in the water column

It can be shown (e.g. DeVries 2022) that if the ocean was a homogeneous reservoir of inorganic carbon, pCO_2^{atm} would be much higher than it is now (roughly 416 parts per million (ppm) as of October 2022 according to the Mauna Loa Observatory). This is explained by the presence of a strong vertical gradient of DIC in the ocean, with deep DIC concentrations more than 200 μmol kg^{-1} higher than at 1,000 m as it can be seen in Figure 1.2.

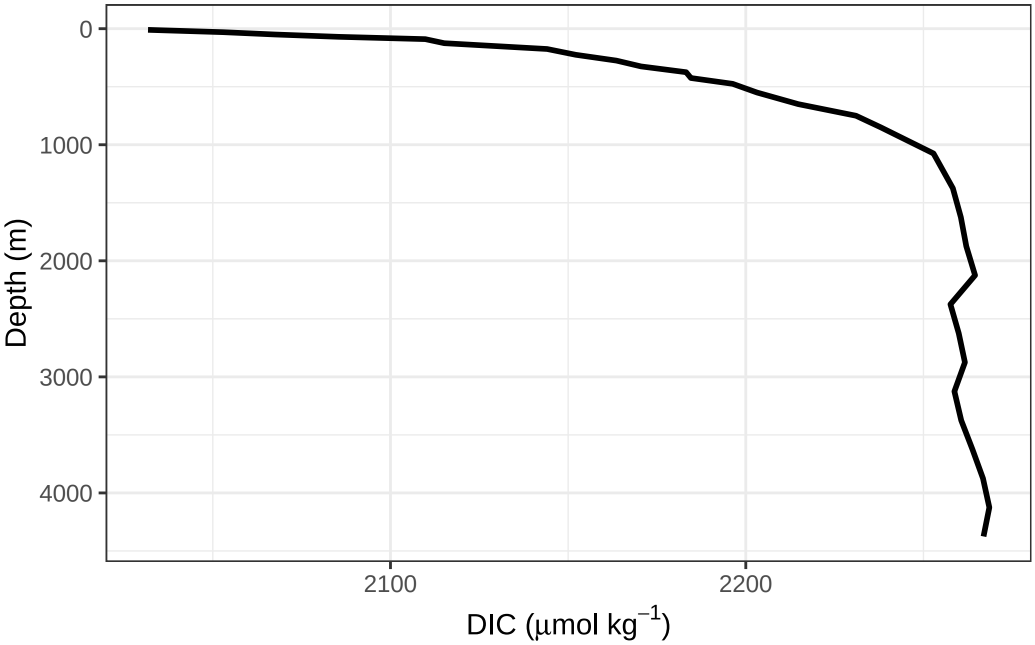

Figure 1.2: Mean DIC distribution in the global ocean. Data taken from the Merged Master File from GLODAPv2, available at https://www.glodap.info/index.php/merged-and-adjusted-data-product-v2-2022/, last accessed on 26/10/2022.

This gradient is mostly due to processes often referred to as carbon pumps, operating against continuous ocean mixing processes that tend to homogenize DIC in the water column (Sarmiento 2006; Claustre et al. 2021). They were originally defined by Volk and Hoffert (1985) as "processes that deplete the ocean surface of DIC relative to the deep-water DIC".

1.2.3 Several carbon pumps at work

1.2.3.1 Solubility pump

From Equation 1.2, one can derive that p$CO_2^{water\ parcel}$ is related to the dissolved CO_2 concentration by the following relation

$$pCO_2^{water\ parcel} = \frac{[CO_2]}{K_0} \tag{1.6}$$

where K_0 is the solubility coefficient of CO_2 in seawater.

K_0 is a function of temperature and salinity with a strong dependence on the former (Sarmiento 2006) such that the solubility of CO_2 increases with decreasing temperature. Consequently, waters that cool as they are transported to higher latitudes by the thermohaline circulation will be undersaturated in CO_2 once they reach the surface. Thus, there will be a net exchange of carbon dioxide from the atmosphere to the ocean, enriching surface waters in DIC before they dive back to the abyss at deep water formation zones in North Atlantic polar regions (e.g. the Labrador Sea) and along the Antarctic shelf in the Southern Ocean (DeVries 2022).

The solubility pump is responsible for the great majority of all anthropogenic CO_2 that has been absorbed by the ocean and it would be contributing to 10% of the observed vertical DIC gradient according to Sarmiento (2006).

1.2.3.2 Carbonate pump

Calcifying organisms (mostly coccolithophores, foraminifera and pteropods) produce particulate inorganic carbon (PIC) by precipitating biogenic $CaCO_3$ (Sarmiento 2006)

$$Ca^{2+} + CO_3^{2-} \rightleftharpoons CaCO_3 \tag{1.7}$$

to form calcite structures such as calcite platelets (coccoliths), calcite shells or spines (Neukermans et al. 2023).

Combining Equation 1.7, Equation 1.3 and Equation 1.4, one can derive another formulation of calcification

$$Ca^{2+} + 2HCO_3^{-} \rightleftharpoons CaCO_3 + CO_2 + H_2O \tag{1.8}$$

This calcification occurs in surface waters, releasing CO_2 in the surrounding waters and subsequently to the atmosphere (0.26-1.19 Pg C year^{-1} according to Neukermans et al. (2023)). That is why this pump is sometimes also referred to as the carbonate counter pump (Zeebe 2012). However, the dissolution of $CaCO_3$ that mainly occurs at depth increases the DIC concentration in contrast with the calcification (see Equation 1.8). In all, Sarmiento (2006) estimated that the carbonate pump contributes to 20% of the observed DIC gradient.

1.2.3.3 Biological pump

Also known as the soft-tissue pump (Volk and Hoffert 1985), the biological carbon pump (BCP), is defined by IPCC (2019) as "a series of ocean processes through which inorganic carbon is fixed as organic matter by photosynthesis (Equation 1.9) in sunlit surface water and then transported to the ocean interior, and possibly the sediment, resulting in the storage of carbon".

$$CO_2 + H_2O \rightarrow CH_2O + O_2 \tag{1.9}$$

The carbon flux leaving the surface layer for the ocean interior is referred to as the export flux (Siegel et al. 2022). For convenience, the export depth is often set at 100 m but Buesseler et al. (2020) strongly emphasized that carbon flux-related studies should now use the base of the euphotic zone (EZ, where there is enough light for net primary production (NPP)) as the export depth to clearly differentiate the layer where particulate organic carbon (POC) is produced (i.e. via photosynthesis) and where POC is consumed (i.e. remineralized). This remineralization (or respiration) consists in the conversion of organic matter back to inorganic forms (i.e. nutrients and DIC) by heterotrophic organisms (Siegel et al. 2022) such as zooplankton and fish.

Photosynthesis and respiration significantly enhance the DIC gradient such that the BCP would thus be responsible for the remaining 70% of the observed DIC gradient (Sarmiento 2006). In an ocean without biology, there would be no production of organic matter in the EZ (consuming DIC) and no remineralization in the ocean interior (producing DIC) resulting in a weaker DIC gradient. In fact, DeVries (2022) calculated that without the present DIC gradient, the ocean carbon inventory would be roughly 10% smaller and the atmospheric CO_2 levels twice as high. Similarly, Kwon et al. (2009) showed that a deepening of the remineralization depth (i.e. where 63% of sinking carbon is respired) would decrease atmospheric CO_2 concentrations due to the redistribution of respired carbon from intermediate waters to bottom waters (i.e. increased DIC gradient).

The sinking carbon that is not remineralized is said to be sequestered. The sequestration (storage) of carbon is usually defined as the long-term removal of CO_2 (or other forms of carbon) from the atmosphere on climatically significant time scales (IPCC 2019; Boyd et al. 2019; Siegel et al. 2022). While this definition seems logical, it does not specify precisely what is meant by "climatically significant time scales". In what follows, I will use the 100-year time horizon to refer to carbon sequestration (unless specified otherwise) as used by some BCP studies (e.g. Lampitt et al. 2008; Passow and Carlson 2012; National Academies of Sciences 2022).

The amount of carbon sequestered by the BCP mainly depends on its strength and its efficiency. In this manuscript, the strength of the BCP is defined as "the magnitude of the POC flux at a reference export depth" (Claustre et al. 2021) and its efficiency (also known as transfer efficiency) is defined as the fraction of POC flux transported to some reference depth below the export depth (Buesseler et al. 2020; Claustre et al. 2021).

Information Box 1. BCP and blue carbon

The BCP is a natural-based solution for carbon sequestration (Equation 1.9). However, natural-based solutions for carbon sequestration are generally aligned with the concept of 'blue carbon' defined by IPCC (2019) as "all biologically-driven carbon fluxes and storage in marine systems that are amenable to management" which usually encompasses only coastal ecosystems (IPCC 2019; Lovelock and Duarte 2019). Coastal blue carbon ecosystems (e.g. mangroves, tidal marshes, seagrass meadows) are thought to store in their living biomass (years to decades) and sediment (millenia) more than 30 Pg C with an estimated absorption of ~0.3 Pg C year^{-1} (Macreadie et al. 2021) though those numbers should be taken with caution because there are major uncertainties in the distribution of seagrass meadows and tidal marshes (Macreadie et al. 2021) as well as in carbon burial rates (Williamson and Gattuso 2022). In spite of that, the current expectation of additional carbon removal by coastal blue carbon by 2100 should be around 25-30 Pg C (Gattuso et al. 2021; Williamson and Gattuso 2022), that is the equivalent of 2.5-3 years of current anthropogenic emissions (Friedlingstein et al. 2022).

Estimates of global carbon export range between 5 and 12 Pg C year^{-1} (Laws et al. 2000; Dunne et al. 2007; Henson et al. 2011; Siegel et al. 2014; DeVries and Weber 2017; Nowicki et al. 2022) with only 0.02-0.4 Pg C year^{-1} reaching the sediment (Dunne et al. 2007; Hayes et al. 2021; Nowicki et al. 2022) where carbon will be sequestered for millions of years. Almost all of the exported organic carbon will therefore be remineralized and sequestered away from the atmosphere on time scales ranging from months to millennia. (Siegel et al. 2022).

Nonetheless, it should be emphasized that in contrast to the solubility pump, the BCP is not responsible for the absorption of excess atmospheric CO_2 released by anthropogenic activities. First, as explained in Sarmiento (2006), atmospheric CO_2 levels were stable for several thousand years before the industrial revolution started, therefore it is assumed that the BCP was operating at steady state. Second, photosynthesis is mostly controlled by light and nutrients availability, not by CO_2.

However, climate change is most likely going to impact the biological (e.g. shift in phytoplankton communities), physical (e.g. temperature) and chemical (e.g. nutrients availability, acidification) drivers of the BCP (Riebesell et al. 2009; Passow and Carlson 2012; Bopp et al. 2013) whose long-term carbon sequestration capacity remains uncertain (Passow and Carlson 2012; Turner 2015; Henson et al. 2022 ; Wilson et al. 2022; DeVries 2022).

1.2.3.4 Microbial pump

Unlike the three previous carbon pumps, the microbial carbon pump (MCP) was only introduced recently by Jiao et al. (2010) as “a conceptual framework to address the role of microbial generation of recalcitrant dissolved organic matter[1] and relevant carbon storage”. In simple terms, it is a suite of marine microbial mechanisms that produce longer-lived DOC such as semi-refractory, refractory and ultra-refractory DOC that have an average lifetime of respectively 205, 16,000 and 40,000 years (Legendre et al. 2015).

The term ‘pump’ is attributed to the MCP because it maintains a gradient between $DOC_{<100\ years}$ (14 Pg C) and $DOC_{>100\ years}$ (non-bioavailable DOC, 636 Pg C) where 100 years corresponds to the 100-year time horizon that I use to refer to carbon sequestration.

In contrast with the other pumps which are depth-dependent, the MCP sequesters carbon by biochemically transforming DOC to non-bioavailable DOC. This process occurs at all depths, making the MCP depth-independent (Legendre et al. 2015).

In order to fully understand the fate of DOC and DIC in the ocean, one would need to integrate both classic carbon pumps and the MCP. However, in this manuscript, I will only focus on the BCP, which was considered as a single process until recently.

1.3 A new paradigm for the BCP

In the frame of the BCP, global carbon budgets have generally been imbalanced such that the exported POC was up to 2-3 orders of magnitude less abundant than it would need to be to sustain heterotrophic respiration in the mesopelagic zone and beyond (Burd et al. 2010; Turner 2015). This imbalance raises one question: are we currently underestimating the export carbon flux or are we overestimating the heterotrophic respiration?

The last part of the question is out of the scope of this manuscript but it should be said that a lot of uncertainties surround those carbon deficits, namely parameters used to estimate the metabolic activity of deep ocean organisms as well as deep food web dynamics and unquantified carbon sources such as the contribution of slowly settling particles and better estimation of POC fluxes (Burd et al. 2010; Martin et al. 2020).

Regarding the latter, Boyd et al. (2019) published a paper in which they review the BCP by adding new biological and physical mechanisms[2] that inject suspended and sinking particles to depth (Figure 1.3). A better understanding of those mechanisms (see next subsections) could help to close the carbon budget.

---

[1] i.e. dissolved organic matter resistant to microbial utilization that can persist in the ocean interior for thousands of years.

[2] More specifically, as stated by Claustre et al. (2021) “the word ‘biological’ in BCP refers to the transfer of biogenic material to depth, mediated by either biological or physical processes.”

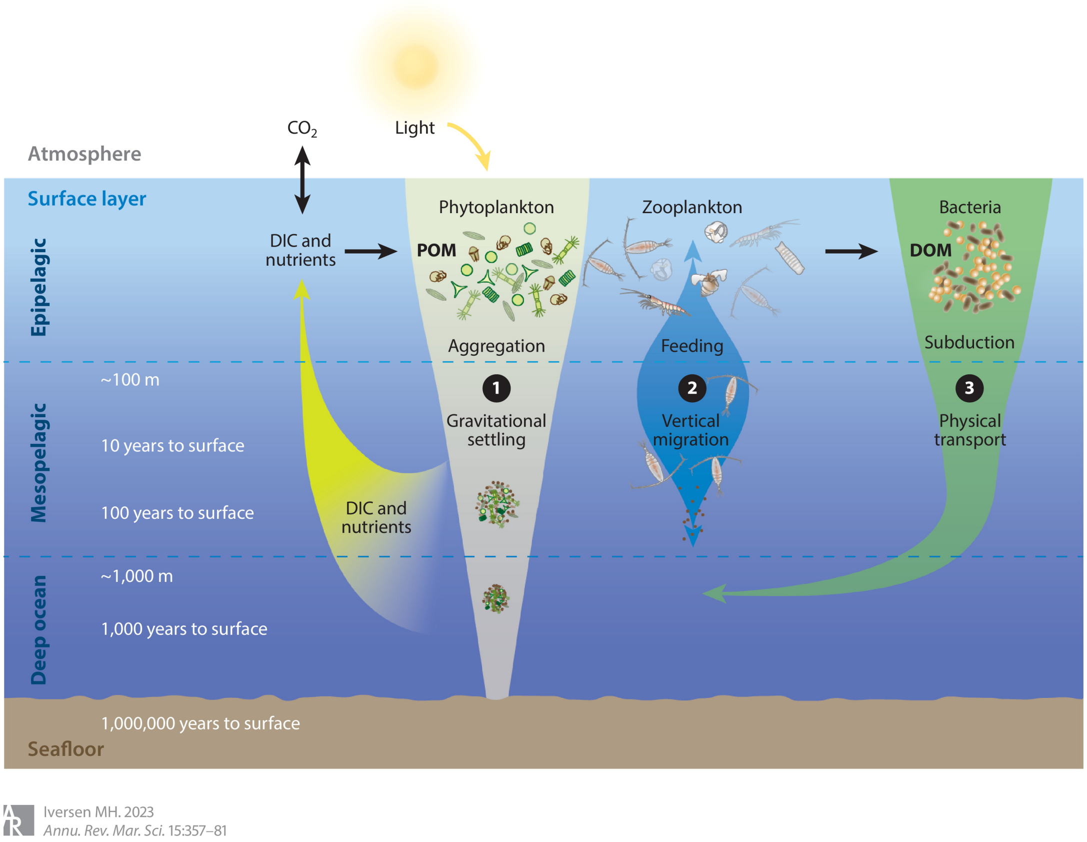

Figure 1.3: Illustration of the three main mechanisms through which the BCP exports carbon downwards. 1) Production of POC and transport to depth by gravitational settling. 2) Vertical migration of zooplankton that feed at the surface and metabolize the ingested carbon at depth (e.g. production of fecal pellets). 3) Subduction of DOC and suspended POC via mixing processes. Sequestration times for DIC are set depending on the depth at which POC and DOC are exported. Figure taken from Iversen (2023).

1.3.1 Biological gravitational pump

The best known biological pump is the gravitational carbon pump (BGP). It consists in the gravitational settling (i.e. sinking) of POC[3] to the deep ocean and it is the main contributor (60-70%) of the export flux (Boyd et al. 2019; Nowicki et al. 2022). Historically, the downward POC flux was directly measured using sediment traps (Martin et al. 1987; Honjo et al. 2008) and indirectly measured using thorium-234 (^{234}Th) deficits as a POC flux proxy (e.g. Buesseler et al. 2006). More recently, the advent of underwater cameras such as the Underwater Vision Profiler 5 (UVP5) (Picheral et al. 2010) allowed the direct measurement of particle size distributions (PSDs, also referred to in the literature as particle size spectra (PSS)) that could then be converted to carbon fluxes (e.g. Guidi et al. 2008).

1.3.2 Physically mediated particle injection pump

The physically mediated particle injection pump (also referred to as the mixing pump in the literature) consists of three separate pumps: the mixed layer pump, the eddy subduction pump and the large-scale subduction pump (Boyd et al. 2019). Contrarily to the BGP, all three pumps also transport DOC to depth where it is injected along with suspended (i.e. neutrally buoyant) and slow-sinking POC below the EZ on different spatial and time scales.

The mixed layer pump can be defined as a 1D mechanism through which organic carbon is exported below the EZ when there is a deepening of the mixed layer followed by the formation of a new shallower mixed layer, isolating the exported carbon from the surface (Dall'Olmo et al. 2016). This pump can occur at different time scales but it is mainly related to the building of the summer stratification in mid and high latitude regions where seasonal variations of the mixed layer are the strongest (Dall'Olmo et al. 2016; Boyd et al. 2019).

The other two pumps are both 2D spatial mechanisms (i.e. they transport POC and DOC vertically and laterally). The eddy subduction pump is associated with fronts and eddies that create a strong vertical circulation that transport particles on time scales of days across horizontal spatial scales of 1-10 km (Omand et al. 2015; Resplandy et al. 2019). The large-scale (100-1000 km) subduction pump corresponds to the slow advective transport of carbon associated with the meridional overturning circulation and Ekman pumping (Levy et al. 2013; Claustre et al. 2021; Siegel et al. 2022).

In all, the mixing pump would represent at least 20% of the export flux by the BCP according to Nowicki et al. (2022) although large uncertainties still remain (see Figure 2C in the paper of Boyd et al. (2019)).

---

[3] There obviously exists a gravitational settling of particulate inorganic carbon but in this manuscript, I focus on the BCP which was defined earlier as only focused on organic carbon as opposed to the carbonate pump.

1.3.3 Biologically mediated particle injection pump

The biologically mediated particle injection pump is usually referred to as the vertical migration pump (VMP) (Boyd et al. 2019). It consists on the vertical migration of zooplankton or fish (Steinberg and Landry 2017; Saba et al. 2021) that directly inject POC (e.g. fecal pellets) below the EZ at the depth of their migration. This pump can act on daily as well as on seasonal time scales. In the case of the diel (i.e. daily) migration pump, animals feed at the surface at night and then migrate to depth during daytime to avoid visual predation (Siegel et al. 2022), metabolizing ingested food at depth[4], by-passing the EZ directly (Steinberg and Landry 2017). In the case of the seasonal migration pump, carbon-rich lipids accumulated in the EZ during summer are catabolized by hibernating copepods at depth, between 600 m and 1,400 m, where they shunt carbon below the permanent pycnocline (Jónasdóttir et al. 2015). This pump is also referred to as the seasonal lipid pump (Jónasdóttir et al. 2015).

In his model, Nowicki et al. (2022) estimates that the VMP accounts for approximately 10% of the total export flux by the BCP, albeit large uncertainties remain on the number of migrating animals and their migration depth. The VMP would thus export less organic carbon than the mixing pump but its sequestration potential would be higher (Table 1.1). In contrast to the mixing pump that mostly acts on DOC, migrating animals release rapid sinking fecal pellets that would reach depths such that subsequent remineralized DIC would be removed from the surface for longer time periods (Table 1.1). As a result, it is estimated that the diel migration pump could potentially sequester 60% as much carbon as the BGP (Boyd et al. 2019).

However, there are still many uncertainties regarding the magnitude of the VMP (Aumont et al. 2018; Archibald et al. 2019; Gorgues et al. 2019) and its sequestration potential (Boyd et al. 2019; Pinti et al. 2023) thus its importance for a better understanding of the BCP.

1.4 The fate of carbon

1.4.1 Biological processes impacting the downward POC flux

Sinking particles are part of a pool of highly diversified materials combining fecal pellets, phytodetritus from sinking phytoplankton, dead zooplankton and organic aggregates referred to as marine snow (i.e. macroscopic organic aggregate > 0.5 mm) (Alldredge and Silver 1988; Turner 2015; Steinberg and Landry 2017). Settling velocities for such particles range from 10-100 m day^{-1} up to 1 km day^{-1} for large salp fecal pellets (Steinberg and Landry 2017; Iversen 2023).

Marine snow is paramount for both the BCP (see Section 1.3) and the support of marine life within the mesopelagic domain (Burd et al. 2010). The remineralization of organic matter

---

[4] They can also die at depth during the day (or their overwintering in the case of the seasonal migration pump) which also contributes directly to the export of carbon at depth.

by heterotrophic organisms releases CO_2 in the water column that will be released back to the atmosphere in a time frame depending both on its geographical location and depth (see Section 1.4.3). Therefore, understanding how biological processes interact with the downward POC flux and where the bulk of the remineralization occurs is important to better understand the efficiency of the BCP.

The Martin curve (Martin et al. 1987) is probably the best known POC flux attenuation curve (Equation 1.10 and Figure 1.4). It is a power-law function described as follow

$$F_z = F_{z_{export}} \left(\frac{z}{z_{export}} \right)^{-b} \tag{1.10}$$

where F_z, z_{export} and b are, respectively, the estimated POC flux at a depth z, the depth of the export flux and the remineralization factor. The latter is adimensional and often set at 0.86 (Martin et al. 1987) although it is well known that the magnitude of flux attenuation varies regionally (and temporally) due to the variability in food web structures beneath the EZ (Passow and Carlson 2012). Geographically variable (Henson et al. 2012) and regionalized (Guidi et al. 2015) estimations of b were proposed to account for non-uniform remineralization at global scale.

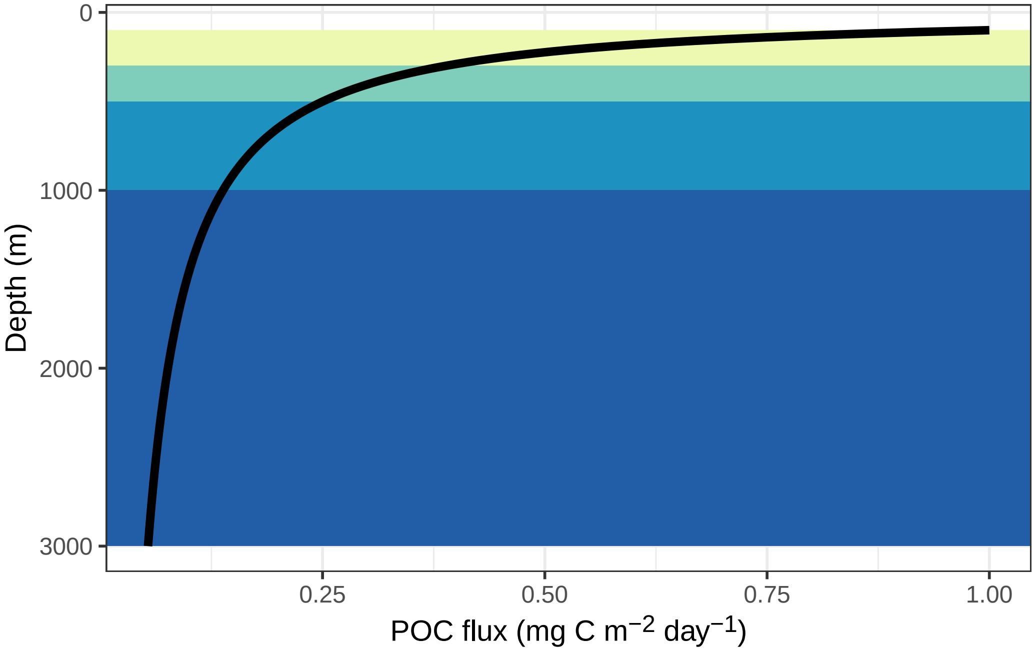

Figure 1.4: Typical attenuation curve of the POC flux obtained with Equation 1.10. The color-coded layers represent regions with carbon-specific degradation rate, decreasing with depth. Figure inspired from Iversen (2023).

Based on the Martin curve, Iversen (2023) divided the water column in 4 layers (Figure 1.4): the upper mesopelagic layer (export depth - 300 m) where there is a rapid attenuation of the downward POC flux, the mid-mesopelagic layer (300 - 500 m) and the lower mesopelagic layer (500 - 1,000 m) where both layers show two levels of intermediate attenuation and the bathypelagic layer (1,000 m - seafloor) where the attenuation is relatively uniform. For each layer, Iversen (2023) estimated a carbon-specific degradation rate in order to better understand the processes responsible of this attenuation. As a result, Iversen (2023) suggests that the POC attenuation in the upper mesopelagic layer is the combined action of microbial degradation and zooplankton that graze on settling aggregates. Here, zooplankton are the main responsible for the attenuation whereas in the middle and lower mesopelagic layers, microbial degradation takes over due to the decrease in zooplankton abundance. Finally, the relatively constant degradation occurring below 1,000 m in the bathypelagic zone could be explained by the increasing pressure and decreasing temperatures on microbial communities.

The impact on the downward POC flux by zooplankton feeding on aggregates are numerous (Turner 2015; Iversen 2023). On the one hand, aggregate feeding, filter-feeding, direct ingestion of fecal pellets (i.e. coprophagy) and fragmentation of large aggregates to small slower-sinking particles will likely decrease the downward POC flux. On the other hand, the ingestion of slow-sinking cells to defecation of large and compact (i.e. fast-settling) fecal pellets will increase it. The remaining organic matter (~15% according to Turner (2015)) will then be degraded by microbial communities. In the end, only a small fraction of the exported carbon will reach the sediment where it will be stored for millions of years.

1.4.2 Physical properties influencing the downward POC flux

The settling speed w is the most important physical parameter controlling the remineralization depth (Figure 1.5) of aggregates and fecal pellets (Laurenceau-Cornec et al. 2015). Using Stokes' Law for a spherical particle at low Reynolds number, the sinking speed can be expressed as

$$w = \frac{g}{18\mu}(\rho_p - \rho_w)d^2 \tag{1.11}$$

where g is the gravitational acceleration, μ is the dynamic viscosity of seawater, ρ_p and ρ_w are the particle and seawater densities and d is the particle diameter. If one assumes that changes in dynamic viscosity are negligible (De La Rocha and Passow 2007) compared to changes from the remaining parameters (i.e. this assumption is reasonable based on the fact that μ can roughly vary by a factor 2 (Sharqawy et al. 2010)), then w should mostly be proportional to the excess density $\Delta\rho$ (i.e. $\rho_p - \rho_w$) and d. It is however a simplification of reality because most aggregates are not spherical and have fractal geometries (Logan and Wilkinson 1990; Logan and Kilps 1995; Laurenceau-Cornec et al. 2020).

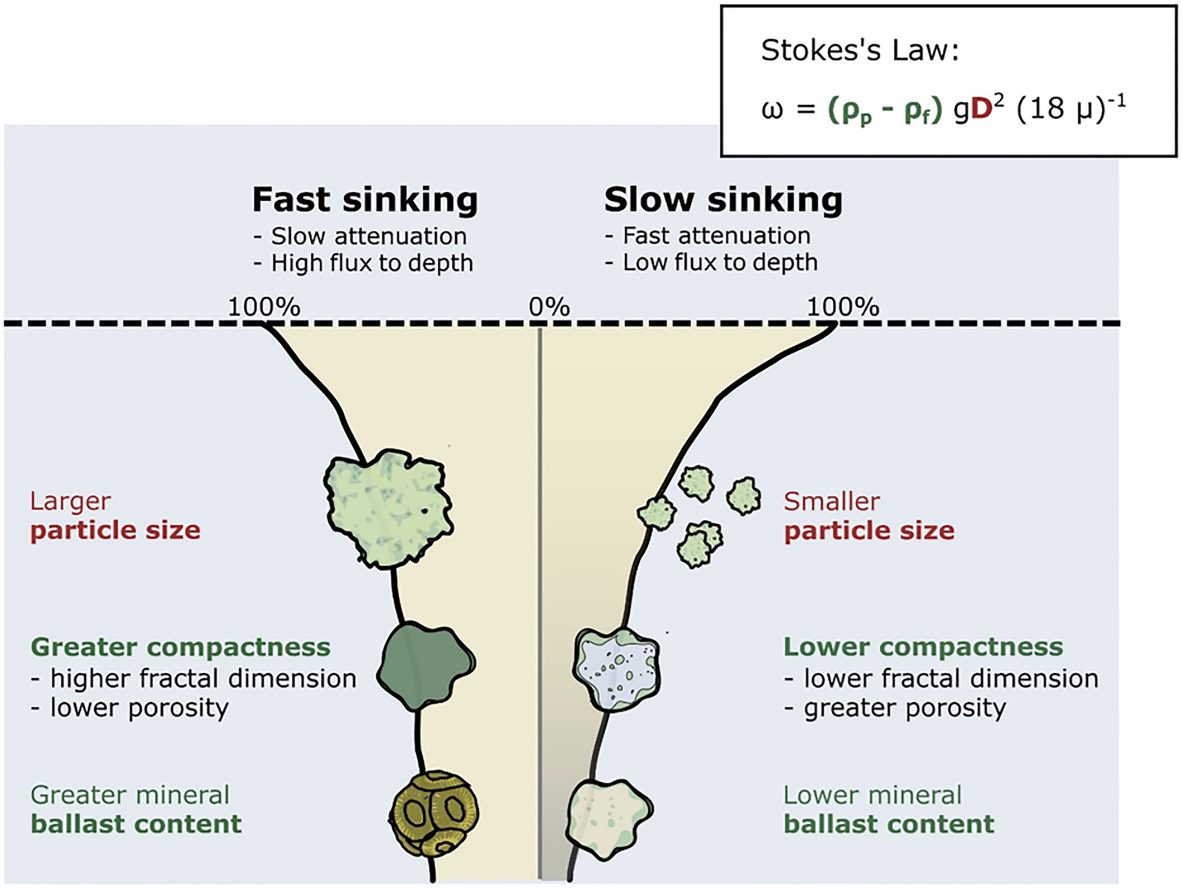

Figure 1.5: Illustration of the main factors influencing the sinking velocity following Stokes' Law and hypothetical attenuation fluxes (in % of export flux) with depth (vertical axis) for slow and fast sinking particles. The latter shows that slow sinking particles experience higher rates of flux attenuation due to increased duration of exposure to remineralization hence contributing less to deep carbon sequestration. Figure taken from Williams and Giering (2022).

Taking this into consideration, several processes can impact the sinking speed of POC such as aggregation (e.g. physical coagulation, incorporation of small particles into fecal pellets (i.e. repackaging)), disaggregation or fragmentation (either physically (e.g. fluid shear) or biologically by microbial degradation and zooplankton feeding), solubilization to DOC by bacteria and mineral ballasting (Turner 2015).

The driving factors of the sinking speed are nevertheless subject to caution. It would make sense that the quadratic dependence of w to the aggregate size would favor d as the main driver. However, aggregates are far from being perfect theoretical objects for Equation 1.11 and the excess density as the main driver is disputed by some authors such as Iversen and Lampitt (2020).

To the best of my knowledge, the most emblematic case of discussions around this question is the mineral ballast hypothesis (De La Rocha and Passow 2007). Mineral ballasting consists in the inclusion of biominerals such as opal (i.e. silicate) and calcite or lithogenic material such as dust that are thought to increase $\Delta\rho$ on the one hand and protect them from microbial degradation on the other hand (Armstrong et al. 2001; Francois et al. 2002; Klaas and Archer 2002). However, several studies argued otherwise. Passow (2004) stipulated that biominerals could instead be collected (i.e. scavenged) and transported downwards by sinking aggregates. Ploug et al. (2008) did not measure significant differences in microbial degradation of non ballasted vs. ballasted material. Finally, Passow and De La Rocha (2006) developed an experiment to investigate the relationship between the incorporation of biominerals into aggregates and their sinking speed. They showed that this relationship was not straigthforward due to the fact that the inclusion of biominerals fragmented aggregates into smaller but denser particles which could either decrease (smaller size) or increase (denser particles) their sinking speed. Other studies on the ballasting effect have been published since but even 20 years after its proposition, no global ballasting mechanism has been found (Neukermans et al. 2023).

The size of aggregates was usually thought to be a key predictor of settling velocity (e.g. Passow and De La Rocha 2006) which is coherent with Equation 1.11. However, Iversen and Lampitt (2020) did not find evidence for a size-sinking relationship therefore suggesting that excess density would be the main controlling factor. Because the sinking speed determines the time available for degradation in the water column, it also directly impacts the potential for carbon sequestration. With all things considered, there is thus a need for direct measurements of morphological characteristics (size, composition, porosity and density) of particles to better estimate their settling velocities (Giering et al. 2020b; Iversen and Lampitt 2020; Williams and Giering 2022; Iversen 2023).

1.4.3 Sequestration potential

Once injected in the ocean interior (Table 1.1), the POC flux originating from the five particle injection pumps is merged back with the BGP. How long is this carbon going to be sequestered from the atmosphere is one of the key questions of carbon cycle studies (Claustre et al. 2021).

Table 1.1: Range of depths generally reached by POC and DOC via the six BCPs (Claustre et al. 2021) and sequestration time potentials evaluated by the model of Boyd et al. (2019) with an average estimation from the model of Nowicki et al. (2022) in brackets. None means that a pump does not transport DOC. N/A means that the pump was not evaluated in the model. (a) 1,400 m corresponds to the overwintering depth of *Calanus finmarchicus* as observed by Jónasdóttir et al. (2015). (b) 54 years depicts the mean sequestration time of the mixing pump, without the contribution of the eddy subduction pump (c) Migration of mesopelagic fish was neglected in the model.

Pump	POC export/injection depth range	DOC injection depth range	Sequestration time potential (years)
Gravitational	export depth - sediment	None	N/A (142)
Mixed layer	200 - 1,000 m	200 - 1,000 m	25 - 100 (54^b)
Eddy subduction	150 - 400 m	150 - 400 m	up to 150 (N/A)
Large-scale subduction	200 - 1,000 m	200 - 1,000 m	25 - 100 (54^b)
Diel migration	200 - 600 m	None	up to 250 (150^c)
Seasonal migration	600 - 1,400 m^a	None	up to 500 (N/A)

A great majority of studies related to carbon sequestration by the BCP usually assumed that only the fraction of the exported carbon reaching 1,000 m was sequestered (e.g. Lampitt et al. 2008; Passow and Carlson 2012). However, Siegel et al. (2021) revised this common assumption by proposing that carbon sequestration could occur on the entire water column, with varying efficiencies (i.e. sequestration times). To come to this conclusion, Siegel et al. (2021) used an ocean inverse circulation model to assess the time over which injected CO_2 (direct injections at different depths) remains sequestered from the atmosphere. For this, they computed a factor f_τ corresponding to the fraction of injected CO_2 that will be stored away from the atmosphere for a given time τ. Their results show that f_τ increases with depth and varies geographically. They also showed that for a time horizon of 100 years (i.e. $\tau = 100$) and an injection depth at 1,000 m, there is a non negligible leakage of CO_2 back to the atmosphere with strong regional disparities (e.g. high leakage in the Northwest Atlantic compared to virtually no leakage in the Central Eastern Pacific).

So far, we have seen that significant uncertainties remain in the estimation of carbon export as well as the sequestration time by the different export pathways of the BCP. To address this issue, biogeochemical models and observation tools are continuously being improved to further our understanding of the BCP (see Chapter 2).

2 Modeling and observing the BCP

2.1 Biogeochemical models

The study of the BCP is of paramount importance to answer the question of how much carbon is exported and how much of the exported carbon will be sequestered. In order to achieve this goal, ocean modelers have developed different kinds of biogeochemical models to better quantify the different export pathways of the BCP.

Because measuring directly the POC export flux is challenging, it is common to estimate the fraction of the total NPP that is exported (i.e. export efficiency) (Henson et al. 2011). This fraction is usually referred to as the $e-ratio$ (see Information Box 2 and Figure 2.1).

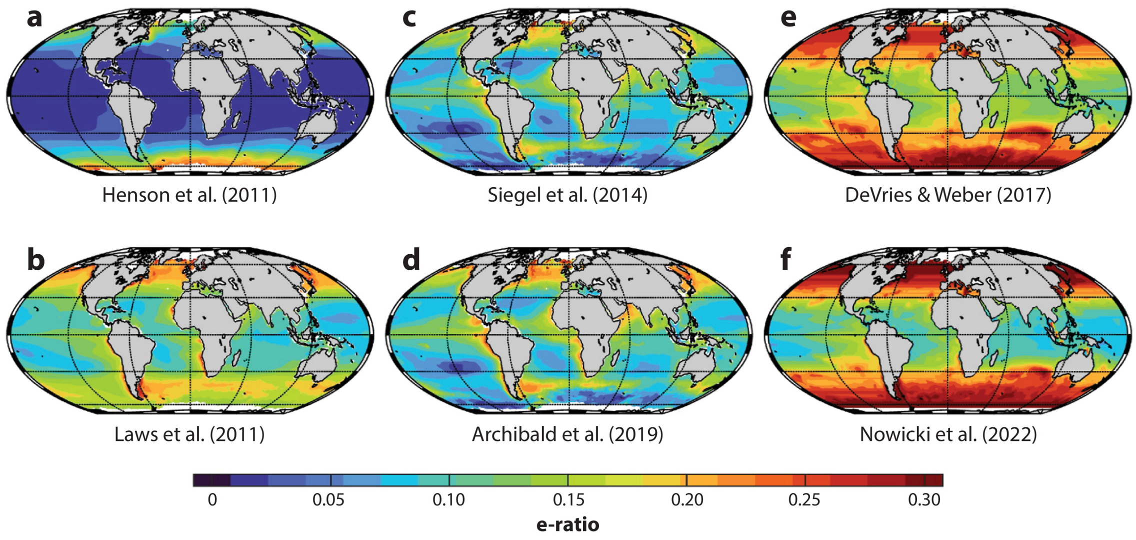

Siegel DA, et al. 2023
Annu. Rev. Mar. Sci. 15:329–56

Figure 2.1: $e-ratio$ estimations obtained with different types of models: empirical models (a, b), food-web models (c, d) and data-assimilated models (e, f). Note that the export value computed by Laws et al. (2011) (9 Pg C year^{-1}) was recomputed by Siegel et al. (2022) (6.9 Pg C year^{-1}), therefore the $e-ratio$ map presented here might not be representative of the one we would have got with the initial export value. Figure taken from Siegel et al. (2022).

Information Box 2. Net primary production and export ratio

Total net primary production includes new production (NP, mainly fueled from the upwelling of nitrogen from deeper water to the EZ) and regenerated production (RP, fueled with nitrogen recycled through the food web within the EZ) (Dugdale and Goering 1967). The ratio of new production over total production is referred to as the $f - ratio$ (Eppley and Peterson 1979).

$$f - ratio = \frac{NP}{NP + RP}$$

In a steady state system, new production equals export production therefore the $f - ratio$ should be equal to the ratio of export production (EP) to total NPP, referred to as the $e - ratio$ by Laws et al. (2000).

$$e - ratio = \frac{EP}{NPP}$$

I will hereafter briefly describe a non exhaustive list of biogeochemical model types to illustrate how the export production can be estimated using the $e - ratio$.

Henson et al. (2011) and Laws et al. (2011) (panels a and b in Figure 2.1) are both empirical models. Henson et al. (2011) parameterized the $e - ratio$ as a decreasing function of sea surface temperature (SST, derived from satellite observations (see Figure 2.2)) tuned on a compilation of ^{234}Th-derived export measurement (see Section 2.2.1) for a total export estimated at 5 Pg C year^{-1}. Laws et al. (2011) modelled the $e - ratio$ as a decreasing linear function of SST and a power-law function of NPP whose parameters were determined using particle export estimates based on estimates of new production (nitrogen-based) and ^{234}Th and sediment trap export flux data compiled by Dunne et al. (2005). They estimated a total export of 9 Pg C year^{-1}.

Siegel et al. (2014) and Archibald et al. (2019) (panels c and d in Figure 2.1) are both food-web models (see Information Box 3). Siegel et al. (2014) used a mechanistic approach using satellite observations (NPP, PSS and phytoplankton carbon concentrations, see also Figure 2.2) to estimate the export of the BGP (6 Pg C year^{-1}). Archibald et al. (2019) added a new module to the model of Siegel et al. (2014) in order to incorporate the diel vertical migration of zooplankton for a total export of 6.5 Pg C year^{-1}.

Information Box 3. Food-web model

A simple food-web model is the NPZD model, which consists of four state variables: Nutrient (DIN), Phytoplankton (PHYTO), Zooplankton (ZOO) and DETRITUS. The arrows represent the flows (or interactions) between the state variables (e.g. f1 represents the DIN uptake by PHYTO, f2 represents the grazing of PHYTO by ZOO, etc.), describing the sources and sinks of a given state variable (Soetaert and Herman 2008). Forcing functions (or external variables) are external factors (i.e. not computed by the model) imposed (i.e. forced) to the model because they drive or regulate the system. Examples of forcing functions (among many others) in ecological models are light intensity (represented here by the solar radiation), temperature or wind. Finally, a model usually contains output variables (represented here by the Chlorophyll) that allow the comparison of the model to reality (Soetaert and Herman 2008).

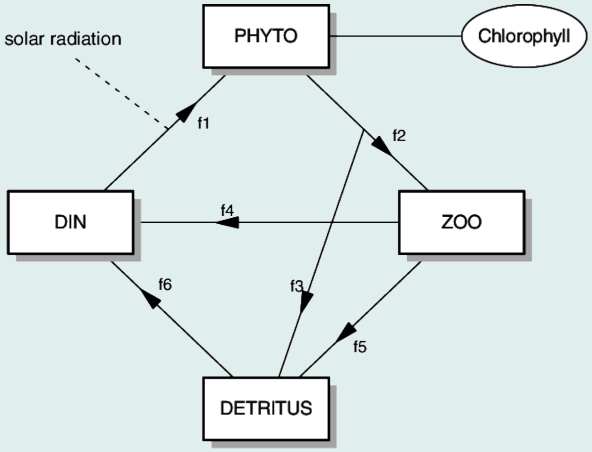

Figure taken from Soetaert and Herman (2008).

DeVries and Weber (2017) and Nowicki et al. (2022) (panels e and f in Figure 2.1) are both data-assimilated models. These models operate by nudging model solutions to the observed fields (e.g. satellite and/or in situ data) or by optimizing model parameters to the observed fields (Siegel et al. 2022). DeVries and Weber (2017) combined both satellite data (NPP and PSS) and in situ observations (POC fluxes, DOC concentrations and dissolved O_2 distributions) to assess the carbon export and its transfer in the mesopelagic zone using a steady state ocean circulation inverse model (i.e. the circulation component of their model). Their carbon export estimates range between 7.3 and 8.6 Pg C year^{-1}, depending on the selected export depth (i.e. respectively, 100 m and the euphotic depth). Nowicki et al. (2022) added a two-phytoplankton/two-zooplankton food-web model with a migration zooplankton component to the model of DeVries and Weber (2017) in order to estimate the magnitude of each BCP export pathway. In all, Nowicki et al. (2022) estimated a carbon export of 10 Pg C year^{-1}.

2.1.1 Model uncertainties

When we compare the $e - ratio$ maps (Figure 2.1) or the carbon export estimations of only six biogeochemical models (see Section 2.1), we already observe significant differences. On the one hand, we see an increase in model complexity from empirical models to data-assimilated inverse models thanks to the increase in the quantity and quality of observations as well as a deeper understanding of the BCP (Section 1.3). On the other hand, each degree of complexity inevitably accumulates more uncertainty due to the increasing number of processing and modeling steps (Figure 2.2).

Current BCP models still disagree on the estimation of the actual carbon export and its response to climate change (Henson et al. 2022). However, the ongoing increase in deployments of autonomous platforms and the development of new sensors is providing new opportunities to enhance the parametrization of key biogeochemical processes to reduce uncertainties and better estimate carbon export and sequestration.

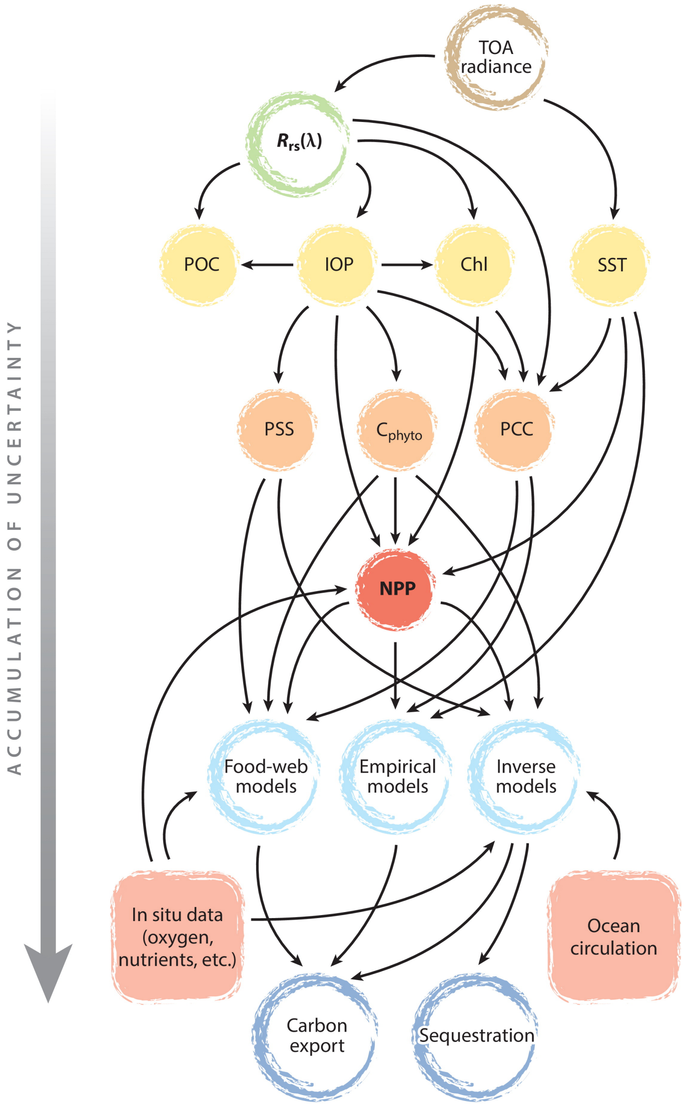

Siegel DA, et al. 2023
Annu. Rev. Mar. Sci. 15:329–56

Figure 2.2: Top of the atmosphere (TOA) radiance is converted into remote sensing reflectance $R_{rs}(\lambda)$, which is the ratio of the radiance leaving the water surface to the downwelling irradiance incident on the sea surface at a given wavelength λ. Using TOA and $R_{rs}(\lambda)$, primary products (yellow circles) can be derived (e.g. POC, inherent optical properties (IOP), chlorophyll (Chl) or sea surface temperature (SST). Those primary products can be used in numerical models (e.g. empirical relationships) to compute secondary products (orange and red circles) such as the phytoplankton commmunity composition (PCC), PSS, phytoplankton carbon concentrations (C$_{phyto}$) and the NPP. Models (light blue circles) therefore incorporate primary and secondary products as well as ancillary data (red squares) either from satellite (e.g. SST), in situ data or model-based data (ocean circulation) to estimate carbon export and sequestration (dark blue circles). Figure taken from Siegel et al. (2022).

2.2 Observation tools

2.2.1 Historical measurements

In the 20th century, the downward POC flux was traditionally measured with sediment traps. Those instruments are composed of one or several collectors of sinking material whose design depends on their use and position in the water column (e.g. moored traps, surface tethered traps, drifting traps) (Honjo et al. 2008). They were extensively used (Honjo et al. 2008) but the number of measurements has been steadily decreasing since 2004, reaching less than 500 measurements per year since 2010 (Figure 2.3).

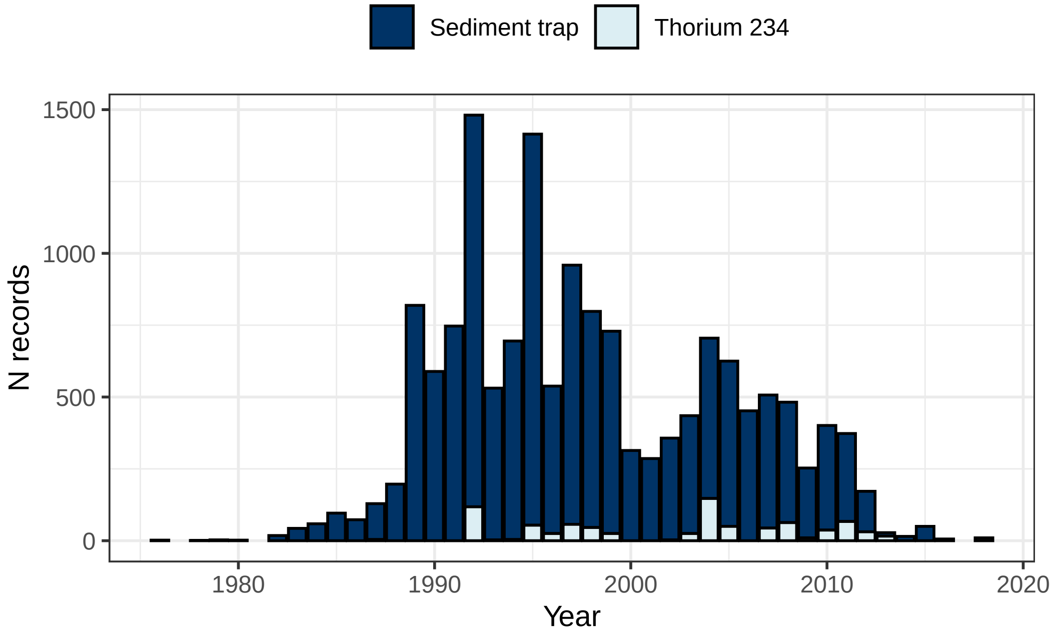

Figure 2.3: Yearly distribution of POC flux measurements by sediment traps or derived from Thorium 234 deficits. Compilation based on Table 6.2 and Table 6.3.

To estimate the downward POC flux, one therefore needs to quantify the amount of POC collected through a given area over a known time period at a given depth. However, the apparent sinking flux measured with sediment traps can be biased due to hydrodynamic issues that could result in over- or under-collection of particles (especially at the surface) or swimmers (zooplankton, small fish) that could enter sediment traps and affect the collected material or solubilization of collected material (e.g. by bacteria) (Buesseler et al. 2007).

Given some potential bias in the carbon fluxes estimated with sediment traps, independent approaches using radionuclide disequilibria have been used to assess the collection efficiency of the latter (Buesseler 1991). This method is based on the fact that ^{238}U is a conservative element in seawater (chemically inert with a half-life of 4.5 billion years) while its daughter nuclide ^{234}Th (half-life of 24.1 days) can be adsorbed onto particle surfaces and therefore be scavenged by sinking particles (Savoye et al. 2006). Consequently, the deficiency of ^{234}Th relative to ^{238}U is used as a measure of removal of surface ^{234}Th through particle scavenging (Buesseler 1991) that is then translated into a flux of exported ^{234}Th and subsequently a flux of exported POC by using a known (e.g. estimated from the material collected in sediment traps) POC/^{234}Th ratio (Buesseler et al. 2007).

While this method seems to cope with some of the issues observed in sediment traps, it also has its caveats, particularly a POC/^{234}Th ratio that varies with particle size and the fact that it only works well in the upper 100-200 m (Buesseler et al. 2007).

In all, POC fluxes derived from sediment traps and ^{234}Th have their own uncertainties and errors thus their estimates of downward POC fluxes should not be seen as ground truth. In addition, they are labor-intensive and require ship support. Their relative contribution to the estimation of POC fluxes is thus expected to keep decreasing (Figure 2.3) with the advent of alternative methods promoted by an increasing use of autonomous underwater vehicles (AUVs). However, the AUV-derived estimates have also their own caveats (see Section 2.2.3) therefore traditional methods to measure POC fluxes will still be needed to calibrate those from autonomous vehicles.

2.2.2 The potential of autonomous platforms

It is admitted that ship-based or fixed-point (e.g. moorings) measurements are potentially the most precise. However, they lack spatiotemporal coverage and they are usually not cost-effective. Consequently, oceanographers have turned to new platforms and have developed new sensors to study the marine carbon cycle and the BCP in particular.

Remote sensing data acquired with ocean color satellites have been used for a long time (Gordon et al. 1980) to study key EZ variables related to carbon export (Claustre et al. 2021) such as phytoplankton biomass (Robinson 2004), phytoplankton communities (Uitz et al. 2015) and particle size distribution (Kostadinov et al. 2009, 2010) to name a few (see also Section 2.1 and Figure 2.2). While having a wide spatial coverage, these platforms are limited to the ocean's surface and their measures can be affected by several factors such as the cloud cover or low solar elevation (e.g. Marshall et al. 1994).

Instrumented moorings have supplemented ship-based and remote sensing measurements by collecting high-resolution data at fixed locations (Chai et al. 2020). Moorings can be equipped with many sensors (e.g. sediment traps or imaging systems to study the type of sinking particles to study carbon-related variables (see Table 1 in Claustre et al. 2021)). They are therefore ideal platforms for long-term time series (e.g. Bermuda Atlantic Time-series Study (BATS) since 1988) with the disadvantage of limited spatial coverage and high maintenance costs (Chai et al. 2020).

In order to fill the scarcity of data from research vessels and moorings as well as coping with surface-constrained satellite measurements, AUVs have been developed to make in situ measurements in all weather conditions and seasons and at all times, only being dependent on their battery life and ocean currents (for drifting AUVs).

Biogeochemical-Argo (BGC-Argo) profiling floats (Figure 2.5) are probably the best known platforms to study the BCP. They are cost-effective, able to monitor biogeochemical processes at a global scale throughout the year and under all weather conditions (Chai et al. 2020). The goal of the BGC-Argo community is to develop an array of 1000 floats that measure 6 key biogeochemical and bio-optical variables: Chlorophyll a (Chla), particle backscatter (b_{bp}), oxygen, nitrate, pH and downwelling irradiance in addition to temperature and salinity (Roemmich et al. 2019). Besides this objective, the BGC-Argo community is testing new sensors (see Section 2.2.3) to explore specific topics related to the BCP (Claustre et al. 2020).

Gliders are also effective platforms to study the BCP (e.g. Omand et al. 2015). In comparison with BGC-Argo floats (Figure 2.4), gliders mostly operate in shallow waters (Chai et al. 2020) and are able to take measurements along a predefined transect due to their ability to change their internal weight distribution (Johnson et al. 2009).

In the future, new types of platforms (e.g. unmanned surface vehicles such as saildrones or wave gliders), new sensors (see Section 2.2.3) and new technologies (e.g. lidar) will be continuously deployed, improved and developed in the hope of better understanding the BCP and its components (Chai et al. 2020; Claustre et al. 2021).

2.2.3 Specific sensors on autonomous platforms for the study of the BCP

The BGC-Argo array has already demonstrated its ability to investigate some aspects of the BCP (e.g. Lacour et al. 2017, 2019; Llort et al. 2018; Briggs et al. 2020; Yang et al. 2021; Wang and Fennel 2022). However, the current array may lack some key data to further our understanding of the BCP. Therefore, other types of sensors are being added to help fill this gap.

In this work, I will focus on two sensors: a transmissometer used as an optical sediment trap (OST) and the Underwater Vision Profiler 6 (UVP6) (Picheral et al. 2021), a miniaturized version of the UVP5 (Figure 2.5).

A transmissometer measures the transmittance (T_r) of a light beam at a given wavelength. Given T_r, the beam attenuation coefficient (c) is computed as

$$c = -\frac{ln(T_r)}{r} \tag{2.1}$$

where r is the transmissometer pathlength.

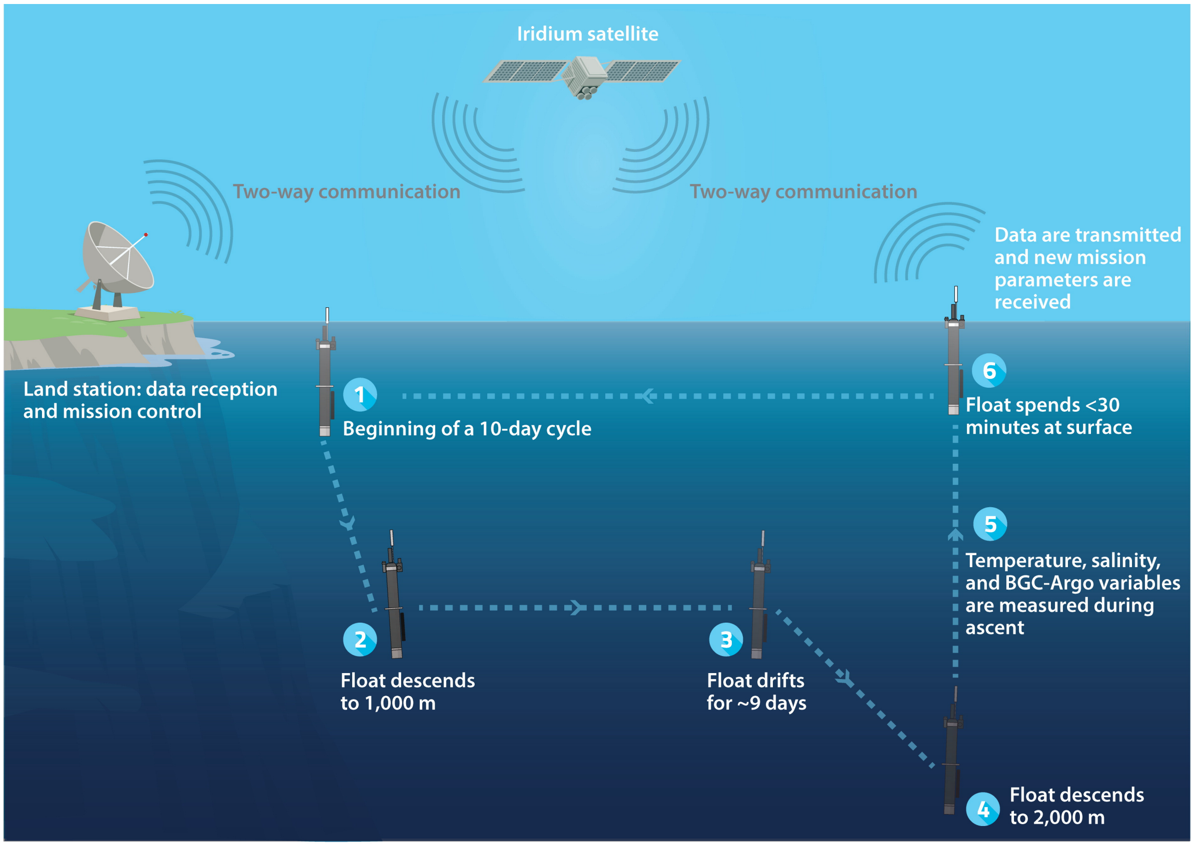

Claustre H, et al. 2020.
Annu. Rev. Mar. Sci. 12:23–48

Figure 2.4: Illustration of a typical BGC-Argo 10-day cycle. From the beginning of the cycle (1), the profiling float descends to its parking depth (2) then drifts for ~ 9 days (3) to dive at 2000 m (4) before the ascent where data are acquired (5) and transmitted to satellite while at the surface (6). Note that the profiling float can be programmed (and reprogrammed during its mission via Iridium transmission) with different configurations, depending on its utilization. For the study of the BCP, some floats could be configured to drift at multiple parking depths to study the BGP or to shorter cycle durations to study the VMP. Image taken from Claustre et al. (2020).

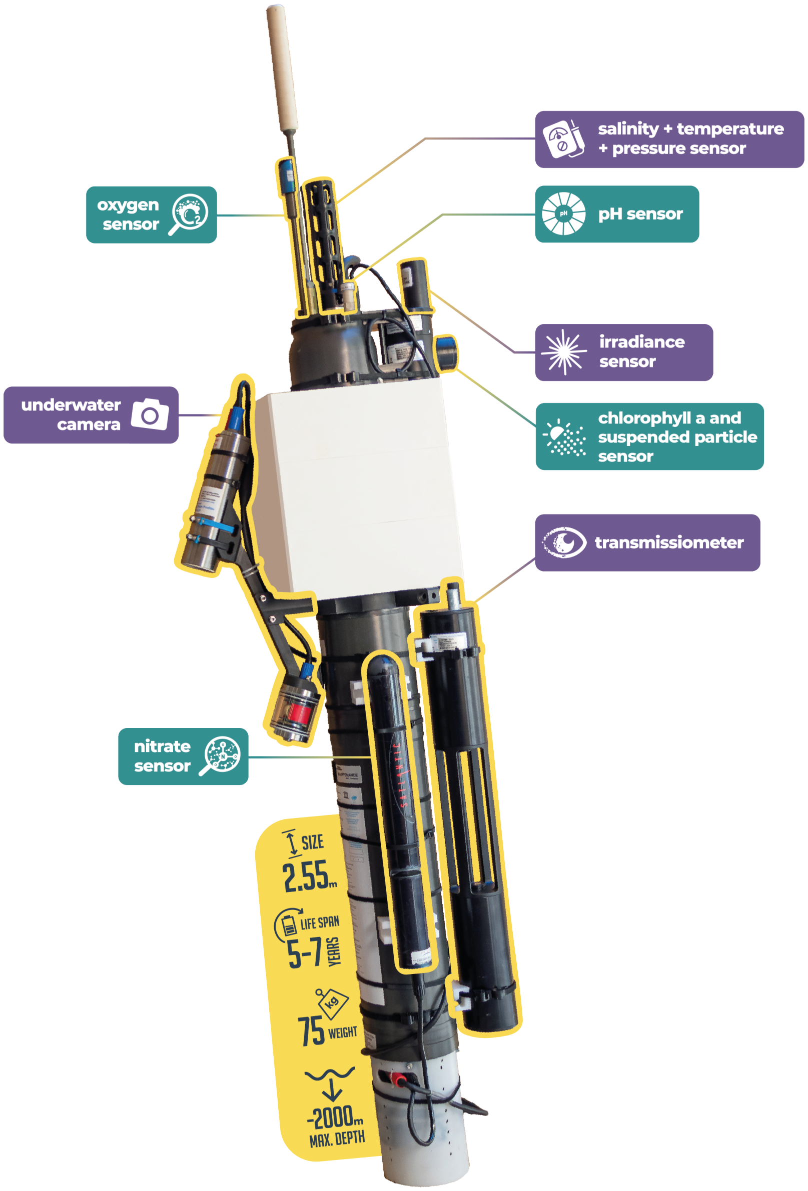

Figure 2.5: Illustration of an augmented BGC-Argo float. From top to bottom: GPS & Iridium (two-way communication) antenna, Oxygen optode, CTD (salinity, temperature and depth), pH sensor, radiometer (downwelling photosynthetic available radiation and downwelling irradiance at 380, 412 and 490 nm), fluorometer (Chla and colored dissolved organic matter) and scattering meter (b_{bp}), underwater camera UVP6 (PSD and images), transmissometer (particle beam attenuation) and nitrate sensor. @Thomas Boniface.

The value of c is the result of absorption and scattering by particles, water and dissolved substances (Zaneveld 1994). The transmissometer uses a light beam at 660 nm whose attenuation coefficient can be splitted into three components: the absorption and scattering of light by particles (c_p), the absorption by water (c_w) and the absorption by dissolved organic matter (c_{DOM}) (Jerlov 1976). At 660 nm, c_w is assumed constant at 0.364 m^{-1} and c_{DOM} is considered negligible (Jerlov 1976) hence variations of c essentially represent variations of c_p.

The use of transmissometers to characterize POC concentrations was shown by Bishop (1999) who found that POC concentrations were well correlated with c_p, regardless of ocean environment, season or depth. Subsequently, the idea of using a transmissometer as an OST was firstly applied by Bishop et al. (2004) where the magnitude of carbon export was quantified based on the particle accumulation on the upward-facing window of vertically oriented transmissometers mounted on autonomous floats while they were drifting (i.e. parked at a specific depth). This method was later improved by Estapa et al. (2013) who divided the attenuation signal into a continuous component, that is the regular accumulation of small particles on the transmissometer window and a discontinuous component resulting in positive jumps likely attributed to the deposition of (rarer) large particles (see Figure 2.6 and Chapter 4). An OST carbon flux proxy was further calibrated using codeployed sediment traps and drifting transmissometers (Estapa et al. 2017, 2023) thus allowing the conversion of c_p attenuation fluxes (units: $\mathrm{m}^{-1}\mathrm{d}^{-1}$) into carbon fluxes (units: mg C $\mathrm{m}^{-2}\mathrm{d}^{-1}$) using empirical POC-to-attenuance (ATN) ratio were ATN (unitless) is the product of c_p and the transmissometer pathlength.

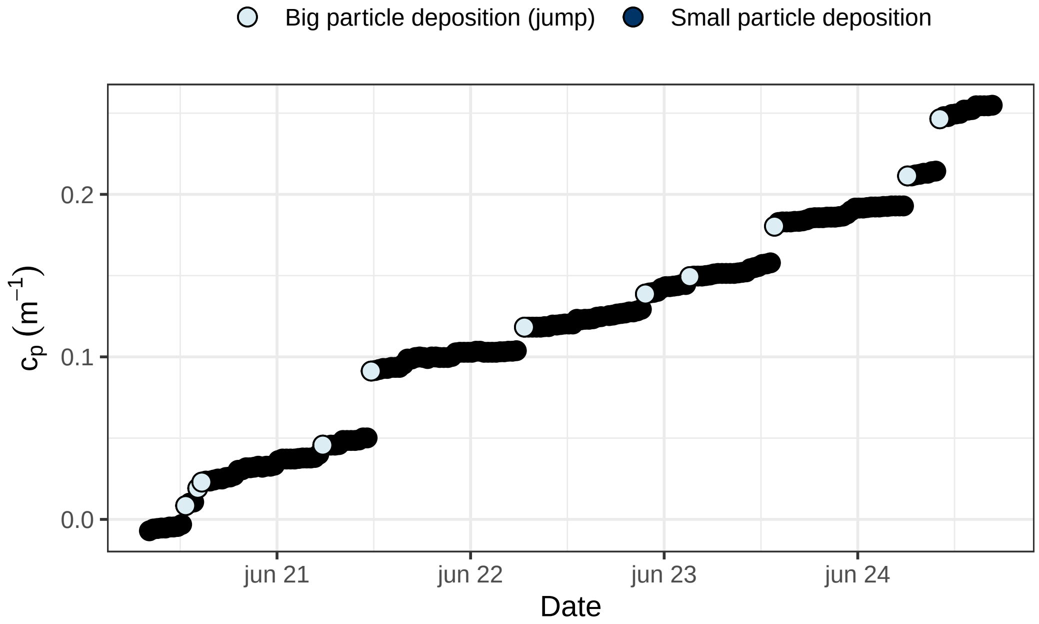

Figure 2.6: Application of the method of Estapa et al. (2017) on a drifting transmissometer to divide the c_p signal into a continuous (dark blue) component, cleaned from spikes and negative jumps (assumed as not related to the carbon flux) and a discontinuous (positive jumps, light blue) component. Data from BGC-ARGO float WMO 4903634, drifting at 1000 m during its 9^{th} cycle.

The UVP6 (Figure 2.7) is a miniaturized version of the UVP5 (Picheral et al. 2021), an imaging system developed to characterize particles (e.g. size, gray level, taxonomic group). Two versions of the UVP6 are available: the UVP6-HF (high frequency), and the UVP6-LP (low power) which has been specifically designed for AUVs that have strict energy requirements (e.g. autonomous floats).

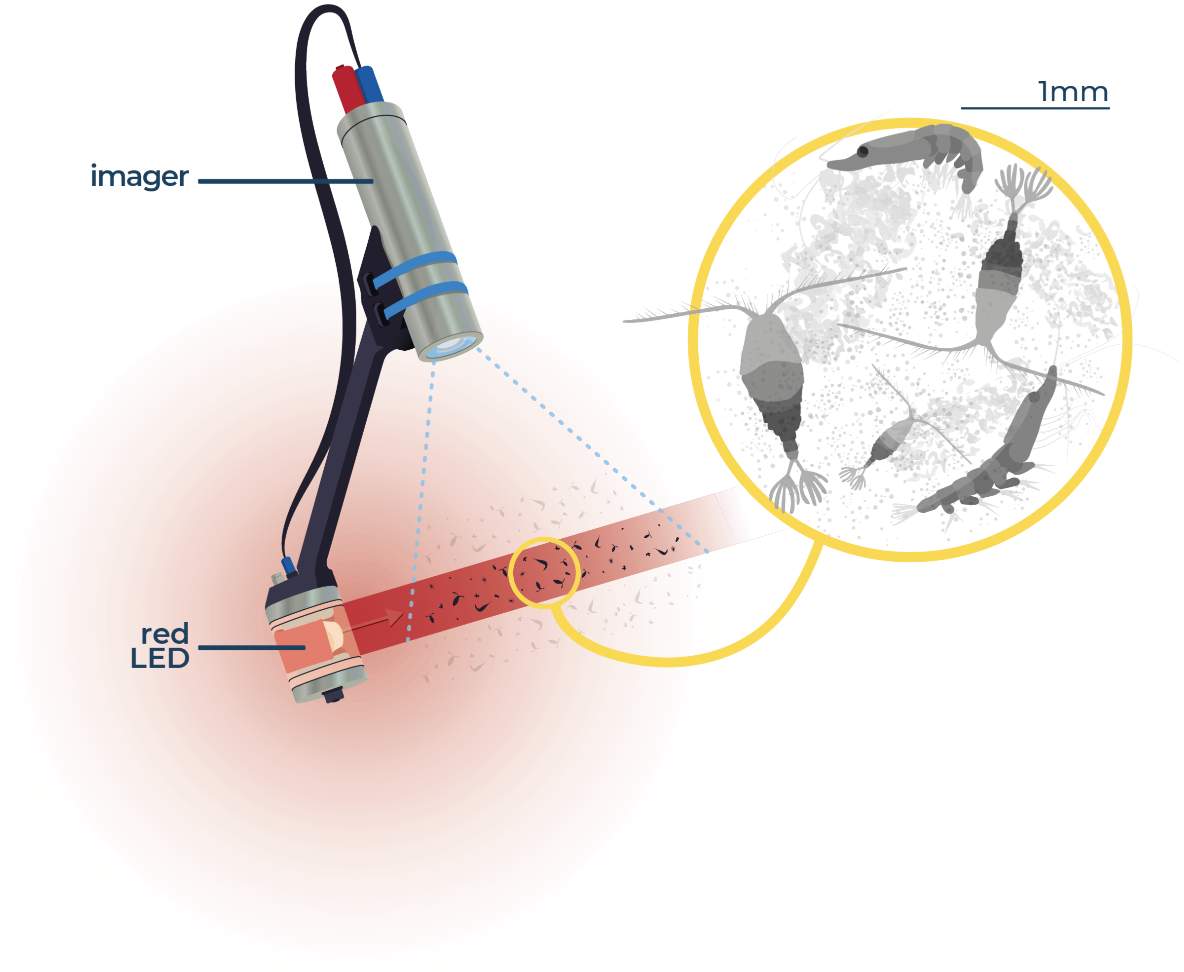

Figure 2.7: Illustration of the basic functioning of the UVP6. A light beam illuminates a region in front of the camera (imaged volume: 0.7L) which takes pictures at a given temporal resolution and subsequently characterizes and classifies relevant objects. @Thomas Boniface.

The UVP6-LP (hereafter referred to as UVP6) is thus both a particle counter for particles in the 0.1 - 2.5 mm size range and a particle classifier (> 0.6 mm). The former counts particles in different size classes in order to compute the PSD while the latter extracts pixel-related and geometric features from each image to classify them (i.e. assign them a taxonomic group) directly on board using artificial intelligence (Chapter 3) with the aim of estimating zooplankton biomass (Claustre et al. 2020, 2021).

The deployment of autonomous platforms equipped with a UVP6 and a zooplankton classification algorithm for the study of the BCP is just beginning (first deployment in May 2022 in the Labrador Sea, see Chapter 4). On the contrary, PSDs in carbon flux studies have been extensively used (Guidi et al. 2008, 2015, 2016; Iversen et al. 2010; Jouandet et al. 2011; McDonnell and Buesseler 2012; Roullier et al. 2014; Ramondenc et al. 2016; Kiko et al. 2017; Fender et al. 2019; Giering et al. 2020a; Cael et al. 2021; Bisson et al. 2022).

Using the PSD, one can compute the number spectrum n_i (Stemmann et al. 2004) which can be defined as the normalized concentration of particles in a given size bin i. Knowing the mass (m) and the sinking speed (w, see Equation 1.11) of aggregates, one can derive the total mass flux (F)

$$F = \int_0^\infty n(d)m(d)w(d)dd \tag{2.2}$$

where d is the aggregate diameter.

Assuming spherical aggregates, m can be written as follow

$$m(d) = \frac{\pi \rho d^3}{6} \tag{2.3}$$

where ρ is the average density of aggregates.

As explained in Section 1.4.2, aggregates have fractal geometries (D) hence Equation 1.11 and Equation 2.3 can be rewritten as follow

$$m(d) = \alpha d^D \tag{2.4}$$

$$w(d) = \beta d^{D-1} \tag{2.5}$$

where α and β are constant.

Aggregate mass and sinking speed are often described using a power law relationship (Alldredge and Gotschalk 1988; Guidi et al. 2008) therefore it can be derived that

$$mw = Ad^B$$

and therefore from Equation 2.4 and Equation 2.5 that $A = \alpha\beta$ and $B = 2D - 1$.

Due to a finite number (N) of size bins, Equation 2.2 is rewritten as

$$F = \sum_{i=1}^{N} n_i A d_i^B \Delta d_i \tag{2.6}$$

where d_i is the mid-point of bin i.

Guidi et al. (2008) used POC fluxes derived from sediment traps and UVP PSD data to estimate the A and B values of Equation 2.6 by minimizing the following cost function

$$Cost = \sum_{j=1}^{n} (log(F_{ST,j}) - log(F_{UVP}, j))^2 \tag{2.7}$$

where $F_{ST,j}$, $F_{UVP,j}$ and n are, respectively, the carbon flux measured in sediment trap j, the carbon flux estimate for the j^{th} UVP PSD and the number of paired measurements (i.e. match-ups) for trap-UVP comparisons.

Guidi et al. (2008) found an optimal couple of parameters $(A, B) = (12.5, 3.81)$ while Iversen et al. (2010) followed the same procedure and found $(A, B) = (273.8, 4.27)$ whereas Fender et al. (2019) found $(A, B) = (15.4, 1.05)$. Iversen et al. (2010) assumed that the difference in the optimal couple of parameters was due to the study site used for the minimization (productive upwelling system versus open ocean in Guidi et al. (2008)). Fender et al. (2019) suggested that a value of $B < 3$ means that either the density or sinking speed of particles is inversely correlated with particle diameter thus they suspected that the flux was dominated by particles in the lower size detection limit of the UVP they were using. Other values for A and B are used in the literature (e.g. Kiko et al. 2017) based on a mechanistic approach developed by Kriest (2002) to investigate the formation of marine aggregates.

It seems that the choice for the values of A and B is critical for deriving realistic carbon fluxes estimations from PSD (Iversen et al. 2010; Fender et al. 2019). Three main limitations highlighted by Bisson et al. (2022) for UVP optically derived estimates of flux would be: (1) assuming that A and B are globally valid at all depths, for all UVP models and across all size classes, (2) the size to sinking rate uncertainty and (3) the size to carbon mass uncertainty.

The assumption that all particles of a given size class have the same carbon content and settling rate questions the formulation of the model itself (Equation 2.6). It has been shown (Durkin et al. 2021) that the pool of sinking particles is varied (e.g. compact fecal pellets, porous aggregates) and that the main driver of the sinking speed is currently subject to debate (Section 1.4.2). Therefore, the size-dependent model of Guidi et al. (2008) could be improved by taking into account the composition and nature of particles (Durkin et al. 2021) and by increasing the number of paired measurements between UVP PSD-derived flux estimates and other direct POC flux estimates (e.g. sediment traps, ^{234}Th, OST).

2.3 Research questions and objectives of this work

In the context of the pressing issue of climate change, better understanding the BCP is of paramount importance (Martin et al. 2020). Although the BCP is not responsible for the absorption of anthropogenic CO_2, any change in its strength or efficiency could have a significant impact on atmospheric CO_2 concentrations (Kwon et al. 2009). Therefore, there is a need to better understand the biological and physical drivers of each component of the BCP to reduce uncertainties in the amount of carbon exported and its sequestration potential.

To this end, a new observational framework has been proposed by Claustre et al. (2021) to combine measurements from several platforms (i.e. research vessels, satellites, moorings and AUVs) to investigate the BCP. Within this framework, AUVs are being deployed with newly developed sensors to characterize the type of sinking particles (e.g. zooplankton, fecal pellets, aggregates), their size and the transformation mechanisms affecting them (e.g. fragmentation, aggregation).

This framework will hopefully address the key points raised so far, i.e. better understand the underlying drivers of each component of the BCP, decouple the contribution of each pump to the observed downward carbon flux lengthily attributed to the BGP and refine carbon export and sequestration estimates (Boyd et al. 2019; Siegel et al. 2022).

This work will therefore address three mains topics related to the study of the BCP:

1. BGC-Argo floats equipped with a UVP6 and a zooplankton classification algorithm are able to classify particles larger than 0.6 mm. However, these AUVs are limited by their battery life. They are typically deployed for several years, which requires to minimize the energy consumption of each sensor. In Chapter 3, I will therefore describe the methodology used to develop a zooplankton classification model for the UVP6 accounting for energy limitations.
2. Four BGC-Argo floats equipped with both an OST and a UVP6 were deployed for the first time in the Labrador Sea in late May 2022 to study the dynamics of carbon fluxes and particle concentrations. In this chapter, I will explore the seasonality of the latter and compare how the two sensors relate as two independent measurements of particle and carbon fluxes.
3. Many studies have assumed that carbon sequestration only occurs in the deep ocean (typically 1,000 m). In Chapter 5, we reassess the global sequestration ($\geq$ 100 years) of the BCP and its components by using a continuous approach to carbon storage as opposed to the common view of long-term sequestration below a fixed reference depth.

3 UVP6 embedded classification algorithm

Building the zooplankton classification model for the UVP6 was the first task of my PhD. To be honest, I knew nothing about machine learning before I started this so I spent the first three weeks reading a nice machine learning book in the corner of my team leader's office. To be even more honest, I basically knew nothing about zooplankton either. I think it is time to admit it.

In machine learning, the no free lunch theorem (Wolpert 1996) states that if you do not make any assumption about your data, then there is no model that is a priori guaranteed to work better (Géron 2019). In other words, it means that you need to get your hands dirty to find a model that works. The first step consisted in developing a full data processing pipeline using UVP5 images. The aim was to be prepared for the UVP6 image data set (not ready at that time) to train the true final classification model. To this end, I developed a python package called UVPec that is able to create a full classification model based on image folders with labeled particle/zooplankton images and some hyperparameters (e.g. learning rate). It really made my life easier when I got the final UVP6 data set and it saved me a lot of time.

In the end, I am rather satisfied with the results. Classifying zooplankton is already difficult for human operators (at least, for me) so building a model to automatically classify them is one challenge but adding technical and energy constraints to it was the icing on the cake. Below is the first draft of a publication on the classification model.

3.1 Embedded classification of zooplankton using the Underwater Vision Profiler 6 for use on autonomous platforms

Florian Ricour, Marc Picheral, Camille Catalano, Edouard Leymarie, Hervé Claustre, Léo Lacour, Lionel Guidi, Jean-Olivier Irisson

3.1.1 Abstract

Millions of images of oceanic particles have been acquired with ship-based imaging instruments. The task of labeling images is time consuming but necessary to train classification models using artificial intelligence algorithms. Autonomous Underwater Vehicles (AUVs) such as Biogeochemical-Argo floats (BGC-Argo) have revolutionized our understanding of oceanic

systems but they are flawed by their battery life and by the time they can spend at the ocean surface to transmit their data. In this paper, we show how we developed the first zooplankton classification model for AUVs using the Underwater Vision Profiler 6 (UVP6). To this end, we used a features-based classifier called eXtreme Gradient Boosting (XGBoost) adapted to specific energy constraints imposed by profiling floats and we compared its performance with a state-of-the-art convolutional neural network as if energy was not a limiting factor. In addition, we show how we dealt with a highly imbalanced data set towards marine snow ($> 80\%$ of detritus) and what were the compromises to improve the classification scores of biological classes. Finally, we show the classification report (precision and recall for each label) of the final classification model and use it to analyse some preliminary results from BGC-Argo floats deployed in the Labrador Sea.

3.1.2 Introduction

Inside the ocean, a cohort of diverse organisms known as zooplankton thrive. Those tiny beasts are so important for our oceans (Steinberg and Landry 2017) that we decided to take pictures of them (Benfield et al. 2007; Cowen and Guigand 2008; Gorsky et al. 2010; Picheral et al. 2010; Lombard et al. 2019). Nonetheless, the amount of images taken by those imaging instruments has become so huge that it is now a massive work to classify them by hand. Fortunately, powerful machine learning techniques have been implemented to tackle the issue of automatic plankton image classification (Luo et al. 2018).

However, it remains a fierce challenge. Within a single taxon, one can find organisms with very different sizes and shapes, organisms with significant morphological differences acquired during their ontogenetic development, partial organisms (e.g. siphonophores) or organisms with various orientations, hindering the automatic classification process (Benfield et al. 2007). In addition to this global heterogeneity, the great majority of images are not composed of zooplankton. Instead, non-living particles (mostly marine snow) steal the show, producing a highly imbalanced data set towards the latter.

The discussion around automatic plankton classification is a key topic in oceanography and the development of convolutional neural networks (CNNs) within that frame has already lead to promising results (Lee et al. 2016; Dai et al. 2017; Orenstein and Beijbom 2017; Cui et al. 2018; Luo et al. 2018; Bochinski et al. 2019; Schröder et al. 2019; Cheng et al. 2019; Ellen et al. 2019; Campbell et al. 2020; Guo et al. 2021). Nevertheless, real-time image processing done at sea is far less mentioned to our knowledge. Usually, images are brought back to the lab and classified with CNNs which, in comparison with features-based classifiers, that is machine learning algorithms using a set of features extracted from the image (e.g. area, eccentricity, gray levels) have outperformed the latter for plankton classification (Ellen et al. 2019). Though, it comes at a cost. CNNs are energy consuming hence their implementation for embedded applications can be limited by power consumption (Oh et al. 2017; Biswas and Chandrakasan 2018; Khabbazan and Mirzakuchaki 2019).

This is of particular importance for autonomous underwater vehicles (AUVs) and especially for a new version of Biogeochemical-Argo (BGC-Argo) floats that will be equipped with the Underwater Vision Profiler 6 (UVP6), the portable version of the UVP5 (Picheral et al. 2010) to better understand the carbon cycle (Xing et al. 2018b). The lifetime of floats is limited by their batteries hence by the power consumed by its sensors. Therefore, using an embedded CNN to classify plankton images or sending images through iridium transmission to be classified in the lab would not be possible for economical (cost of iridium transmission) and technical reasons. Typically, a BGC-Argo float samples the water column between the surface and 1,000 m, it would therefore have to stay at the surface for a time long enough to transmit all images collected after each profile, consuming energy proportionally to the size of the image set while being subject to biofouling or unpredictable hazards. For all these reasons, it was decided to use a features-based classifier for the development of the embedded plankton classification algorithm on board the UVP6.

In the literature, such algorithms (e.g. Decision Tree (DT), Random Forest (RF), Support Vector Machine (SVM)) have already been used for plankton classification (see Table 1 of González et al. (2017) for an exhaustive list). For instance, Blaschko et al. (2005) obtained an accuracy of 71% using a SVM on a set of 982 images among 13 classes using a 10-fold cross-validation (CV), Sosik and Olson (2007) obtained a global accuracy of 88% using a SVM on a test set of 3300 images covering 22 classes, Bell and Hopcroft (2008) obtained 82% of accuracy using a 10-fold CV RF algorithm on 53 classes with 10 to 30 images per class. However, it should be noted that this accuracy dropped to 63% after the removal of non-biological classes such as detritus and fiber. For bigger training sets, which will be the case in this study, Orenstein and Beijbom (2017) trained a RF model on approximately 650.000 images across 70 classes for an accuracy of 91% on the test set (2.75 million images). Though, one class in that test set contained 1.6 million images and if the classifier had put every object in that class, the accuracy would have been around 60% so caution must be applied when interpreting performance metrics. Faillettaz et al. (2016) trained a RF model on 6000 images across 14 classes, reaching an accuracy of 56% on a test set of 1.5 million objects, discarding those below a certain probability threshold. This allowed to improve the global accuracy by 16% but resulted in the loss of 72% of objects in the predicted data set.

It is quite difficult to compare all methods due to the diversity of imaging instruments hence the variety of image formats (e.g. resolution), the number of classes (trade off between the model performance and the number of classes as illustrated in Fernandes et al. (2009), the training set (e.g. number of images per class, diversity, balance), the scientific objective (e.g. precision-recall trade off), the type and number of features and the algorithm used. In many cases, RF seemed to be the best classifier (Gorsky et al. 2010; Faillettaz et al. 2016) but in embedded applications, energy constraints need to be taken into account. Therefore, the model needs to be small and the classification should be easy and fast. Gradient Boosting Tree (GBT) seems to offer this compromise when compared to RF (model size) and SVM (computation complexity). For these reasons, we chose XGBoost (Chen and Guestrin 2016), an optimized implementation of GBT, also known to be one of the best assets to win Kaggle's machine learning competitions.

In this paper, we present the results of an embedded zooplankton classification algorithm using XGBoost on UVP5 data. We show how we built the embedded classification (EC) model under strict technical constraints, what were our compromises and what techniques we used to improve the classification. We also compare the performances of our features-based algorithm with a state-of-the-art neural network as if energy was not a limiting factor. Finally, we apply the method and follow the recommendations learnt from the preliminary UVP5 model to the UVP6 data set to build the EC model that will be included in the UVP6 for AUVs.

3.1.3 Material and method

3.1.3.1 Instruments

The UVP6 is the miniaturized version of the UVP5 (Picheral et al. 2021). It is smaller, it uses less energy and it has been specifically developed to be mounted on AUVs such as BGC-Argo floats with the aim of providing data of similar quality than from the UVP5. There are 2 versions: the LP (low power) and the HF (high frequency). The former uses less energy (lower image acquisition rate) and will be deployed on AUVs while the latter is designed to be used on CTD rosettes and cruising AUVs (Picheral et al. 2021).

UVP5 Standard Definition (SD) profiles have been collected since 2008 at a global scale (Figure 3.1) whereas the UVP6 has been deployed very recently in specific locations and thus lacks spatial coverage to be fully representative. For this reason, UVP5 data will be used to create a preliminary EC model and explore ways of improvement. Ultimately, we will train the EC model for the UVP6 by applying the lessons learnt from the preliminary UVP5 model.

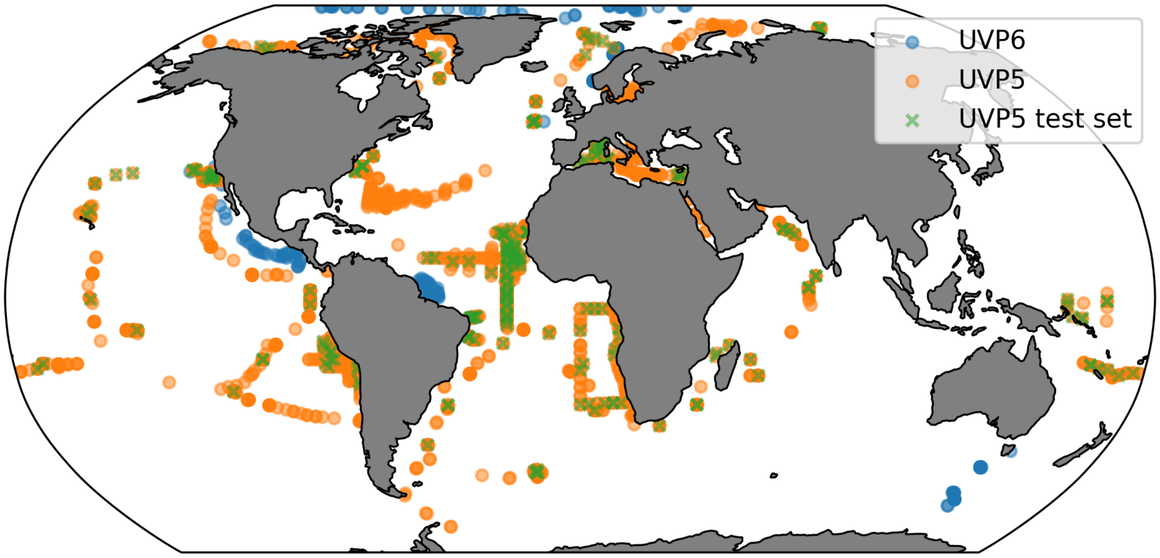

Figure 3.1: UVP5 and UVP6 profile coverage used in this study. UVP5 profiles used in the test set are depicted by green crosses.

3.1.3.2 Data preparation

The full UVP5 SD data set is composed of 3.578.901 hand-annotated (i.e. labeled) images whereas the full UVP6 LP data set has 634.459 labeled images. Each image was segmented to find the main object (i.e. the biggest connected region in pixels). From it, 55 features were extracted to describe this object in terms of shape (e.g. pixel area, eccentricity), gray levels and statistical moments (see Table 3.1). All UVP6 images with a pixel area below 79 pixels were removed (7% of images) to fit with the size bins used in EcoPart, that is starting at 645 μm.

All objects were manually classified into specific taxa belonging to well known biological groups such as *Rhizaria*, *Copepoda* or *Cnidaria* to name a few. However, the maximum number of classes (also referred to as labels or taxa) for the EC was fixed to 40 in order to limit the size of the EC model and the volume of data that needs to be transmitted. We chose to aggregate classes iteratively to find the best number of classes for the EC. The first level (i.e. all labels (>40) are retained) served as a baseline for a prior model, without making any assumptions. The next level was used as a first aggregation step based on the number of objects in each class and the purity of the class. Below a given threshold, rare classes were manually merged with their most look-alike taxa and parents on the phylogenetic tree were removed when their children were abundant (i.e. parents could not be classified to a deeper taxonomic level, likely causing confusion with their children during training). The second level of aggregation was based on statistical metrics post training (see hereafter how a model is trained), meaning that we looked at the confusion matrix and the classification report (Figure 3.2 and Table 3.2,

Table 3.1: List of 55 features (abbreviations used in our python package UVPec (https://github.com/ecotaxa/uvpec) and their descriptions) extracted from each object based on their geometry and gray levels.

Features name	**Description**
area	number of pixels
width	bounding box width
height	bounding box height
major	major axis
minor	minor axis
angle	orientation angle
eccentricity	eccentricity
esd	equivalent spherical diameter
bbox_area	bounding box area
extent	pixel ratio between object and bounding box
mean	mean pixel intensity
stddev	standard deviation of pixel intensity
mode	pixel intensity mode
min	min pixel intensity
max	max pixel intensity
x	local centroid (x direction)
y	local centroid (y direction)
xm	weighted local centroid (x direction)
ym	weighted local centroid (y direction)
intden	sum of all pixel values
median	median pixel intensity
histcum1	pixel intensity first quartile
histcum3	pixel intensity third quartile
vrange	vmax - vmin
meanpos	(vmax - vmin)/range
cv	100*(stddev/mean)
sr	100*(stddev/vrange)
hu_moment-i (i: 1 to 7)	Hu moment
gray_hu_moment-i (i: 1 to 7)	weighted Hu moment
central_moment-i-j (2-0;1-1;0-2;3-0;2-1;1-2;0-3)	central moment
gray_central_moment-i-j (2-0;1-1;0-2;3-0;2-1;1-2;0-3)	weighted central moment

Table 3.2: Precision, recall and f1-score for each class and globally in the UVP5 model (XGBoost and CNN). The abbreviation avg stands for average.

	XGBoost			CNN		
Labels	**Precision**	**Recall**	**F1-score**	**Precision**	**Recall**	**F1-score**
Acantharia	0.68	0.68	0.68	0.60	0.79	0.68
Aulacanthidae	0.63	0.69	0.66	0.61	0.73	0.66
Aulosphaeridae	0.80	0.84	0.82	0.89	0.87	0.88
Copepoda	0.54	0.50	0.52	0.56	0.72	0.63
Trichodesmium	0.68	0.75	0.71	0.56	0.89	0.69
artefact	0.60	0.75	0.67	0.63	0.63	0.63
bubble	0.77	0.81	0.79	0.76	0.89	0.82
darksphere	0.57	0.68	0.62	0.59	0.58	0.58
detritus	0.90	0.86	0.88	0.91	0.87	0.89
fiber	0.50	0.52	0.51	0.56	0.58	0.57
other<living	0.36	0.48	0.41	0.52	0.61	0.56
accuracy	0.81	0.81	0.81	0.82	0.82	0.82
macro avg	0.64	0.69	0.66	0.65	0.74	0.69
weighted avg	0.82	0.81	0.82	0.83	0.82	0.82
living macro avg	0.61	0.66	0.63	0.62	0.74	0.67
living weighted avg	0.60	0.65	0.62	0.59	0.78	0.67

respectively) to find which classes did not perform well such that they had to be merged to improve the classification score. This last step was repeated until an agreement was found. Thus, classes were merged only if they were confused amongst the same biological group on the phylogenetic tree or if they had a similar ecological role. This involves that some classes ended up with a variety of organisms that do not necessarily show similar morphological traits (e.g. other<living). It is definitely not ideal but we were bound to keep as many biological classes as possible to counterbalance non-living classes.

In machine learning tasks, it is common to split the data into a training set, a validation set and a test set. The validation set is usually used to assess the quality of a model by tuning hyperparameters while avoiding overfitting (stopping the training before the model is too acquainted with the data). Ideally, the test set is not to be used during any step except at the very end where it is used to assess the global quality of the final model. In our case, both data sets (UVP5 and UVP6) are very imbalanced towards few non-biological classes (mostly detritus). As a result, in order for the model to see as much biological data as possible during training, we did not use a validation set but instead we did a threefold cross-validation.

One objective of the EC for the UVP6 is to be used on AUVs such as BGC-Argo floats to study the vertical migration pump (Claustre et al. 2021). Hence, we built the test set with entire UVP5 profiles going at least to 1,000 m depth, the typical parking depth of BGC-Argo floats. Those profiles were also chosen to be representative of the global ocean (Figure 3.1).

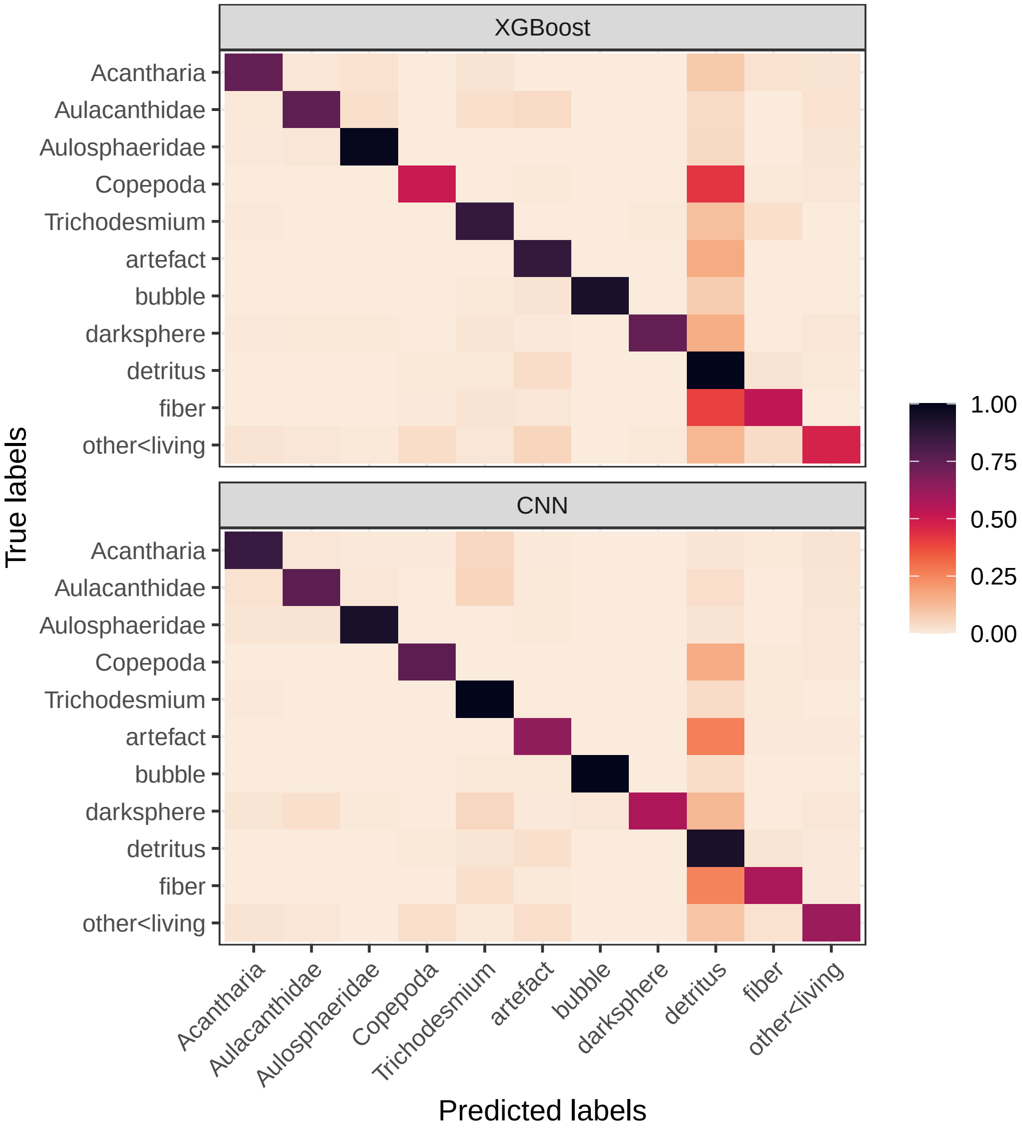

Figure 3.2: Confusion matrix (normalized on true labels) for the best UVP5 model trained with XGBoost and a CNN.

For UVP6 data, we did not select entire profiles because we were limited by the number of images in comparison with the UVP5 to build the biggest training set possible (80% of detritus in the UVP6 data set). Therefore, we splitted the data set in a 10-90 % stratified test-train fashion regardless of specific profiles.

Following the previous steps, the UVP5 test and training sets are composed of, respectively, 315.277 and 3.023.506 images while the UVP6 has 59.054 and 531.483 images for its test and training sets.

3.1.4 Gradient boosting and model training

GBT generates a sequence of trees, each one trying to cope with the errors made by their predecessors. XGBoost is designed to be an optimized and regularized version of GBT. To learn from the data and derive a model, XGBoost first minimizes a regularized objective function L

$$L = \sum_i l(\hat{y}_i, y_i) + \sum_k \Omega(f_k) \tag{3.1}$$

with

$$\Omega(f) = \gamma T + \frac{1}{2}\lambda ||w||^2$$

where l is a loss function that measures the difference between the prediction $\hat{y}_i$ and the true value y_i and Ω is the regularization term, for each k decision tree f_k. Ω is then splitted into two terms where γT penalizes the complexity of a tree proportionally to the number of leaves (T) and where the L2 norm penalizes the weights (w) of the leaves to avoid overfitting (both γ and λ are hyperparameters that can be tuned by the user). By doing so, XGBoost encourages both a simple and predictive model. From Equation 3.1, a scoring function that measures the quality of a tree structure can be derived (see Eq. 6 in Chen and Guestrin (2016) for details). However, in practice, it is not possible to test all suitable trees because there are infinite possibilities. Instead, the algorithm starts from a single leaf and iteratively adds branches to the tree, searching for the best split options.

To build the EC model, the first step consisted in a threefold cross-validation using XGBoost parameterized with a set of given hyperparameters (i.e. learning rate (η), maximum depth of a tree (D_{max}) and weight sensitivity (ω)). The second step consisted in the search of the optimal number of boosting rounds (i.e. k) before the model overfits. For this, we searched for the minimum value of the multiclass log loss (also known as cross-entropy loss) evaluated at each boosting round. Using that optimal k value, we then trained the EC model with the entire training set. Therefore, finding the best model consisted in finding the set of hyperparameters (k, η, D_{max}) that respected the energy constraints and returned the best global metrics. The latter were determined using a customary grid search (Figure 3.3) while ω was chosen empirically (see hereafter).

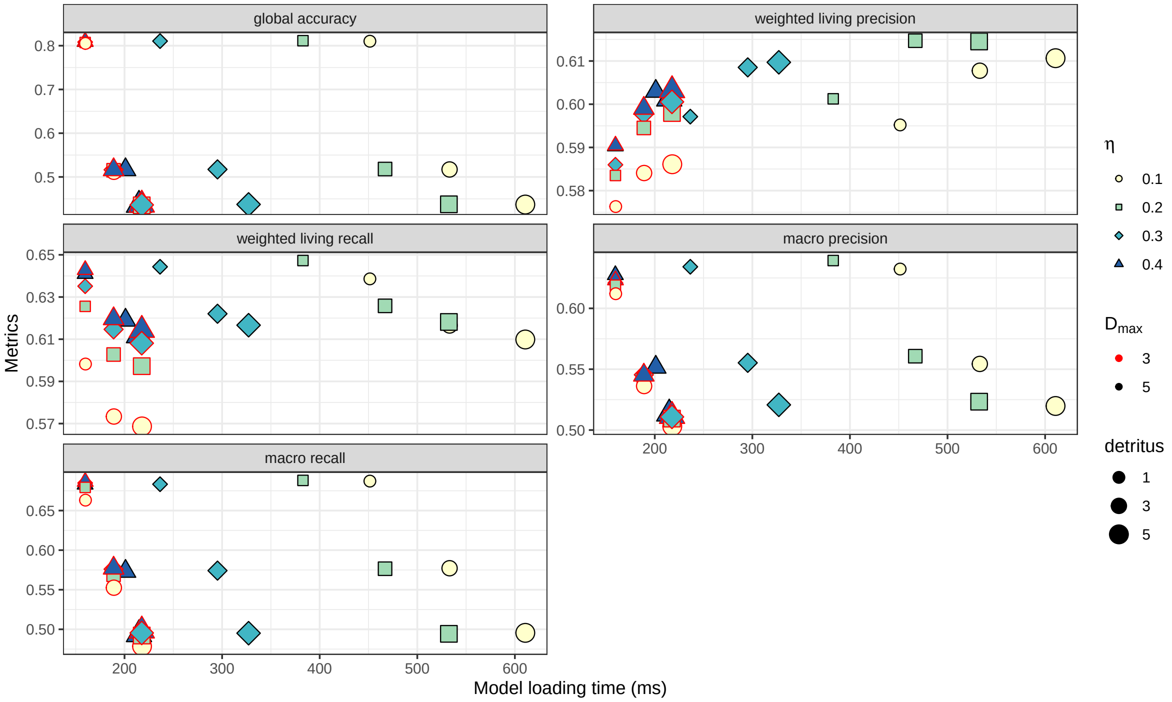

Figure 3.3: Grid search results with several classes of detritus (1, 3 or 5 classes). D$_{max}$ is depicted by the colour of the border of each shape (red or black).

To cope with our unbalanced data set (more than 70% of detritus in the UVP5 data set), several options were available. We could artificially increase the number of biological data with an oversampling technique such as SMOTE (Chawla et al. 2002; Fernandez et al. 2018) in order to oversample the minority classes, decrease the number of detritus (random undersampling, keep only detritus close to unsupervised cluster centroids, etc.) or add a weight to each label during training to nudge the model towards under-represented classes (i.e. biological classes). In order to compare a features-based classifier with a state-of-the-art CNN, we chose the latter and we defined the weight of a class as follows:

$$class\ weight = \left(\frac{size\ max}{size\ class}\right)^{\omega} \tag{3.2}$$

where *size max* and *size class* are, respectively, the size of the biggest class (i.e. detritus) and the size of each class. Hence, the weight of detritus is 1 and all other classes have a weight > 1.

We decided to select the best ω among 0 (no weights), 0.25, 0.50 and 0.75 (model very biased towards biological classes). In order to decipher between all options, we compared the predicted concentrations of classes for each ω with the real concentrations of each class in different regions of the global ocean. As always in machine learning, we encountered a trade off between precision and recall. However, given that the UVP6 is more focused on carbon flux estimation (high precision) than on the detection of rare objects (high recall with low precision), a weight sensitivity of 0.25 seemed to be the best compromise.

In order to compare our features-based model with a state-of-the-art neural network not limited by energy constraints, we used a MobileNetV2 (CNN designed to perform well on mobile devices) pre-trained on ImageNet, an image database with millions of hand-annotated images. This is known as transfer learning and it was already applied with success for zooplankton classification in Orenstein and Beijbom (2017). The CNN was fed with images of size 224 x 224 pixels, the size of the features extractor vector was 1792 and it was followed by a fully connected layer (600 nodes) with a dropout of 0.4 to avoid overfitting. The classification layer at the end of the network also had a dropout of 0.2. The CNN was trained with a decaying learning rate, a categorical cross entropy loss function and weights were defined with the same weight sensitivity of 0.25. The CNN was trained with a sufficient number of epochs such that its training reached a validation plateau (i.e. the model was not learning much with additional epochs).

3.1.5 Results

It is well known that the task of labeling images in supervised machine learning tasks is time consuming and most probably painful when you have millions of images to annotate. It is also very frustrating to see that one class (largely) dominates when you are interested in the small ones and that some of them are so scarce that you need to merge them with their siblings (at the very best) on the phylogenetic tree. Overall, we found - after multiple trials and errors - 11 classes fulfilling a first compromise between classification performances and ecological importance: 7 biological classes (*Acantharia*, *Aulacanthidae*, *Aulosphaeridae*, *Copepoda*, *Trichodesmium*, darksphere (round black object, supposed to be part of the living) and other<living) and 4 non-living classes (detritus, bubble, fiber and artefact).

Once the number of classes is known, hyperparameters can be tuned to find the optimal set for the classification results (i.e. grid search results shown in Figure 3.3). In our case, the optimal model hyperparameters were 0.2 for η and 5 for D_{max} (also with only 1 class of detritus, see Discussion) to have both a good weighted living (or biological) precision and recall and a loading time (i.e. loading of the EC model in memory) below 700 ms for energy reasons. In that configuration, the UVP5 model had an accuracy of 81%, a macro (i.e. label imbalance not taken into account) precision and recall of, respectively, 64% and 69% and a weighted living precision and recall of, respectively, 60% and 65%. The CV found an optimal number of 850 boosting rounds before overfitting and the expected loading time is 382 ms.

The classification report (CR) gives the precision, the recall, the f1-score (harmonic mean of the precision and recall) and global metrics on the test set. As it can be seen in Table 3.2, detritus have a recall of 86% thus because detritus are abundant (more than 230.000 in the test set), it results in more than 30.000 detritus wrongly predicted as such and therefore disseminated in all other classes. The confusion matrix (CM) helps to see where those false negatives have been predicted. Figure 3.2 shows that a lot of Copepoda are confused with detritus as well as fiber. The worst class in the CR is other<living, which is not surprising because this class is composed of organisms that are not all morphologically and ecologically related. The best biological class is Aulosphaeridae with a f1-score of 82%.

In comparison with a CNN trained on UVP5 images, the CR (Table 3.2) shows that the global accuracy is 1% higher (82%) with a macro precision and recall of, respectively, 65% and 74% and a weighted living precision and recall of, respectively, 59% and 78%. *Copepoda* are better detected (higher recall) but are still often (56% precision) misclassified. The *Aulosphaeridae* class has improved its f1-score to 88%. The class other<living has also greatly improved even though this class cannot be interpreted further in terms of ecology. Overall, the CNN performs slightly better on biological (living) classes than XGBoost if we consider the f1-score but this 4% increase is mostly due to an increase in global recall and not in precision. For instance, the 14% increase in recall for *Trichodesmium* is followed by a 12% decrease in precision so there is still a lot of confusion at this stage for the UVP5 for some classes, even with a CNN that is not limited by any energy constraints.

3.1.6 Discussion

3.1.6.1 Ways to improve the classification

The on board classification of plankton is definitely not an easy task. In order to improve the classification scores of biological classes, we tried several adjustments such as quantifying planktonic samples, splitting the detritus class into several subgroups and assigning weights to classes proportional to their size, which was the only option that enhanced the classification of scarce classes (see Methods).

Quantification is a concept that focuses on the sample instead of the individual. It was already shown in Solow et al. (2001), using plankton images from the Video Plankton Recorder, that the estimation of taxonomic abundances could be improved by computing the confusion matrix $\boldsymbol{P}$ where $p_{i,j}$ is the probability that a taxon i is classified as taxon j. If the classifier is perfect then $p_{i,j} = 1$ where $i = j$ thus the quantification resumes to a simple Classify and Count method (CC, see Forman (2005)). However, a perfect (especially in plankton ecology) classifier does not exist. Therefore, quantification is a tool to better estimate the abundance of planktonic groups while perfectly knowing that the classifier is biased. This quantification method was successively applied in the paper of Sosik and Olson (2007) on a 2 month data set although it is very likely that $\boldsymbol{P}$ needs to be adapted to the sampling conditions. This reevaluation of $\boldsymbol{P}$ is due to what is defined as a data set shift where part of the unseen data follows a different distribution than the one from the training data (Moreno-Torres et al. 2012; Orenstein et al. 2020)). It is especially true for EC systems deployed on AUVs where planktonic communities change throughout the year. Thus, we tested different quantification methods (CC, adjusted count (AC), threshold count (TC), probabilistic adjusted count (PAC) and scaled probability adjusted count (SPAC), see González et al. (2017) for a review on those quantification methods) assuming that the estimation of $\boldsymbol{P}$ was accurate enough ($>$ 3M images in our training set) and that the global coverage of UVP5 profiles in the training set was sufficient to cover various planktonic distributions from the test set.

We compared the abundance estimations of all quantification methods on the entire test set, all profiles included ($>$ 300k images). The SPAC showed the best estimations whereas TC drastically underestimated them (85% of data were lost using a probability threshold of 0.9). However, the aim of the EC is to be deployed on AUVs sampling vertical profiles in the water column therefore we applied the SPAC on 10.000 profile-like subsets and we summed all taxonomic abundances. In that configuration, the SPAC overestimated the real total abundance by 1 to 15% depending on the projected (high or low) number of objects in each profile. These percentages were exponentially increasing for small classes in both projections (also with PAC) therefore quantification was discarded for use on autonomous profilers at this stage.

Increasing the number of detritus classes was also considered in the hope of clustering them in the features space. Detritus display a variety of size, shape and gray levels so it must be possible to cluster them (Trudnowska et al. 2021; Durkin et al. 2021) and therefore improve the classification score. For this, we applied a classic K-Means algorithm (Hartigan and Wong 1979) on detritus cleaned from likely outliers using an Isolation Forest Algorithm (Liu et al. 2012) and we executed a grid search as described earlier. Figure 3.3 clearly shows that using more than 1 class of detritus drastically decreases the global accuracy of the model, decreases the weighted living recall and only increases by 1% the weighted living precision. In addition, the confusion matrix (Figure 3.4) shows that it does not improve the EC model because there is a high confusion between subgroups of detritus. Essentially, it seems that detritus form a continuum in the features space and that more research should be done on the choice of features, clustering algorithms and related methods to better differentiate them in separate entities, which is not the purpose of this study.

3.1.6.2 Application to the UVP6 data set

The aim of building an EC model was intended towards its implementation on the UVP6 for future deployments on BGC-Argo floats (or other profiling AUVs). Following the work done with the UVP5 data set, we applied the same method on UVP6 data. Thus, we started with the data aggregation step (choice of classes) where, in contrast with UVP5 data, some classes were kept (see Table 3.3) because of their ecological role (e.g. small<*Cnidaria* or tuff, an elongated cyanobacteria belonging to *Trichodesmium*) even though their classification metrics (precision and recall) were not particularly convincing. In the end, we reached an agreement on

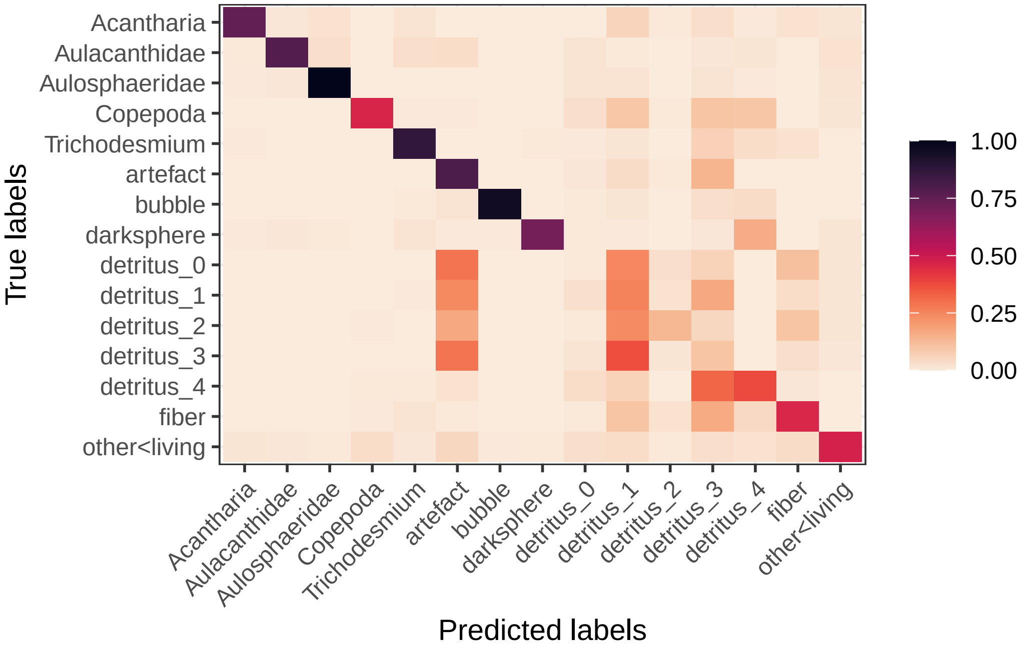

Figure 3.4: Confusion matrix (normalized on true labels) of a UVP5 XGBoost model with 5 classes of detritus.

20 classes. Among them, there are 16 biological classes (*Acantharia*, *Actinopterygii*, *Appendicularia*, *Aulacanthidae*, *Calanoida*, *Chaetognatha*, *Collodaria*, *Creseis*, *Foraminifera*, *Rhizaria*, *Salpida*, other<living, tuff and puff [another *Trichodesmium*], small<*Cnidaria*, solitaryglobule [part of the *Rhizaria* group] and 4 non-living classes (detritus, fiber, artefact, crystal). One will notice that we have the *Rhizaria* class as well as *Acantharia*, *Collodaria* and solitaryglobule. Those children of *Rhizaria* on the phylogenetic tree showed satisfying classification metrics compared to other *Rhizaria* subgroups (e.g. *Aulosphaeridae*, *Phaeodaria*, *Coelodendridae*, etc) hence we decided to separate them from their parent. Therefore, we assume that those classes are well recognized by human classifiers so that their parent *Rhizaria* is virtually free from them. Afterwards, we executed a grid search to find the optimal couple η and D_{max} (ω and the number of classes of detritus were fixed based on UVP5 results) and trained the final EC model whose CM and CR are reported in Figure 3.5 and Table 3.3.

The specifications of the final UVP6 EC model are the following: η: 0.2, D_{max}: 3, ω: 0.25, number of boosting rounds: 400 for a total loading time of 73 ms. Note that the CV initially found an optimal number of boosting rounds of 555 for a loading time of 101 ms). However, we observed that the log loss curve had already reached a plateau hence we were able to decrease the size of the model without losing much ($< 1\%$) in biological precision or recall, decreasing a bit more the energy consumption of the UVP6.

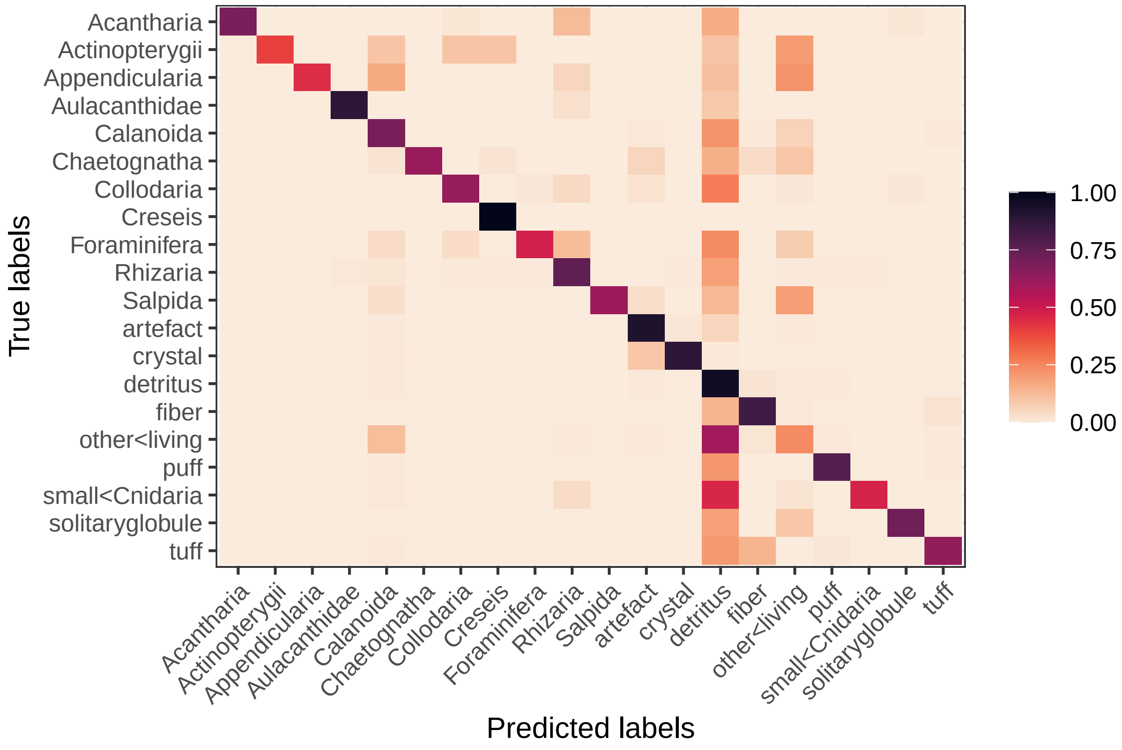

Figure 3.5: Confusion matrix (normalized on true labels) of the final UVP6 model trained with XGBoost.

Table 3.3: Precision, recall and f1-score for each class and globally of the best UVP6 model trained with XGBoost and a CNN. The abbreviation avg stands for average.

	XGBoost			CNN		
Labels	**Precision**	**Recall**	**F1-score**	**Precision**	**Recall**	**F1-score**
Acantharia	0.89	0.69	0.78	0.98	1.00	0.99
Actinopterygii	1.00	0.40	0.57	0.47	0.73	0.57
Appendicularia	0.89	0.44	0.59	0.38	0.64	0.47
Aulacanthidae	0.82	0.89	0.85	0.86	0.86	0.86
Calanoida	0.66	0.69	0.68	0.82	0.89	0.86
Chaetognatha	0.80	0.62	0.70	0.52	0.88	0.65
Collodaria	0.73	0.62	0.67	0.74	0.88	0.81
Creseis	0.81	1.00	0.89	0.42	1.00	0.59
Foraminifera	0.71	0.48	0.57	0.76	0.89	0.82
Rhizaria	0.69	0.75	0.72	0.71	0.92	0.80
Salpida	0.63	0.61	0.62	0.74	0.89	0.81
artefact	0.91	0.92	0.91	0.94	0.92	0.93
crystal	0.89	0.89	0.89	0.69	0.97	0.81
detritus	0.95	0.95	0.95	0.98	0.96	0.97
fiber	0.73	0.83	0.78	0.77	0.85	0.80
other<living	0.44	0.24	0.31	0.55	0.62	0.59
puff	0.73	0.78	0.75	0.84	0.94	0.89
small<Cnidaria	0.55	0.47	0.51	0.72	0.86	0.79
solitaryglobule	0.83	0.71	0.77	0.81	0.88	0.84
tuff	0.55	0.63	0.59	0.68	0.93	0.79
accuracy	0.91	0.91	0.91	0.94	0.94	0.94
macro avg	0.76	0.68	0.71	0.72	0.88	0.78
weighted avg	0.91	0.91	0.91	0.94	0.94	0.94
living macro avg	0.73	0.63	0.66	0.69	0.86	0.76
living weighted avg	0.61	0.56	0.57	0.71	0.82	0.76

3.1.6.3 How to use the CR in real applications?

4 BGC-Argo floats equipped with the EC were deployed in late May 2022 in the southern part of the Labrador Sea at the time of the spring bloom. As it can be seen in Figure 3.6, *Calanoida* are more abundant around the deep chlorophyll maximum (DCM) and they might be observed in very low concentrations even below 1000 m. The CR for *Calanoida* shows that the model has a precision of 66% and a recall of 69% for that class. It implies that caution must be applied when interpreting the presence or absence of such copepods. In that case, we theoretically miss 31% of them (i.e. 31% of *Calanoida* are not detected as such, they are classified in another class) and out of the 69% that we detect as *Calanoida*, we are wrong 34% of the time. As a result, even though *Calanoida* have been shown to overwinter in deep waters (> 1000 m) (Krumhansl et al. 2018), an isolated signal at depth does not mean a copepod was really there. Similarly, *Trichodesmium* are usually observed in the tropical and subtropical regions (Westberry and Siegel 2006) therefore depending on the sampling region, the presence/absence of specific organisms should be discussed. Finally, the interpretation of the detritus class is more straightforward because they have excellent metrics in the CR. For instance, it can be seen that detritus nicely follow the DCM curve. In contrast with biological classes where we are looking for patterns of presence or absence, we know that detritus are ubiquitous but their successive abundances could be interesting for carbon flux studies.

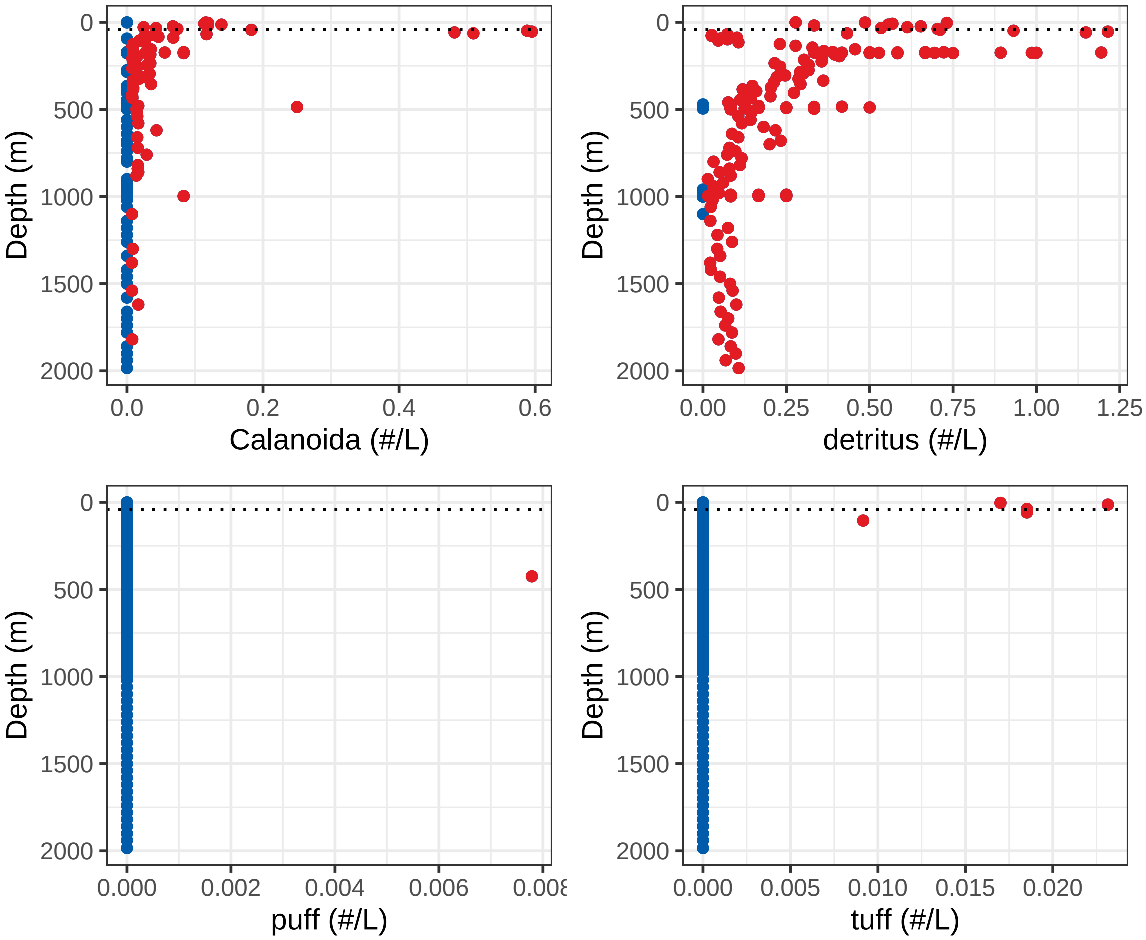

Figure 3.6: Concentrations of 4 classes (3 biological and the detritus class) estimated with data acquired from the UVP6 on board the BGC-Argo float (WMO 4903634) on the 15^{th} of June 2022 in the Labrador Sea. Red points represent positive concentrations while blue points represent the absence of the specified class. Dotted lines represent the depth of the deep chlorophyll maximum.

3.1.6.4 Prospects

The EC of zooplankton on board AUVs is just at its beginning. As expected, the CNN trained on UVP6 data (see Table 3.3) outperforms the results of our features-based classifier. However, it should be noted that not all biological classes are better classified with the CNN (e.g. *Actinopterygii*, *Appendicularia*, *Chaetognatha*, *Creseis*). One can also observe that the difference between XGBoost and the CNN trained on UVP5 data on biological classes is less significant than for UVP6 data. This is likely explained by the fact that we were able to keep more (smaller) classes for the UVP6. Nevertheless, previous tests on UVP5 data with more classes increased the gap between XGBoost and CNN weighted results therefore the latter better classifies small classes. If energy and hardware constraints limit the performances of our current EC model, it is not forbidden to think about light-weight CNNs for future applications on AUVs to better understand the dynamics and the behavior of zooplankton.

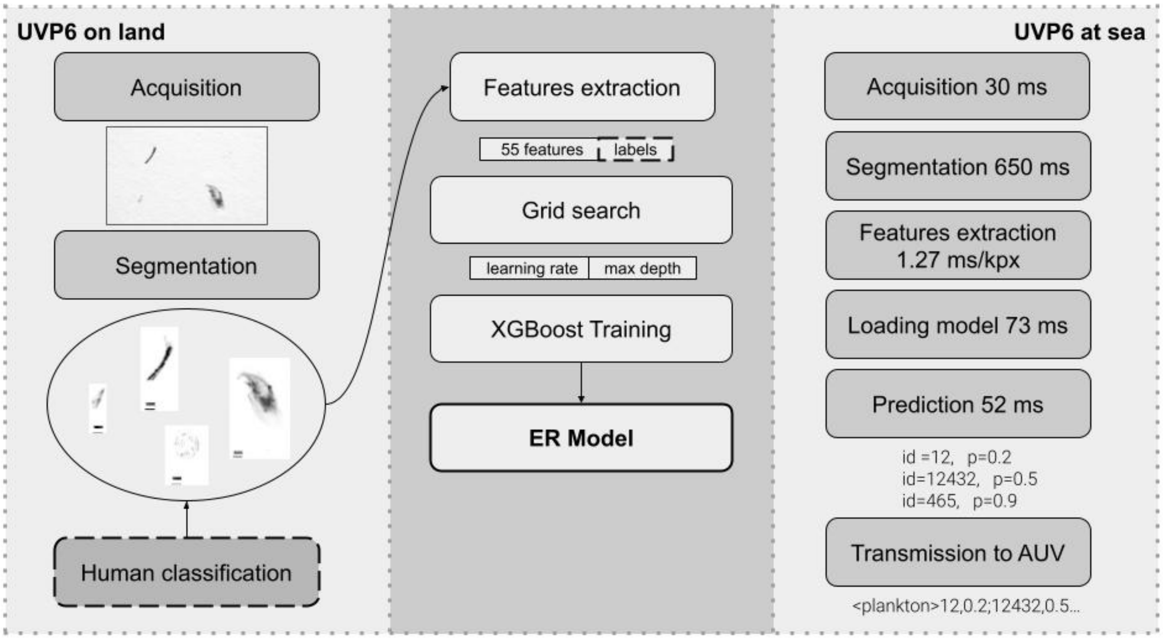

Figure 3.7: Scheme of the UVP6 pipeline with the processing done in the lab to create the EC model and the processing time (in ms) of the main steps when the UVP6 is deployed on board an AUV. kpx, id and p means, respectively, kilo pixel, the numeric id of a given taxonomic class and the prediction probability returned by the classification model for that class.

3.1.7 Conclusion

The objective of this paper was to develop a zooplankton classification model under strict energy constraints for the UVP6 to be deployed on BGC-Argo floats. It was clear at the beginning that the use of powerful energy consuming CNNs had to be disregarded and that we needed to build a satisfactory features-based model instead. To this aim, we firstly used XGBoost on UVP5 data, a more spatially and temporally representative data set than the recent UVP6 data set to create the data processing pipeline (class aggregation, hyperparameter tuning, model training, see also Figure 3.7) and investigate ways to improve classification scores (quantification, detritus subgroups, label weights). In order to see how the model could be improved, we compared the XGBoost model with results from a CNN not limited by energy. Afterwards, we applied the data processing pipeline and the recommendations from the UVP5 data set analysis on the UVP6 data set to create the final EC model. This model contains 20 labels, 16 biological and 4 non-living classes, with a total loading time of 73 ms. The initial upper limit for the loading time was 700 ms therefore we are saving precious energy to extend the lifetime of BGC-Argo floats. Finally, we showed the CM and CR of the final model and how to use it to interpret some UVP6 taxonomic profiles observed by the float WMO 4903634 during the spring bloom in the southern part of the Labrador Sea.

4 Case study in the Labrador Sea

In the first chapter, I explained the different steps that led to the creation of the embedded zooplankton classification model for the UVP6. However, I did not specify that in spite of the technical and energy constraints, the model was also due for April 2022 for a deployment of BGC-Argo floats in the Labrador Sea a month later. Once deployed, it was only a question of time before I could dig into the UVP6 and the OST data. In the meantime I asked myself, what could be a cool thing to do about those data? I already had some experience with BGC-Argo floats during my master's degree (I published a paper on the study of the deep chlorophyll maximum in the Black Sea, DOI: 10.5194/bg-18-755-2021) and so while I was waiting for new profiles, I thought it would be useful to have a visualization tool in the form of a web app to investigate incoming data and already prepare the ground for the following study. Here is the link to the web app, which is still currently being automatically updated every day with new data (almost) live from the Labrador Sea and hopefully soon with other BGC-Argo floats equipped with the UVP6 and the OST to investigate carbon and particle fluxes in other regions. This study uses preliminary data (not even one year of data) and a new BGC-Argo float configuration, hence more work should be addressed to better understand the dynamics of the system.

4.1 Introduction

The biological carbon pump (BCP) refers to a series of processes that transport biogenic carbon produced in sunlit surface waters to the ocean interior (Claustre et al. 2021). It is composed of three main pathways (Boyd et al. 2019; Claustre et al. 2021; Siegel et al. 2022): the biological gravitational pump that is the gravitational settling of particulate organic carbon (POC); the physically mediated particle injection pump that represents physical mechanisms that transport both POC and dissolved organic carbon (DOC) to depth via mixing processes; and the biologically mediated particle injection pump that characterizes the transport of POC by diel and seasonal migration of animals in the water column. Historically, the BCP was mainly studied with sediment traps (Honjo et al. 2008) and Thorium-234 radionuclide disequilibria (Buesseler et al. 2007) focused on the gravitational pump hence the contribution of DOC and migrating animals to the BCP was poorly known. However, the advent of autonomous underwater vehicles (AUVs) equipped with a variety of physical and biogeochemical sensors have demonstrated their ability to better understand them (e.g. Omand et al. 2015; Dall'Olmo et al. 2016; Stukel et al. 2017; Llort et al. 2018; Lacour et al. 2019; Haëntjens et al. 2020).

Still, we are missing processes to close the carbon budget (Giering et al. 2014; Boyd et al. 2019) and unknowns remain in the under-sampled mesopelagic (i.e. twilight) zone (Martin et al. 2020). In order to fill the observational gaps, the Biogeochemical-Argo (BGC-Argo) network aims to develop an operational global array of 1000 profiling floats measuring six core variables from the surface to 2000 m (Claustre et al. 2020): oxygen, nitrate, pH, chlorophyll a (Chla), suspended particles and downwelling irradiance. In addition to the six core variables, new sensors have been developed to target specific BCP-related questions (Claustre et al. 2020, 2021; Chai et al. 2020). In this study, we will focus on BGC-Argo floats equipped with two additional sensors: the Underwater Vision Profiler (UVP6) (Picheral et al. 2021) and a transmissometer used as an optical sediment trap (OST).

The UVP6 is a portable version of the UVP5 (Picheral et al. 2010), specifically designed for AUVs (Picheral et al. 2021). It consists of an underwater camera that counts particles and takes images of objects in, respectively, the 0.1 - 2.5 mm and 0.6 - 2.5 cm size range. In contrast with UVP5 deployments on cabled platforms, UVP6 deployed on long-term drifting AUVs (e.g. BGC-Argo floats) are rarely recovered. Therefore, the latest version of the UVP6 also embarks an embedded image classification algorithm that transmits the abundance of 20 classes (16 biological classes) in near-real time. The OST consists of a vertically mounted transmissometer whose upward-facing optical window intercepts sinking particles to estimate the downward POC flux. The latter have already been used on AUVs (Bishop et al. 2004; Bishop 2009; Estapa et al. 2013, 2017, 2019) and have demonstrated their usefulness to characterize the gravitational pump.

For the first time, BGC-Argo floats equipped with both the UVP6 and an OST were deployed in the Labrador Sea (LS) to investigate the seasonal and episodic dynamics of particles and carbon fluxes. The LS is a basin of the subpolar North Atlantic (NA) ocean which represents 20% of the global ocean carbon sink (Takahashi et al. 2009). The efficiency of this sink is explained by both deep winter convection that traps CO_2 from the atmosphere (Våge et al. 2008; Yashayaev and Loder 2009, 2017) and by the largest spring phytoplankton bloom (Siegel et al. 2002) that consumes CO_2 for the photosynthetic production of organic matter. The triggering mechanism of the NA bloom was initially explained by the 'Critical Depth Hypothesis' of Sverdrup (1953) that defines a critical surface mixing depth where phytoplankton growth is equal to phytoplankton losses. According to Sverdrup (1953), a bloom is therefore triggered when the surface mixed layer depth (MLD) is shallower than this critical depth resulting in a positive phytoplankton growth rate. However, this hypothesis was challenged by Behrenfeld (2010) who suggested that the initiation of the NA bloom begins in winter with a slow phytoplankton biomass increase over the following months (i.e. 'Dilution-Recoupling' hypothesis). These hypotheses have been investigated with BGC-Argo floats but the debate still remains (Boss and Behrenfeld 2010; Mignot et al. 2018; Yang et al. 2020). Distinct NA bloom phenologies were highlighted by Lacour et al. (2015) who used a climatology of satellite Chla to divide the NA into 6 bioregions. In their bioregionalization (see also their Figure 2), the LS is characterized by two bioregions with distinct bloom phenologies on both side of the 60°N parallel. The northern part is characterized by a short and potentially more intense spring bloom in late April whereas the bloom in the southern part starts in April-May and slowly develops to reach its maximum in June. Lacour et al. (2015) concluded that the concurrent influence of surface light and mixing was the first order mechanism controlling the onset of the spring bloom in both bioregions. This is coherent with the results of Wu et al. (2008) and Frajka-Williams and Rhines (2010) who found that the early bloom in the northern part is due to a very shallow mixed layer associated with low-salinity waters (i.e. haline stratification) while the southern bloom is related to the development of the seasonal thermocline (i.e. thermal stratification due to increased solar radiation). In late May 2022, two pairs of BGC-Argo floats were deployed in the southern part of the LS at the time of the spring bloom. While BGC-Argo floats typically drift at 1000 m for 10 days between each ascending profile, all floats were configured to drift at three distinct parking depths (200 m, 500 m and 1000 m) to study the downward POC flux and its attenuation derived from beam attenuance (Estapa et al. 2013, 2019) and to study particle size distributions (PSDs) and concentrations with the UVP6.

The goals of this study are threefold: 1) the comparison of the UVP6 and the OST as two independent measurements of downward carbon fluxes and particle abundance on BGC-Argo floats; 2) the exploration of the seasonality (bloom and non-bloom periods) of downward POC fluxes and particle abundance in the LS; 3) the evaluation of the new drifting configuration and how it could be improved to study specific BCP-related questions.

4.2 Methods

4.2.1 Deployment and floats configuration

Two pairs of BGC-Argo floats were deployed in the Labrador Sea in late May 2022 (Figure 4.1). The first pair (WMO 6904240 and 4903634) was deployed on the 22^{nd} at coordinates (-49.3°E, 58.9°N) while the second pair (WMO 6904241 and 1902578) was deployed on the 29^{th} at coordinates (-52.4°E, 56.8°N).

All 4 floats used in this study are PROVOR Jumbo floats (NKE Instrumentation, France) equipped with a CTD SBE41-CP (Sea-Bird Scientific, USA), a UVP6-LP (Hydroptic, France), a c-Rover 660 nm beam transmissometer (WETLabs, USA) and a ECO FLBBCD (WETLabs, USA) that includes a Chla fluorometer (excitation at 470 nm, emission at 695 nm), a colored dissolved organic matter (CDOM) fluorometer (excitation at 370 nm, emission at 460 nm) and a 700 nm particle backscatteringmeter (b_{bp}).

All 4 floats have been configured to drift at 3 distinct parking depths (respectively, 200 m, 500 m and 1000 m for approximately 1, 3 and 5 days) to study the downward carbon flux and its attenuation. During these drift phases, measurements of particle abundance (14 size classes, between 0.1 mm and 2.5 mm) are taken every 20 minutes at 200 m and every 2h at 500 m and 1000 m whereas c_p measurements are taken every 30 minutes at all depths. This configuration can be adjusted during the mission of the float via two-way Iridium communication. Finally, the vertical orientation of the transmissometer causes the accumulation of sinking material on the optical window. Therefore, a dedicated pump is used to clean the latter to remove the accumulated material between each drifting phase and subsequently avoid sensor drift.

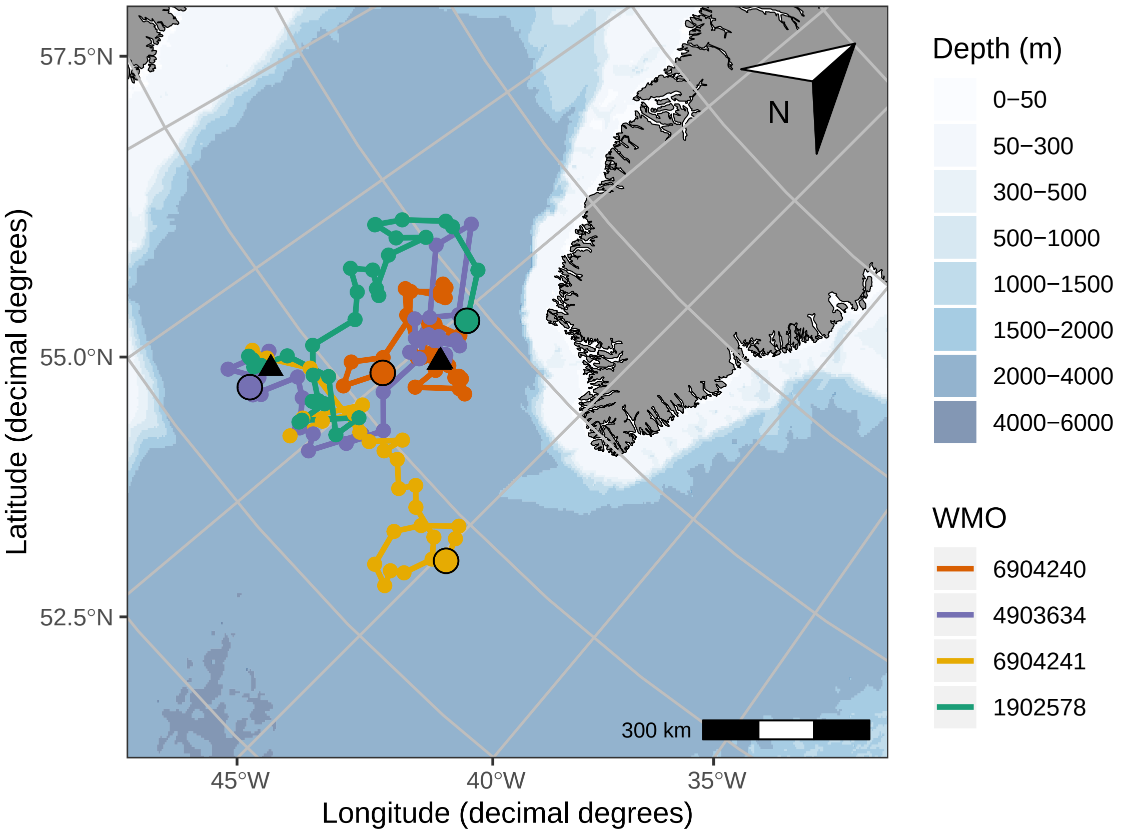

Figure 4.1: Trajectory of each float since their deployment (black triangles). Dots represent ascending profiles. The profile that concludes the time series for each float is highlighted by a black contour.

4.2.2 Data processing

Data were downloaded from the Coriolis data center (*ftp://ftp.ifremer.fr/ifremer/argo/*, with biogeochemical data at *dac/coriolis/* and UVP6 data at *aux/coriolis/*, last accessed: March 6, 2023). Chla data were quality controlled for Non-Photochemical Quenching (NPQ), a photoprotective mechanism that decreases the apparent fluorescence per unit of Chla following the method implemented by Terrats et al. (2020) who modified the method of Xing et al. (2018a) for shallow-mixing cases. Chla data were also divided by a slope factor of 2 following the recommendation of Roesler et al. (2017) for obtaining unbiased Chla estimates from in situ WETLabs ECO fluorometers. Temperature and salinity data were quality controlled using Wong et al. (2022). The potential density anomaly was computed with the function swSigma0 of the oce R package (Kelley and Richards 2021) and the MLD was determined using the 0.03 kg m^{-3} density criterion at a reference depth of 10 m (Boyer Montégut 2004). c_p data were converted from counts to physical units (m^{-1}) using the following relationship

$$c_p\ [m^{-1}] = -\frac{1}{x}\ log\left(\frac{c_p\ [counts] - CSC_{dark}}{CSC_{cal} - CSC_{dark}}\right)$$

where x, CSC_{dark} and CSC_{cal} are respectively the transmissometer pathlength (0.25 m), the sensor output when the beam is blocked (i.e. offset, 0 for each c-Rover of this study) and the sensor output with clean water in the path (12998, 13598, 13115 and 12855 for, respectively, float 4903634, 6904240, 6904241 and 1902578). The latter were obtained from the calibration sheets of each c-Rover. In practice, this calibration is not necessary to use the transmissometer in OST mode for the estimation of small and large sinking particles (see next section).

UVP6 data and in particular the averaged number of particles per size class (i.e. PSD) was divided by the number of images at each depth and the water volume imaged by the UVP (0.7 L) to obtain particle concentrations (units: #/L).

All data were divided into vertical profiles and drifting data using time stamps for profiling and drifting acquisition periods. Finally, data were checked for instrumental anomalies. As a result, c_p values from float 6904241 cannot be used from its 20^{th} cycle onwards (> November 17) due to a likely failure of the pump cleaning the optical window of the transmissometer. In total, the data coverage of this study spans a period of 9 months (end of May 2022 to early March 2023).

4.2.3 Derivation of carbon fluxes from the OST

We applied a similar approach to (Estapa et al. 2013, 2017) to derive the continuous component (i.e. continuous deposition of small particles on the upward-facing window of the transmissometer) and discontinuous (i.e. deposition of stochastic large particles) components of the downward POC flux, hereafter referred to as, respectively, F_{small} and F_{large}.

First, the drifting c_p signal was cleaned from spikes (assumed as transient particles not landing on the window or active swimmers (Estapa et al. 2013)). For this, we computed a 7-point moving median and a 7-point moving median absolute deviation (MAD). Then, we computed the anomaly to the moving median as the difference between the drifting c_p signal and the moving median. We considered that a c_p measurement was a spike when the anomaly was above $5.2 \times MAD$ following Leys et al. (2013). Despiked c_p data were then smoothed with a 7-point moving median filter.

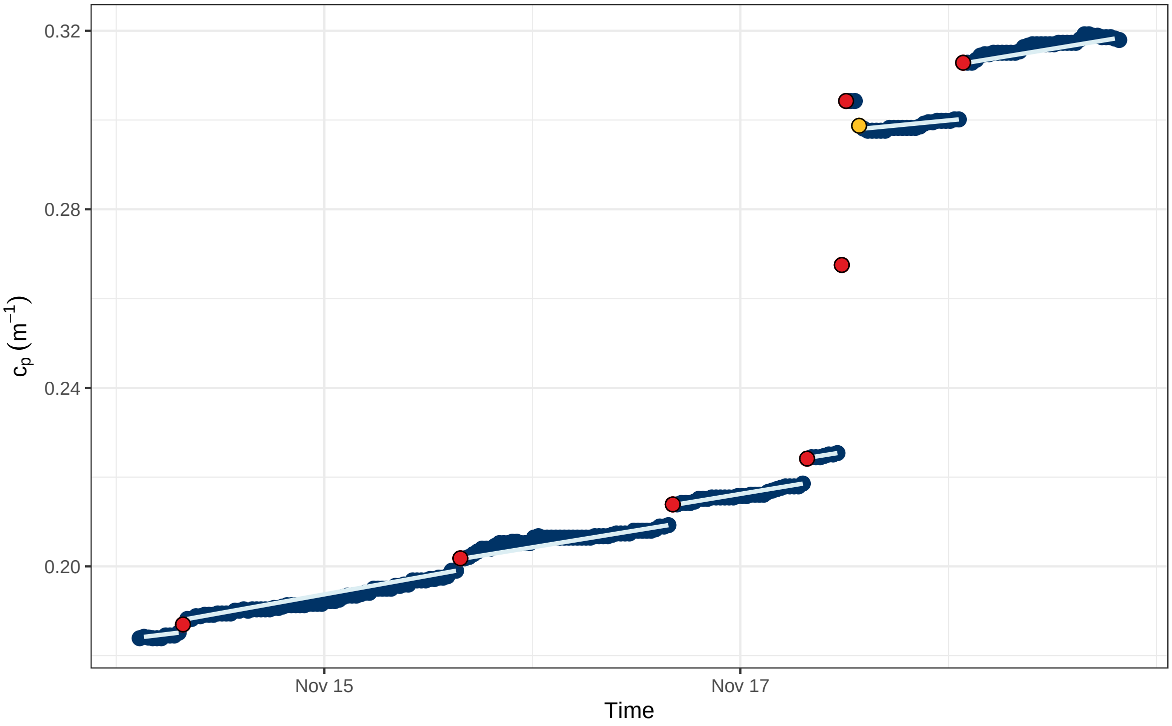

Figure 4.2: Example of the jump detection method on a drifting transmissometer where the c_p signal is divided into a continuous (dark blue) component and a discontinuous (positive jumps, red) component. Slopes for each segment are depicted in light blue. A negative jump was also detected (yellow). Data from BGC-Argo float WMO 6904240, drifting at 1000 m during its 21^{st} cycle.

Contrarily to previous works (Estapa et al. 2013, 2017, 2019), we chose an empirical statistical approach instead of thresholds to detect the deposition of large particles (hereafter referred to as jumps) in the c_p signal. Therefore, we firstly computed the slope between each c_p observation for each drifting phase. The detection of jumps consisted in spotting outliers in the slope distribution. For this, we computed the interquartile range (IQR) between the first (Q_1) and third (Q_3) quartiles. Positive and negative jumps were defined as, respectively, a slope above $Q_3 + 1.5 \times IQR$ and below $Q_1 - 1.5 \times IQR$. We found that this method better detected outliers than the one used to despike the c_p signal.

In order to compute F_{small}, we firstly computed the slope of each segment between jumps (positive and/or negative, see Figure 4.2). Any segment with less than 4 observations or a negative slope was removed assuming that either the so-called fit failed (leading to undetected jumps) either the transmissometer window was perturbed by factors other than the pump cleaning the optical window (e.g. turbulence or zooplankton consumption of accumulated material). Afterwards, we computed the weighted average slope ($slope_w$) of each segment to derive the small particle flux using the linear relationship between the beam attenuance flux and the POC flux (see first panel of Figure 2 in Estapa et al. (2023)).

$$F_{small} = 633(0.25\ slope_w)^{0.77} \tag{4.1}$$

where $slope_w$ is multiplied by the transmissometer pathlength because Equation 4.1 is an empirical POC-to-attenuance (ATN) relationship where ATN is the product of c_p and the transmissometer pathlength.

We used the same relationship to compute F_{large} by replacing $slope_w$ as the sum of positive jumps divided by the drifting time.

4.2.4 Satellite data

Satellite Chla data were downloaded from a daily-merged cloud free GlobColour product (doi: 10.48670/moi-00281) with a spatial resolution of 4 km. MLD data were downloaded from near-real time weekly data from the ARMOR3D product (doi: 10.48670/moi-00052) with a spatial resolution of 0.25°.

4.3 Results

4.3.1 UVP6 particle abundance

4.3.1.1 On profiling mode

Vertical profiles of particle concentrations in the lower (102 - 512 μm, see Figure 4.3) and upper (0.512 - 2.5 mm, see Figure 4.4) size range of the UVP6 show similar patterns across all floats. In the lower part of the size range, Figure 4.3 shows the rapid emptying of the water column in November. This process occurred on the entire water column (e.g. size class 406, float 4903634) but also started with more intensity from below the surface (e.g. size class 102, float 6904240). All floats also measured a local particle abundance maximum around 800 - 1000 m whose origin is analyzed in the Discussion. In the upper part of the size range, Figure 4.4 shows a rapid emptying of the entire water column starting in November. In contrast with small classes (referred to here as below 512 μm), some particles, especially above 1.5 mm, have almost entirely disappeared from the water column by September. However, the rapid increase and decrease of particles on the entire water column around July-August for floats 6904241 and 1902578 (still in the same geographical zone at that time) could suggest an export event.

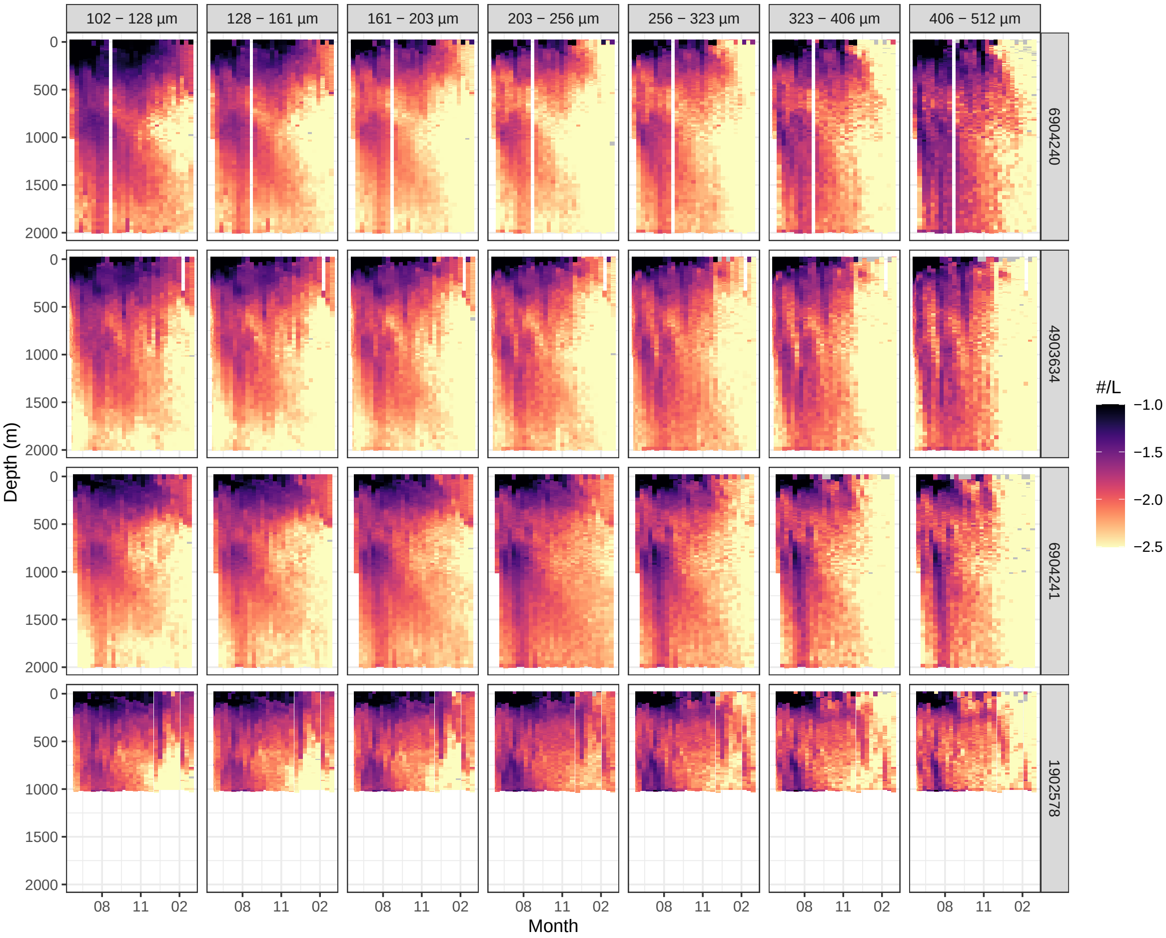

Figure 4.3: Vertical profiles of UVP6 particle concentrations for size classes in the 102 - 512 μm size range. Concentrations were normalized for each size class. The colorbar is in $\log_{10}$ scale.

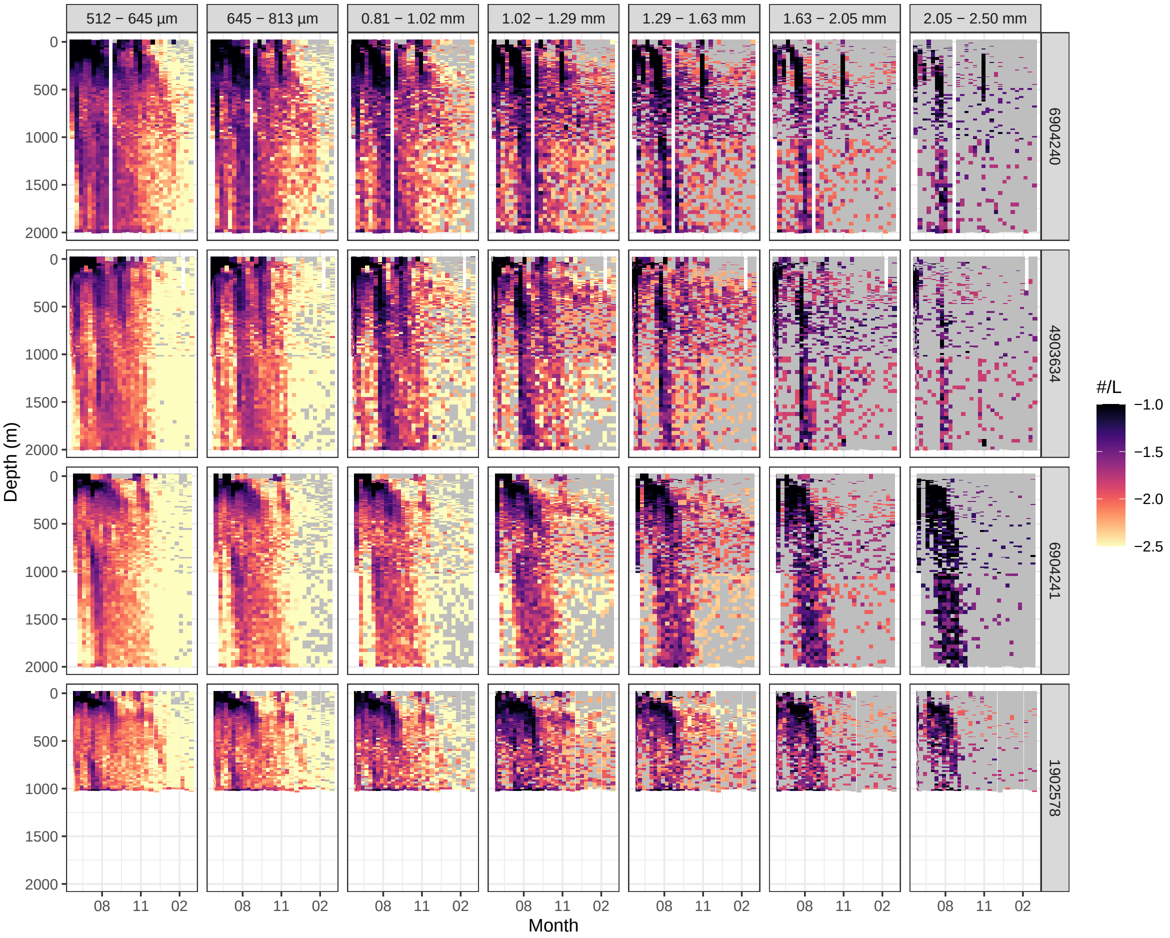

Figure 4.4: Vertical profiles of UVP6 particle concentrations for size classes in the 0.512 - 2.5 mm size range. Concentrations were normalized for each size class. The colorbar is in $\log_{10}$ scale. The gray background depicts the absence of particle in the specified size class.

4.3.1.2 On drifting mode

In this study, we focus on 14 size classes, from 102 μm to 2.5 mm. In Figure 4.5, Figure 4.6 and Figure 4.7, we show the daily averaged concentrations of particles in each size class for each float at their respective drifting depth. At 200 m, it can be observed that particle concentrations in the 102 - 512 μm range are relatively uniform between June and October before decreasing sharply towards January. Between 512 μm and 1.63 mm, concentrations are steadily decreasing from June. Above 1.63 mm, the particle abundance is already very low ($<$ 0.1 particle/L) in June but keeps decreasing until September when they are practically absent ($<$ 0.01 particle/L). At 500 m, particle concentrations in the 102 - 645 μm range slowly decrease from July to September with a sharp decrease starting in October. Above 645 μm, the trend shows a maximum between the end of July and the first half of August though the concentrations of particles in those classes are very low ($<$ 0.5 particle/L) on the entire time series. At 1000 m, all 4 floats measured a clear maximum in particle abundance in the 102 - 645 μm in the second half of July. Above 645 μm, the same trend can still be observed with concentrations of less than 1 particle/L.

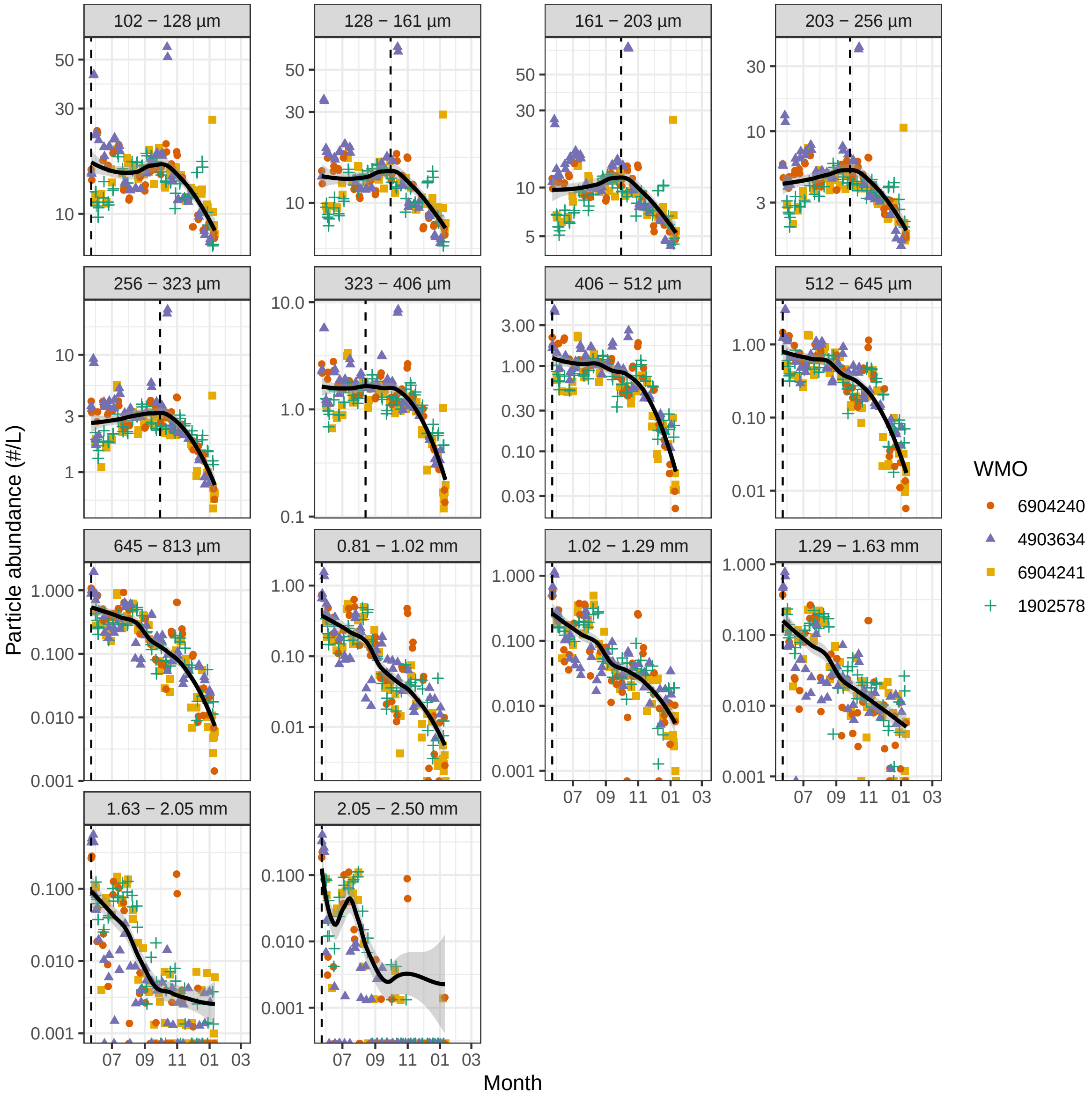

Figure 4.5: Daily averaged concentrations of particle abundance in 14 size classes measured by the UVP6 for each float at 200 m. Black lines and shaded areas represent, respectively, the daily mean particle abundance and the 95% confidence interval around the mean. Dashed vertical lines indicate the time at which the daily mean particle abundance is maximum.

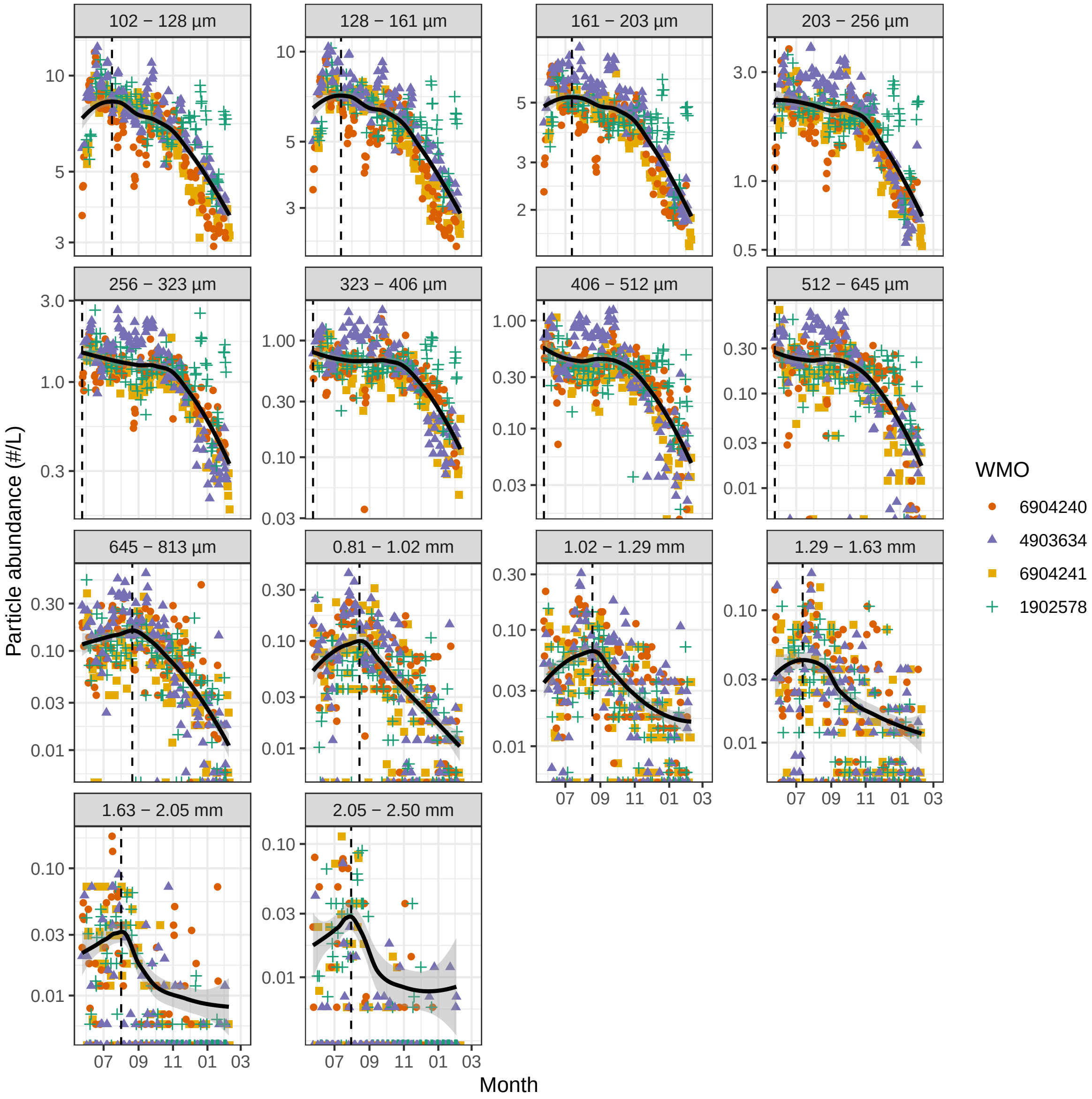

Figure 4.6: Daily averaged concentrations of particle abundance in 14 size classes measured by the UVP6 for each float at 500 m. Black lines and shaded areas represent, respectively, the daily mean particle abundance and the 95% confidence interval around the mean. Dashed vertical lines indicate the time at which the daily mean particle abundance is maximum.

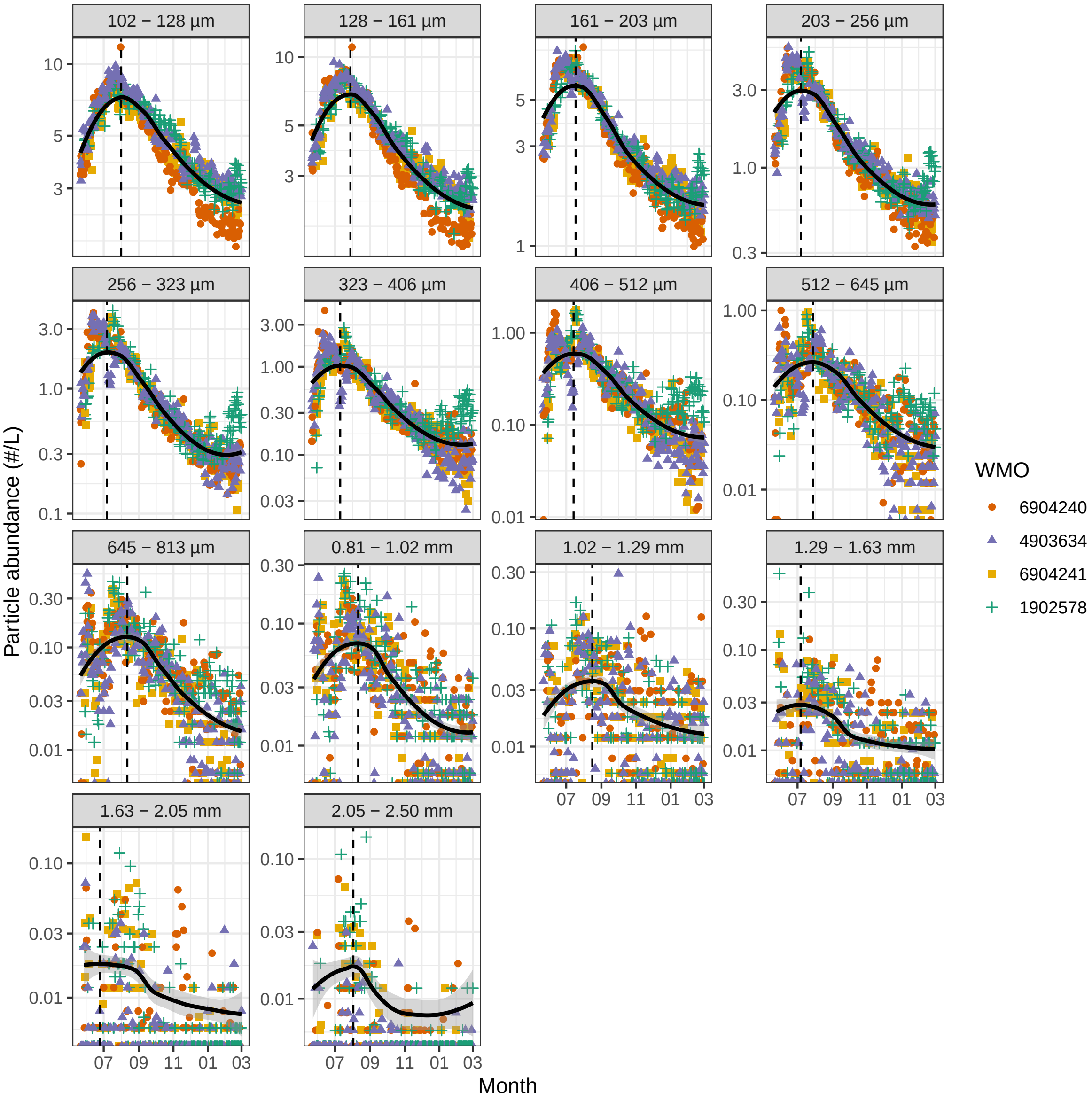

Figure 4.7: Daily averaged concentrations of particle abundance in 14 size classes measured by the UVP6 for each float at 1000 m. Black lines and shaded areas represent, respectively, the daily mean particle abundance and the 95% confidence interval around the mean. Dashed vertical lines indicate the time at which the daily mean particle abundance is maximum.

4.3.2 OST-derived carbon fluxes

F_{small} and F_{large} were computed at each drifting depth for all floats (Figure 4.8). At 200 m, F_{small} ranges between 2.2 and 89.2 mg C m^{-2} day^{-1} with an average of 14.7 ± 11.3 mg C m^{-2} day^{-1} (average ± standard deviation). At 500 m, F_{small} is comprised between 4.8 and 44.9 mg C m^{-2} day^{-1} with an average of 8.7 ± 4.5 mg C m^{-2} day^{-1}. For both drifting depths, the trend shows a decrease of F_{small} from June to, respectively, January and February before the drift was stopped at those depths due to the deepening of the winter MLD (Figure 4.9) in order to ensure the float stability. At 1000 m, all floats measured an increase of F_{small} from late May to July followed by a steady decrease towards March, with F_{small} ranging between 2.2 and 12.5 mg C m^{-2} day^{-1} and 6 ± 2 mg C m^{-2} day^{-1} on average.

F_{large} was estimated at 200 m between 0 (no deposition of large particles on the transmissometer window) and 303.6 mg C m^{-2} day^{-1} with an average of 28.4 ± 51.3 mg C m^{-2} day^{-1}. High fluxes ($>$ 100 mg C m^{-2} day^{-1}) were measured by 3 out of 4 floats at the end of May before a sharp decrease towards July. At 500 m, F_{large} ranges between 1.9 mg C m^{-2} day^{-1} and 146 mg C m^{-2} day^{-1} with an average of 17 ± 21.1 mg C m^{-2} day^{-1}, decreasing from September to February. At 1000 m, F_{large} shows a similar pattern than the one observed for F_{small} with an increase from June to mid-July, followed by a decrease towards March, with values ranging from 0 to 47.8 mg C m^{-2} day^{-1} and an average of 10.6 ± 10.1 mg C m^{-2} day^{-1}.

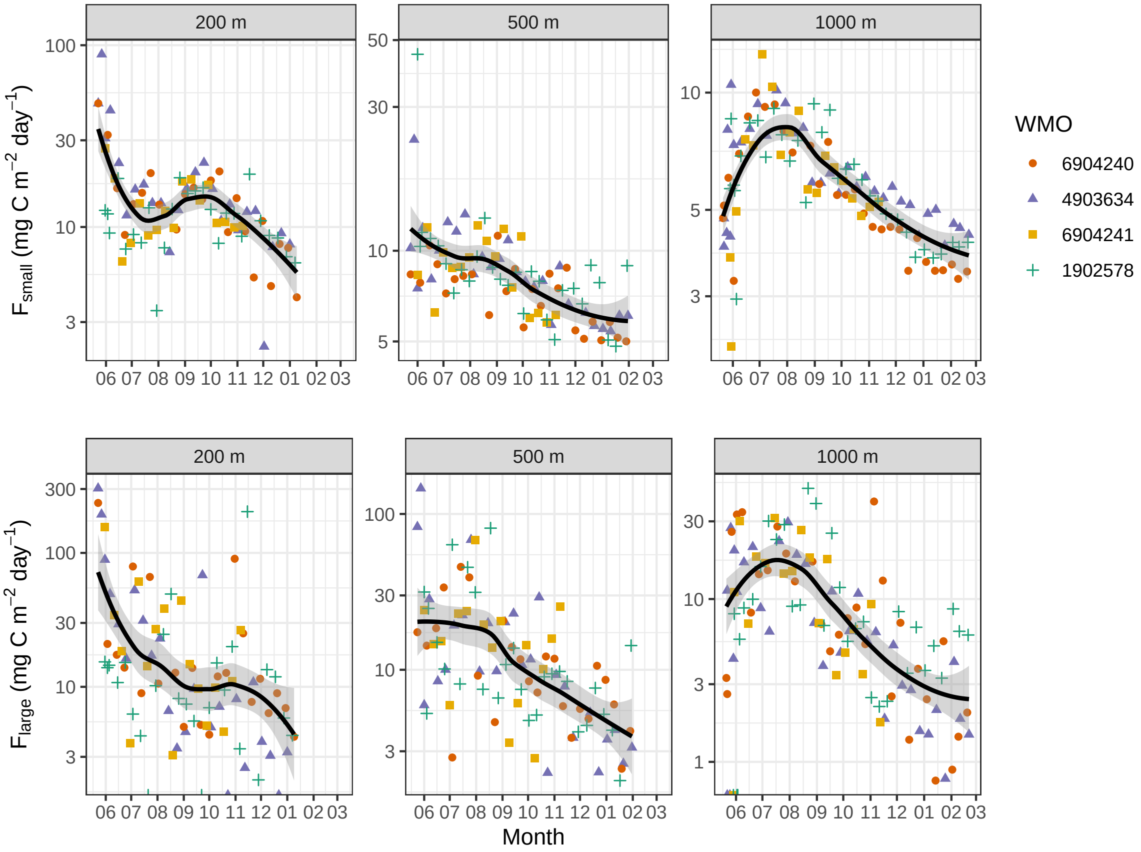

Figure 4.8: OST-derived small (top) and large (bottom) particle carbon fluxes for all floats at each drifting depth. Black lines and shaded areas represent, respectively, the monthly mean flux and the 95% confidence interval around the mean. There is no data after January and February at, respectively, 200 m and 500 m because the drifting was stopped at those depths due to the deepening of the MLD associated with convection and the impossibility to stabilize the floats.

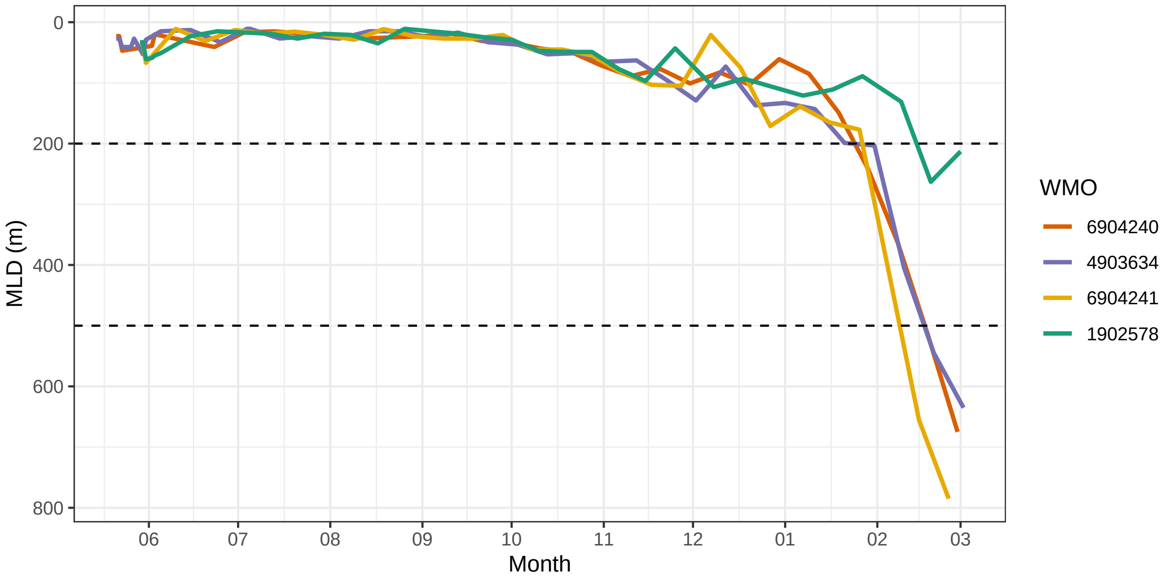

Figure 4.9: MLD measured by all floats from the end of May 2022 to early March 2023. Black dashed lines represent the first two drifting depths.

4.4 Discussion

4.4.1 Dynamics of the spring bloom in the Labrador Sea

To estimate the time of the bloom in the deployment area, we compared MLD and surface (i.e. upper 20 m) Chla concentrations from both satellite and in situ data in a 100 km radius around each deployment. Figure 4.10 shows that satellite and in situ Chla and MLD data concur. Therefore we assume that the former can be used to study environmental conditions before the floats deployment. Taking this into consideration, Figure 4.10 indicates that the 6904240-4903634 pair likely missed a bloom that occurred in early May whereas the 6904241-1902578 pair missed a first (satellite) Chla increase at the end of May days before their deployment. However, a second (satellite and in situ) Chla increase reached a peak at the end of June before it decreased again towards July.

The Chla satellite pattern for the 6904240-4903634 pair typically describes the dynamics of the spring bloom in the northern part of the LS (Lacour et al. 2015). This is not surprising given that this pair was deployed one degree southward to the so-called 60°N limit (Lacour et al. 2015). Figure 4.10 shows that the satellite MLD in that region had already shoaled below 100 m since March and that the water column was stable and relatively well stratified in May which might explain the intensity of surface Chla concentrations in contrast with those measured at the second deployment site. The latter is located in the bioregion where the phytoplankton biomass typically develops slowly in May to reach its maximum in June (Lacour et al. 2015).

However, the Chla pattern observed in Figure 4.10 could suggest that the development of the phytoplankton biomass was stopped by a mixing event at the end of May and that it started again in mid-June when the water column was well stratified.

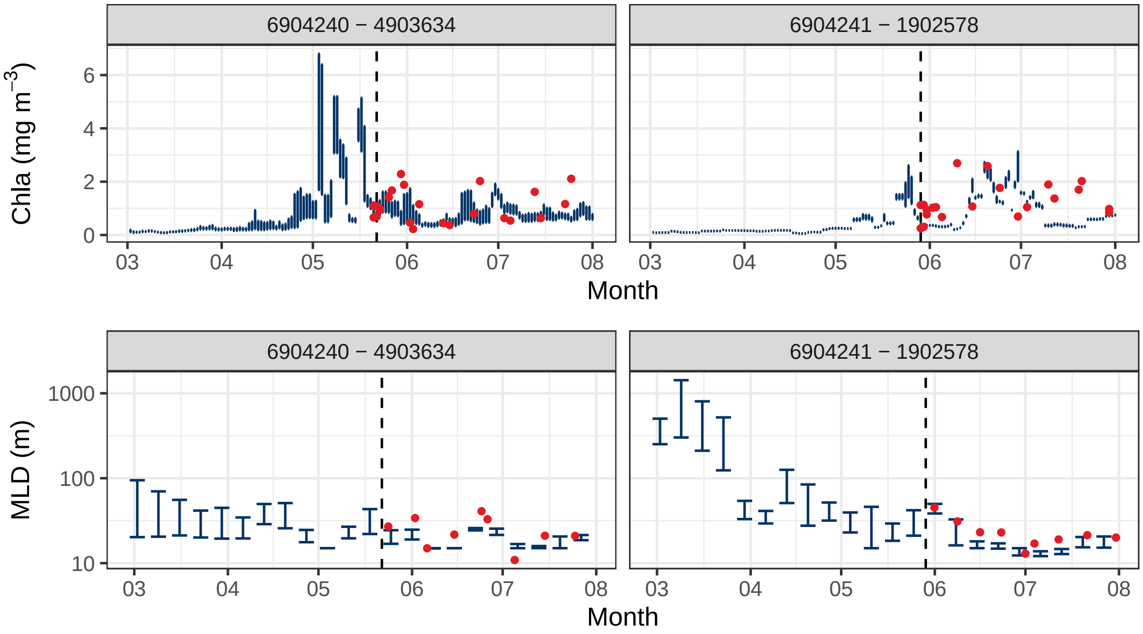

Figure 4.10: Comparison of MLD and Chla concentrations measured from satellites (dark blue) and BGC-Argo floats (red) following their deployment (in pairs). Satellite error bars represent the first and third quartiles around the median in a 100 km radius around each deployment coordinates. In situ Chla represents the Chla median in the upper 20 m of the water column.

4.4.2 Phytoplankton communities at deployment sites

High Performance Liquid Chromatography (HPLC) analyses were performed on samples taken during the two deployments. The selected pigments, their taxonomic significance and their size class were taken from Table 2 in Petit et al. (2022). The pair 6904240-4903634 showed Chla concentrations (TChla pigment in Figure 4.11) two times higher than the pair 6904241-1902578 in the first 100 m as well as higher concentrations of diatoms (Fucoxanthin). The pair 6904241-1902578 showed higher concentrations of cryptophytes (Alloxanthin), dinoflagellates (Peridin) and green flagellates and prochlorophytes (TChlb). However, their absolute concentrations are quite low (usually less than 0.05 mg m^{-3}). Taking that into consideration, it seems that, at the time of float deployment, the northern site was located in a more productive area than the southern site and that it was dominated by diatoms (i.e. microphytoplankton) whereas the latter was composed of a majority of smaller phytoplankton species (mostly nano and picophytoplankton). This supports the idea of two distinct biological dynamics as inferred from float and satellite data.

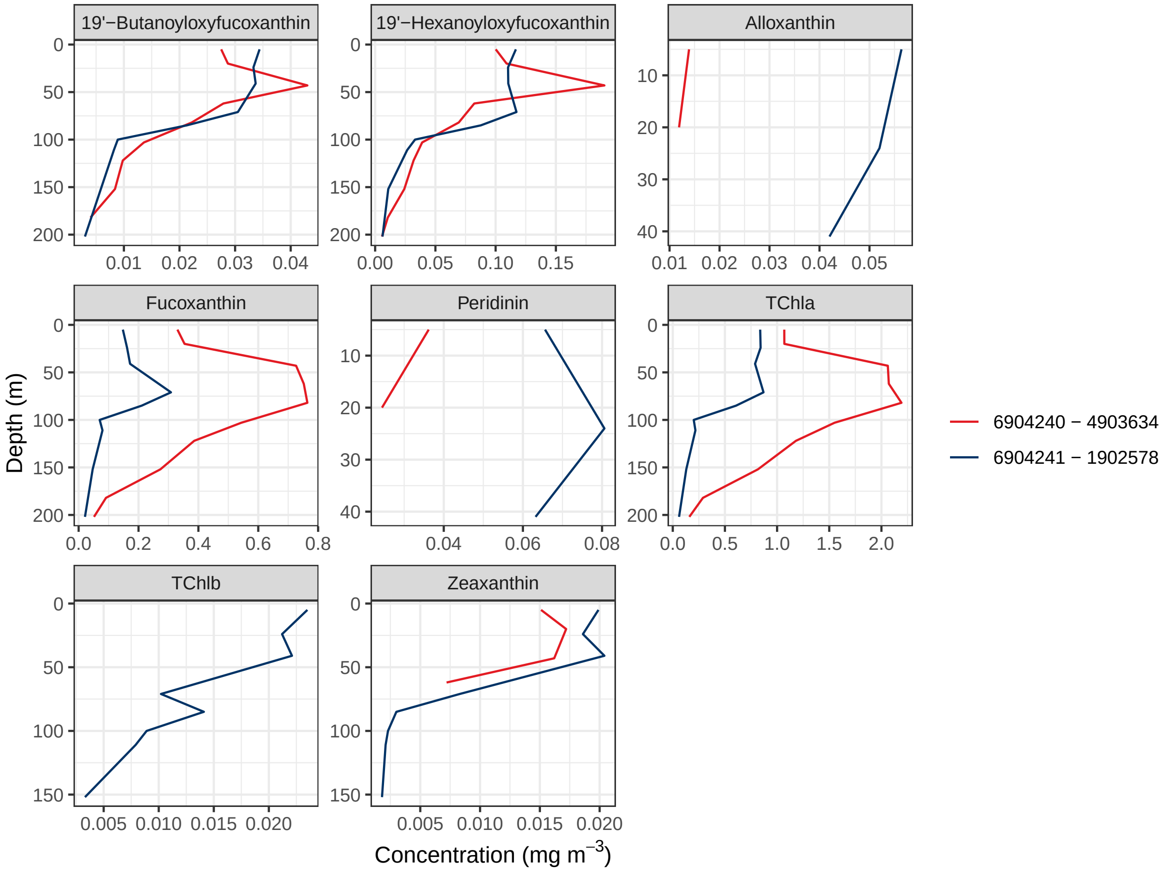

Figure 4.11: Pigments derived from HPLC analyses in the northern (floats 6904240 and 4903634) and southern (floats 6904241 and 1902578) deployment sites.

4.4.3 Unclear particle export signature

Even though we suggested that the two pairs of floats were deployed in two different bloom regimes, they all measured an increase in particle concentrations in the 102 - 512 μm range (Figure 4.3) around 800 - 1000 m as well as an increase in the abundance of large particles (Figure 4.4) between June and August. This increase raises the question of a possible particle export event. For classes > 512 μm, the vertical concentration profiles highlight a larger particle plume for the 6904241-1902578 pair than for the other one. However, apart from the float 6904240, all floats measured similar integrated Chla content in the upper 100 m and in the mixed layer (Figure 4.12). Figure 4.8 also shows that F_{small} is similar across all floats at all parking depths and that F_{large} is also similar across all floats at 1000 m with an increase from June to August as observed in F_{small}. The same behavior is observed for UVP6 particles in the lower size range at 1000 m (Figure 4.7). Observing similar properties across a wide geographical range around deployments suggests that we observe the latent (i.e. seasonal) dynamics of the system rather than episodic export events.

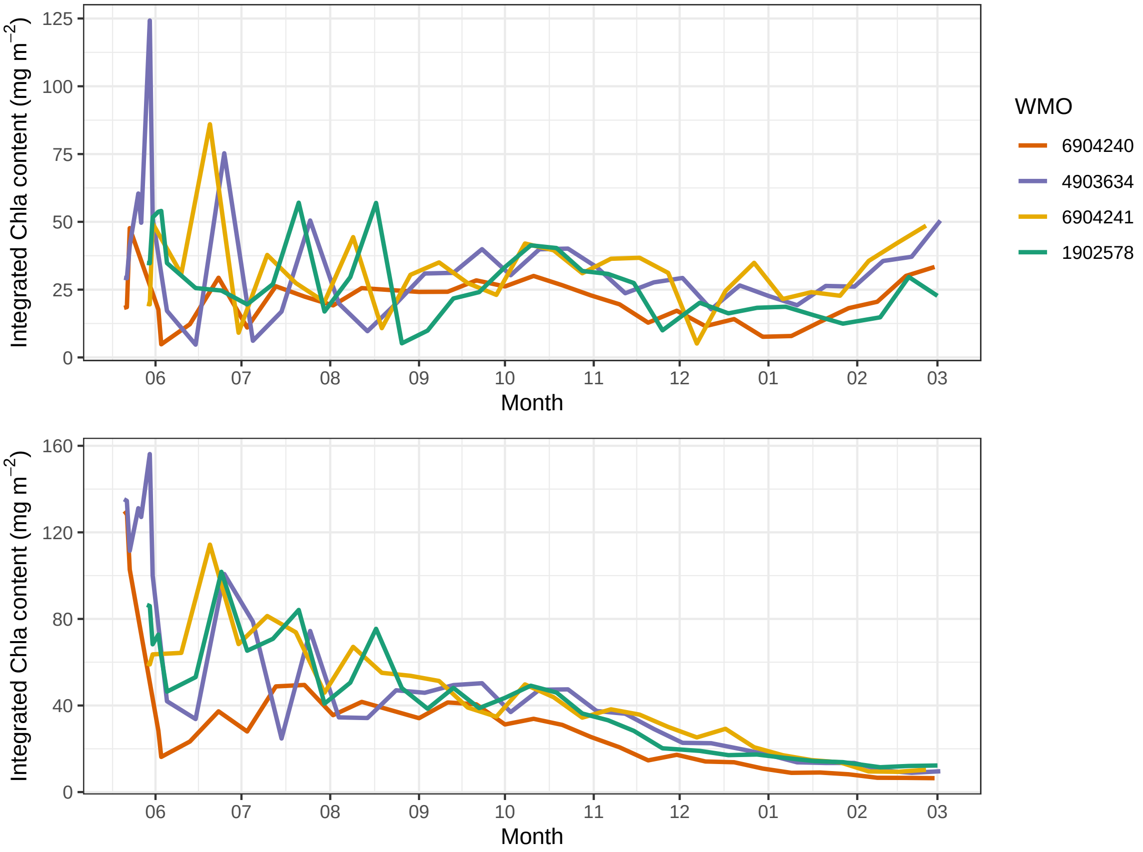

Figure 4.12: Integrated Chla content in the mixed layer (up) and in the upper 100 m (down) for each float.

Still, it is unclear why we observe a progressive emptying of the water column starting below 500 m for size classes below 323 μm (Figure 4.3). This pattern could result from several causes. It could either be the signature of a subduction event (Llort et al. 2018) either the end of a slow sinking export (i.e seasonal dynamics of the system) or a sign of fragmentation processes by zooplankton (i.e. zooplankton feeding). Therefore, we looked at physical properties (density anomaly and spiciness) and well as particle characteristics (zooplankton concentration and spectral slope) to investigate this particularity (Figure 4.13). Spiciness is a variable that allows the differentiation of water masses with distinct thermohaline properties but similar density (Flament 2002). Figure 4.13 shows that both the density and the spiciness fields are uniform below 500 m hence it is unlikely that a subduction event would be the reason for this decrease in particle abundance below 500 m. Using the embedded zooplankton classification results from the UVP6, we looked at concentrations of *Calanoida*, a species that is abundant in the NA (Corkett and McLaren 1979). Figure 4.13 shows that the concentration of *Calanoida* is higher from the end of May to July in the surface layer. There also seems to be a lower patch between 250 and 500 m from August to November however it is difficult to estimate their impact on particle concentrations at this stage because more data are needed. Finally, we computed the spectral slope to look for aggregation/fragmentation processes. The spectral slope defines the slope of the PSD where a high (in absolute values) spectral slope indicates that small particules dominate the PSD. Here, the panel on spectral slopes in Figure 4.13 shows a lower (in absolute values) spectral slope (i.e. large particles dominate) at the beginning of the time series but it is also difficult to relate it to biological processes such as zooplankton feeding without any additional data.

All things considered, it is not straightforward to conclude for the presence of a carbon export event. First, the 10-day profiling configuration hinders the characterization of particle export events that are transient processes. Second, the plume of large particles can be misleading because the abundance measured by the UVP6 are very low (usually < 0.1 #/L). However, the plume could be the result of aggregation (repackaging) by zooplankton feeding on small particles. Third, all floats measured the same particle dynamics in distinct zones which suggests that if the two systems were initially different (i.e. different bloom dynamics), they merged back after the bloom of May. Therefore, we suggest that we mostly observe the seasonal dynamics of the system rather than clear export signatures that would likely be spotted with both higher bloom intensities (e.g. the May bloom that was missed) and a higher profiling temporal resolution.

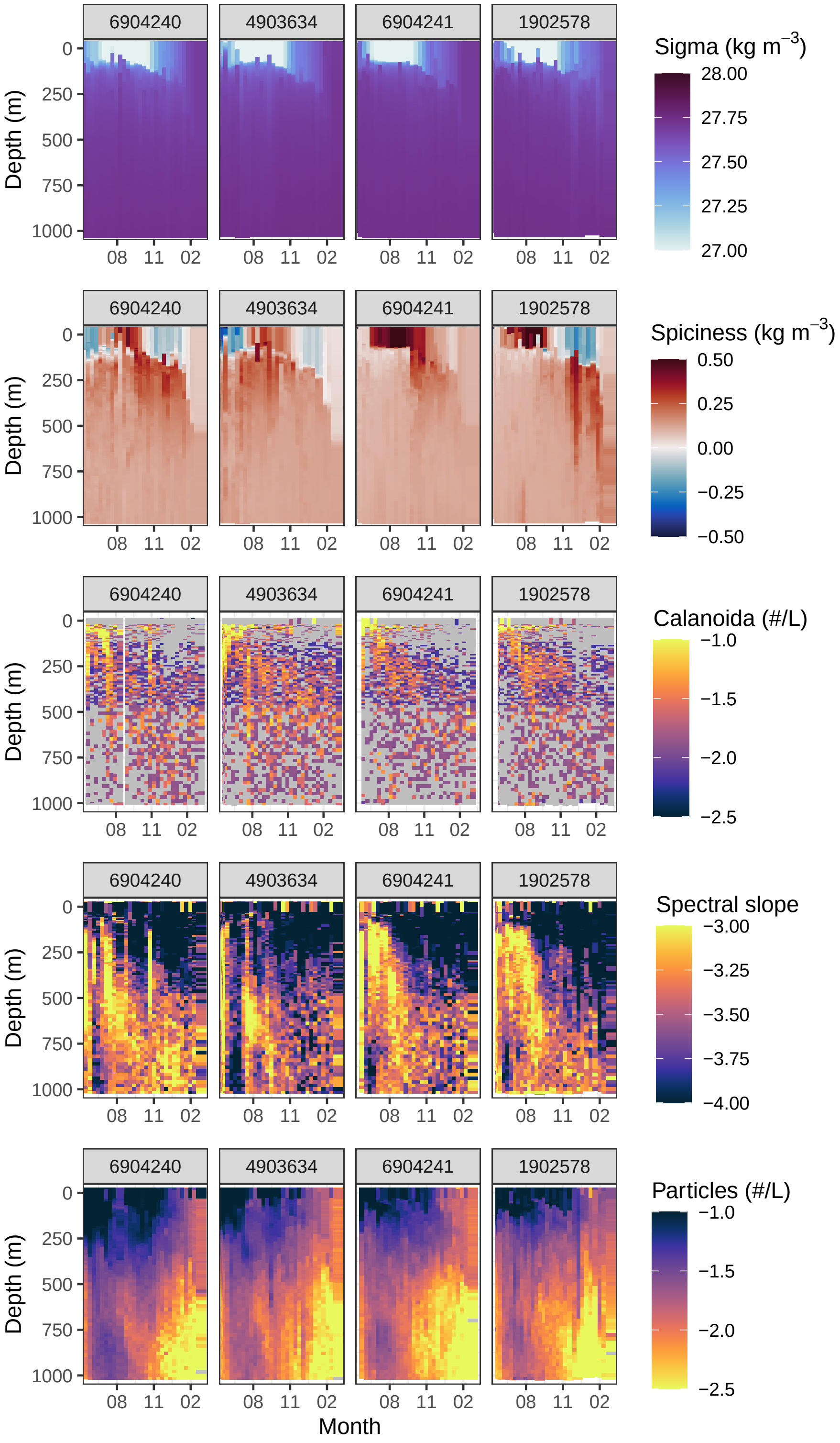

Figure 4.13: Potential density anomaly, spiciness, *Calanoida* concentrations ($\log_{10}$ colorscale), spectral slope and particle concentrations for the 102-128 μm size class ($\log_{10}$ colorscale) for each float.

4.4.4 Comparing OST and UVP6 data

4.4.4.1 Carbon flux trends and estimations

For the first time, BGC-Argo floats equipped with both an OST and the UVP6 have been deployed to better characterize the downward carbon flux and the nature of sinking particles from a multi-instruments approach (Claustre et al. 2021). The quantification of the POC flux using the OST method (Bishop et al. 2004; Estapa et al. 2013, 2017, 2019, 2023) is based on an empirical POC:ATN ratio (Estapa et al. 2023) whereas UVP6 PSD measurements are used to compute POC fluxes using Equation 4.2:

$$F = \sum_{i}^{N} C_i A d_i^B \tag{4.2}$$

where C_i, A and B represent, respectively, the concentration of particles (#/L) for the i^{th} class of mean diameter d_i (in mm) and 2 constants with B being related to the fractal dimension (D) of an aggregate by $D = (B + 1)/2$ (Guidi et al. 2008).

The use of Equation 4.2 to derive carbon fluxes from PSD was firstly implemented by Guidi et al. (2008) who used a minimization procedure between sediment traps data and estimated fluxes using PSD from several previous versions of the UVP to find the optimal value of A and B (i.e. 12.5 and 3.81). Iversen et al. (2010) and Fender et al. (2019) followed the same procedure and concluded that the couple of parameters found by (Guidi et al. 2008) could not be used globally at the expense of greatly over- or underestimating POC fluxes, depending on the sampling region. In addition, the formulation of such a model implies that A and B would be valid at global scale, at all depths, for all UVP models and across all size classes which is arguable (Bisson et al. 2022). Equation 4.2 also assumes that the flux is only size-dependent though the main driver for the settling of aggregates is still debated (Iversen and Lampitt 2020; Iversen 2023). As a result, the direct comparison of carbon fluxes derived from both OST and UVP data with Equation 4.2 should be focused on the trend rather than on absolute carbon flux values.

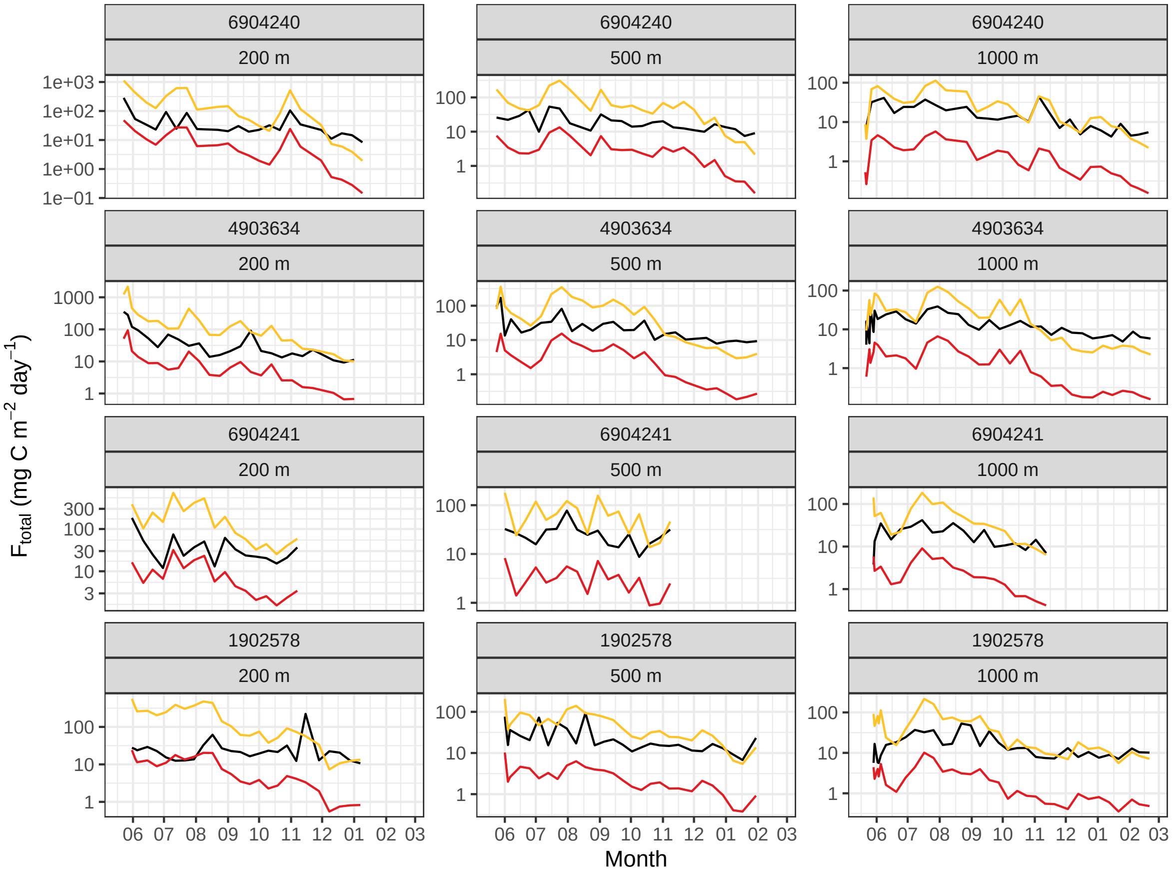

Figure 4.14: Comparison of total carbon fluxes ($F_{small} + F_{large}$) derived from the OST (black) and the UVP6 using the A and B values of Guidi et al. (2008) (red) and Iversen et al. (2010) (yellow) in Equation 4.2. OST data from float 6904241 stops in November due to a transmissometer failure.

Table 4.1: Pearson correlations (all statistically significant with a p-value < 0.01) between UVP6 PSD-derived carbon fluxes and total, large and small particle carbon fluxes measured by the OST at 3 drifting depths.

	Small flux			Large flux			Total flux		
WMO	200 m	500 m	1000 m	200 m	500 m	1000 m	200 m	500 m	1000 m
6904240	0.78	0.55	0.71	0.84	0.72	0.75	0.86	0.74	0.80
4903634	0.90	0.73	0.77	0.81	0.74	0.86	0.86	0.76	0.86
6904241	0.09	0.13	0.61	0.52	0.33	0.69	0.48	0.34	0.74
1902578	-0.09	0.62	0.64	-0.02	0.32	0.56	-0.02	0.41	0.60

Figure 4.14 shows the comparison between the total carbon flux measured by the OST ($F_{total} = F_{small} + F_{large}$) and the UVP6 (median of all UVP measurements while the float was drifting) at all drifting depths. Overall, carbon fluxes estimated with the A and B coefficients of Guidi et al. (2008) are lower than the ones measured by the OST whereas the same estimation using the coefficient of Iversen et al. (2010) generally overestimates the OST at 200 m but is of the same order at 500 m and 1000 m. Without additional measurements (e.g. co-deployed sediment traps), it is however impossible to decipher which measurement is closest to the truth. Nonetheless, carbon fluxes measured at 1000 m by the OST and the UVP6 with the coefficients of Iversen et al. (2010) are both well correlated (> 0.6 for all floats) and of similar magnitudes while carbon fluxes using Guidi et al. (2008) are one order of magnitude lower. In their paper, Iversen et al. (2010) proposed that the carbon fluxes discrepancy could be due to different biogeochemical regimes where the relationship of Guidi et al. (2008) was rather based on sediment traps at open ocean sites with lower carbon fluxes (Honjo et al. 2008) while the study site of Iversen et al. (2010) was located in a highly productive system at the continental margin off Cape Blanc in Mauritania. The LS is productive during the spring bloom (Lacour et al. 2015) therefore it is coherent to find a closer relationship with estimations based on a highly productive system.

The trends of total flux measured by both instruments are very well correlated at all drifting depths for floats 6904240 and 4903634 with correlations (see Table 4.1) ranging from 0.74 to 0.86. Table 4.1 also shows that the correlation between UVP-derived carbon fluxes and F_{small} and F_{large} for that pair is 0.76 on average. We calculated lower correlations with the other two floats, especially the float 1902578 at 200 m, where correlations between the UVP-derived carbon fluxes and all fluxes (small, large and total) are close to 0. Overall, it nevertheless suggests that there is a possibility to get more accurate estimations of carbon fluxes using only the PSD hence using only the particle size as an estimator of carbon flux, contrarily to what other studies have argued (McDonnell and Buesseler 2010; Iversen and Lampitt 2020; Iversen 2023).

4.4.4.2 Nature of particles seen by the OST and the UVP6

F_{small} represents the continuous accumulation of small particles hence it could be related to the accumulated biovolume of particles seen by the UVP6. Similarly, F_{large} could be related to the biovolume seen by the UVP6 when the OST detects jumps in the attenuation signal. Consequently, we firstly computed the slope of each segment (see lightblue straight lines in Figure 4.2) and all the jumps at all drifting depths as well as the total biovolume seen by the UVP6 while the float was drifting. Then, we computed the average biovolume seen during each segment duration and we associated the closest total biovolume (in time) with a jump.

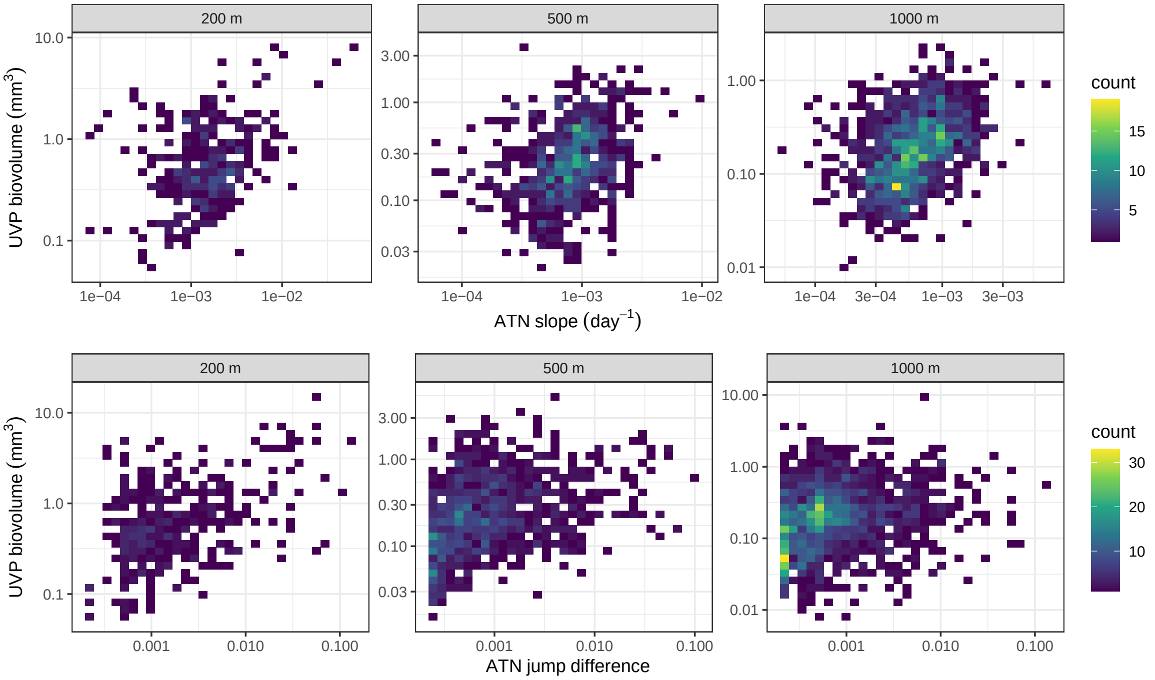

Figure 4.15: Average biovolume seen by the UVP6 as a function of the attenuance slope (top) and total biovolume seen by the UVP6 as a function of the intensity of the jump seen by the OST (bottom) at each drifting depth.

Figure 4.15 shows that there is no clear relationship between the biovolume seen by the UVP6 and the attenuation (continuous or stochastic) measured by the OST. For small particles, the relationship between the ATN slope and the average biovolume shows a weak correlation (0.30 at 500 m and 1000 m). For large particles, the OST misses particles that are seen by the UVP6 (see 500 m and 1000 m in the lower panel). It is coherent with the fact that OSTs were not designed to intercept and detect large sinking particles (Estapa et al. 2023). The current version of the OST has a housing above the optical window which, together with the float itself, can produce a “self-shading” effect (Estapa et al. 2017) that prevents the collection of fast sinking particles (assumed here to be large particles). In addition, the nature of particles is also a source of uncertainty in the optical attenuation signal. Mathematically, the attenuation efficiency (Q_c) of a spherical particle can be defined (Mobley 2022) as

$$Q_c = Q_a + Q_b \tag{4.3}$$

where Q_a and Q_b are, respectively, the absorption and scattering efficiencies. Consequently, Mobley (2022) defines the attenuance cross section (σ_c) as Q_c multiplied by the geometrical cross section of that particle (πr^2 for a spherical particle). Therefore, if a particle of a given size has a small σ_c (e.g. mostly transparent) or a high σ_c (e.g. opaque), the attenuation will be different (lower for a smaller σ_c) but the size measured by the UVP6 will be the same.

Therefore, if the UVP6 and the OST are well correlated at first order (Figure 4.14, Table 4.1), it is more difficult to directly link the attenuance to the biovolume (hence the size) of a particle because of the nature of particles themselves. Overall, further exploration analyses are needed to better understand the particle dynamics and their composition, especially considering a broader range of trophic situations.

4.5 Perspectives

4.5.1 A complementary variable to investigate POC fluxes - b_{bp}

I did not use b_{bp} data, a proxy for suspended particle concentration, that has already been used to derive POC concentrations, POC fluxes and particle size (Briggs et al. 2011, 2020; Alkire et al. 2012; Cetinić et al. 2012; Briggs et al. 2013; Dall'Olmo and Mork 2014; Rasse et al. 2017; Lacour et al. 2019; Giering et al. 2020a). In Briggs et al. (2011), the authors explain that when a large particle goes through the sampling volume of the b_{bp} sensor, it causes a spike in the b_{bp} signal. However, the height of this spike depends on many factors such as the cross section of the particle (or aggregate), Q_b, the sampling volume, the fraction of the particle in the sampling volume and the time the particle spends in the sampling volume. Using an empirical relationship between ship-based b_{bp} and POC, they were able to derive POC concentrations (mg C m^{-3}) and then POC fluxes (mg C m^{-2} day^{-1}) by multiplying those concentrations by a given sinking speed (m day^{-1}).

As of today (March 15, 2023), 111361 b_{bp} profiles were acquired by BGC-Argo floats. With the advent of floats equipped with both the UVP6 and a b_{bp} sensor, it would be interesting to investigate the relationship between the size measured by the UVP6 and the size derived by spikes (i.e. spike height) in the b_{bp} signal. Such an empirical relationship could bring information on the abundance of large particles at global scale using the huge, already available, b_{bp} database.

4.5.2 Configuration adaptation to specific BCP-related processes

The current configuration of all floats in the LS was a 10-day ascending profile acquisition with drifting at 200 m for one day, 500 m for 3 days and 1000 m for 5 days. During drifting, OST measurements were taken every 30 minutes at all depths whereas UVP measurements were taken every 20 minutes at 200 m and every 2h at 500 m and 1000 m. This initial configuration was based on a compromise between science targets and energy consumption limitations for long-term deployment (years). However, I think this configuration could be adapted depending on the period of the year to target specific processes. For instance, I tried to evaluate sinking speeds from particle concentrations using a gaussian fit in different water layers to follow the gaussian peak with time and depth for each size class. I managed to compute realistic sinking speeds but the uncertainty was huge and potentially biased because I was just trying to fit something I saw in the data. Therefore, I did not use those estimations here but I think it would be possible to compute them if the float was sampling every day when the abundance of particles is at its maximum (e.g. during the spring bloom). Similarly, to address the question of the vertical migration, a 10-day temporal resolution is way too low because plankton images are rare compared to detritus so the sampling volume should be greatly increased to have a better estimation of the presence (or absence) of zooplankton. Finally, it would perhaps be interesting to increase the time spent at 200 m (to 3 days) and decrease the time spent at 1000 m (to 3 days instead of 5) where the probability of capturing big particles is lower than at 200 m. There could also be UVP6 and OST measurements closer in time at all drifting depths to have a better comparison of attenuation slopes/jumps and biovolumes.

5 Revisiting the BCP with the CONVERSE framework

Initially, it was not intended that I work on this topic. As I will briefly explain in the general discussion, my attempts to find a global (or regional) relationship to derive POC fluxes from UVP5 size spectra failed constantly. Therefore, I was proposed to work on a new concept related to carbon sequestration. I was told I would be co-author, that it would be done quickly and that it was only about revising the carbon sequestration flux of the gravitational pump.

Why revise one pump when you can revise them all? 1 year and a half later, hundreds of emails, one promotion to first author, one negative review and one strong rebuttal, we are still on the road to publication. Here below is the revised version of our paper submitted in Nature Geoscience about the reassessment of the global sequestration ($\geq$ 100 years) of the BCP and its components by using a continuous approach to carbon storage as opposed to the common view of long-term sequestration below a fixed reference depth.

Revisiting the biological pump using the new continuous vertical sequestration approach

Florian Ricour[1,2*], Lionel Guidi[2], Marion Gehlen[3], Timothy DeVries[4] and Louis Legendre[2*]

[1]Sorbonne University, CNRS, Laboratoire d'Océanographie de Villefranche, LOV, F-06230 Villefranche-sur-Mer, France.
[2]Freshwater and OCeanic science Unit of reSearch (FOCUS), University of Liège, Liège, Belgium.
[3]LSCE-IPSL, CEA, CNRS, Université Paris-Saclay, Gif-sur-Yvette, France.
[4]Department of Geography / ERI / IGPMS, University of California, Santa Barbara, CA, USA.
*Corresponding authors: florian.ricour@uliege.be and legendre@imev-mer.fr

Running title: Continuous vertical sequestration approach

The ocean contains about 40 times more carbon than the atmosphere, i.e. it stores 38,000 Pg C of dissolved inorganic carbon (DIC) vs. 900 Pg C of carbon dioxide (CO_2) in the present atmosphere. The biological carbon pump contributes to ocean carbon storage by moving DIC out of the surface ocean into deeper waters. Many studies have assumed that storage of biogenic DIC (DIC_{bio}) on climate-relevant timescales (typically ≥100 years) only occurs in the deep ocean. Here we show, in contrast, that this storage can occur at all depths in the water column, mostly above 2,000 and even 1,000 m. To illustrate this continuous vertical sequestration, we use the fraction of water that remains in the ocean interior for ≥100 years, computed with a data-assimilated inverse circulation model, to estimate the DIC_{bio} sequestration fluxes resulting from the combined action of different biological pump pathways. With this new approach, global carbon sequestration for ≥100 years driven by the biological pump is 0.9-2.6 Pg C y^{-1}, which is up to 6 times larger than usual estimates that ignore the contribution of upper-ocean sequestration.

The biological carbon pump is an important process of natural carbon sequestration in the ocean[1,2]. Photosynthesis in sunlit surface waters converts dissolved inorganic carbon (DIC) to organic carbon, and gravitational settling, ocean mixing and animal migrations export this organic matter downwards where its remineralization (respiration) produces biogenic DIC (DIC_{bio}; also called C_{soft}[3] and C_{seq}[1]). However, not all of this DIC_{bio} is sequestered on climatically relevant timescales, since much is remineralized in the upper ocean where CO_2 can be returned to the atmosphere relatively quickly[4–6]. Although the timescale of "climatically significant" carbon storage (i.e. sequestration) does not have a strict definition[7], it is conventionally considered to be ≥100 years[8]. This 100-year time horizon has been used as a guideline to assess carbon sequestration by the biological pump[9,10], to distinguish between regions of efficient and inefficient carbon sequestration[11,12], and to define durable carbon sequestration in assessments of the efficacy of ocean-based deliberate carbon dioxide removal (CDR) approaches[13]. In the ocean sequestration literature, some studies address the inventory of sequestered carbon[1,5], and others the sequestration flux[2]. The present work deals with the latter. Ocean carbon sequestration is detailed in Supplementary Information 1, and the acronyms and symbols used in the text are listed in Supplementary Table S1.

Despite the widespread use of the 100-year time threshold, few studies have explicitly quantified the flux of carbon sequestered by the biological pump for ≥100 years, due to difficulties in assessing how long DIC_{bio} will be retained in the ocean. In order to estimate the biological pump sequestration flux, most previous studies have assumed that carbon transported below a fixed depth or isopycnal surface – generally located between 1,000 and 2,000 m[2,11,14–19] – is stored for long enough to be considered “sequestered”. An implicit assumption of these studies is that DIC_{bio} above this “sequestration depth” does not remain in the ocean for ≥100 years.

A modelling study using Lagrangian tracking found that only about 70% of the biogenic carbon flux at 1000 m was sequestered for >100 years in the North Atlantic[6]. Similar calculations using a global ocean circulation inverse model found that carbon injected as CO_2 at different ocean depths and locations showed large geographic variations in the amounts retained for ≥100 years in the ocean interior[5]. For example, only about 20% of the carbon injected at a depth of 1,000 m in the western North Atlantic was retained for ≥100 years, while the corresponding value for injection at a similar depth in the Northeast Pacific was nearly 80%. However, no study has yet assessed on the global scale how much of the carbon flux driven by the biological pump is sequestered for ≥100 years.

Here, we use published values of the fraction of a water parcel at a given location and depth that will remain in the ocean for ≥100 years (f_{100}), calculated[5] using a data-assimilated ocean circulation inverse model[20] to determine the fraction of DIC_{bio} sequestered in the ocean interior for ≥100 years. We combine f_{100} with estimates of carbon fluxes by different biological pump pathways to compute how much carbon is sequestered for ≥100 years under various assumptions. To emphasize the point that sequestration for ≥100 years can occur at any depth in the water column, we refer to our approach as Continuous Vertical Sequestration (CONVERSE; Fig. 1). In this study, we compare the CONVERSE results with estimates based on fixed depth horizons. This approach is relevant to open-ocean CDR deployments, which are intended to induce large-scale export fluxes to sequester atmospheric carbon as DIC in the water column.

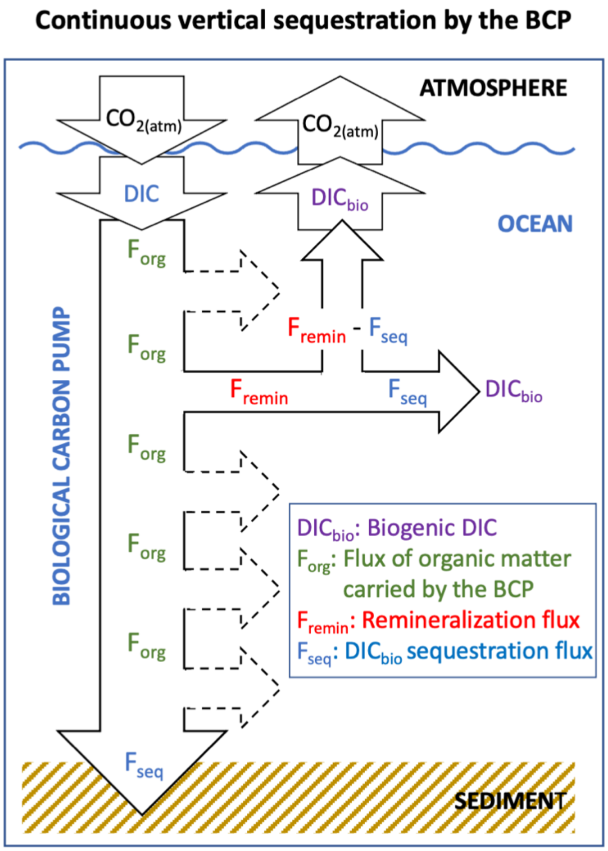

Fig. 1. The CONVERSE fluxes driven by the biological pump. Throughout the water column, part of the downward flux of organic carbon (F_{org}) is remineralized to CO_2 (F_{remin}). Some of the resulting DIC_{bio} returns to the atmosphere within 100 years, and the remainder is sequestered for ≥100 years (F_{seq}). The fraction sequestered increases with depth, but is not null even at relatively shallow depths (Fig. 2), causing continuous vertical sequestration of DIC_{bio}. In addition, a very small fraction of F_{org} (which "overflows" the biological pump) is not remineralized to DIC_{bio} at the bottom of the water column, and may be sequestered in sediment for long times reaching millions of years. The CONVERSE processes occur at all depths, but are illustrated here at only one depth, while their occurrences at some other depths are represented by dashed arrows. The widths of arrows do not reflect the magnitudes of fluxes.

Fraction of biogenic DIC sequestered at different depths and locations in the ocean

Across the ocean, there is large geographic variability in the fraction of DIC_{bio} that can be sequestered for ≥100 years. The median depth-average value of f_{100} is roughly 0.7, a value which can be used to separate regions with relatively lower and higher DIC_{bio} sequestration potential (Fig. 2a). The depth distribution of globally averaged f_{100} increases rapidly from 0 at the sea surface (by definition) to ~0.6 at 1,000 m, quite rapidly from 1,000 m to 2,000 m, and progressively up to 1.0 at the seafloor where 1.0 indicates 100% retention of DIC_{bio} for ≥100 years (Fig. 2b).

The geographic distribution of f_{100} at different depths shows that the areas occupied by higher f_{100} increase with water depth (Fig. 2c-d, and Supplementary Fig. S1). However, many areas of relatively shallow depths have high f_{100} values, with f_{100} exceeding 0.5 at 530 m in regions such as the North Indian Ocean, Eastern Pacific, and Antarctic margin (Fig. 2c). Sequestration occurring in these regions would be missed by traditional metrics that consider sequestration to occur only below 1,000 or 2,000 m. In contrast, there are significant areas of the ocean at 1,000 m depth where f_{100} values are as low as 0.2-0.3 (Fig. 2d), and some deep waters with relatively large areas where f_{100} <1.0, e.g. at 2101 m and deeper in most of the Antarctic Circumpolar Current (Fig. 2e).

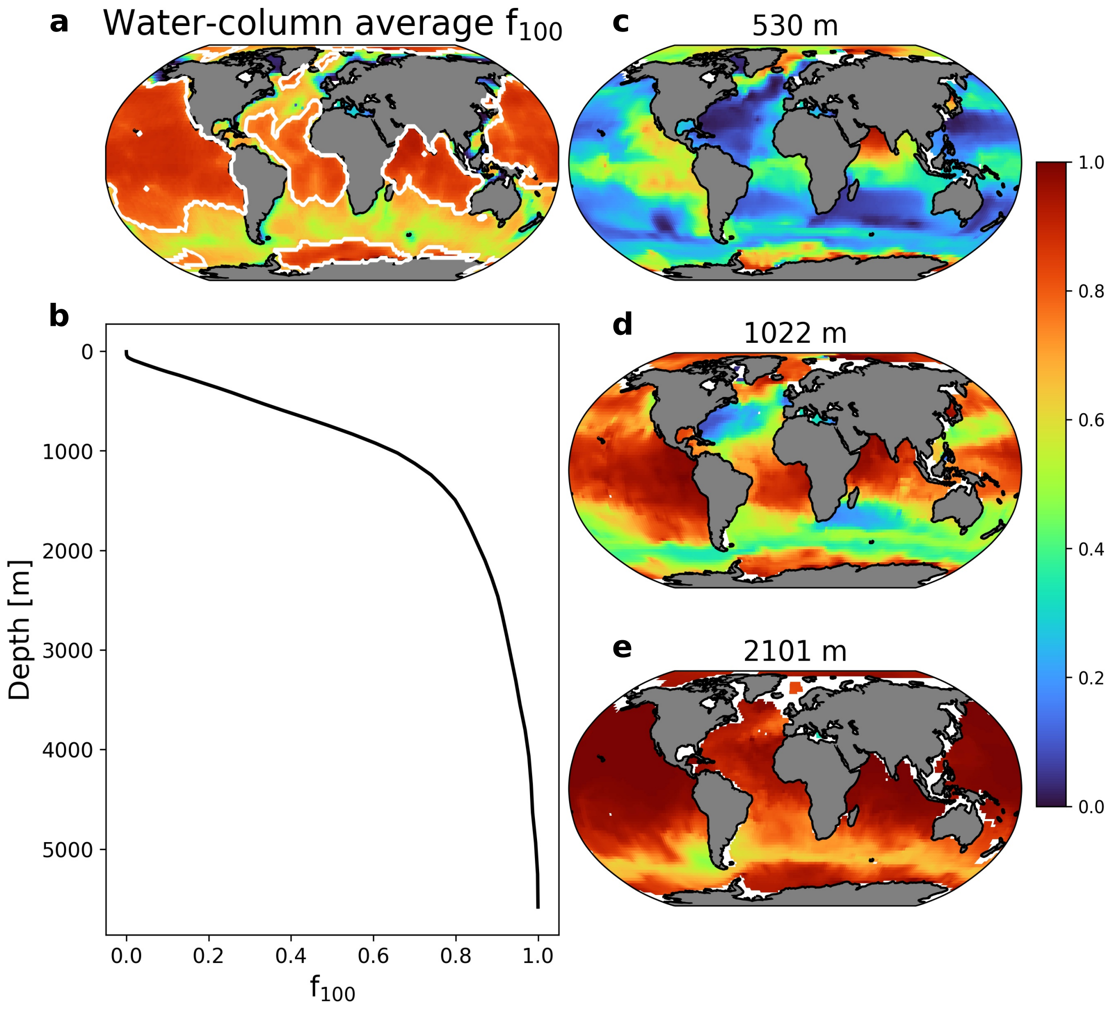

Fig. 2. Geographic and vertical distributions of f_{100}: (a) depth-averaged values of f_{100} below the base of the euphotic zone (z_{eu}); continuous white lines: median value of 0.7; (b) ocean-averaged vertical profile of f_{100}; (c-e) f_{100} values at three depths. White areas correspond to pixels with water depths shallower than the depth illustrated (more depths in Supplementary Fig. S1).

The results in Fig. 2 highlight important points regarding biological pump-driven carbon sequestration. First, not all water at depths ≥1,000 or ≥2,000 m is stored away from the atmosphere (and thus the carbon it contains sequestered) for ≥100 years, contrary to the tacit assumption of studies that use a fixed depth horizon for assessing sequestration fluxes. Second, sequestration in the form of DIC_{bio} can occur throughout the entire water column. The global-ocean depth-averaged f_{100} for depths >1,000 m is 0.87, indicating that most, but not all, of the water in the deep sea is stored away from the atmosphere with the carbon it contains for ≥100 years. However, the more important point from Fig. 2 is that a substantial fraction of the water above 1,000 m is also stored away from the atmosphere for ≥100 years, thus sequestering the carbon it contains, for example at 530 and 319 m where the global average f_{100} is 0.33 and 0.18, respectively.

Mechanisms of biological-pump carbon transport and remineralization profiles

In order to assess the carbon sequestered by the biological pump for ≥100 years, we combined our estimates of f_{100} with estimates of carbon fluxes due to the biological pump. The latter operates by three distinct mechanisms or "pathways" which all contribute to carbon sequestration[1] (details in Supplementary Information 2). The *gravitational pump* is driven by the sinking of particulate organic carbon (POC), consisting mostly of phytoplankton cells and aggregates[21] and zooplankton faecal pellets and debris[22]. Some of the sinking POC reaches the seafloor, although most is remineralized in the water column[23]. The physical *mixing pump* is driven by the seasonal shoaling and deepening of the mixed layer[24], the subduction of water masses and their organic carbon along mesoscale to sub-mesoscale fronts associated with eddies[25,26] and the large-scale advection and overturning of the ocean[27–29]. The mixing pump mechanisms transport surface water downwards with its POC and dissolved organic carbon (DOC). The *migrant pump* is composed of animals that perform diel or seasonal vertical migrations[30,31]. During these migrations, animals defecate, excrete DOC and release respiratory CO_2 deep in the water column, the source of this carbon being POC grazed in upper waters. Migrating animals also release some biogenic carbon at various depths during their vertical journeys.

a Maximum depths of POC and DOC vertical BCP fluxes

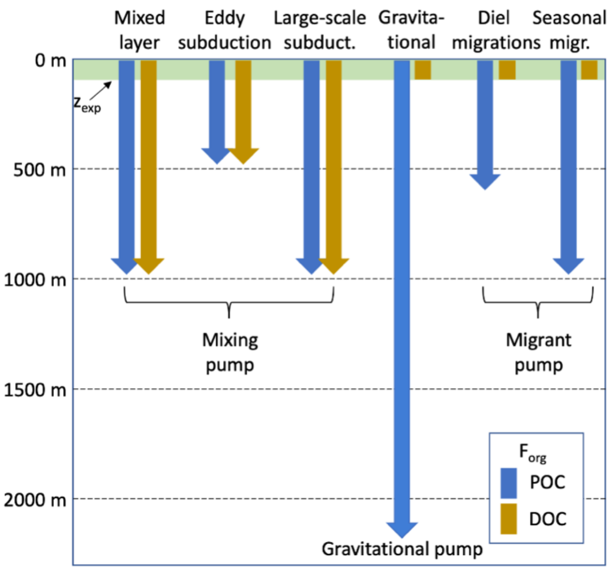

b Organic matter remineralization by the combined pumps

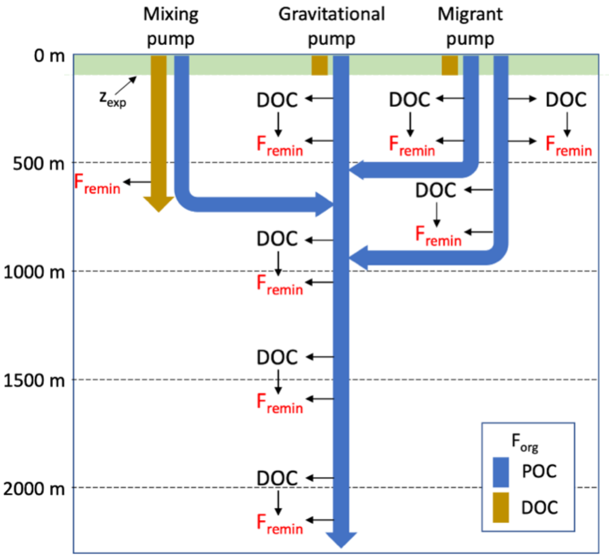

Fig. 3. The biological carbon pump. (a) Maximum depths to which each mechanism transports POC and DOC below the export depth (z_{exp}), and the carbon pump to which each belongs. (b) Combined action of the three pumps on F_{remin}: one part of the POC flux is remineralized directly, and another part is solubilized to DOC by bacteria or released as DOC by grazers, after which most of this DOC is remineralized. There are reports of zooplankton seasonal vertical migrations deeper than 1000 m.

Each of these pathways has a characteristic depth above which the exported carbon is remineralized to CO_2 in the water column (Fig. 3a; values from Table 2 of a published paper[32]), this depth determining how much of the resulting DIC_{bio} can be sequestered for ≥100 years. The deepest depth is reached by the gravitational pump, which can potentially transport POC all the way to the seafloor. The POC carried by the other pumps that is not remineralized above the depths they reach is incorporated into the gravitational pump for the remainder of its journey downwards (Fig. 3b). Most of the carbon exported by the mixing pump, which is the only pump that carries DOC, is remineralized to CO_2 in the upper 1000 m, except in areas of deep convection where labile DOC can be found ≥1000 m[33] .A small fraction of labile DOC is converted into refractory DOC, thus sequestering carbon chemically[17,34,35], but this "microbial pump" is beyond the scope of the present study. In the migrant pump, vertically migrating animals remineralize at depth carbon transported in their bodies. The depth of diel migrations generally does not exceed 200 m, but can reach a maximum of 600 m in some cases[36,37] while seasonal migrants can reach 1400 m[38] and even deeper[39–41].

For each of these pumps, we estimated the flux sequestered for ≥100 years (F_{seq}) by calculating the three-dimensional remineralization rate of carbon in the interior ocean and multiplying it by the corresponding value of f_{100} (see Methods). We refer to the global integral of this quantity as the global sequestration flux. We define the interior ocean as all depths below a fixed "export depth", which we choose as 100 m or the base of the euphotic zone, depending on our model configuration (Table 1). Although it is theoretically possible for sequestration to occur above this depth horizon due to non-zero values of f_{100} at relatively shallow depths (Fig. 2 and Supplementary Fig. S1), for purposes of this study we assumed that sequestration above the export depth is negligible. We computed F_{seq} using seven different CONVERSE versions, whose characteristics are summarized in Table 1 and Supplementary Table S2. We use various published estimates of carbon export and remineralization fluxes (F_{remin}) driven by the gravitational, mixing and migrant pumps. We compare the CONVERSE F_{seq} to estimates at fixed depth horizons of 1,000 and 2,000 m (Table 1) and also to previously published values[14,15,18] (Supplementary Table S3).

Table 1. *Upper part.* Estimates of biological pump fluxes for the seven CONVERSE versions (C1 to C7): export depth; characteristics of calculations of F_{remin} for POC, DOC, vertical migrations and sediment. We multiplied F_{remin} by the corresponding f_{100} to calculate F_{seq}. *Lower part.* Values of global-ocean CONVERSE F_{seq} (Pg C y^{-1}) and percent ratios (%) over the water column by the gravitational and all pumps, and also calculated at 1000 and 2,000 m and above and below 2000 m; values normalized to the corresponding export flux at 100 m. Ratios of CONVERSE F_{seq} to POC fluxes calculated at 1,000 and 2,000 m. Equations and detailed values are given in Supplementary Tables S2 to S5. The global distributions of F_{seq} in C1, C2 and C4 are illustrated in Fig. 5.

CONVERSE	**1**	**2**	**3**	**4**	**5**	**6**	**7**
Export depth	100 m	100 m	100 m	z_{eu}	100 m	100 m	100 m
Pump or flux	***Computation of pixel remineralization fluxes (F_{remin}) (Pg C m^{-2} y^{-1})***						
Gravitational[*]	$b = 0.86$	Variable b	Regional b	C4-C5:Taken from a model[4]		Based on C5[†]	Same as C1
Mixing	C1-C3: based on C5[†]			C4-C5: Taken from a model[4]		Based on C5[†]	Based on POC export at 100 m
Migrant diel	C1-C7: Derived from POC export at 100 m						
Migrant seasonal[‡]	C1-C3: Derived from POC flux at 597 m			C4-C5: Derived from POC flux at 619 m		Based on C5[†]	Same as C1
Sediment	C1-C7: Published global-ocean estimates of fluxes in the sediment[42]						
Pumps	***Global water-column sequestration fluxes (F_{seq}) and % ratios***						
Gravitational[*]	0.63	0.92	0.71	1.89	1.86	0.76	0.63
Biological (all)[*]	0.88	1.16	0.95	2.61	2.44	1.00	0.96
Gravitational[*] **/all**	72%	79%	75%	72%	76%	76%	66%
Mixing+migrant / all	28%	21%	25%	28%	24%	24%	34%
Fluxes	***Global fluxes calculated at 1,000 and 2,000 m (F_{seq})***						
POC at 1,000 m[§]	0.38	0.68	0.47	1.13	1.13	0.46	0.38
POC at 2,000 m[§]	0.19	0.42	0.26	0.47	0.47	0.19	0.19
Pumps	***Global sequestration fluxes integrated above and below 2,000 m (F_{seq}) and % ratios***						
Gravitational ≤2,000 m	0.48	0.54	0.49	1.61	1.58	0.64	0.48
Gravitational >2,000 m[*]	0.15	0.38	0.22	0.28	0.28	0.12	0.15
All ≤2,000 m	0.71	0.77	0.71	2.30	2.13	0.87	0.81
All >2,000 m[*]	0.17	0.39	0.24	0.31	0.31	0.13	0.15
$All_{\leq 2000}$ / All_{owc}[**]	81%	66%	75%	88%	87%	87%	84%
$All_{>2000}$ / All_{owc}[**]	19%	33%	25%	12%	11%	13%	16%
Pumps or fluxes	***Global sequestration fluxes normalized to POC export fluxes at 100 m (F^*_{seq})***[††]						
Gravitational[*]	0.21	0.31	0.24	0.22	0.25	0.25	0.21
Biological (all)[*]	0.29	0.39	0.32	0.30	0.33	0.33	0.32
POC at 1,000 m[§]	0.13	0.23	0.16	0.13	0.15	0.15	0.13
POC at 2,000 m[§]	0.06	0.14	0.09	0.05	0.06	0.06	0.06
Pump ratios	***CONVERSE sequestration fluxes to POC fluxes at 1,000 and 2,000 m***						
• ***to POC flux at 1,000 m***							
Gravitational[*]	1.7	1.4	1.5	1.7	1.6	1.7	1.7
Biological[*]	2.3	1.7	2.0	2.3	2.2	2.2	2.5
• ***to POC flux at 2,000 m***							
Gravitational[*]	3.3	2.2	2.7	4.0	4.0	4.0	3.3
Biological (all) [*]	4.6	2.8	3.7	5.6	5.2	5.3	5.1

[*] Water column only, i.e. does not include F_{seq} in sediment

[†] Value from C5 multiplied by the ratio of the global POC export flux at 100 m of C1 to C5

[‡] Northern North Atlantic only

[§] Calculated at 1,000 or 2000 m**,** assuming that the POC flux at 1,000 or 2,000 m is entirely sequestered below

[**] All_{owc}: F_{seq} for all pumps over the water column

[††] F^*_{seq}(global) = F_{seq} (global)/F_{exp}(global), where F_{exp} is the POC flux at the export depth (Supplementary Tables S3-S5)

Estimates of sequestration fluxes by the biological pump

For calculating carbon sequestration by the gravitational pump, we use two approaches. The first combines estimates of carbon export at 100 m from a model[15] with an empirical power-law relationship governing the attenuation of particle flux with depth[43] to determine F_{remin}. The coefficient of POC attenuation with depth (b) in this model is varied in our different calculations using a globally uniform $b = 0.86$[43], a geographically variable b from an empirical model[15], and a regionalized b in biogeochemical provinces[18]. The second approach uses model output (SIMPLE-TRIM) from a data-assimilated biological pump model[4] to determine F_{remin}, with an export depth of either 100 m or the base of the euphotic zone. Carbon export at 100 m from these models is illustrated in Supplementary Fig. S2.

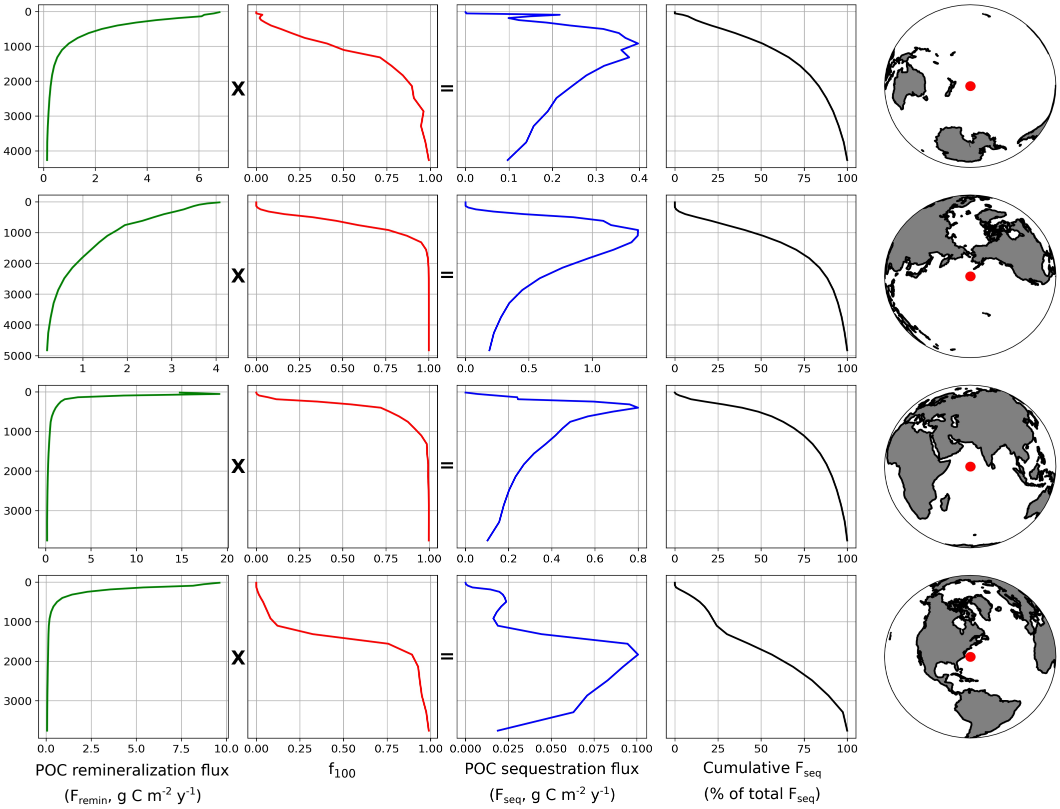

Fig. 4. Vertical profiles of F_{remin} (Supplementary eq. 24), f_{100}, and the resulting F_{seq} (eq. 6) for POC and cumulative F_{seq} from surface to depth, in four ocean pixels representative of different ocean configurations identified in the present study. The vertical profiles of F_{remin} are calculated with data from SIMPLE-TRIM[4]. The values of F_{remin} and F_{seq} (X-axes) are different for the four sites.

The vertical profiles of POC F_{seq}, resulting from the combination of vertical profiles of F_{remin} and f_{100}, generally showed maxima above 2,000 and even 1,000 m and at least 50% of vertical F_{seq} accumulation by 1,000 m (Fig. 4). This shows that the time-honored use of 2,000 m or 1,000 m as sequestration depth misses most of the ocean sequestration flux, and thus stresses the significance of the CONVERSE approach. The location of F_{seq} maxima between 1,000 and 2,000 m reflects the relatively high values of both f_{100} and F_{remin} at these depths, whereas studies that estimate F_{seq} at 1,000 or 2,000 m[2,11,14–19] only consider sequestration below these depths where f_{100} is high but very little POC is left to be remineralized.

The results in Fig. 4 explain why the sequestration flux of POC due to the gravitational pump estimated by the CONVERSE approach is 0.63-1.89 Pg C y^{-1}, depending on the set of parameters used in the calculations, while the corresponding sinking POC flux calculated at 2,000 m is only 0.19-0.47 Pg C y^{-1} (Table 1). The fraction of the global POC export flux by the gravitational pump at 100 m that is sequestered for ≥ 100 years (F^*_{seq}) is 0.21-0.31, which is up to 2 and 4 times greater than the fraction of the carbon export flux that reaches 1,000 and 2000 m, respectively (Table 1). Similarly, F^*_{seq} of previous studies underestimate the corresponding CONVERSE F^*_{seq} by a factor of 1.8-3.0 when the gravitational pump global POC was estimated at 2,000 m[14,15], and by a factor of 1.3 when it was estimated at the top of the permanent pycnocline[18] (Supplementary Table S3).

Our F^*_{seq} calculated at 1,000 m can be compared to the particle transfer efficiency used in some studies to quantify the fraction of the POC exported at 100 m that bypasses remineralization above 1,000 m, although these studies did not consider possible sequestration of DIC_{bio} above 1,000 m[11,16,19]. Our F^*_{seq} at 1,000 m (0.13-0.23; Table 1) are consistent with published average regional transfer efficiencies to 1,000 m ranging between <0.05 and 0.25[11,19].

In our calculations, F_{seq} by the biological pump (all components together) ranges from 0.88 to 2.61 Pg C y^{-1} (Table 1). This wide range largely results from the wide range of carbon export values used in our calculations (3.0-8.6 Pg C $year^{-1}$, Supplementary Tables S3 and S4), and also the wide methodological differences among the seven CONVERSE versions. When considering F^*_{seq} (i.e. the fraction of the carbon export flux included in F_{seq}), the much narrower range of 0.29-0.39 (Table 1) indicates that this fraction is less variable.

While the gravitational pump accounts for 66-79% of the carbon sequestration flux by the biological pump (Table 1), the mixing and migrant pumps contribute together the remaining 21-34%, which is substantial. Using F_{seq} for DOC (by the mixing pump) and a combination of model-based estimates and correlations with POC export (migrant pump) (see Methods), we estimate that the two pumps represent 11-23 and 9-12%, respectively, of the global sequestration driven by the biological pump (the role of the migrant pump is underestimated because we only have flux estimates for the northern North Atlantic) (Supplementary Tables S3 and S4; Supplementary Information 3 provides comparisons with values from the literature).

When adding the mixing and migrant pumps to the CONVERSE framework, we estimate that global F^*_{seq} is 0.29-0.39, an increase of 0.08 relative to the sole gravitational pump, and 2-3 or 3-6 times higher than the global F^*_{seq} of 0.13-0.23 and 0.05-0.14 when considering only the POC flux at 1,000 or 2,000 m, respectively (Table 1). Similarly, previous studies cited above underestimated biological pump global F^*_{seq} by a factor of 1.8-4.0 relative to the CONVERSE calculations (Supplementary Table S3). This reinforces our above finding that the POC flux estimated at either 1,000 and 2000 m significantly underestimates the sequestration efficiency of the biological pump. Global F_{seq} in sediment represents a small additional sequestration flux, corresponding to 0.3-1% of global POC export and 1-3% of the global water-column sequestration flux (Supplementary Tables S3 and S4).

Sequestration above and below 2,000 m accounts for 66-88% and 11-33%, respectively, of the global flux (Table 1). Corresponding values for 1,000 m are 47-68% and 32-53%, respectively (Supplementary Table S5). The sequestration flux below 2,000 m is slightly lower than the sinking POC flux at 2,000 m (0.15-0.38 and 0.19-0.47 Pg C y^{-1}, respectively) because some of the DIC_{bio} in waters >2000 m is not stored there for ≥100 years, a point also made by other authors[6]. However, this DIC_{bio} loss is more than compensated by the sequestration of DIC_{bio} above 2,000 m (0.48-1.61 Pg C y^{-1}). Thus, neglecting sequestration above 2,000 m results in significant underestimation of global F_{seq}.

The geographic distributions of carbon sequestration fluxes by the three pumps and the whole biological pump, illustrated for three representative CONVERSE versions in Fig. 5 (all versions in Supplementary Figs. S3 and S4), are similar among versions and provide insights into the environmental controls of sequestration. The global distribution of F_{seq} by the whole biological pump mainly reflects that of the gravitational pump (Fig. 5a,d). Sequestration by the biological and gravitational pumps is low in subtropical gyres where export and f_{100} <1,000 m are both low, and high in equatorial and subarctic waters and the Antarctic Circumpolar Current where POC export and/or f_{100} <1,000 m are high (Fig. 2 and Supplementary Figs. S1 and S2). This is also the case of the diel migrant pump and the POC flux calculated at 1,000 and 2,000 m. Values of F_{seq} by the mixing pump generally reflect those of POC export. The distributions of the POC flux calculated at 1,000 and 2,000 m are qualitatively similar to those of the CONVERSE biological and gravitational pump, but quantitatively much lower consistent with the above global F_{seq} values.

Discussion

The main finding of our study is that remineralization of carbon transported by the biological pump can sequester carbon (as DIC_{bio}) not only in deep waters but throughout the water column. This is contrary to previous studies that assessed the sequestration flux of the biological pump by measuring or computing carbon flux at a given depth horizon, as deep as 2,000 m. These studies calculated the sequestration flux as if it only occurred below the given depth, and did not include sequestration in the upper and mid-water column as if DIC_{bio} above the sequestration depth was rapidly lost to the atmosphere. In the CONVERSE framework, our calculations show significant DIC_{bio} sequestration fluxes (i.e. storage for ≥100 years) over most of the water column (Fig. 4), and much greater carbon sequestration driven by remineralization above 2,000 m than below (Table 1). Furthermore, the migration and mixing pumps contribute at least 21-34% of the sequestration flux by the biological pump (Table 1) even though they do not transport carbon into the deep ocean. These pumps are ignored by most traditional metrics of carbon sequestration.

Our calculations show that the carbon sequestration flux by the whole biological pump is 2-3 or 3-6 times larger than usually estimated based on POC fluxes at 1,000 or 2,000 m, respectively, and the CONVERSE sequestration flux estimates are up to 4 times larger than those from previously published studies. Biogeochemical models should thus compute F_{seq} over all water-column depths. We suggest that F_{seq} be implemented in the model experiments used to evaluate future CDR options[44], with the required f_{100} values computed with available equations[1]. The f_{100} values could instead be the same as the published values[1] used in this study, which may however be affected by changes in ocean circulation due to climate change and variability. In evaluations of future ocean CDR strategies, biologically-driven carbon sequestration fluxes should also be estimated over the whole water column."

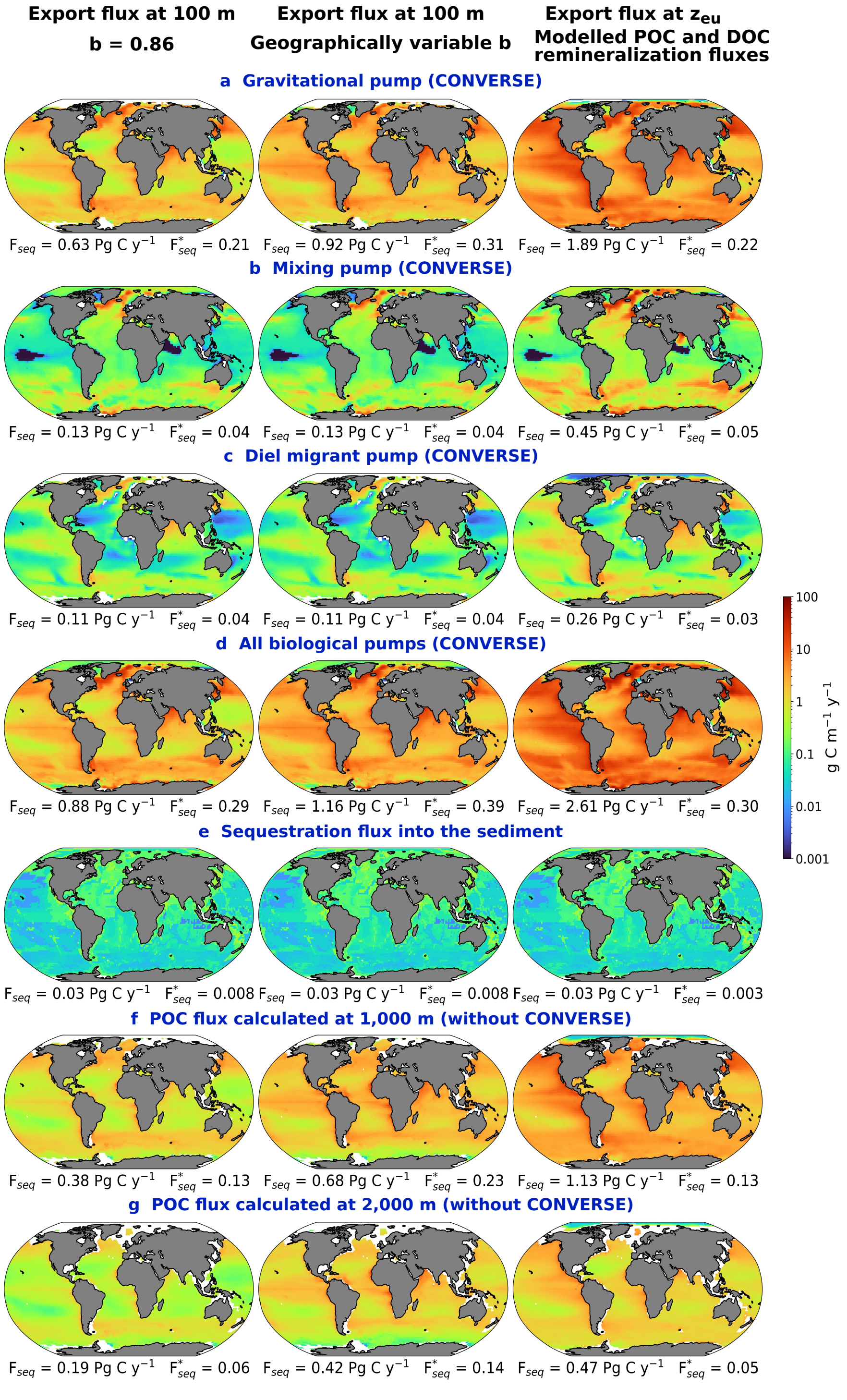

Fig. 5. Biogenic carbon F_{seq} in CONVERSE 1, 2 and 4: (a-d) carbon pumps; (e) F_{seq} into the sediment, and the POC flux calculated at (f) 1,000 m and (g) 2000 m. The latter two are the total sequestration fluxes estimated in many studies. The seasonal migrant pump is not illustrated because our results concern the sole northern North Atlantic. Ocean areas shallower than 100 m are without colour.

Methods

Calculation of F^{*}_{seq}

We calculated the fraction of the global POC export flux by the gravitational pump at 100 m that is sequestered for more than 100 years as a ratio of fluxes. This generated a dimensionless quantity:

$$F^{*}_{seq}(\text{global}) = F_{seq}(\text{global})/F_{exp}(\text{global}) \quad (1)$$

where F_{exp} is the POC flux at the export depth $z_{exp} = 100$ m.

Estimation of the fraction of sequestered biogenic CO₂ at different depths and locations in the global ocean

The fraction of water at different depths and locations that does not come back to the ocean surface (upper 10 m) within 100 years (f_{100}; called *f(t)* in another publication[5] is a dimensionless quantity ranging from 0.0 at surface to 1.0 at bottom although the deepest calculated f_{100} may be <1.0 in some pixels (2° longitude x 2° latitude). We generated f_{100} for 48 discrete depths (z') from 5 m down to the maximum value of 5582 m in each pixel of the global ocean with water depth ≥5 m, i.e. all $f_{100}(<5\text{ m}) = 0.0$. The f_{100} values are available at https://doi.org/10.6084/m9.figshare.15228690.v2 However as explained in the text, we did not use the $f_{100} < z_{eu}$.

For further calculations, we considered that each $f_{100}(z')$ was representative of a depth interval Δz ranging from depth z [mid-point between the depth above z' (i.e. z'-1) and z'] to (z+1) [mid-point between z' and the depth below z' (i.e. z'+1)]. Hence:

$$\Delta z = (z+1) - z = [(z' + 1) - (z' - 1)] / 2 \quad (2)$$

where the dimensions of z, z' and Δz were [L]. The shallowest Δz ranged from below z_{eu} to the next calculable z. The deepest Δz ranged from the deepest calculable z [mid-point between the deepest z' and z' above] to the deepest z'.

The correspondence between f_{100} values for each depth z' and depth interval Δz was as follows:

$$f_{100}(z') = f_{100}(\Delta z) \quad (3)$$

We calculated the weighted depth-averaged fraction of biogenic CO_2 sequestered over the whole water column below z_{eu} as follows:

$$f_{100}(\text{pixel}) = \sum_{\Delta z=\text{shallowest}}^{\text{deepest}} \left[f_{100}(\Delta z) \times \left(\frac{\Delta z}{\sum_{\Delta z=\text{shallowest}}^{\text{deepest}} \Delta z} \right) \right] \quad (4)$$

where Δz were the successive depth intervals from below z_{eu} to depth, and $\left(\frac{\Delta z}{\sum_{\Delta z=\text{shallowest}}^{\text{deepest}} \Delta z} \right)$ were the weights.

Continuous vertical approach to the estimation of sequestration fluxes

We used three different data sources for our calculations of seven different CONVERSE versions. The first was an empirical model of POC F_{seq} (F_{seqPOC}) in the global ocean[15]. Using these data, we computed 1-D (vertical) downward fluxes. The second source was a numerical

3-D circulation-biological pump model[4], whose data were available at https://tdevries.eri.ucsb.edu/models-and-data-products/ under the SIMPLE-TRIM output. We used the concentrations and remineralization rates of different fractions of POC and DOC at various depths to compute POC and DOC F_{remin}. The third source was a global synthesis of sediment composition and burial flux[42], which provided values of the flux of organic carbon in the sediment (F_{seqSed}). The data sources we used for the different CONVERSE versions are identified in Supplementary Table S2, and input POC F_{exp} values are illustrated in Supplementary Fig. S2. We estimated sequestration by the different pumps only in the pixels where water depth was >100 m.

In addition, the second dataset[4] contained 12 versions of the data we used for our calculations. The authors ran their model separately for each of the 12 versions, after which they computed mean values. We did the same for our CONVERSE calculations with these data.

We generally calculated the flux of organic carbon remineralized to DIC_{bio} in each depth interval Δz in the water column as the difference between the downward flux of organic carbon $F_{org}(z)$ at two successive depths z and (z + 1):

$$F_{remin}(\Delta z) = F_{org}(z) - F_{org}(z + 1) \qquad (5)$$

where all fluxes (F) had dimensions $[M\ L^{-2}\ T^{-1}]$, and the masses were in units of carbon. In eq. 5, we assumed that the decrease in F_{org} between depths z and (z + 1) caused an equivalent increase in F_{remin}, i.e. the remineralization biogenic carbon produced an equivalent flux of DIC_{bio}. The Δz could differ among biological pumps depending on the data used in the calculations.

We then computed the sequestration flux of DIC_{bio} in Δz by multiplying $F_{remin}(\Delta z)$ by the corresponding $f_{100}(\Delta z)$ value (eq. 3):

$$F_{seq}(\Delta z) = F_{remin}(\Delta z) \times f_{100}(\Delta z) \qquad (6)$$

Calculations corresponding to eq. 6 are illustrated for POC in Fig. 4. We obtained local F_{seq} in each pixel with water depth >100 m by summing up the $F_{seq}(\Delta z)$ over all depth intervals in the pixel:

$$\text{Pixel } F_{seq} = \sum_{\Delta z=\text{shallowest}}^{\text{deepest}} F_{seq}(\Delta z) \qquad (7)$$

Finally, we estimated global-ocean F_{seq} by summing up pixel F_{seq} multiplied by the pixel's area over all pixels containing data:

$$\text{Global } F_{seq} = \sum_{\text{All pixels}} \left[\text{Pixel } F_{seq} \times \text{Pixel area}\right] \qquad (8)$$

where the dimensions of pixel areas and F_{seq}(global) were $[L^2]$ and $[M\ T^{-1}]$, respectively. All equations below provide estimates of fluxes in ocean pixels ($g\ C\ m^{-2}\ y^{-1}$).

Continuous vertical estimation of pixel sequestration fluxes in CONVERSE 1

We describe here the calculations for CONVERSE 1. We provide in the *Supplementary Methods* the differences between CONVERSE 2 to CONVERSE 7 and CONVERSE 1 or other versions.

• *Sediment*

We did not include the carbon sequestration flux into the sediment in the pumps because F_{seqSed} is not always considered to be part of biological-pump-driven sequestration (Supplementary Information 1). However, we needed estimates of F_{seqSed} below to calculate the gravitational-pump sequestration flux (eq. 12).

We derived F_{seqSed} from published fluxes of total organic carbon in world-ocean sediment (F_{TOC}[42]). In the publication (their Fig. 4C), there were no pixel F_{TOC} values for areas shallower than 1,000 m or without observations, and we replaced the missing data by median F_{TOC} values in depth bins (Supplementary Table S6).

We checked that the F_{TOC} values were consistent with our calculations by comparing them to the values of the sequestration flux of all pumps together (F_{seqAll}; eq. 20) in pixels. Supplementary Table S7 shows that F_{TOC} was only a small fraction of F_{seqAll} (median of all pixels: 0.02). We thus assumed that:

$$F_{seqSed} = F_{TOC} \tag{9}$$

• *Gravitational pump*

The gravitational pump consists of the POC sinking flux below z_{exp}. For CONVERSE 1, we estimated F_{seqPOC} by calculating $F_{orgPOC}(z)$ with a widely-used empirical model[43]:

$$F_{orgPOC}(z) = F_{expPOC} \times (z/z_{exp})^{-b} \tag{10}$$

where F_{expPOC} and $F_{orgPOC}(z)$ are the downward fluxes of POC at depth z_{exp} = 100 m and any depth z below z_{exp}, respectively, and the coefficient of POC flux attenuation with depth b = 0.86[43]. The dimensions of F and z are [M L^{-2} T^{-1}] and [L], respectively, and exponent b is dimensionless.

For all depth intervals Δz deeper than z_{exp}, we calculated $F_{reminPOC}(\Delta z)$ with eq. 5, using $F_{orgPOC}(z)$ from eq. 10:

$$F_{reminPOC}(\Delta z) = F_{orgPOC}(z) - F_{orgPOC}(z + 1) \tag{11}$$

where the shallowest Δz ranged from z_{exp} to the next z below. We calculated $F_{seqPOC}(\Delta z)$ with eq. 6.

For F_{orgPOC} remaining at the bottom of the deepest Δz, F_{orgPOC}(deepest z'), we considered that the F_{seqSed} fraction in the pixel (eq. 9) was entirely sequestered in the sediment and the remaining fraction was partly sequestered in deep waters:

$$F_{seqPOC}(\text{deep}) = [F_{orgPOC}(\text{deepest } z') - F_{seqSed}] \times f_{100}(\text{deepest } \Delta z) \tag{12}$$

Because real f_{100} below the deepest Δz may be larger than our f_{100}(deepest Δz), it is possible that eq. 12 slightly underestimated F_{seqPOC}(deep) in some pixels. We calculated F_{seqPOC} with eq. 7.

• *Mixing pump*

We explain in the text that the estimates of F_{seqPOC} reflect the combined action of the three pumps on these fluxes. (Fig. 3b). The mixing pump transports not only POC, but also DOC produced above z_{exp}. The different components of this pump reach different injection depths, which we combined into a single z_{mix}, and their combination creates F_{orgDOC} from z_{mix} downwards.

A practical problem is that the data required to estimate the magnitude of $F_{reminDOC}(\Delta z)$ by each of the three physical injection mechanisms of the mixing pump in all pixels of the global ocean – which would be required to calculate pixel and global F_{seqDOC} – do not generally exist in the literature. To get around this constraint, we computed estimates of $F_{reminDOC}$ and F_{seqDOC} for the whole mixing pump.

For CONVERSE 1, we used the concentrations of DOC ([DOC]; [M L^{-3}]) and their remineralization rates (k; [T^{-1}]) in four DOC fractions (labile, semi-labile, semi-refractory, and refractory) within each depth interval Δz [L] from SIMPLE-TRIM. With these data, we computed $F_{reminDOC}(\Delta z)$ as follows:

$$F_{reminDOC}(\Delta z) = \sum\nolimits_{4\ \text{fractions}}([\text{DOC}] \times k \times \Delta z) \tag{13}$$

where the dimensions of [DOC], k and Δz were [M L^{-3}], [T^{-1}] and [L], respectively. We calculated Δz and pixel F_{seq} with eqs. 6 and 7.

However, the value of F_{expPOC} = 3.0 Pg C y^{-1} at z_{exp} = 100 m[15] we used in CONVERSE 1 was different from the corresponding value of 7.3 Pg C y^{-1} in SIMPLE-TRIM[4] (see also the legend of Supplementary Fig. S2), and we thus multiplied the values of F_{seqDOC} derived from eqs. 13, 6 and 7 by the ratio of the two F_{exp}:

$$F_{seqDOC} = F_{seqDOC} \text{ from eqs. 13, 6 and 7} \times (3.0 \text{ Pg C y}^{-1} / 7.3 \text{ Pg C y}^{-1}) \tag{14}$$

The geographic distributions of the two F_{expPOC} at z_{exp} = 100 m are illustrated in Supplementary Fig. S2).

• *Migrant pump: diel vertical migrations*

Diel vertical migrations by zooplankton, fish, jellies and other animals transport organic matter from the upper water column downwards, where part of it is released to surrounding waters as POC and DOC and is remineralized to DIC_{bio}, thus creating $F_{reminMigrD}$.

In all versions of CONVERSE, we assumed that remineralization occurred at the depth reached by migrating animals, i.e. no remineralization of $F_{expMigrD}$ above this depth:

$$F_{reminMigrD} = F_{expMigrD} \tag{15}$$

Modelling studies estimated that global $F_{expMigrD}$ by zooplankton was equal to 14% of global F_{expPOC} at the base of the euphotic zone[36], and by all migrating animals ranging in size between 0.2 mm and 20 cm was 18% of global F_{expPOC} at 150 m[31]. We used these two estimates as follows. On the one hand, given that the global ratio euphotic/100 m of F_{expPOC}(global) is 8.6 Pg C y^{-1} / 7.3 Pg C y^{-1} = 1.2 (corrected values, which are slightly different from those in the original publication[4]), we multiplied the above 14%[36] by 1.2 to obtain global $F_{expMigrD}$ by zooplankton = 17% of global F_{expPOC} at 100 m. On the other hand, using the above 18% of global F_{expPOC} at 150 m[31] and eq. 10 with $b = 0.86$, we back calculated global F_{expPOC} by zooplankton and other animals up to 20 cm as 25% of global F_{expPOC} at 100 m. We used the latter value because it included zooplankton and other migrating animals, and applied it to all pixels of the global ocean:

$$F_{reminMigrD} = F_{expMigrD} = 0.25\ F_{expPOC}, \text{ at } z_{exp} = 100 \text{ m} \tag{16}$$

Vertically migrating animals reach depths z_{migrD} = 200 to 600 m (Supplementary Information 2), and we assumed for our calculations that all migrating animals reached the f_{100} depth of z_{migrD} = 320 m (depth for which f_{100} values were available):

$$F_{\mathrm{seqMigrD}} = F_{\mathrm{reminMigrD}} \times f_{100}(320\ \mathrm{m}) \tag{17}$$

- ***Migrant pump: seasonal vertical migrations***

Deep seasonal vertical migrations of zooplankton occur in different regions of the world ocean, and are best documented in the northern North Atlantic. We estimated the carbon flux created by these migrations in the latter region, where a study reported that the copepod *Calanus finmarchicus* generated a seasonally remineralization flux (the study used the word "sequestered") at z_{migrS} = 600 to 1,400 m[38]. For CONVERSE 1, we used eq. 10 to compute $F_{\mathrm{orgPOC}}(z)$:

$$F_{\mathrm{reminMigrS}} = F_{\mathrm{expPOC}} \times (z_{\mathrm{migrS}}/z_{\mathrm{exp}})^{b} \tag{18}$$

where z_{migrS} = 597 m, z_{exp} = 100 m, and b = 0.86.

We assumed that all migrating animals overwintered at the f_{100} depth of z_{migrS} = 597 m (depth for which f_{100} values were available), and used eq. 6 to obtain F_{seqMigrS}:

$$F_{\mathrm{seqMigrS}} = F_{\mathrm{reminMigrS}} \times f_{100}(597\ \mathrm{m}) \tag{19}$$

We calculated F_{seqMigrS} in the northern North Atlantic by adding together the fluxes from this region (eq. 8).

- ***All pumps together***

To obtain the sequestration fluxes of all pumps together, we combined the above estimates for the four pathways for both pixels and the global ocean:

$$F_{\mathrm{seqAll}} = F_{\mathrm{seqPOC}} + F_{\mathrm{seqDOC}} + F_{\mathrm{seqMigrD}} + F_{\mathrm{seqMigrS}} \tag{20}$$

Because our estimates of F_{seqMigrS} were limited to the northern North Atlantic, our global values of F_{seqAll} outside this region were slightly underestimated as were also our values of F_{seqAll}.

The fact that F_{seqSed} was subtracted in eq. 12 and not included in eq. 20 means that our F_{seqAll} estimates did not include F_{seqSed}, as explained above. If one wished to include F_{seqSed} in the pumps, its values (eq. 9) could easily be added to the pixel estimates of F_{seqAll} (eq. 20) and thus included in global F_{seqAll}.

- ***Gravitational pump at 1,000 and 2000 m***

We calculated the POC flux at two fixed depths, z_{fixed} = 1,000 m and 2,000 m, assuming that the POC flux at z_{fixed} was entirely sequestered below, i.e. f_{100} = 1.0. We calculated the POC flux at each z_{fixed} using eq. 10 with $z = z_{\mathrm{fixed}}$, z_{exp} = 100 m, and b = 0.86.

- ***Gravitational pump and all pumps below and above 1,000 and 2000 m***

We calculated F_{seqPOC} and F_{seqDOC} below and above the two z_{fixed}. Given that most vertical migrations do not exceed 1,000 m (Fig. 3a), we considered that there were only two sequestration fluxes below either z_{fixed} value, i.e. F_{seqPOC} and F_{seqDOC}. We used the same equations for the two z_{fixed} values:

$$F_{seqAll}(>z_{fixed}) = F_{seqPOC}(>z_{fixed}) + F_{seqDOC}(>z_{fixed}) \quad (21)$$

First, we calculated pixel $F_{seqPOC}(>z_{fixed})$ for all CONVERSE versions as we had done for the whole water column, including only the depth intervals $\Delta z > z_{fixed}$. We then calculated pixel $F_{seqPOC}(\leq z_{fixed})$ as follows:

$$F_{seqPOC}(\leq z_{fixed}) = F_{seqPOC} \text{ over the water column } - F_{seqPOC}(>z_{fixed}) \quad (22)$$

Second, we calculated $F_{seqDOC}(>z_{fixed})$ as we had done for the whole water column, including only the depth intervals $\Delta z > z_{fixed}$. We calculated $F_{seqDOC}(\leq z_{fixed})$ as we had done for POC (eq. 22).

Third, we used eq. 21 to calculate pixel $F_{seqAll}(>z_{fixed})$, and the resulting value to calculate $F_{seqAll}(\leq z_{fixed})$:

$$F_{seqAll}(\leq z_{fixed}) = F_{seqAll} \text{ over the water column } - F_{seqAll}(>z_{fixed}) \quad (23)$$

References

1. Siegel, D. A., DeVries, T., Cetinić, I. & Bisson, K. M. Quantifying the ocean's biological pump and its carbon cycle impacts on global scales. *Ann. Rev. Mar. Sci.* **15**, (2022).
2. Iversen, M. H. Carbon export in the ocean: A biologist's perspective. *Ann. Rev. Mar. Sci.* **15**, (2023).
3. Wilson, J. D. *et al.* The biological carbon pump in CMIP6 models: 21st century trends and uncertainties. *Proc. Natl. Acad. Sci. U. S. A.* **119**, e2204369119 (2022).
4. DeVries, T. & Weber, T. The export and fate of organic matter in the ocean: New constraints from combining satellite and oceanographic tracer observations. *Global Biogeochem. Cycles* **31**, 535–555 (2017).
5. Siegel, D. A., DeVries, T., Doney, S. & Bell, T. Assessing the sequestration time scales of some ocean-based carbon dioxide reduction strategies. *Environ. Res. Lett.* (2021) doi:10.1088/1748-9326/ac0be0.
6. Baker, C. A., Martin, A. P., Yool, A. & Popova, E. Biological carbon pump sequestration efficiency in the north Atlantic: A leaky or a long-term sink? *Global Biogeochem. Cycles* **36**, (2022).
7. IPCC. Annex I: Glossary [Weyer, N.M. (ed.)]. In: IPCC Special Report on the Ocean and Cryosphere in a Changing Climate [Pörtner, H.-O. *et al.* (eds.)], pp. 677–702 (Cambridge University Press, 2019).
8. Fearnside, P. M. Why a 100-Year Time Horizon should be used for GlobalWarming Mitigation Calculations. *Mitigation and Adaptation Strategies for Global Change* **7**, 19–30 (2002).
9. Lampitt, R. S. *et al.* Ocean fertilization: a potential means of geoengineering? *Philos. Trans. A Math. Phys. Eng. Sci.* **366**, 3919–3945 (2008).
10. Passow, U. & Carlson, C. A. The biological pump in a high CO_2 world. *Mar. Ecol. Prog. Ser.* **470**, 249–272 (2012).
11. Weber, T., Cram, J. A., Leung, S. W., DeVries, T. & Deutsch, C. Deep ocean nutrients imply large latitudinal variation in particle transfer efficiency. *Proc. Natl. Acad. Sci. U. S. A.* **113**, 8606–8611 (2016).
12. Boyd, P. W., Claustre, H., Levy, M., Siegel, D. A. & Weber, T. Multi-faceted particle pumps drive carbon sequestration in the ocean. *Nature* **568**, 327–335 (2019).
13. National Academies of Sciences, Engineering, and Medicine; Division on Earth and Life Studies; Ocean Studies Board; Committee on A Research Strategy for Ocean-based Carbon Dioxide Removal and Sequestration. *A Research Strategy for Ocean-based Carbon Dioxide Removal and Sequestration*. (National Academies Press (US), 2022).
14. Honjo, S., Manganini, S. J., Krishfield, R. A. & Francois, R. Particulate organic carbon fluxes to the ocean interior and factors controlling the biological pump: A synthesis of global sediment trap programs since 1983. *Prog. Oceanogr.* **76**, 217–285 (2008).
15. Henson, S. A., Sanders, R. & Madsen, E. Global patterns in efficiency of particulate organic carbon export and transfer to the deep ocean. *Global Biogeochem. Cycles* **26**, (2012).
16. Robinson, J. *et al.* How deep is deep enough? Ocean iron fertilization and carbon sequestration in the Southern Ocean. *Geophys. Res. Lett.* **41**, 2489–2495 (2014).
17. Legendre, L., Rivkin, R. B., Weinbauer, M. G., Guidi, L. & Uitz, J. The microbial carbon pump concept: Potential biogeochemical significance in the globally changing ocean. *Prog. Oceanogr.* **134**, 432–450 (2015).
18. Guidi, L. *et al.* A new look at ocean carbon remineralization for estimating deepwater sequestration. *Global Biogeochem. Cycles* **29**, 1044–1059 (2015).

19. Cram, J. A. *et al.* The role of particle size, ballast, temperature, and oxygen in the sinking flux to the deep sea. *Global Biogeochem. Cycles* **32**, 858–876 (2018).
20. Holzer, M., DeVries, T. & de Lavergne, C. Diffusion controls the ventilation of a Pacific Shadow Zone above abyssal overturning. *Nat. Commun.* **12**, 4348 (2021).
21. Alldredge, A. L. & Gotschalk, C. C. Direct observations of the mass flocculation of diatom blooms: characteristics, settling velocities and formation of diatom aggregates. *Deep Sea Res. A* **36**, 159–171 (1989).
22. Turner, J. T. Zooplankton fecal pellets, marine snow, phytodetritus and the ocean's biological pump. *Prog. Oceanogr.* **130**, 205–248 (2015).
23. Dunne, J. P., Sarmiento, J. L. & Gnanadesikan, A. A synthesis of global particle export from the surface ocean and cycling through the ocean interior and on the seafloor. *Global Biogeochem. Cycles* **21**, (2007).
24. Dall'Olmo, G., Dingle, J., Polimene, L., Brewin, R. J. W. & Claustre, H. Substantial energy input to the mesopelagic ecosystem from the seasonal mixed-layer pump. *Nat. Geosci.* **9**, 820–823 (2016).
25. Omand, M. M. *et al.* Eddy-driven subduction exports particulate organic carbon from the spring bloom. *Science* **348**, 222–225 (2015).
26. Resplandy, L., Lévy, M. & McGillicuddy, D. J., Jr. Effects of eddy-driven subduction on ocean biological carbon pump. *Global Biogeochem. Cycles* **33**, 1071–1084 (2019).
27. Hansell, D., Carlson, C., Repeta, D. & Schlitzer, R. Dissolved organic matter in the ocean: A controversy stimulates new insights. *Oceanography* **22**, 202–211 (2009).
28. Liu, L. L. & Huang, R. X. The global subduction/obduction rates: Their interannual and decadal variability. *J. Clim.* (2012).
29. Levy, M. *et al.* Physical pathways for carbon transfers between the surface mixed layer and the ocean interior. *Global Biogeochem. Cycles* **27**, 1001–1012 (2013).
30. Bianchi, D., Stock, C., Galbraith, E. D. & Sarmiento, J. L. Diel vertical migration: Ecological controls and impacts on the biological pump in a one-dimensional ocean model. *Global Biogeochem. Cycles* **27**, 478–491 (2013).
31. Aumont, O., Maury, O., Lefort, S. & Bopp, L. Evaluating the potential impacts of the diurnal vertical migration by marine organisms on marine biogeochemistry. *Global Biogeochem. Cycles* **32**, 1622–1643 (2018).
32. Claustre, H., Legendre, L., Boyd, P. W. & Levy, M. The Oceans' Biological Carbon Pumps: Framework for a Research Observational Community Approach. *Frontiers in Marine Science* **8**, (2021).
33. Hansell, D. A. Recalcitrant dissolved organic carbon fractions. *Ann. Rev. Mar. Sci.* **5**, 421–445 (2013).
34. Jiao, N. *et al.* Microbial production of recalcitrant dissolved organic matter: long-term carbon storage in the global ocean. *Nat. Rev. Microbiol.* **8**, 593–599 (2010).
35. Jiao, N. *et al.* The microbial carbon pump and the oceanic recalcitrant dissolved organic matter pool. *Nat. Rev. Microbiol.* **9**, 555–555 (2011).
36. Archibald, K. M., Siegel, D. A. & Doney, S. C. Modeling the impact of zooplankton Diel vertical migration on the carbon export flux of the biological pump. *Global Biogeochem. Cycles* **33**, 181–199 (2019).
37. Brun, P. *et al.* Climate change has altered zooplankton-fuelled carbon export in the North Atlantic. *Nat Ecol Evol* **3**, 416–423 (2019).
38. Jónasdóttir, S. H., Visser, A. W., Richardson, K. & Heath, M. R. Seasonal copepod lipid pump promotes carbon sequestration in the deep North Atlantic. *Proc. Natl. Acad. Sci. U. S. A.* **112**, 12122–12126 (2015).

39. Auel, H., Klages, M. & Werner, I. Respiration and lipid content of the Arctic copepod Calanus hyperboreus overwintering 1 m above the seafloor at 2,300 m water depth in the Fram Strait. *Mar. Biol.* **143**, 275–282 (2003).
40. Hirche, H. J., Muyakshin, S., Klages, M. & Auel, H. Aggregation of the Arctic copepod Calanus hyperboreus over the ocean floor of the Greenland Sea. *Deep Sea Res. Part I* **53**, 310–320 (2006).
41. Visser, A. W., Grønning, J. & Jónasdóttir, S. H. Calanus hyperboreus and the lipid pump. *Limnol. Oceanogr.* **62**, 1155–1165 (2017).
42. Hayes, C. T. *et al.* Global ocean sediment composition and burial flux in the deep sea. *Global Biogeochem. Cycles* **35**, (2021).
43. Martin, J. H., Knauer, G. A., Karl, D. & Broenkow, W. W. VERTEX: carbon cycling in the northeast Pacific. *Deep Sea Research Part A. Oceanographic Research Papers* **34**, 267–285 (1987).
44. Boyd, P. *et al.* Operational monitoring of open-ocean carbon dioxide removal deployments: Detection, attribution, and determination of side effects. *Oceanography* (2023) doi:10.5670/oceanog.2023.s1.2.

Acknowledgements

We thank Dr. Louis Prieur for his calculations for early versions of the manuscript and numerous suggestions, and Dr. Gabriel Reygondeau for his contributions to early versions. We are grateful to Prof. Stephanie Henson (Henson et al. 2012) for providing us her data of POC F_{exp}, which we used to calculate sequestration fluxes in CONVERSE 1-3, 6 and 7. We also thank Dr. Sigrún Huld Jónasdóttir and Prof. Andy Visser for additional information on values in their 2015 paper (Jónasdóttir et al. 2015). We also thank the two reviewers for their very useful comments and suggestions.

This work was supported by the Fonds de la Recherche Scientifique (FNRS) of Belgium (F.R.). L.G and M.G have received funding from the European Union's Horizon 2020 research and innovation programme under grant agreement No 862923. This output reflects only the authors' views, and the European Union cannot be held responsible for any use that may be made of the information contained therein.

Author contributions

L.G., T.D. and L.L. conceived the initial project. F.R. and T.D. performed data curation. F.R., T.D. and L.L. conducted the modelling and analyses, and wrote the manuscript with inputs from L.G. and M.G. All authors discussed and contributed intellectually to the interpretation of the results.

Competing financial interests

The authors declare no competing financial interests.

Additional information

Supplementary information for this paper is available at ###.

Reprints and permissions information is available at www.nature.com/reprints.

Correspondence and requests for materials should be addressed to Florian Ricour.

The codes for the data analysis were developed by F. Ricour. They were uploaded on GitHub (at XXX) and are also available in the Zenodo repository (XXX).

Revisiting the biological pump using the new continuous vertical sequestration approach

Florian Ricour[1,2*], Lionel Guidi[2], Marion Gehlen[3], Timothy DeVries[4] and Louis Legendre[2*]

[1]Sorbonne University, CNRS, Laboratoire d'Océanographie de Villefranche, LOV, F-06230 Villefranche-sur-Mer, France.
[2]Freshwater and OCeanic science Unit of reSearch (FOCUS), University of Liège, Liège, Belgium.
[3]LSCE-IPSL, CEA, CNRS, Université Paris-Saclay, Gif-sur-Yvette, France.
[4]Department of Geography / ERI / IGPMS, University of California, Santa Barbara, CA, USA.
*Corresponding authors: florian.ricour@uliege.be and legendre@imev-mer.fr

SUPPLEMENTARY INFORMATION

1. Mechanisms involved in ocean carbon sequestration, including the ocean carbon pumps

Marine biogeochemists group carbon sequestration mechanisms into *carbon pumps*. This concept was originally created to explain the observed increasing DIC concentration with depth in the global ocean[45] and consequently did not consider the storage of organic carbon in the sediment. The carbon pumps were later applied to ocean carbon sequestration, in which case their definition included organic carbon transport to the ocean interior and possibly the sediment. Indeed, IPCC[7] definitions of the ocean carbon pumps are as follows: the *solubility pump* is “a physicochemical process that transports dissolved inorganic carbon from the ocean’s surface to its interior […] primarily driven by the solubility of carbon dioxide (CO_2) […] and the large-scale, thermohaline patterns of ocean circulation”; the *carbonate pump* consists of "the biological formation of carbonates, primarily by plankton that generate bio-mineral particles that sink to the ocean interior, and possibly the sediment […] accompanied by the release of CO_2 to surrounding water and subsequently to the atmosphere"; and the *biological carbon pump*, which is the focus of this study, transports POC and DOC "to the ocean interior, and possibly the sediment".

Other biologically-driven sequestration mechanisms that are technically not part of the BCPs include[7]: the *microbial carbon pump*, which consists of "microbial processes that transform organic carbon from rapidly-degradable states to biologically-unavailable forms, resulting in long-term carbon storage in the ocean, […] and is the principal mechanism generating and sustaining refractory dissolved organic carbon in the ocean"[17,34,35]; and coastal *blue carbon*, which consists of "rooted vegetation in the coastal zone, such as tidal marshes, mangroves and seagrasses. The latter ecosystems have high carbon burial rates on a per unit area basis and accumulate carbon in their soils and sediments". Coastal blue carbon sequestration is actively debated in the literature[46-49].

2. Functioning of the biological carbon pump mechanisms

Six BCP mechanisms contribute to global ocean carbon sequestration[12]. In the following bullets, we briefly describe the functioning of the six mechanisms, and Fig. 3a (main text) illustrates the maximum depth to which each of them transports POC and/or DOC. Organic carbon is progressively remineralized to CO_2 in the water column, and part of the resulting DIC_{bio} is sequestered at different depths (Fig. 3).

The remineralization processes of POC transported by BCPs include ingestion by heterotrophs, which respire part of their food to CO_2, and transformation of POC into DOC by various food-web processes such as solubilization by bacterial exoenzymes and excretion by microbes and animals. Most of the DOC, either remineralized *in situ* or transported downwards by BCP mechanisms, is used and respired to CO_2 by heterotrophic bacteria. Respiratory CO_2 fuels DIC_{bio}.

The different BCP mechanisms are grouped into pumps, which are known under different names proposed by various authors. The settling of organic particles is known as *biological gravitational pump*[12], the three physically-driven mechanisms (mixed layer, eddy subduction, and large scale advection and overturning) as *physical (injection) pumps*[26] or *mixing pump*[50], the diel vertical migrations as *mesopelagic migrant pump*[12]; the seasonal vertical migrations as *seasonal lipid pump*[38], and all mechanisms other than gravitational as *particle injection pumps*[12].

- *Biological gravitational mechanism.* Part of the organic particles produced by photosynthesis and other processes of the pelagic food web in the upper ocean's layer continuously sinks downwards. The sinking POC is progressively remineralized to CO_2 during its downward journey, and the non-remineralized POC may be sequestered in sediment for times reaching millions of years[17].

- *Mixed layer mechanism.* During the seasonal transition from the deepest winter mixed layer to summer stratification at high and mid-latitudes, there are variations in the depth of the mixed layer. These variations cause the downward injection, by deep mixing, of POC and DOC produced in the upper layer, and their isolation at depth when a new shallower mixed layer is formed. The succession of shoaling and deepening of the mixed layer injects POC and DOC to depths between 200 and 1000 m[24].

- *Eddy subduction mechanism.* Frontal circulation with horizontal dimensions ranging from the mesoscale (10–100 km) to the sub-mesoscale (1–10 km) creates "hotspots" of downward vertical transport (i.e. subduction). In these hotspots, POC and DOC are injected down to depths of 150 to 400 and even 500 m[25,26].

- *Large-scale advection and overturning (or Ekman) mechanism.* Large-scale wind-driven circulation causes the injection of POC and DOC from the seasonal mixed layer into the ocean interior, down to depths of 500 to 1000 m[27-29].

- *Diel (nycthemeral) vertical migrations.* During their diel vertical migrations, zooplankton and also fish, jellies and other animals larger than zooplankton[31] ingest organic particles at surface, generally at night time, and release part of the ingested material at depth, a few hours later, under the form of faecal material (POC, mostly zooplankton faecal pellets), excreted DOC and respiratory CO_2. Migrating animals also defecate, excrete and respire during their vertical journeys. The depth of these migrations does not generally exceed 200 m, but can reach a maximum of 600 m in some cases[36,37].

- *Seasonal (ontogenic) vertical migrations.* At high latitudes, some zooplankton taxa spend several months of the year at depths >600 and even 1000 m or more, where they release part of the carbon they had acquired at surface under the form of faecal pellets, excreted DOC, respiratory CO_2 and carcasses of dead organisms. The carbon transported by these organisms is largely under the form of lipid reserves. This pump transports POC down to depths that can reach 1400 m[38].

3. Comparisons between our calculations or results for the mixing and migrant pumps and values from the literature

Our F_{seq} for the gravitational pump in CONVERSE 1-3 are compared with flux values from the literature Table S3, and this comparison is included in the main text. As a complement, our CONVERSE calculations or results for the two other pumps are compared with values from the literature in the following paragraphs.

- *Mixing pump*. We use eq. 13 to estimate the remineralization flux of DOC driven by the mixing pump ($F_{reminDOC}$). In the field, the downward mixing flux of DOC and total export flux below 50 m were estimated to be 15 and 92 mg C m^{-2} d^{-1}, respectively, in the eastern North Atlantic Ocean[51]. Assuming that the two fluxes were entirely remineralized below 50 m, then $F_{reminDOC}$ accounted for ~15% of all F_{remin} ($F_{reminAll}$). This does not necessarily mean that F_{seqDOC} accounted for ~15% of F_{seqAll}, as differential sequestration of $F_{reminDOC}$ and $F_{reminAll}$ may have happened depending on their remineralization depths. Nevertheless, our CONVERSE 1-7 estimates of 11-23% of the biological pump F_{seq} accounted for by the mixing pump F_{seq} (Supplementary Tables S3 and S4) are of the same order as the above field ~15% for F_{remin}, which suggests that our estimates are realistic.

- *Migrant pump: diel vertical migrations.* Our eq. 16 computes F_{remin} for diel vertical migrations by all animals as follows:

$$F_{reminMigrD} = 0.25\ F_{expPOC},\ \text{at}\ z_{exp} = 100\ \text{m} \tag{16}$$

Hence:

$$F_{reminMigrD} / F_{expPOC} = 0.25 \tag{16a}$$

A synthesis of literature values for zooplankton diel migrations[52] provides the following relationship (parameters of the regression equation derived from the line drawn on Fig. 5b in that review):

$$F_{reminMigrD}\ /\ F_{expPOC} \simeq 0.1 + 0.017\ F_{reminMigrD},\ \text{at}\ z_{exp} = 100\text{-}200\ \text{m} \tag{16b}$$

where the units of $F_{\mathrm{reminMigrD}}$ and F_{expPOC} are mg C m^{-2} d^{-1}. According to eq. 16b, our eq. 16 corresponds to $F_{\mathrm{reminMigrD}} \simeq 9$ mg C m^{-2} d^{-1}. This $F_{\mathrm{reminMigrD}}$ is in the bulk of values used to derive eq. 16b, indicating that our CONVERSE F_{seqMigrD} values (eq. 17) are realistic.

- *Migrant pump: seasonal vertical migrations*. The study[38] from which we derived our eq. 18 was conducted in the northern North Atlantic and concerned the seasonal vertical migrations of the copepod *Calanus finmarchicus*, which were estimated to export 2 to 6 g C m^{-2} y^{-1}. Similar values for other cold waters are[52]: 3.1 g C m^{-2} y^{-1} (Arctic Ocean, mostly large copepods *C. hyperboreus* and *C. glacialis*), 2.0 to 4.3 g C m^{-2} y^{-1} (subarctic North Pacific, *Neocalanus* copepods), and 1.7 to 9.3 g C m^{-2} y^{-1} (subantarctic Southern Ocean, *N. tonsus*). These values are in the same range as those of the study on which we based our CONVERSE calculations, which suggest that our approach could also be used in other cold-water areas than the northern North Atlantic Ocean.

4. Supplementary Tables

Table S1 lists the acronyms and symbols used in the main text.

In order to assess the significance of the CONVERSE approach, we estimated BCP F_{seq} and their pathways (POC, DOC, and diel and seasonal vertical migrations). We used data from three sources[4,15,42], and computed flux estimates with seven different CONVERSE versions which combined data from the three sources differently. Characteristics of the seven versions are summarized in Table S2.

In Table S3, the F_{seq} from CONVERSE 1-3 are summarized and compared with corresponding POC F_{seq} from studies in the literature. Table S4 summarizes the F_{seq} results from CONVERSE 4-7. Table S5 summarizes the fluxes calculated below, at and above 1,000 m and 2,000 m corresponding to CONVERSE 1-7.

Table S6 gives global-ocean median F_{TOC}(pixel)[42] and number of observations in different depth bins from surface to bottom, and Table S7 provides information on the use of F_{TOC} in the calculation of F_{seq}.

Table S1. Acronyms and symbols used in the main text, excluding those used only in the Methods and/or the Supplementary Information.

Symbols	**Definitions**	**Notes**
$\mathrm{All}_{\mathrm{owc}}$	F_{seq} for all carbon pumps (i.e., the whole biological carbon pump) over the water column	Only used in Table 1
CONVERSE	Continuous vertical sequestration	
CDR	Carbon Dioxide Removal	
C1 to C7	CONVERSE versions 1 to 7	
DIC	Dissolved inorganic carbon	DIC = $CO_2 + H_2CO_3 + HCO_3^- + CO_3^{2-}$
$\mathrm{DIC}_{\mathrm{bio}}$	Biogenic DIC, i.e. DIC resulting from the remineralization (respiration) of organic matter	Also called C_{soft}[3] and C_{seq}[1]
DOC	Dissolved organic carbon	
F_{exp}	Downward flux of organic carbon at the export depth z_{exp}	F_{org} at z_{exp}
F_{org}	Downward flux of organic carbon	Flux driven by the biological carbon pump
F_{remin}	Remineralization flux of organic carbon to $\mathrm{DIC}_{\mathrm{bio}}$	Fraction of F_{org}, computed differently for each pump
F_{seq}	Sequestration flux of $\mathrm{DIC}_{\mathrm{bio}}$	$F_{\mathrm{seq}} = F_{\mathrm{remin}} \times f_{100}$
F^*_{seq}	Sequestration flux normalized to POC export flux at the export depth z_{exp}	$F^*_{\mathrm{seq}} = F_{\mathrm{seq}}/F_{\mathrm{exp}}$
f_{100}	Fraction of a parcel of water at a given location and depth that will remain in the ocean for ≥100 years	From a published paper[2]
POC	Particulate organic carbon	
z_{exp}	Export depth	100 m, or bottom of the euphotic zone (z_{eu})

Table S2. Characteristics of the seven versions of CONVERSE F_{remin} estimates for POC, DOC, vertical migrations, and sediment. To further obtain F_{seq}, the F_{remin} estimates were multiplied by corresponding f_{100}, i.e. $F_{seq} = F_{remin} \times f_{100}$. The initial computations for POC and DOC produced values for successive depth intervals in the water column (Δz), which were summed up from shallowest to deepest: $F_{seq}(\text{pixel}) = \sum_{\Delta z=shallowest}^{deepest} F_{seq}(\Delta z)$. Further calculations were: $F_{seq}(\text{global}) = \sum_{\text{All pixels}} [F_{seq}(\text{pixel}) \times \text{Area}(\text{pixel})]$; and $F_{seqAll} = \sum_{4\ \text{components}} F_{seqComponent}$. The sources of data are identified **He**[15], **DW**[4], and **Ha**[42]. References to CONVERSE results are abbreviated C#, e.g. C5 refers to CONVERSE 5.

CONVERSE	**1**	**2**	**3**	**4**	**5**	**6**	**7**
Export depth (z_{exp})							
	100 m	100 m	100 m	z_{eu}	100 m	100 m	100 m
Global ocean (gravitational pump)							
No. pixels	9202	9202	9202	10,309	10,276	10,276	9202
Area (10^6 km^2)	343	343	343	352	352	352	343
Estimation of $F_{remin}(\Delta z)$							
b	0.86	Variable	Regional	C4-C5: None		0.86	0.86
Gravitational pump[*]	C1-C3: $F_{orgPOC}(z)$ - $F_{orgPOC}(z+1)$, values being computed using *b* **He**			C4-C5: $[([POC]_{slow} \times k_{slow}) + ([POC]_{fast} \times k_{fast})] \times \Delta z$ **DW**		C5 × Export ratio[‡]	Same as C1
Mixing pump	C1-C3: C5 × Export ratio[‡]			$\sum_{4\ \text{fractions}} ([DOC] \times k \times \Delta z)$[§] **DW**		C5 × Export ratio[‡]	F_{expPOC} at 100 m × 0.25 **He**
Estimation of $F_{remin}(\text{pixel})$							
Migrant pump diel	C1-C3: F_{expPOC} × 0.25 (z_{exp} = 100 m) **He**			C4-C5: F_{expPOC} × 0.25 (z_{exp} = 100 m) **DW**		Same as C1-C3	Same as C1-C3
Migrant pump seasonal[†]	C1-C3: $F_{expPOC} \times (z/z_{exp})^{-b} \times 0.5$ (z = 597 m and z_{exp} = 100 m) **He**			C4-C5: $F_{orgPOC}(z)$ × 0.5 (z = 619 m) **DW**		C5 × Export ratio[‡]	Same as C1
Sediment	C1-C7: F_{TOC} **Ha**						

[*] Water column only, i.e. does not include F_{seqSed}

[†] Northern North Atlantic only

[‡] Export ratio: F_{expPOC}(global, C1) / F_{expPOC}(global, C5) at z_{exp} = 100 m, from **He** and **DW**, respectively

[§] DOC concentration ([DOC]; g C m^{-3}) and remineralization rate (k; y^{-1}) in 4 fractions (labile, semi-labile, semi-refractory, and refractory) within depth interval Δz (m), from **DW**

Table S3. Estimates of sequestration fluxes (F_{seq}, Pg C y^{-1}) in the whole water column corresponding to seven versions characterized by different sequestration depths (CONVERSE, or z_{seq}), *b* and F_{exp} at 100 m (same z_{exp} = 100 m), calculated in this study (CONVERSE) or taken from previously published works. The CONVERSE POC sequestration fluxes were computed with the same *b* as in the corresponding previous studies. Because the values for DOC and diel vertical migrations were computed without using *b*, these are the same across the Table. The F^{*}_{seq} ratios (eq. 1, values in italics) are dimensionless.

CONVERSE, or z_{seq}	**CON-VERSE 1**	**2000 m[†]**	**CON-VERSE 2**	**2000 m[‡]**	**CON-VERSE 3**	**2000 m[**]**	**σ_θ = 1027.6 kg m^{-3}[**]**
b	**0.86[43]**		**Geographically variable[15]**		**Regionalized[18]**		
F_{exp}(global) at 100 m (Pg C y^{-1})	**3.0**	**5.7**	**3.0**	**4.0**	**3.0**	**4.0**	**4.0**
Pumps and flux	***Global water-column sequestration fluxes (F_{seq})***						
Gravitational	0.63	0.43	0.92	0.66	0.71	0.33	0.72
Mixing	0.13	–	0.13	–	0.13	–	–
Migrant diel	0.11	–	0.11	–	0.11	–	–
Migrant seasonal[*]	0.004	–	0.004	–	0.001	–	–
Biological (all)	0.88	0.43	1.16	0.66	0.95	0.33	0.72
Sediment	0.03	–	0.03	–	0.03	–	–
Pumps and flux	***% Biological pump (all)***						
Gravitational	72	–	79	–	75	–	–
Mixing	15	–	11	–	14	–	–
Migrant diel	12	–	9	–	12	–	–
Migrant seasonal[*]	0.4	–	0.3	–	0.1	–	–
Sediment	3	–	3	–	3	–	–
Pumps and flux	***Global sequestration fluxes normalized to POC export fluxes at z_{exp} = 100 m (F^{*}_{seq})***						
Gravitational	*0.21*	*0.08*	*0.31*	*0.17*	*0.24*	*0.08*	*0.18*
Mixing	*0.04*	–	*0.04*	–	*0.04*	–	–
Migrant diel	*0.04*	–	*0.04*	–	*0.04*	–	–
Migrant seasonal[*]	*0.001*	–	*0.001*	–	*0.001*	–	–
Biological (all)	*0.29*	*0.08*	*0.39*	*0.17*	*0.32*	*0.08*	*0.18*
Sediment	*0.008*	–	*0.008*	–	*0.008*	–	–
Pumps	***F^{*}_{seq}(global)$_{CONVERSE}$ / F^{*}_{seq}(global) from published studies[††]***						
Gravitational		2.6		1.8		3.0	1.3
Biological (all)		3.6		2.3		4.0	1.8

[*] Northern North Atlantic only

[†] Deep sediment trap data normalized to 2,000 m using *b* = 0.86[14]

[‡] Modelling estimates[15]

[**] Estimates do not include pixels with water depths between 100 and 200 m; σ_θ = 1027.6 kg m^{-3} corresponds to the top of the permanent pycnocline[18]

[††] For example, the first value, 2.6, was calculated as follows:
0.21 (POC F_{seq} in CONVERSE 1) / 0.08 (POC F_{seq} from the published studies[14, 15,18])

Table S4. Estimates of sequestration fluxes (F_{seq}, Pg C y^{-1}) in the whole water column calculated in this study, corresponding to four CONVERSE versions characterized by different z_{exp}, calculations of F_{seqDOC} and F_{exp}. In CONVERSE 7, four of the five F_{seq} pathways are the same as in CONVERSE 1 (Table S3), except F_{seqDOC}(global) which was derived from F_{exp}POC. The F^{*}_{seq} ratios (eq. 1, values in italics) are dimensionless. BCP: Biological carbon pump.

CONVERSE	**CONVERSE 4**	**CONVERSE 5**	**CONVERSE 6**	**CONVERSE 7**
$\mathbf{z_{exp}}$	$\mathbf{z_{eu}}$	**100 m**	**100 m**	**100 m**
$\mathbf{F_{seqDOC}}$	**From a BCP model**[4]		***f*(BCP model)**	***f*($\mathbf{F_{exp}}$POC)**[†]
$\mathbf{F_{exp}}$**(global)** **(Pg C year^{-1})**	**8.6**	**7.3**	**3.0**	**3.0**
Pumps and flux	***Global water-column sequestration fluxes (F_{seq})***			
Gravitational	1.89	1.86	0.76[‡]	0.63
Mixing	0.45	0.32	0.13[‡]	0.22[§]
Migrant diel	0.26	0.26	0.11	0.11
Migrant seasonal[*]	0.01	0.01	0.004	0.004
Biological (all)	2.61	2.44	1.00	0.96
Sediment	0.03	0.03	0.03	0.03
Pumps and flux	***% Biological pump (all)***			
Gravitational	72	76	76	66
Mixing	17	13	13	23
Migrant diel	10	11	11	11
Migrant seasonal[*]	0.4	0.4	0.4	0.4
Sediment	1	1	3	3
Pumps and flux	***Global sequestration fluxes normalized to POC export fluxes at $z_{exp} = z_{eu}$ or 100 m (F^{*}_{seq})***			
Gravitational	*0.22*	*0.25*	*0.25*	*0.21*
Mixing	*0.05*	*0.04*	*0.04*	*0.07*
Migrant diel	*0.03*	*0.04*	*0.04*	*0.04*
Migrant seasonal[*]	*0.001*	*0.001*	*0.001*	*0.001*
Biological (all)	*0.30*	*0.33*	*0.33*	*0.32*
Sediment	*0.003*	*0.004*	*0.008*	*0.008*

[*] Northern North Atlantic only

[†] Same value as in CONVERSE 1, expect for F_{seqDOC}

[‡] Value in CONVERSE 5 × [F_{exp}(pixel, CONVERSE 1) / F_{exp}(pixel, CONVERSE 5)] at z_{exp} = 100 m

[§] $F_{seqDOC} = 0.25 \times F_{expPOC}$ at 100 m × f_{100} at 531 m

Table S5. Estimates of sequestration fluxes (F_{seq}, Pg C y^{-1}) at, below and above 1,000 m and 2,000 m calculated in this study, corresponding to CONVERSE 1-7, the characteristics of which are given in Tables S2-S4. The F^*_{seq} ratios (eq. 1, values in italics) are dimensionless.

CONVERSE	**1**	**2**	**3**	**4**	**5**	**6**	**7**
Fluxes	***Global POC fluxes calculated at 1,000 and 2,000 m (F_{seq})***						
POC at 1,000 m[*]	0.38	0.68	0.47	1.13	1.13	0.46	0.38
POC at 2,000 m[*]	0.19	0.42	0.26	0.47	0.47	0.19	0.19
Pumps	***Global sequestration fluxes integrated above and below 1,000 m (F_{seq}) and % ratios***						
Gravitational ≤1,000 m	0.32	0.33	0.32	1.09	1.06	0.43	0.32
Gravitational >1,000 m	0.31	0.59	0.39	0.80	0.80	0.33	0.31
All ≤1,000 m	0.55	0.55	0.54	1.75	1.58	0.65	0.65
All >1,000 m[†]	0.33	0.61	0.41	0.86	0.86	0.35	0.31
$\text{All}_{\le 1000}$ / All_{owc}[‡]	63%	47%	57%	67%	65%	65%	68%
$\text{All}_{>1000}$ / All_{owc}[‡]	37%	53%	43%	33%	35%	35%	32%
Pumps	***Global sequestration fluxes integrated above and below 2,000 m (F_{seq}) and % ratios***						
Gravitational ≤2,000 m	0.48	0.54	0.49	1.61	1.58	0.64	0.48
Gravitational >2,000 m	0.15	0.38	0.22	0.28	0.28	0.12	0.15
All ≤2,000 m	0.71	0.77	0.71	2.30	2.13	0.87	0.81
All >2,000 m[†]	0.17	0.39	0.24	0.31	0.31	0.13	0.15
$\text{All}_{\le 2000}$ / All_{owc}[‡]	81%	66%	75%	88%	87%	87%	84%
$\text{All}_{>2000}$ / All_{owc}[‡]	19%	33%	25%	12%	13%	13%	16%
Fluxes	***Global sequestration fluxes normalized to POC export fluxes at $z_{exp} = z_{eu}$ or 100 m (F^*_{seq})***						
POC at 1,000 m[*]	*0.13*	*0.23*	*0.16*	0.13	0.15	0.15	0.13
POC at 2,000 m[*]	*0.06*	*0.14*	*0.09*	0.05	0.06	0.06	0.06
Pump ratios	***CONVERSE sequestration fluxes to POC fluxes at 1,000 and 2,000 m***						
• to POC flux at 1,000 m*							
Gravitational[†]	1.7	1.4	1.5	1.7	1.6	1.7	1.7
Biological[†]	2.3	1.7	2.0	2.3	2.2	2.2	2.5
• to POC flux at 2,000 m*							
Gravitational[†]	3.3	2.2	2.7	4.0	4.0	4.0	3.3
Biological (all) [†]	4.6	2.8	3.7	5.6	5.2	5.3	5.1

[*] Calculated at z_{seq} = 1,000 m or 2000 m, assuming that POC F_{org} at z_{seq} is entirely sequestered below

[†] Water column only, i.e. does not include F_{seq} in sediment

[‡] All_{owc}: F_{seq} for all pumps over the water column

Table S6. Median F_{TOC} in pixels of the world ocean[42] and number of observations in different depth bins. Pixel depths were obtained via the function getNOAA.bathy using the *marmap* package on Rstudio at https://cran.r-project.org/web/packages/marmap/marmap.pdf

Depth bin	**Median F_{TOC} (g C m^{-2} y^{-1})**	**Number of observations**
<2000 m[*]	0.13	1625
2000 – 3000 m	0.123	3832
3000 – 3500 m	0.0542	3814
3500 – 4000 m	0.044	5570
4000 – 4500 m	0.0397	6228
4500 – 5000 m	0.0305	4788
>5000 m	0.0305	5756

[*] In the publication[42], there are no F_{TOC} values in pixels <1000 m.

Table S7. Median and lower and upper quartiles of [F_{TOC} / F_{SeqAll}] in pixels, in the seven CONVERSE versions and all versions together.

		F_{seqSed} / F_{seqAll}	
CONVERSE	**Median**	**Lower quartile**	**Upper quartile**
1	0.03	0.01	0.07
2	0.02	0.01	0.04
3	0.03	0.01	0.06
4	0.01	0.01	0.02
5	0.01	0.01	0.02
6	0.02	0.01	0.05
7	0.02	0.07	0.05
All	0.02	0.08	0.04

5. Supplementary figures

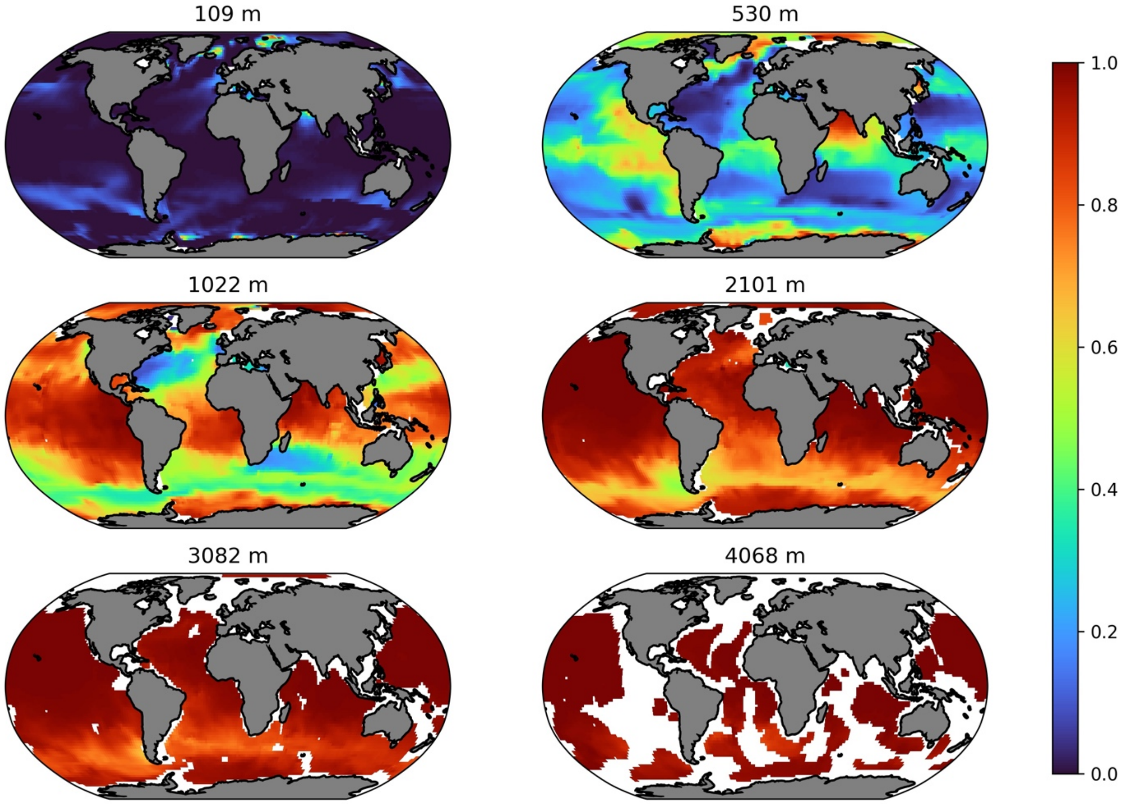

Fig. S1. Global-ocean distributions of f_{100} at six selected depths. White areas: pixels with water depths shallower than the depth illustrated. Another publication[5] provides additional representations of f_{100} distributions can be found in Supplemental Fig. S2 of another publication[5].

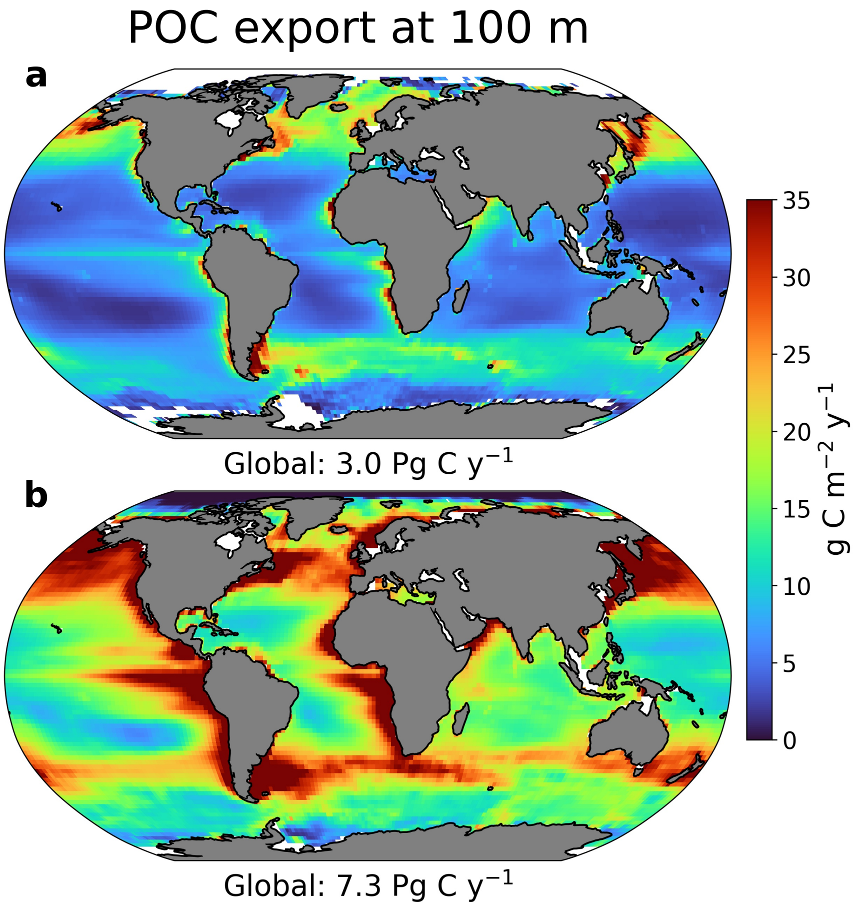

Fig. S2. Global distributions of POC F_{exp} at $z_{exp} = 100$ m used in this study, and corresponding global POC F_{exp} (a) value from the original publication[15], and (b) value of 7.3 Pg C y^{-1} corrected from the published[4] 6.7 Pg C y^{-1}.

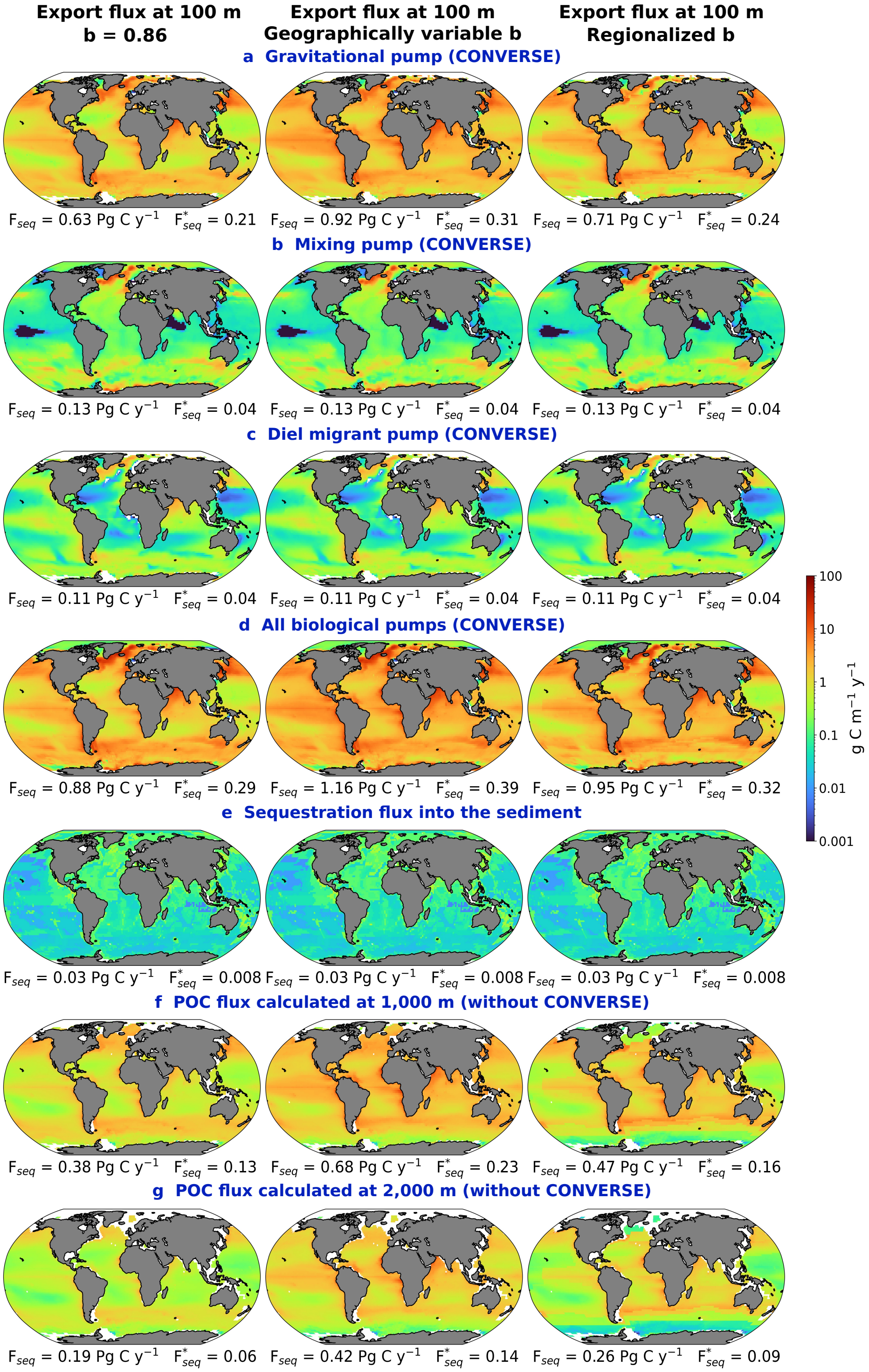

Fig. S3. Sequestration fluxes of biogenic carbon in CONVERSE 1-3: (a-d) carbon pumps, (e) F_{seq} into the sediment, and F_{seq} calculated at z_{seq} of (f) 1000 m and (g) 2000 m (assuming entire sequestration of the POC flux below z_{seq}). The latter two are the total sequestration fluxes estimated in many studies. Ocean areas shallower than 100 m are without colour. The seasonal migrant pump is not illustrated because our results concern the sole northern North Atlantic. Corresponding results are in Supplementary Tables S3 and S5.

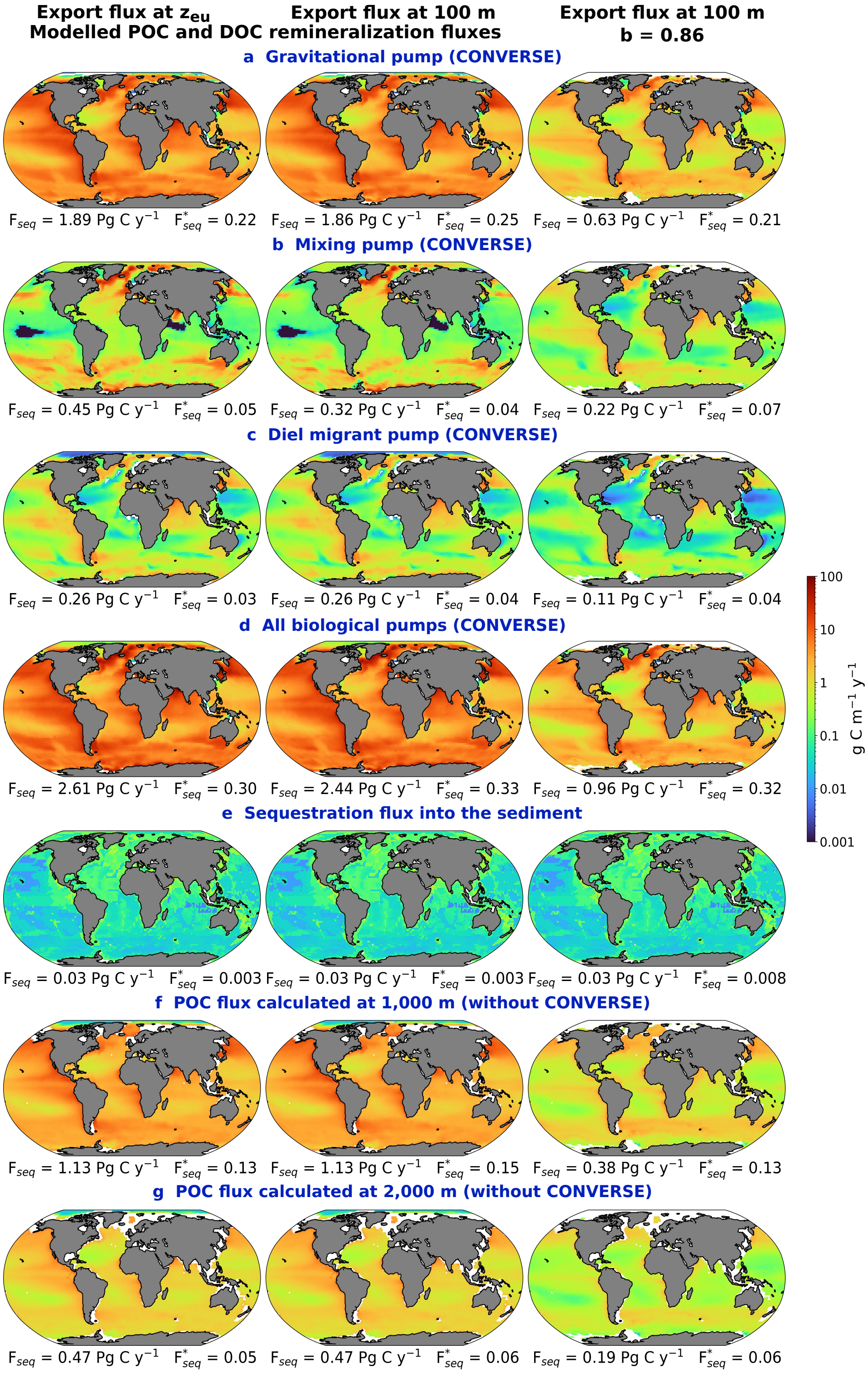

Fig. S4. Sequestration fluxes of biogenic carbon in CONVERSE 4, 5 and 7: (a-d) carbon pumps, (e) F_{seq} into the sediment, and F_{seq} calculated at z_{seq} of (f) 1000 m and (g) 2000 m (assuming entire sequestration of the POC flux below z_{seq}). The latter two are the total sequestration fluxes estimated in many studies. Ocean areas shallower than 100 m are without colour. The seasonal migrant pump is not illustrated because our results concern the sole northern North Atlantic. Corresponding results are in Supplementary Tables S4 and S5.

6. Supplementary Methods

We described in the main text the calculations for CONVERSE 1. We provide here the differences between CONVERSE 2 to CONVERSE 7 and CONVERSE 1 or other versions.

Continuous vertical estimation of pixel sequestration fluxes in CONVERSE 2

There was one difference between CONVERSE 2 and CONVERSE 1, i.e. b values in eqs. 10 and 18 were geographically variable values from a model[15] instead of fixed $b = 0.86$[43].

Continuous vertical estimation of pixel sequestration fluxes in CONVERSE 3

There was one difference between CONVERSE 3 and CONVERSE 1, i.e. b values in eqs. 10 and 18 were regionalized estimates in biogeochemical provinces[18] instead of fixed $b = 0.86$[43].

Continuous vertical estimation of pixel sequestration fluxes in CONVERSE 4

There were five differences between CONVERSE 4 and CONVERSE 1.

First, we used $z_{exp} = z_{eu}$. Hence, the shallowest Δz considered in each pixel was z_{eu} (eq. 7).

Second, we did not calculate $F_{reminPOC}(\Delta z)$ with eqs. 10 and 11, but instead used the concentrations of POC ([POC]; $[M\ L^{-3}]$) and its remineralization rates (k; $[T^{-1}]$) in two POC fractions (slow-sinking and fast-sinking) within each depth interval Δz [L] from SIMPLE-TRIM. With these data, we computed $F_{POC}(\Delta z)$ as follows:

$$F_{reminPOC}(\Delta z) = [([POC]_{slow} \times k_{slow}) + ([POC]_{fast} \times k_{fast})] \times \Delta z \qquad (24)$$

We calculated $F_{seqPOC}(\Delta z)$ with eq. 6.

We treated F_{orgPOC} remaining in the deepest Δz as done for CONVERSE 1, i.e. we first computed $F_{reminPOC}$(deepest Δz) with eq. (24), and then F_{seqPOC}(deep) with eq. 12 replacing F_{orgPOC}(deepest Δz) by $F_{reminPOC}$(deepest Δz).

Third, for $F_{reminDOC}$, we used directly the values that we had derived from SIMPLE-TRIM (eq. 13), i.e. without multiplying by the export ratio as done in eq. 14.

Fourth, for $F_{reminMigrS}$, we used values in the study cited above[38] whereby the copepod *Calanus finmarchicus* generated a seasonally remineralization flux $F_{reminMigrS} = 1$ to $4\ g\ C\ m^{-2}\ y^{-1}$ at $z_{migrS} = 600$ to 1,400 m, corresponding to $F_{orgPOC}(z) = 2$ to $8\ g\ C\ m^{-2}\ y^{-1}$. Hence, $F_{reminMigrS} = 50\%\ F_{orgPOC}(z)$ at $z_{migrS} = 600$ to 1,400 m. We computed $F_{reminMigrS}$ as follows:

$$F_{reminMigrS} = 0.5\ F_{orgPOC}(z) \text{ at } z_{migrS} \qquad (25)$$

We used $F_{orgPOC}(z)$ from SIMPLE-TRIM at $z_{migrS} = 619$ m, which was the depth closest to 597 m for which values were available in that database.

Fifth, F_{seqPOC} at two fixed depths (z_{fixed}), we linearly interpolated $F_{orgPOC}(z)$ from SIMPLE-TRIM at z = 919 and 1,104 m for the POC flux at 1,000 m, and at z = 1,833 and 2,141 m for the POC flux at 2,000 m

Continuous vertical estimation of pixel sequestration fluxes in CONVERSE 5

There was one difference between CONVERSE 5 and CONVERSE 4, i.e. $z_{exp} = 100$ m. Hence, the shallowest Δz considered for each pixel in eq. 7 was 100 m.

Continuous vertical estimation of pixel sequestration fluxes in CONVERSE 6

CONVERSE 6 was a mix between CONVERSE 1 AND CONVERSE 5, which considered $F_{expPOC} = 3.0$ Pg C y^{-1} at $z_{exp} = 100$ m[15] as in CONVERSE 1, but derived the fluxes of the gravitational and mixing pumps from CONVERSE 5.

We used the fluxes from CONVERSE 5 to compute all the pump fluxes of CONVERSE 6 (except one flux, below), and also the fluxes at, below and above 1,000 m and 2,000 m. We multiplied the fluxes from CONVERSE 5 by the export ratio used in eq. 14, i.e. 3.0 Pg C y^{-1} / 7.3 Pg C y^{-1}. This was necessary because the values in CONVERSE 5 were derived from SIMPLE-TRIM where $F_{expPOC} = 7.3$ Pg C y^{-1} at $z_{exp} = 100$ m[4] (see also the legend of Supplementary Fig. S2):

$$F_{reminPOC} = F_{reminPOC} \text{ from CONVERSE 5} \times (3.0 \text{ Pg C y}^{-1} / 7.3 \text{ Pg C y}^{-1}) \quad (26)$$

We computed the fluxes of the diel migrant pump as in CONVERSE 1.

Continuous vertical estimation of pixel sequestration fluxes in CONVERSE 7

There were two differences between CONVERSE 7 and CONVERSE 1.

First, for F_{expDOC}, we did not use eqs. 13 and 14, but implemented information from the literature whereby the downward flux of DOC at z_{exp} accounts for ca. 20% of $F_{exp(POC+DOC)}$[53]. Hence:

$$F_{expDOC} = 0.25\, F_{expPOC} \quad (27)$$

where F_{expPOC} was the value at $z_{exp} = 100$ m from CONVERSE 1. We assumed that the mixing pump transported DOC rapidly from above z_{exp} to z_{mix}, with the consequence that properties at z_{mix} were the same as those at z_{exp}, hence:

$$F_{mixDOC} = F_{expDOC} \quad (28)$$

In the mixing pump, both $F_{reminDOC}(\Delta z)$ and $f_{100}(\Delta z)$ may be > 0 in some Δz below z_{mix}. Because of the lack of information on the vertical distribution of F_{orgDOC} in the global ocean, we used the following bulk approach to obtain estimates of F_{seqDOC}(pixel) and F_{seqDOC}(global) from z_{mix} downwards.

We assumed that the F_{orgDOC} injected at z_{mix} in a pixel was entirely remineralized at or below z_{mix}:

$$F_{reminDOC} = F_{mixDOC} \quad (29)$$

We also assumed that remineralization occurred above the permanent pycnocline[33], which is traced by isopycnal[18] $\sigma_\theta = 1027.6$ kg m^{-3}. To be certain of not overestimating $F_{reminDOC}$(pixel), we further assumed that all DOC remineralization occurred within the Δz that included $z_{mix} = 500$ m, so that the relevant $f_{100}(\Delta z)$ was the value at z' = 530 m (depth for which there were values in the f_{100} database; Fig. 2 and Supplementary Fig. S1). We used eqs. 6 and 27-29 to calculate F_{seqDOC} at and below z_{mix}:

$$F_{seqDOC} = 0.25\ F_{expPOC} \times f_{100}(531\ m) \quad (30)$$

Second, for the calculation of pixel F_{seqPOC} ≤2,000 m (eq. 22), we considered that $F_{seqDOC} = 0$ because we assumed above (eq. 29) that all DOC remineralization occurred within the Δz that included $z_{mix} = 500$ m.

7. Additional references

45. Volk, T. & Hoffert, M. I. Ocean carbon pumps: Analysis of relative strengths and efficiencies in ocean-driven atmospheric CO_2 changes. *The Carbon Cycle and Atmospheric* CO_2*: Natural Variations Archean to Present* **32**, 99–110 (1985).

46. Lovelock, C. E. & Duarte, C. M. Dimensions of blue carbon and emerging perspectives. *Biol. Lett.* **15**, 20180781 (2019).

47. Boyd, P. W. *et al.* Potential negative effects of ocean afforestation on offshore ecosystems. *Nat Ecol Evol* **6**, 675–683 (2022).

48. Gallagher, J. B., Shelamoff, V. & Layton, C. Seaweed ecosystems may not mitigate CO_2 emissions. *ICES J. Mar. Sci.* **79**, 585–592 (2022).

49. Williamson, P. & Gattuso, J.-P. Carbon removal using coastal blue carbon ecosystems is uncertain and unreliable, with questionable climatic cost-effectiveness. *Frontiers in Climate* **4**, (2022).

50. Nowicki, M., DeVries, T. & Siegel, D. A. Quantifying the carbon export and sequestration pathways of the ocean's biological carbon pump. *Global Biogeochem. Cycles* **36**, (2022).

51. Giering, S. L. C., Sanders R., Lampitt, R.S., et al. Reconciliation of the carbon budget in the ocean's twilight zone. *Nature* **507**, 480–483 (2014)

52. Steinberg, D. K. & Landry, M. R. Zooplankton and the ocean carbon cycle. *Annu. Rev. Mar. Sci.* **9**, 413–44 (2017).

53. Hansell, D. A. & Carlson, C. A. Net community production of dissolved organic carbon. *Global Biogeochem. Cycles* **12**, 443–453 (1998).

6 General discussion and perspectives

6.1 UVP6 classification model: From start to finish

The development of the UVP6 classification model started without a data set of labeled UVP6 images. Therefore, a significant part of my work was to test and prepare a fully functional data preparation and model training pipeline for the upcoming UVP6 data set using UVP5 images. In the following sections, I will describe a brief history of what has been done prior to the acquisition and human labeling of UVP6 images and discuss about the use and perspectives on the embedded classification.

6.1.1 Trust index

In multiclass classification task, the goal is to predict the label (i.e. class) of a given input among a defined number of labels. In Chapter 3, I explained that XGBoost minimizes a regularized objective function L (see Equation 3.1) during model training. In practice, the XGBoost library proposes two choices of objective functions for multiclass classification problems: `multi:softmax` and `multi:softprob` (https://xgboost.readthedocs.io/en/latest/parameter.html, last accessed: 03/03/2023). Both functions are based on the softmax normalization which normalizes the classification score of each class using an exponential function (Equation 6.1). `multi:softmax` returns the class of highest probability whereas `multi:softprob` returns a class probability array, which allows the computation of custom objective functions.

$$\sigma(x_i) = \frac{e^{x_i}}{\sum_{j=1}^{N} e^{x_j}}, i = 1, ..., N \tag{6.1}$$

where x_i and N are, respectively, the classification score of the i^{th} class and the number of classes.

Information Box 4. Cross entropy loss

Cross entropy loss is a loss function often used in multiclass classification problems (Géron 2019).

$$J(\Theta) = -\frac{1}{m}\sum_{i=1}^{m}\sum_{k=1}^{K} y_k^{(i)} log(\hat{p}_k^{(i)})$$

where J is the loss (i.e. cost) function, Θ a parameter matrix, m the number of training data (i.e. instances), K the number of classes, $y_k^{(i)}$ the true probability that the i^{th} instance belongs to class k (0 or 1) and $\hat{p}_k^{(i)}$ the predicted probability that the instance belongs to class k. In practice, if one sets the objective function to `multi:softmax`, it means that the objective of the model is to predict the highest probability for the true class while minimizing the cross entropy loss.

By definition, `multi:softmax` amplifies the difference between classification scores. Here is a simple illustration of this effect. Let A, B and C, three classes of zooplankton whose classification scores are $(1, 7, 8)$. Using Equation 6.1, the output probabilities are $(0.0006, 0.26, 0.73)$. Therefore, a unit difference in the classification scores of class B and class C results in a probability three times higher for class C than class B.

This led us to define what we called a trust index, that is a metric whose score indicates the degree of confidence in the classification score. In other words, we looked for the best error estimator (Figure 6.1). To this end, we trained a first classification model with classes from the UVP5 data set using a `multi:softprob` objective function. Then, we used the model to make a prediction on a test set that returned a matrix $(M \times N)$ of M images and N probabilities (N classes in the model). Afterwards, we computed four metrics on each row of the probability matrix: the maximum probability (max, equivalent to `multi:softmax`), the softmax of the probability array ($softmax$, equivalent to a double `multi:softmax`), the difference between the highest and the second highest probability ($diff_{max}$) and the difference between the highest and second highest probability of the softmax array ($diff_{softmax}$). We compared those metrics for each class of the test set in Figure 6.1 which clearly shows that all metrics were very similar and that they captured the errors at the same speed. This result is threefold: 1) in our case, there is no need to use a trust index in addition to the probabilities given by `multi:softprob`, 2) some classes kept accumulating errors in the prediction with increasing rank (e.g. *Copepoda*, darksphere and fiber<detritus) thus an increasing rank is not always a trustworthy indicator of increasing confidence, 3) it partly explains why the quantification did not improve the overall classification by either using a fixed probability threshold (i.e. TC) or using the probability matrix (i.e. SPAC).

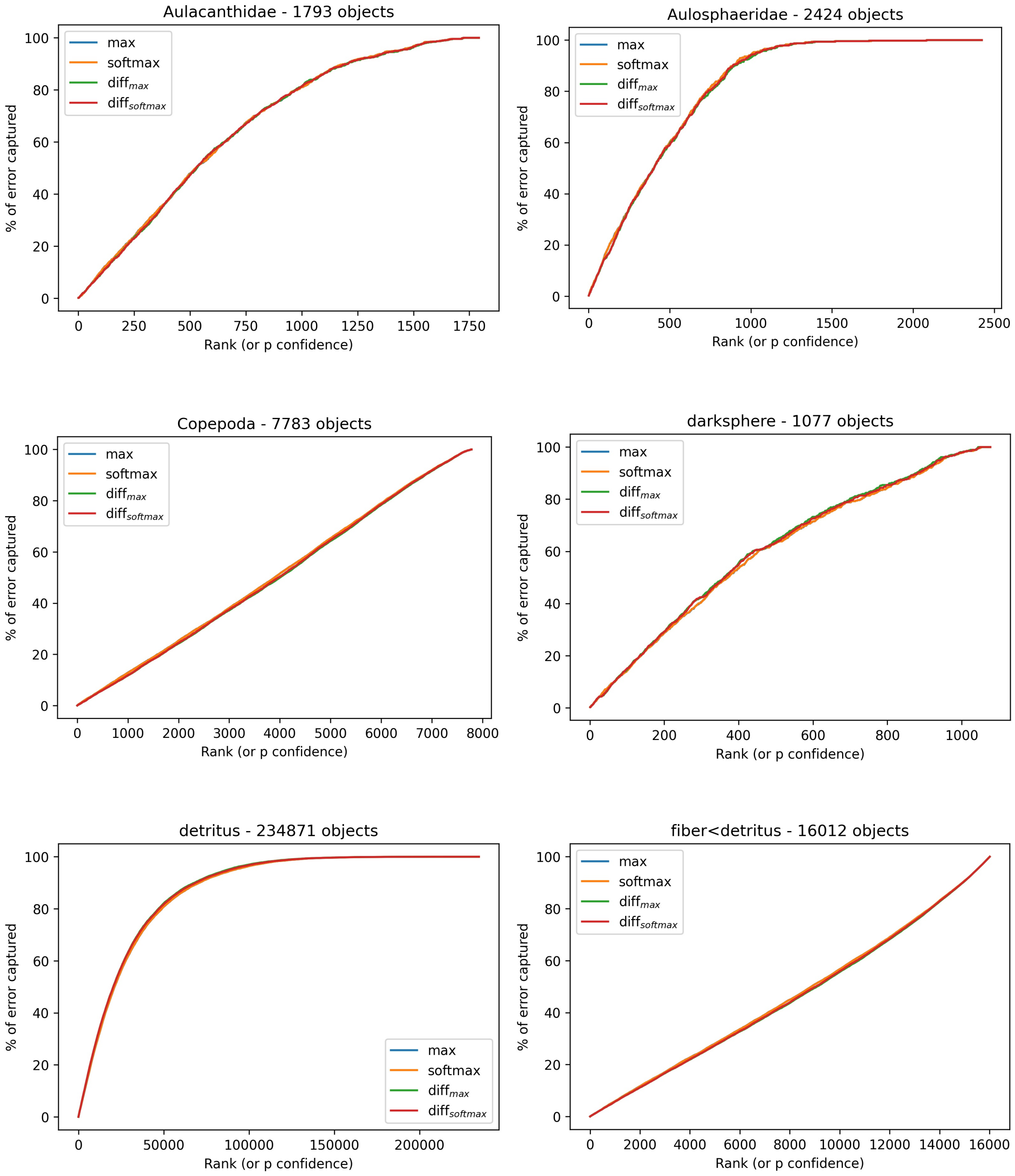
Aulacanthidae - 1793 objects

Aulosphaeridae - 2424 objects

Copepoda - 7783 objects

darksphere - 1077 objects

detritus - 234871 objects

fiber<detritus - 16012 objects

Figure 6.1: Percentage of error captured as a function of rank for four metrics (max, softmax, diff$_{max}$ and diff$_{softmax}$) on six UVP5 classes (4 biological, 2 non-biological). The number of objects predicted in each class is provided in the title of each subplot.

6.1.2 Technical constraints on the classification model

Because the UVP6-LP is designed to work on AUVs, several constraints were imposed on the model to fulfill technical and energy requirements. The UVP6 data treatment at sea shown in Figure 3.7 briefly describes the steps from the image acquisition to the prediction. The two most energy consuming steps are the image segmentation (median execution time of 650 ms) and the loading of the classification model whose execution time was capped at 700 ms. This limitation imposed a direct constraint on the prediction quality of the model because it implied a limitation on the choice of the model hyperparameters (learning rate, tree depth) and the number of boosting rounds.

The second critical aspect of the model was its limitation at 40 classes. In the UVP5 SD data set, the most detailed (human) classification at a taxonomic level was roughly 150 classes (referred to as $level_0$). It was therefore necessary to merge classes based on morphological and ecological attributes to decrease that number in order to get to $level_1$ that had 38 classes (reminder, it is currently limited at 40). From $level_1$, we thus experimented a lot of different prediction models with a hyperparameters grid search in order to find both the right set of hyperparameters and the right number of classes. Still, some $level_1$ classes had very low precision and recall scores because they were confused with some specific taxonomic groups hence we merged them accordingly with those groups. This trial-error approach was necessary to create the final aggregation level ($level_2$) used for the final UVP5 model. The same work had to be done later with the UVP6 data because the taxonomic groups were not identical.

The last technical limitation was the number of features (see Table 3.1). Before I started my PhD, 55 features (basically geometry, gray levels and statistical moments) were defined and were compliant with the energy budget imposed by the float (the UVP6 is adapted for other AUVs but it was especially designed for profiling floats). When XGBoost results are compared with a state-of-the-art CNN, the main difference does not likely come from the classifiers themselves but most likely from the selected features. We could have done some feature engineering, that is either doing feature selection (selecting the most useful features) either doing feature combination (combining existing features to create new ones) or creating new features by collecting new data (Géron 2019). Therefore, texture features could have been added to our global 55 features. The main issue with the latter (e.g. histogram of oriented gradients for detecting edges, gray-level co-occurrence matrix for homogeneity and contrast) is that their processing time is proportional to the size of the image hence it was difficult to evaluate them in the energy budget.

6.1.3 Detritus, this ubiquitous mess

Table 6.1 shows that the median number of objects detected in 3.5 m^3 is roughly 300. In addition, it is usual to have less than 20% of living objects hence the vast majority of images are labeled as detritus. The latter are ubiquitous in the ocean and display a wide variety of shapes, sizes and textures (Figure 6.2). In Section 3.1.6.1, I showed that using several classes of detritus did not improve the classification model and that it actually made it worse because the different detritus classes showed a high level of confusion between each other.

Table 6.1: Mean and median concentrations and number of segmented objects whose size is above 0.6 mm (referred to as "vignettes" in french) expected from a standard vertical profile taken by a BGC-Argo float equipped with a UVP6 in different parts of the water column.

Concentration (#/L)		Number			
Mean	Median	Mean	Median	Depth range (m)	Sampled volume (L)
0.119	0.085	426	305	0-2000	3570
0.457	0.332	146	106	0-100	320
0.110	0.059	143	77	100-500	1300
0.076	0.038	137	75	500-2000	1950

We assumed that detritus form a continuum in the 55-dimensional feature space. Therefore, we tried several methods to break this continuum while also trying to cope with the data set class imbalance. For this, we tried under-sampling the detritus to decrease their number and non random under-sampling by keeping only detritus close to K-means clustered centroids but it did not improve the classification model. Using a clustering method to split the detritus into several classes (e.g. fluffy gray or dark compact) to improve the classification of biological objects was based on the strong belief that it would improve the classification. However, my work and the work of another PhD student that tried using several detritus classes using a CNN (not published yet) showed that it did not improve the classification model either. Nonetheless, it is true that other clustering methods could be further explored. Clustering algorithms such as DBSCAN (Schubert et al. 2017) and HDBSCAN (Campello et al. 2013) are density-based in contrast to K-Means with is a partitioning clustering algorithm that needs a predefined number of clusters in input. Other clustering methods could obviously be explored (see Géron 2019, pp. 259–260) based on their computational complexity and the data set characteristics (number of instances and features).

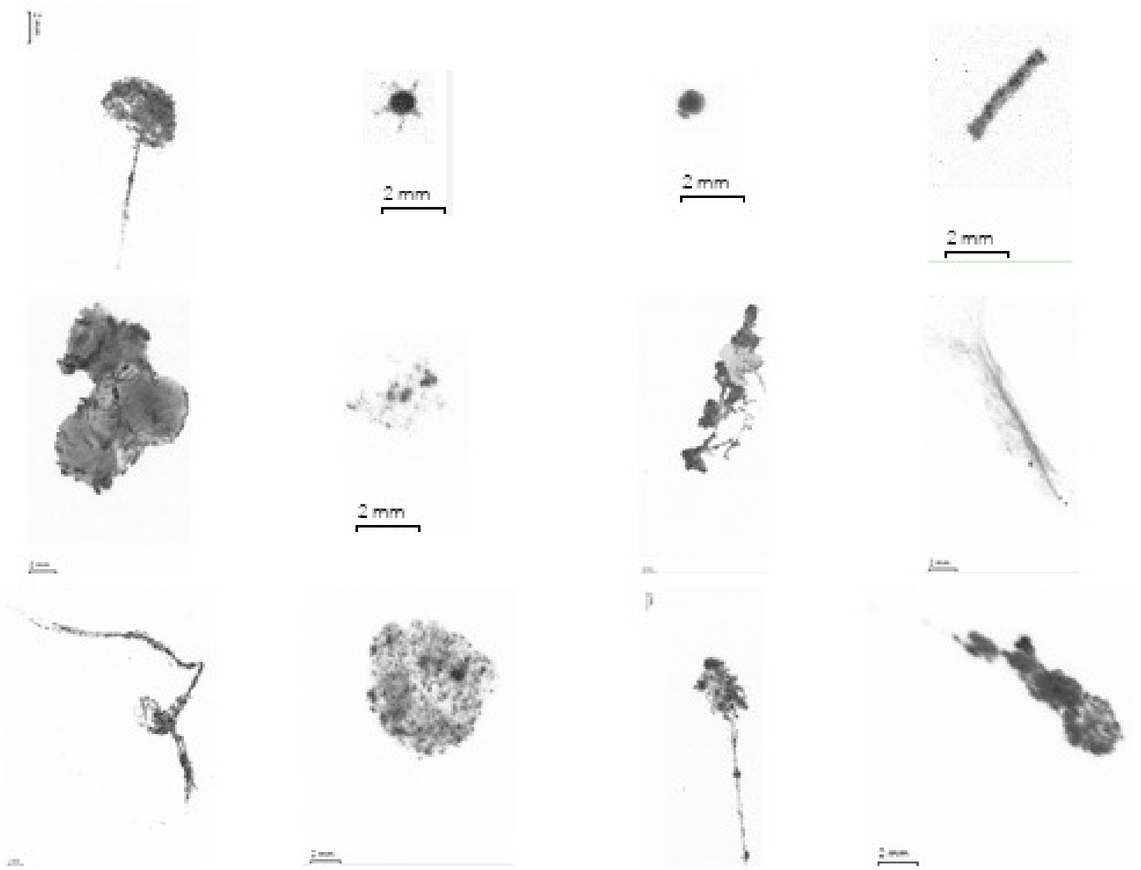

Figure 6.2: Examples of UVP objects labeled as detritus. The scale bar is the same for all (2 mm).

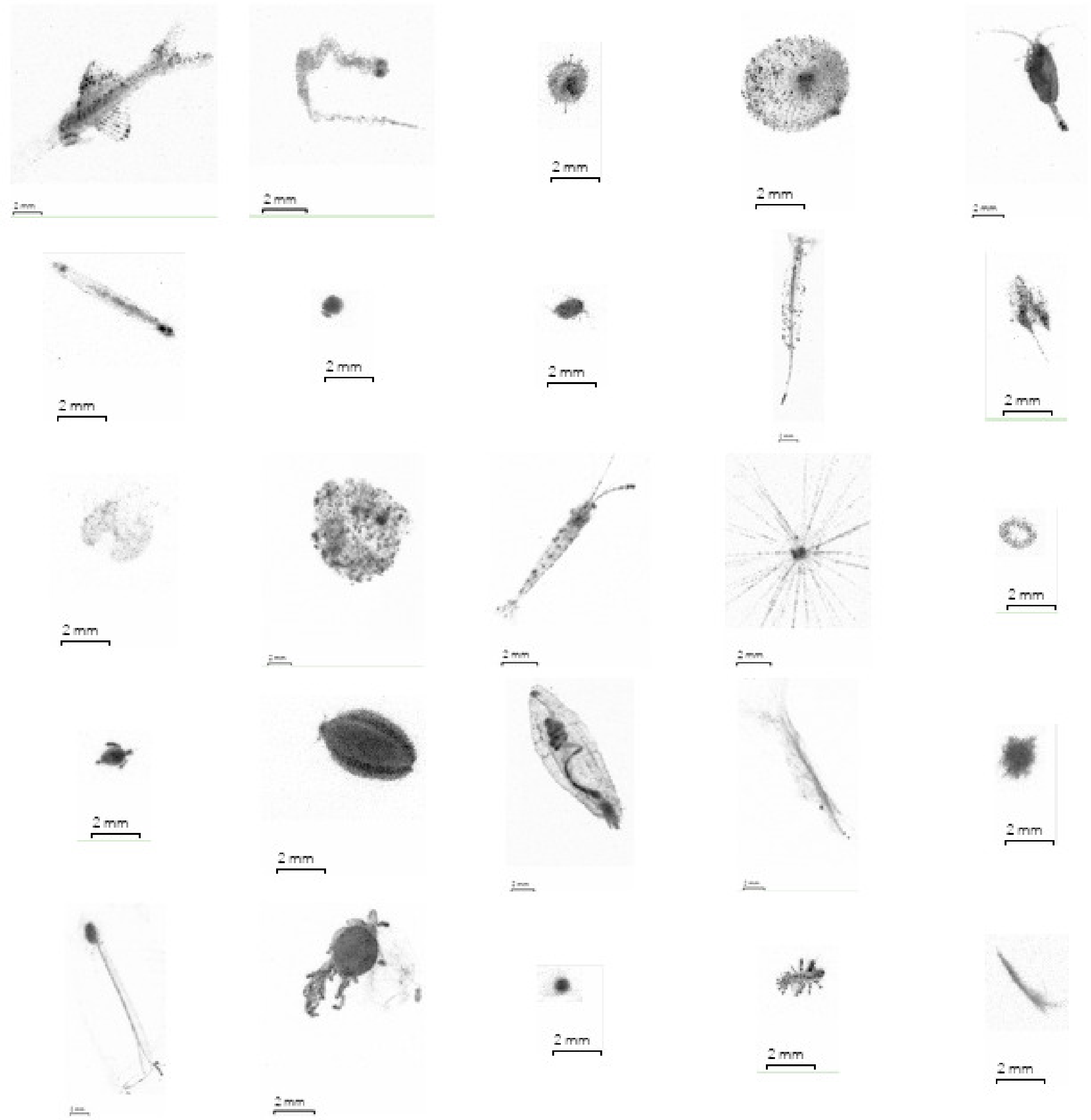

Figure 6.3: Examples of UVP objects labeled as living material. The scale bar is the same for all (2 mm). Note that I have hidden three detritus from Figure 6.2 to highlight the difficulty of classifying plankton already at the human level.

6.1.4 The future of the embedded classification

6.1.4.1 UVPec

UVPec (https://github.com/ecotaxa/uvpec/) - short name for Underwater Vision Profiler Embedded Classifier - is a toolbox to train classification models for UVP6 images and evaluate their performance. This python package has been designed to be as user-friendly as possible in order to be accessible to the largest number of users. Basically, the user only needs to create folders (40 maximum because the maximum number of classes is fixed at 40) of labeled UVP6 images and specify some hyperparameters (e.g. learning rate) to train a classification model. The evaluation of the created model provides a confusion matrix and a classification report to help the user evaluate the quality of the model as well as the cross entropy curve to have information on the optimal boosting round number (before the model overfits).

Overall, the goal of this package is to propose a simple and fast way to create new classification models for UVP6 applications on platforms that need to send data in near-real time or that cannot be easily retrieved.

6.1.4.2 More regions to be explored

The Labrador Sea was the first of 9 key oceanic regions studied in the frame of the REFINE (Robots Explore plankton-driven Fluxes in the marine twIlight zoNE) project (see https://erc-refine.eu). The latter aims to study regions with distinct biogeochemical conditions and responses to climate (Figure 6.4).

Figure 6.5 present some preliminary results from the UVP6 embedded classification that highlights the difference in *Calanoida*, *Chaetognatha*, detritus, puff and tuff concentrations between February and March 2023 in the western and eastern part of the Kerguelen Plateau. For these floats, the configuration was different from the ones deployed in the Labrador Sea with a higher profiling time resolution after deployment.

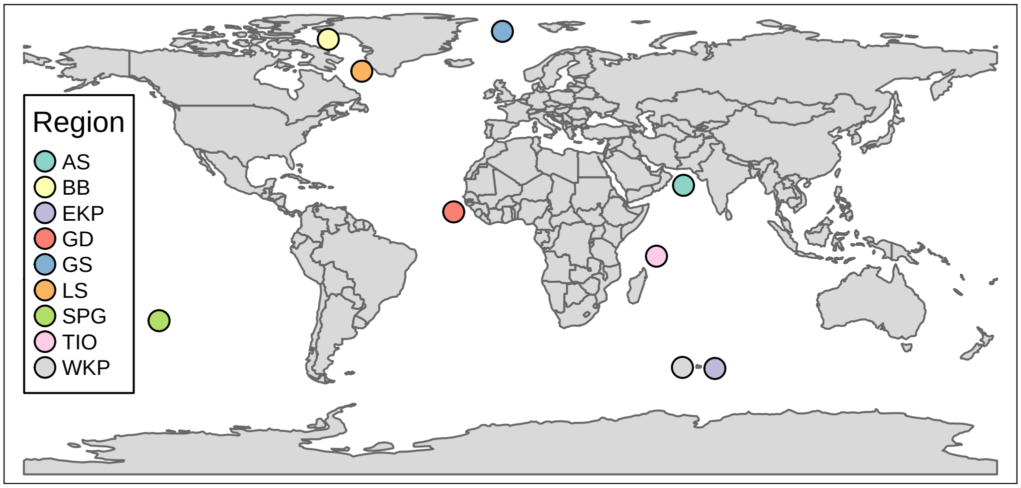

Figure 6.4: Oceanic regions (Baffin Bay (BB), Labrador Sea (LS), Greenland Sea (GS), Guinea Dome (GD), Arabian Sea (AS), Tropical Indian Ocean (TIO), South Pacific subtropical Gyre (SPG), West Kerguelen Plateau (WKP), East Kerguelen Plateau (EKP)) investigated in the frame of REFINE.

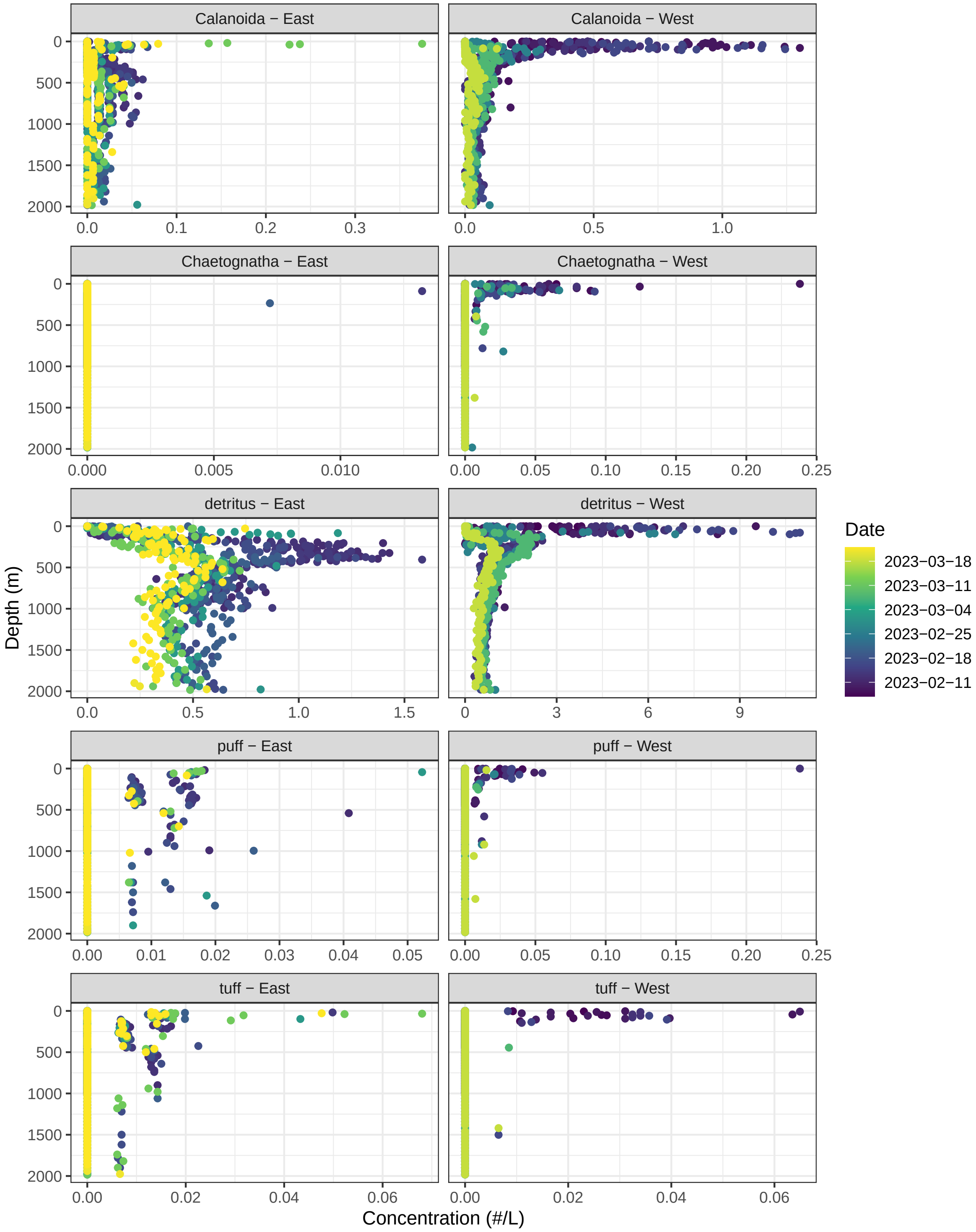

Figure 6.5: *Calanoida*, *Chaetognatha*, detritus, puff and tuff (i.e. *Trichodesmium*) concentrations in February-March 2023 on the Kerguelen Plateau.

The observed concentrations of the 4 biological classes in Figure 6.5 needs to be interpreted with the UVP6 classification report (Table 3.3). *Calanoida* have a precision and recall of, respectively, 66% and 69% thus we potentially miss 31% of them (i.e. 31% of *Calanoida* are non detected because they are classified in another class) but 34% of images classified as *Calanoida* are false positives and should be placed in another class. In that case, the observed concentrations can therefore be assumed as the real concentration. *Chaetognatha* have a precision and recall of, respectively, 80% and 62% therefore when a *Chaetognatha* is detected, the model is confident (20% of false positives) but it misses 38% of them so we might have more *Chaetognatha* than measured by the UVP6. However, One must also look at the concentration values because it is likely that the 2 points measured on the eastern part of the Kerguelen Plateau are misclassified objects. We could therefore conclude to the absence of *Chaetognatha* on the eastern part while their presence is likely on the western part because, on the one hand, this class has a high precision and, on the other hand, they are observed on successive short-lapsed vertical profiles and between 0-500 m where they likely feed on *Calanoida*.

Puff and tuff are both *Trichodesmium* which are usually observed in tropical and subtropical regions (Westberry and Siegel 2006) hence their presence on the Kerguelen Plateau is dubious. Tuff have a low precision and recall (55% and 63%) in contrast to puff (73% and 78%). On the eastern part, both classes have low concentrations and their position in the water column should be questioned for photosynthetic organisms. On the western part, they also both have low concentrations (0.25 #/L for puff is likely false) even though detritus concentrations are 5-10 times higher than on the eastern part.

The first results of the embedded classification are promising. However, they need to be interpreted with the UVP6 classification report and contextualized (e.g. species geographical and temporal distribution, correlation with the presence of other species, position in the water column).

6.1.4.3 New algorithms

Unless we find a cheap and efficient (low power) way to send UVP6 images via Iridium communication, we are stuck with the issue of embedded classification. In Chapter 3, I showed that CNNs usually outperform features-based classifiers. However, the field of computer vision is constantly evolving with the arrival of new technologies that could help improve the automatic classification of zooplankton images. Transformers (Vaswani et al. 2017), also referred to as Foundation Models in Bommasani et al. (2021) are the latest cutting-edge tools in the field of computer vision and natural language processing (e.g. Liu et al. 2021; Li and Li 2022). The structure of transformers relies on attention mechanisms able to draw global dependencies between input and output (Vaswani et al. 2017). In other words, it is able to learn dependencies between distant positions in a network architecture in constrast to CNNs. As an example, Li and Li (2022) used a vision transformer model combining a CNN and a vision transformer to identify apple diseases. In their model, the CNN is used to extract the global features of the input image while the transformer extracts local features of the disease region to help the CNN see better. How does it help the CNN? In the case of apple images with different backgrounds (different weather conditions, brightness changes, other objects in the field of view), the CNN could be “distracted” hence the transformer is able to focus the attention of the CNN on the region of interest (the disease region) and not on irrelevant features such as the weather. The use of transformers for automatic zooplankton classification has just begun (Kyathanahally et al. 2022) but it should certainly be explored further in the near future.

6.1.4.4 UVP6m

There is a class called “other<living” in the UVP6 classification model. I did not mention earlier that we were forced to place copepods (except *Calanoida*) in that class. Indeed, *Calanoida* are a “large” species of copepods compared to other copepods found in the Mediterranean Sea that are smaller. The classification score of the latter was low (low precision and low recall) hence we put them in the “other<living” class, which is a shame.

The good news is that the next generation of UVPs is already in the making with the UVP6m (m for micro) which will be able to look at smaller objects (particle counter between 10 and 200 μm and plankton/particle imaging > 100 μm). The UVP6m will be more compact than the UVP6 but the principles will be the same and both instruments will share 5 size classes for intercalibration.

6.2 Deriving carbon fluxes from particle size distribution

Before working on the CONVERSE framework, I was trying to find a global relationship (I also tried to find a regional one, without more success) to derive carbon fluxes from UVP5 PSDs. The idea was to reproduce the method of Guidi et al. (2008) on the newly quality controlled UVP5 PSD data set of Kiko et al. (2022). For this, I needed to build a global data set of POC measurements derived from sediment traps and ^{234}Th (see Table 6.2, Table 6.3 and here for a more interactive view). Here below, I briefly review three methods we explored to find a POC-PSD relationship and what could be further investigated.

Table 6.2: Compilation of POC flux measurements from sediment traps. Data taken from public databases listed on PANGAEA or extracted from articles (with the help of Frédéric Le Moigne and Meike Vogt). The number of measurements could be different from the original publication after data cleaning and potential removal of duplicates.

Source of data	Period covered	Number of observations
10.1594/PANGAEA.855600	1976-2012	13474
10.1016/j.dsr.2016.08.015	1995-2008	185
10.1594/PANGAEA.901800	2005-2012	73
10.1594/PANGAEA.855472	2010-2011	60
10.1594/PANGAEA.855473	2011-2012	60
10.1594/PANGAEA.879532	2007-2008	57
10.1594/PANGAEA.828349	1995-2012	52
10.1594/PANGAEA.855467	2005-2006	48
10.1594/PANGAEA.855465	2002-2003	40
10.1594/PANGAEA.855468	2006-2007	40
10.1594/PANGAEA.855470	2008-2009	39
10.1594/PANGAEA.855562	2006-2007	39
10.1594/PANGAEA.855466	2004-2005	38
10.1594/PANGAEA.855564	2008-2009	38
10.1594/PANGAEA.910883	2015	38
10.1594/PANGAEA.855565	2010-2011	36
10.1073/pnas.1415311112	2009-2011	21
10.1594/PANGAEA.757777	2002-2003	20
10.1594/PANGAEA.855561	2006-2007	20
10.1594/PANGAEA.855566	2004-2005	20
10.1594/PANGAEA.855563	2007-2008	19
10.1594/PANGAEA.855463	2000-2001	18
10.5194/bg-14-1825-2017	2014	15
10.3354/meps10453	2007-2008	14
10.5194/bg-13-2077-2016	2007	14
10.1007/s00227-018-3376-1	2012-2013	13
10.1016/j.dsr.2013.07.001	2010-2011	11
10.1594/PANGAEA.855464	2001-2002	11
10.5194/bg-16-1-2019	2015	8
10.1016/j.dsr2.2007.06.008	2004-2005	7
10.1002/2013JC009754	2011	6
10.1016/S0016-7037(01)00787-6	1999	6
10.1029/2020GL087465	2016	6
10.1038/srep40850	2015	4
10.12952/journal.elementa.000140	2010-2011	4
10.1016/j.pocean.2006.10.003	1998	2

Table 6.3: Compilation of POC flux measurements derived from Thorium 234. Data taken from public databases listed on PANGAEA or extracted from articles (with the help of Frédéric Le Moigne). The number of measurements could be different from the original publication after data cleaning and potential removal of duplicates.

Source of data	Period covered	Number of observations
10.1594/PANGAEA.809717	1987-2009	678
10.1029/2018GB00615	2010-2013	151
10.1525/elementa.2020.030	2018	10

6.2.1 The straightforward approach

This approach consisted in simply applying the method of Guidi et al. (2008) (see Equation 2.6). Therefore, we looked for match-ups (i.e. spatially and temporally close observations) between UVP5 and POC observations within a 0.2° latitude and longitude window, a 10 m vertical depth range and a 5-day window. Guidi et al. (2008) found 118 match-ups (with UVP2/3/4 data) whereas we only found 108 match-ups with UVP5 data, located on the western and eastern parts of the Kerguelen Plateau, in the Guinea Dome and in the California Current (panel D in Figure 6.6). Consequently, we decided not to go further because the number of match-ups was too low to improve the minimization (see Equation 2.7).

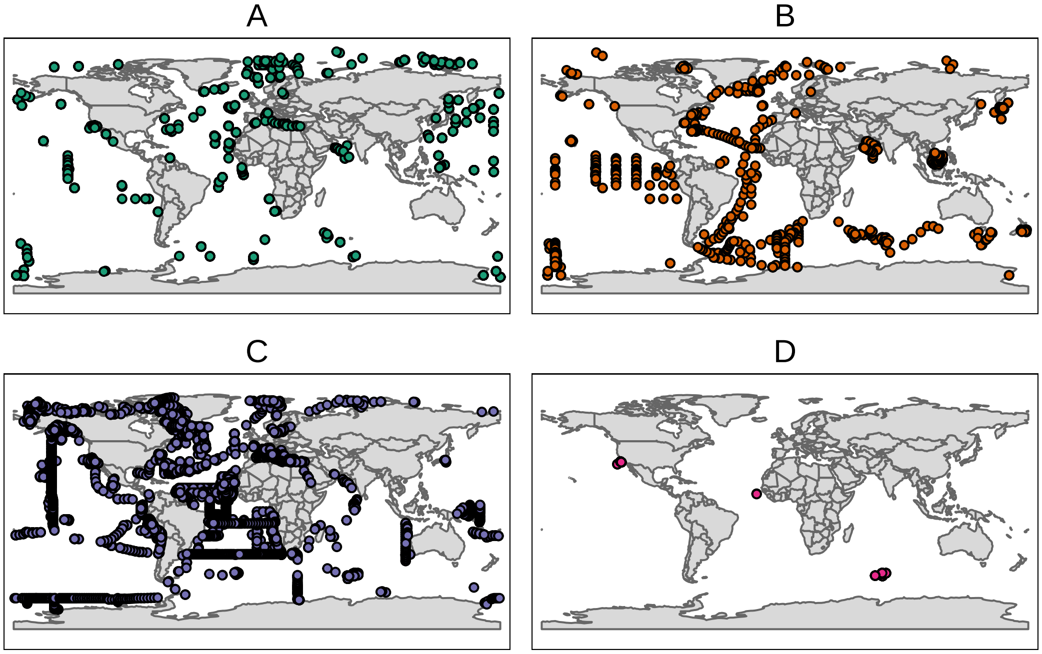

Figure 6.6: Spatial distribution of (A) sediment traps, (B) ^{234}Th, (C) UVP5 and (D) their spatio-temporal match-ups.

6.2.2 The environmental match-ups approach

The spatio-temporal approach lacks match-ups between UVP5 and sediment traps and ^{234}Th data. This is not really surprising when we look at their spatial distribution (Figure 6.6) and especially their temporal distribution (Figure 2.3) because the UVP5 was firstly used in 2008 while the ‘historical’ data reached their observation peak before 2000. Therefore, we thought of using environmental data to increase the number of match-ups.

The idea was based on the assumption that carbon fluxes could be similar in distinct regions of the ocean if those regions had similar environmental conditions thus removing spatial (horizontal) and temporal constraints on match-ups. For this, we tried different combinations of environmental variables such as surface temperature, salinity, nutrients, Chla, b_{bp} or water column properties such as integrated Chla content, oxygen minimum and MLD from monthly climatologies. Then, we used those environmental variables to build a 3D environmental space using a 3D principal component analysis (PCA) decomposition and we projected UVP5 data and trap/^{234}Th in that space based on the environmental characteristics from the respective coordinates and month of each UVP5 and trap/^{234}Th profiles.

Once all data were projected in the environmental space, we needed a new match-up procedure. Because the PCA projection conserves the euclidean distance, we firstly computed the pairwise distance between each UVP5 profile and all trap/^{234}Th profiles. Then, we looked at the minimal euclidean distance for each UVP5 profile and we plotted the minimal distance distribution (~8000 points in the distribution). From this distribution, we computed a radius of interest (ROI) corresponding to a threshold based on the 95^{th} percentile (considered as a rather objective decision criterion). For each UVP5 profile in the environmental space, we kept the closest trap/^{234}Th profiles within that radius (Figure 6.7). Finally, we still needed to find the PSD-POC match-ups on the vertical axis (depth). For this, we used a depth range proportional to the depth of the trap or ^{234}Th measurement following Martin’s curve (Martin et al. 1987) because the downward carbon flux is less attenuated with depth. Then, we averaged PSDs in that depth range (weighted by the water volume for each depth bin) to obtain a table with weighted averaged PSDs in front of POC fluxes to proceed with the minimization procedure of Guidi et al. (2008).

This method increased the number of match-ups to ~7800 however the minimization did not find a non ambiguous minimum in the solution space (Figure 6.8). Instead of having a global minimum, Figure 6.8 shows what looks like a 2D solution plane. In addition, I think the choice of A and D (or B, $B = 2D - 1$) is not constrained enough. In Figure 5 of Guidi et al. (2008), the light gray color area (low residual error) encompasses a wide region of A and B values where their jackknife procedure found local minima with (A, B) pairs such as (50, 2) or (150, 5). A is the single-particle carbon or mass flux for particles of size d_0 (i.e. a reference size bin) however it is mostly the values of B that should really be questioned since it is related to the fractal dimension D of particles and aggregates. Fractal dimensions should not exceed 3 (physical limit) but they have been estimated down to 1.1-1.3 (Alldredge and Gotschalk 1988).

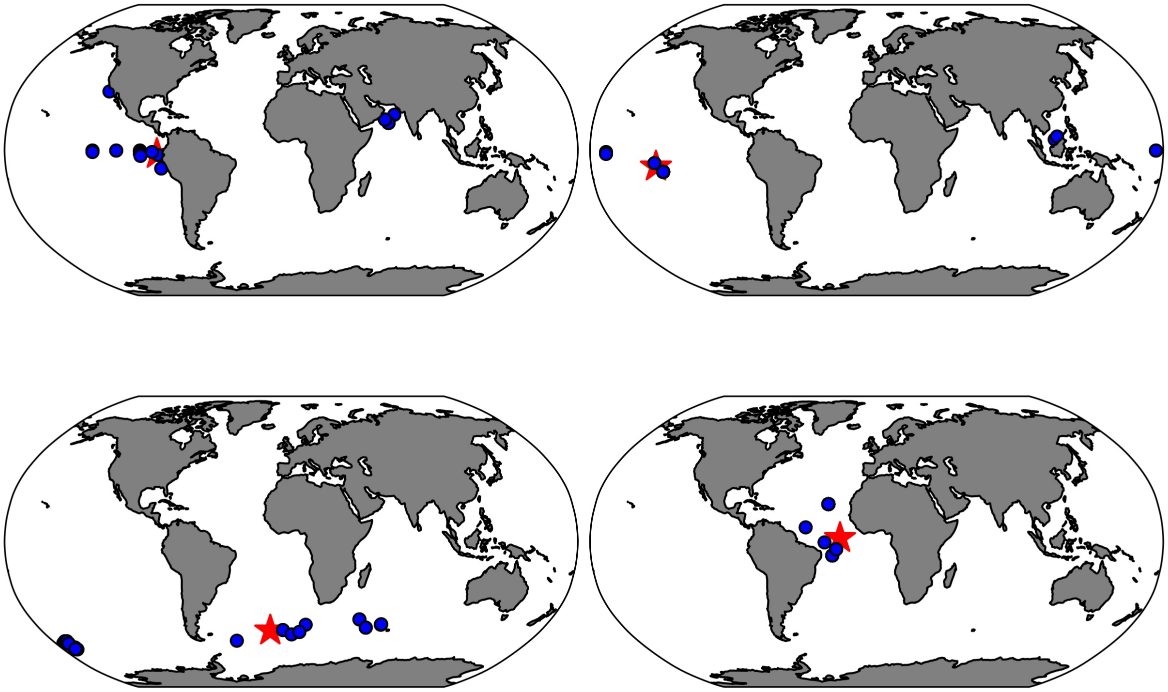

Figure 6.7: Examples of trap/^{234}Th match-ups (blue dots) in the geographical space that were within the ROI in the environmental space for 4 UVP5 profiles (red star).

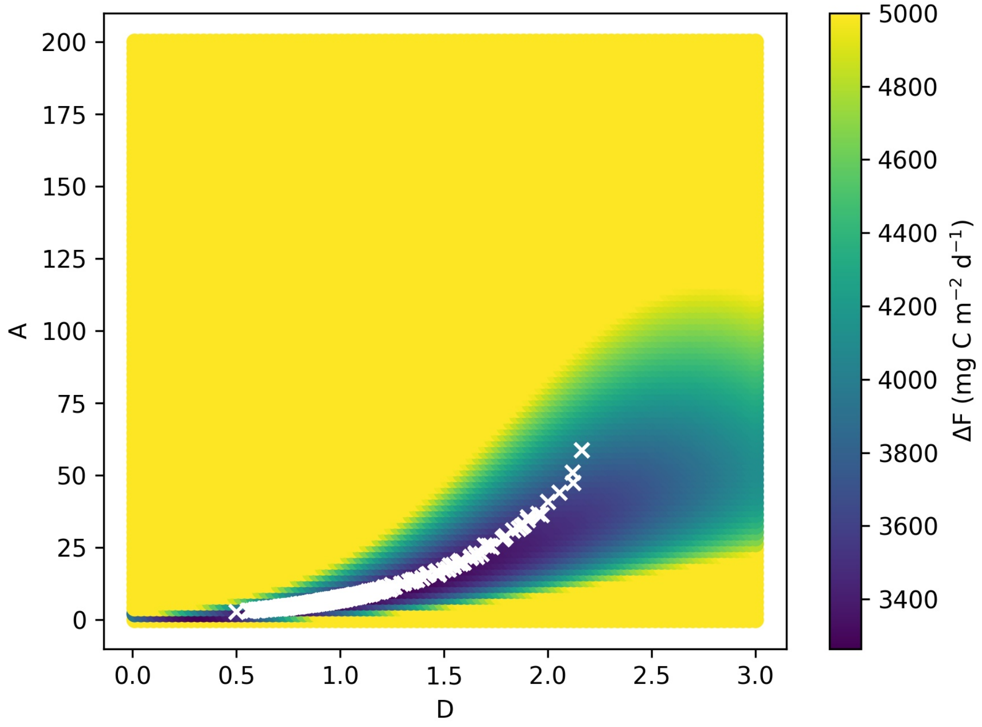

Figure 6.8: Residual error ΔF (for the carbon flux) as a function of A and D (i.e. $B = 2D-1$). White crosses correspond to the best (A, D) values computed during the jackknife error analysis (i.e. 1000 random subsamples of 30% of the match-ups data set).

In addition, it is possible to obtain coherent POC fluxes by tuning the A value for a fixed B therefore I am not sure that A and B are truly independent.

Several other reasons could explain the 'failure' of this method. Firstly, the match-up procedure relies on a very strong initial assumption, especially when we deal with PSD measurements (i.e. direct measurements) and monthly climatologies. Second, the choice of environmental variables we used was limited and most likely insufficient to represent the dynamics of the system at surface responsible for the downward POC flux. Thirdly, the UVP5 data set of Kiko et al. (2022) is composed of UVP5 SD and HD data hence the choice of size classes is also an issue if the minimization is done on a wide size spectrum due to instrumental differences. Fourthly, the model itself as well as the minimization procedure could be revised. In their paper, Bisson et al. (2022) clearly enonciates the limitations of using the UVP to assess POC fluxes and I agree (see also Section 2.2.3). All things considered, I think the search for a global relationship to derive POC fluxes from UVP data might try to generalize a relationship that cannot be generalized. Some studies did try to apply the (A, B) coefficients of Guidi et al. (2008) but the results were orders of magnitude different from local (A, B) estimations (Iversen et al. 2010; Fender et al. 2019) hence the question of its global applicability.

6.2.3 The machine learning approach

So far, we have seen that the match-up quest was not enough in the geographical space and not working in the environmental space but what about a method that does not need any match-ups? With XGBoost, it is possible to create a regression model to predict carbon fluxes using environmental variables and geographical variables (depth) as predictors (i.e. explanatory variables) and trap/^{234}Th POC fluxes as target variables. Once the model is trained, it can be applied to the entire data set of PSDs ($>$ 1.5 million) to derive POC fluxes. We tried to build such a model with a few predictors (i.e. depth, surface temperature, Chla, b_{bp} and the oxygen minimum in the water column). Our model had a R^2 of 0.47 with a percentage of explained variance dominated by depth (54%), surface Chla (16%), surface temperature (13%) and the oxygen minimum (10%). The minimization of Guidi et al. (2008) applied on all true PSDs and predicted POC fluxes led to the same kind of solution space as shown in Figure 6.8.

Instead of directly predicting carbon fluxes using environmental variables, we could focus on predicting PSD slopes or PSDs. In a recent paper, Clements et al. (2022) used physical and biological variables (see their Table 1) to predict global maps of PSD slope and biovolume at the base of the EZ using UVP5 data and a random forest algorithm. Clements et al. (2022) highlighted the importance of Chla (i.e. proxy of biomass), oxygen (i.e. proxy of respiration) and MLD as predictors in their random forest model. They also emphasized the importance of including phytoplankton functional groups and abundance as key controlling factors on both the PSD slope and the biovolume in future models due to their impact on the downward POC flux (i.e. aggregation/disaggregation processes). The study of Denvil-Sommer et al. (2022) used both random forest and XGBoost models to predict small and large POC concentrations using geographical (depth, latitude and longitude), physical (incident light, MLD and temperature), chemical (phosphate and nitrate) and biological variables (Chla and 12 Plankton Functional Types (PFTs) such as diatoms or microzooplankton). Denvil-Sommer et al. (2022) showed that for small POC, the most important predictors are the depth level, temperature, microzooplankton and phosphate while the large POC is mostly driven by depth, temperature, MLD, microzooplankton, phaeocystis (another PFT), phosphate and Chla averaged over the MLD. Overall, the results of these studies suggest that it is possible to link the surface environmental and ecosystem structure to the POC distribution in the ocean interior.

6.2.4 Improving the PSD-POC relationship

I used three methods to derive POC fluxes from UVP5 PSDs. The main issues I encountered were related to the number and accuracy of match-ups as well as the choice of environmental variables to link the surface ocean to the POC distribution below. With the deployment of new BGC-Argo floats equipped with both the UVP6 and the OST as well as the core biogeochemical variables (e.g. Chla, b_{bp}, incident light) of the BGC-Argo program, we will hopefully be able to better constraint the PSD-POC relationship however it will probably need a few more years to acquire enough profiles in different oceanic regions to better understand the key drivers of the downward POC flux.

6.3 Continuous vertical sequestration

Using the CONVERSE approach, we have estimated that the global carbon sequestration ($\geq$ 100 years) flux by the BCP is 0.9-2.6 Pg C y^{-1}. This is 2-3 and 3-6 times larger than POC fluxes at, respectively, 1,000 and 2,000 m. CONVERSE sequestration flux estimates are also up to 4 times larger than those from studies assuming that sequestration occurs below a fixed reference depth (Honjo et al. 2008; Henson et al. 2012; Guidi et al. 2015). Here below, I highlight some key points and ways to improve our estimations.

6.3.1 Marine carbon dioxide removal strategies

The goal of marine carbon dioxide removal (mCDR) strategies (Boyd et al. 2023) is the removal of excess CO_2 from the atmosphere and the sequestration of carbon away from the atmosphere for a given time period (National Academies of Sciences 2022). Several mCDR strategies have been proposed such as increasing alkalinity to enhance the chemical uptake of atmospheric CO_2 (Hartmann et al. 2023), increasing the photosynthetic uptake of atmospheric CO_2 with iron and macronutrients fertilization (Blain et al. 2007) or directly injecting CO_2 into the deep ocean (Siegel et al. 2021).

We have seen with CONVERSE that carbon sequestration occurs on the whole water column and that using a fixed reference depth would likely miss the bulk of sequestration. Therefore, the evaluation of future mCDR strategies using biologically-driven carbon sequestration fluxes should be estimated over the entire water column.

6.3.2 Particle injection pumps

Our study on the sequestration flux by the BCP also shows that the contribution of the vertical migration and mixing pumps represent at least 21-34% of the sequestration flux by the BCP. However, those two pumps could probably be better estimated with a multi-instruments approach (Claustre et al. 2021).

6.3.2.1 Physically mediated particle injection pump

With CONVERSE, we estimate that the mixing pump contributes to 11-23% of the sequestration flux by the BCP. However, we were not able to distinct the contribution of the three identified pathways composing the mixing pump due to lacking information in the literature. This could be improved by using the observational framework developed in Claustre et al. (2021) by combining satellite, ship-based, mooring and AUV data. BGC-Argo floats have shown that they are adapted to study the detrainment of mixed-layer particles (Dall'Olmo and Mork 2014; Dall'Olmo et al. 2016) and so have gliders for the eddy subduction pump (Omand et al. 2015; Stukel et al. 2017). Nonetheless, the study of the large-scale subduction pump will be more challenging because it will require a larger number of measurements made at the scale of ocean basins and over annual cycles (Claustre et al. 2021), hence the need for a multi-instruments approach to better understand it.

6.3.2.2 Biologically mediated particle injection pump

With CONVERSE, we estimate that the vertical migration pump contributes to 9-12% (diel) and 0.1-0.4% (seasonal). The estimation of the latter was limited to the northern North Atlantic thus it is clearly underestimated. However, the estimation of vertically migrating (either daily or seasonally) zooplankton and other animals (e.g. fish, jellyfish) is expected to improve with robotic measurements at high temporal resolution and over the entire annual cycle (Claustre et al. 2021). The combination of acoustic sensors (Reiss et al. 2021; De Robertis et al. 2021), optical sensors (Picheral et al. 2021) and vertical profiles of biogeochemical variables (e.g. Chla, b_{bp}, CDOM) have already shown promising results to detect the migration of mesopelagic organisms in the water column (Haëntjens et al. 2020).

6.4 Contributions of this work

The embedded classification for AUVs will contribute to a better comprehension and quantification of the vertical migration pump. So far, BGC-Argo floats equipped with the UVP6 and the classification model have been deployed in some oceanic regions (e.g. Labrador Sea, Kerguelen Plateau) and have just started to acquire data. In addition to the particle (> 0.6 mm) identification, the UVP6 also sends their mean area and gray levels which will hopefully contribute to better characterize their morphological traits and therefore better predict their sinking rates (cfr. size versus excess density debate). The latter are important to estimate the downward carbon flux and the sequestration time.

The BCP can no longer be seen as the sole gravitational settling of particles. Physically and biologically mediated particle injection pumps need to be taken into consideration which is highlighted by our work that estimates their contribution to 21-34% of the total BCP sequestration flux. Our work also shows that the common assumption of sequestration below a fixed reference depth (typically 1,000 or 2,000 m) misses the bulk of sequestration flux. Therefore, the evaluation of mCDR efficiencies using biologically-driven carbon sequestration fluxes should be estimated over the entire water column.

This work has shown the first comparison of BGC-Argo floats equipped with both the UVP6 and an OST to better quantify carbon fluxes from particle counts and beam attenuation. If the prediction of carbon fluxes at global scale was not a success, this work has highlighted current difficulties and ways to move forward using machine learning approaches. The deployment of BGC-Argo floats in the frame of REFINE with the combination of UVP6 measurements (particle counts and identification), OST beam attenuation fluxes as well as bio-optical variables (e.g. Chla, b_{bp}, incident light) will likely improve our understanding of processes that affect the attenuation of the downward carbon flux at local scale.

References

Alkire MB, D'Asaro E, Lee C, et al (2012) Estimates of net community production and export using high-resolution, lagrangian measurements of O2, NO3−, and POC through the evolution of a spring diatom bloom in the north atlantic. Deep Sea Res Part I 64:157–174. https://doi.org/10.1016/j.dsr.2012.01.012

Alldredge AL, Gotschalk C (1988) In situ settling behavior of marine snow. Limnol Oceanogr 33:339–351. https://doi.org/10.4319/lo.1988.33.3.0339

Alldredge AL, Silver MW (1988) Characteristics, dynamics and significance of marine snow. Prog Oceanogr 20:41. https://doi.org/10.1016/0079-6611(88)90053-5

Archibald KM, Siegel DA, Doney SC (2019) Modeling the impact of zooplankton diel vertical migration on the carbon export flux of the biological pump. Global Biogeochem Cycles 33:181–199. https://doi.org/10.1029/2018gb005983

Armstrong RA, Lee C, Hedges JI, et al (2001) A new, mechanistic model for organic carbon fluxes in the ocean based on the quantitative association of POC with ballast minerals. Deep Sea Res Part 2 Top Stud Oceanogr 49:219–236. https://doi.org/10.1016/S0967-0645(01)00101-1

Aumont O, Maury O, Lefort S, Bopp L (2018) Evaluating the potential impacts of the diurnal vertical migration by marine organisms on marine biogeochemistry. Global Biogeochem Cycles 32:1622–1643. https://doi.org/10.1029/2018gb005886

Behrenfeld MJ (2010) Abandoning sverdrup's critical depth hypothesis on phytoplankton blooms. Ecology 91:977–989. https://doi.org/10.1890/09-1207.1

Bell JL, Hopcroft RR (2008) Assessment of ZooImage as a tool for the classification of zooplankton. J Plankton Res 30:1351–1367. https://doi.org/10.1093/plankt/fbn092

Benfield MC, Grosjean P, Culverhouse PF, et al (2007) RAPID: Research on automated plankton identification. Oceanography 20:172–187

Bertrand P, Legendre L (2021) Earth, our living planet. Springer International Publishing

Bishop JKB (2009) Autonomous observations of the ocean biological carbon pump. Oceanography 22:182–193

Bishop JKB (1999) Transmissometer measurement of POC. Deep Sea Res Part I 46:353–369. https://doi.org/10.1016/S0967-0637(98)00069-7

Bishop JKB, Wood TJ, Davis RE, Sherman JT (2004) Robotic observations of enhanced carbon biomass and export at 55 degrees during SOFeX. Science 304:417–420. https://doi.org/10.1126/science.1087717

Bisson KM, Kiko R, Siegel DA, et al (2022) Sampling uncertainties of particle size distributions and derived fluxes. Limnol Oceanogr Methods. https://doi.org/10.1002/lom3.10524

Biswas A, Chandrakasan AP (2018) Conv-RAM: An energy-efficient SRAM with embedded convolution computation for low-power CNN-based machine learning applications. In: 2018 IEEE international solid - state circuits conference - (ISSCC). pp 488–490

Blain S, Quéguiner B, Armand L, et al (2007) Effect of natural iron fertilization on carbon sequestration in the southern ocean. Nature 446:1070–1074. https://doi.org/10.1038/nature05700

Blaschko MB, Holness G, Mattar MA, et al (2005) Automatic in situ identification of plankton. In: 2005 seventh IEEE workshops on applications of computer vision (WACV/MOTION'05) - volume 1. ieeexplore.ieee.org, pp 79–86

Bochinski E, Bacha G, Eiselein V, et al (2019) Deep active learning for in situ plankton classification. In: Pattern recognition and information forensics. Springer International Publishing, pp 5–15

Bommasani R, Hudson DA, Adeli E, et al (2021) On the opportunities and risks of foundation models

Bopp L, Resplandy L, Orr JC, et al (2013) Multiple stressors of ocean ecosystems in the 21st century: Projections with CMIP5 models. Biogeosciences 10:6225–6245. https://doi.org/10.5194/bg-10-6225-2013

Boss E, Behrenfeld M (2010) In situ evaluation of the initiation of the north atlantic phytoplankton bloom. Geophys Res Lett. https://doi.org/10.1029/2010GL044174

Boyd P, University of Tasmania, Claustre H, et al (2023) Operational monitoring of open-ocean carbon dioxide removal deployments: Detection, attribution, and determination of side effects. Oceanography. https://doi.org/10.5670/oceanog.2023.s1.2

Boyd PW, Claustre H, Levy M, et al (2019) Multi-faceted particle pumps drive carbon sequestration in the ocean. Nature 568:327–335. https://doi.org/10.1038/s41586-019-1098-2

Boyer Montégut C de (2004) Mixed layer depth over the global ocean: An examination of profile data and a profile-based climatology. J Geophys Res 109: https://doi.org/10.1029/2004jc002378

Briggs N, Dall'Olmo G, Claustre H (2020) Major role of particle fragmentation in regulating biological sequestration of CO2 by the oceans. Science 367:791–793. https://doi.org/10.1126/science.aay1790

Briggs N, Perry MJ, Cetinić I, et al (2011) High-resolution observations of aggregate flux during a sub-polar north atlantic spring bloom. Deep Sea Res Part I 58:1031–1039. https://doi.org/10.1016/j.dsr.2011.07.007

Briggs NT, Slade WH, Boss E, Perry MJ (2013) Method for estimating mean particle size from high-frequency fluctuations in beam attenuation or scattering measurements. Appl Opt 52:6710–6725. https://doi.org/10.1364/AO.52.006710

Buesseler KO (1991) Do upper-ocean sediment traps provide an accurate record of particle flux? Nature 353:420–423. https://doi.org/10.1038/353420a0

Buesseler KO, Antia AN, Chen M, et al (2007) An assessment of the use of sediment traps for estimating upper ocean particle fluxes. J Mar Res 65:345–416. https://doi.org/10.1357/002224007781567621

Buesseler KO, Benitez-Nelson CR, Moran SB, et al (2006) An assessment of particulate organic carbon to thorium-234 ratios in the ocean and their impact on the application of 234Th as a POC flux proxy. Mar Chem 100:213–233. https://doi.org/10.1016/j.marchem.2005.10.

013

Buesseler KO, Boyd PW, Black EE, Siegel DA (2020) Metrics that matter for assessing the ocean biological carbon pump. Proc Natl Acad Sci U S A 117:9679–9687. https://doi.org/10.1073/pnas.1918114117

Burd AB, Hansell DA, Steinberg DK, et al (2010) Assessing the apparent imbalance between geochemical and biochemical indicators of meso- and bathypelagic biological activity: What the @$! Is wrong with present calculations of carbon budgets? Deep Sea Res Part 2 Top Stud Oceanogr 57:1557–1571. https://doi.org/10.1016/j.dsr2.2010.02.022

Cael BB, Cavan EL, Britten GL (2021) Reconciling the size-dependence of marine particle sinking speed. Geophys Res Lett 48: https://doi.org/10.1029/2020gl091771

Campbell RW, Roberts PL, Jaffe J (2020) The prince william sound plankton camera: A profiling in situ observatory of plankton and particulates. ICES J Mar Sci 77:1440–1455. https://doi.org/10.1093/icesjms/fsaa029

Campello RJGB, Moulavi D, Sander J (2013) Density-Based clustering based on hierarchical density estimates. In: Advances in knowledge discovery and data mining. Springer Berlin Heidelberg, pp 160–172

Canadell JG, Monteiro PMS, Costa MH, et al (2021) Global carbon and other biogeochemical cycles and feedbacks

Cetinić I, Perry MJ, Briggs NT, et al (2012) Particulate organic carbon and inherent optical properties during 2008 north atlantic bloom experiment. J Geophys Res 117: https://doi.org/10.1029/2011jc007771

Chai F, Johnson KS, Claustre H, et al (2020) Monitoring ocean biogeochemistry with autonomous platforms. Nature Reviews Earth & Environment 1:315–326. https://doi.org/10.1038/s43017-020-0053-y

Chawla NV, Bowyer KW, Hall LO, Kegelmeyer WP (2002) SMOTE: Synthetic minority oversampling technique. J Artif Intell Res 16:321–357. https://doi.org/10.1613/jair.953

Chen T, Guestrin C (2016) XGBoost: A scalable tree boosting system

Cheng K, Cheng X, Wang Y, et al (2019) Enhanced convolutional neural network for plankton identification and enumeration. PLoS One 14:e0219570. https://doi.org/10.1371/journal.pone.0219570

Claustre H, Johnson KS, Takeshita Y (2020) Observing the global ocean with Biogeochemical-Argo. Ann Rev Mar Sci 12:23–48. https://doi.org/10.1146/annurev-marine-010419-010956

Claustre H, Legendre L, Boyd PW, Levy M (2021) The oceans' biological carbon pumps: Framework for a research observational community approach. Frontiers in Marine Science 8: https://doi.org/10.3389/fmars.2021.780052

Clements DJ, Yang S, Weber T, et al (2022) Constraining the particle size distribution of large marine particles in the global ocean with *in situ* optical observations and supervised learning. Global Biogeochem Cycles 36: https://doi.org/10.1029/2021gb007276

Corkett CJ, McLaren IA (1979) The biology of pseudocalanus. In: Russell FS, Yonge M (eds) Advances in marine biology. Academic Press, pp 1–231

Cowen RK, Guigand CM (2008) In situ ichthyoplankton imaging system (ISIIS): System design and preliminary results. Limnol Oceanogr Methods 6:126–132. https://doi.org/10.4319/

lom.2008.6.126

Cui J, Wei B, Wang C, et al (2018) Texture and shape information fusion of convolutional neural network for plankton image classification. In: 2018 OCEANS - MTS/IEEE kobe Techno-Oceans (OTO). IEEE, Kobe

Dai J, Yu Z, Zheng H, et al (2017) A hybrid convolutional neural network for plankton classification. In: Computer vision – ACCV 2016 workshops. Springer International Publishing, Cham, pp 102–114

Dall'Olmo G, Dingle J, Polimene L, et al (2016) Substantial energy input to the mesopelagic ecosystem from the seasonal mixed-layer pump. Nat Geosci 9:820–823. https://doi.org/10.1038/ngeo2818

Dall'Olmo G, Mork KA (2014) Carbon export by small particles in the norwegian sea. Geophys Res Lett 41:2921–2927. https://doi.org/10.1002/2014gl059244

De La Rocha CL, Passow U (2007) Factors influencing the sinking of POC and the efficiency of the biological carbon pump. Deep Sea Res Part 2 Top Stud Oceanogr 54:639–658. https://doi.org/10.1016/j.dsr2.2007.01.004

De Robertis A, Levine M, Lauffenburger N, et al (2021) Uncrewed surface vehicle (USV) survey of walleye pollock, gadus chalcogrammus, in response to the cancellation of ship-based surveys. ICES J Mar Sci 78:2797–2808. https://doi.org/10.1093/icesjms/fsab155

Denvil-Sommer A, Buitenhuis ET, Kiko R, et al (2022) Testing the reconstruction of modelled particulate organic carbon from surface ecosystem components using PlankTOM12 and machine learning. Geoscientific Model Development Discussions 1–21

DeVries T (2022) The ocean carbon cycle. Annu Rev Environ Resour. https://doi.org/10.1146/annurev-environ-120920-111307

DeVries T, Weber T (2017) The export and fate of organic matter in the ocean: New constraints from combining satellite and oceanographic tracer observations. Global Biogeochem Cycles 31:535–555. https://doi.org/10.1002/2016gb005551

Dugdale RC, Goering JJ (1967) Uptake of new and regenerated forms of nitrogen in primary productivity1. Limnol Oceanogr 12:196–206. https://doi.org/10.4319/lo.1967.12.2.0196

Dunne JP, Armstrong RA, et al (2005) Empirical and mechanistic models for the particle export ratio. Global. https://doi.org/10.1029/2004GB002390

Dunne JP, Sarmiento JL, Gnanadesikan A (2007) A synthesis of global particle export from the surface ocean and cycling through the ocean interior and on the seafloor. Global Biogeochem Cycles 21: https://doi.org/10.1029/2006gb002907

Durkin CA, Buesseler KO, Cetinić I, et al (2021) A visual tour of carbon export by sinking particles. Global Biogeochem Cycles 35: https://doi.org/10.1029/2021gb006985

Ellen JS, Graff CA, Ohman MD (2019) Improving plankton image classification using context metadata. Limnol Oceanogr Methods 17:439–461. https://doi.org/10.1002/lom3.10324

Eppley RW, Peterson BJ (1979) Particulate organic matter flux and planktonic new production in the deep ocean. Nature 282:677–680. https://doi.org/10.1038/282677a0

Estapa ML, Buesseler K, Boss E, Gerbi G (2013) Autonomous, high-resolution observations of particle flux in the oligotrophic ocean. Biogeosciences 10:5517–5531. https://doi.org/10.5194/bg-10-5517-2013

Estapa ML, Durkin C, Buesseler K, et al (2017) Carbon flux from bio-optical profiling floats:

Calibrating transmissometers for use as optical sediment traps. Deep Sea Res Part I 120:100–111. https://doi.org/10.1016/j.dsr.2016.12.003

Estapa ML, Durkin C, Slade W, et al (2023) A new, global optical sediment trap calibration. EarthArXiv

Estapa ML, Feen ML, Breves E (2019) Direct observations of biological carbon export from profiling floats in the subtropical north atlantic. Global Biogeochem Cycles 33:282–300. https://doi.org/10.1029/2018gb006098

Faillettaz R, Picheral M, Luo JY, et al (2016) Imperfect automatic image classification successfully describes plankton distribution patterns. Methods in Oceanography 15-16:60–77. https://doi.org/10.1016/j.mio.2016.04.003

Fender CK, Kelly TB, Guidi L, et al (2019) Investigating particle Size-Flux relationships and the biological pump across a range of plankton ecosystem states from coastal to oligotrophic. Frontiers in Marine Science 6: https://doi.org/10.3389/fmars.2019.00603

Fernandes JA, Irigoien X, Boyra G, et al (2009) Optimizing the number of classes in automated zooplankton classification. J Plankton Res 31:19–29. https://doi.org/10.1093/plankt/fbn098

Fernandez A, Garcia S, Herrera F, Chawla NV (2018) SMOTE for learning from imbalanced data: Progress and challenges, marking the 15-year anniversary. J Artif Intell Res 61:863–905. https://doi.org/10.1613/jair.1.11192

Flament P (2002) A state variable for characterizing water masses and their diffusive stability: spiciness. Prog Oceanogr 54:493–501. https://doi.org/10.1016/S0079-6611(02)00065-4

Forman G (2005) Counting positives accurately despite inaccurate classification. ECML 564–575

Frajka-Williams E, Rhines PB (2010) Physical controls and interannual variability of the labrador sea spring phytoplankton bloom in distinct regions. Deep Sea Res Part I 57:541–552. https://doi.org/10.1016/j.dsr.2010.01.003

Francois R, Honjo S, Krishfield R, Manganini S (2002) Factors controlling the flux of organic carbon to the bathypelagic zone of the ocean. Global Biogeochem Cycles 16:34-1-34-20. https://doi.org/10.1029/2001gb001722

Friedlingstein P, O'Sullivan M, Jones MW, et al (2022) Global carbon budget 2022. Earth Syst Sci Data 14:4811–4900. https://doi.org/10.5194/essd-14-4811-2022

Gattuso J-P, Hansson L (2011) Ocean acidification. OUP Oxford

Gattuso J-P, Williamson P, Duarte CM, Magnan AK (2021) The potential for Ocean-Based climate action: Negative emissions technologies and beyond. Frontiers in Climate 2:575716. https://doi.org/10.3389/fclim.2020.575716

Géron A (2019) Hands-On machine learning with Scikit-Learn, keras, and TensorFlow: Concepts, tools, and techniques to build intelligent systems. "O'Reilly Media, Inc."

Giering SLC, Cavan EL, Basedow SL, et al (2020a) Sinking organic particles in the Ocean—Flux estimates from in situ optical devices. Frontiers in Marine Science 6: https://doi.org/10.3389/fmars.2019.00834

Giering SLC, Hosking B, Briggs N, Iversen MH (2020b) The interpretation of particle size, shape, and carbon flux of marine particle images is strongly affected by the choice of particle detection algorithm. Frontiers in Marine Science 7: https://doi.org/10.3389/fmars.

2020.00564

Giering SLC, Sanders R, Lampitt RS, et al (2014) Reconciliation of the carbon budget in the ocean's twilight zone. Nature 507:480–483. https://doi.org/10.1038/nature13123

González P, Castaño A, Chawla NV, Coz JJD (2017) A review on quantification learning. ACM Comput Surv 50:1–40. https://doi.org/10.1145/3117807

Gordon HR, Clark DK, Mueller JL, Hovis WA (1980) Phytoplankton pigments from the nimbus-7 coastal zone color scanner: Comparisons with surface measurements. Science 210:63–66. https://doi.org/10.1126/science.210.4465.63

Gorgues T, Aumont O, Memery L (2019) Simulated changes in the particulate carbon export efficiency due to diel vertical migration of zooplankton in the north atlantic. Geophys Res Lett 46:5387–5395. https://doi.org/10.1029/2018gl081748

Gorsky G, Ohman MD, Picheral M, et al (2010) Digital zooplankton image analysis using the ZooScan integrated system. J Plankton Res 32:285–303. https://doi.org/10.1093/plankt/fbp124

Guidi L, Chaffron S, Bittner L, et al (2016) Plankton networks driving carbon export in the oligotrophic ocean. Nature 532:465–470. https://doi.org/10.1038/nature16942

Guidi L, Jackson GA, Stemmann L, et al (2008) Relationship between particle size distribution and flux in the mesopelagic zone. Deep Sea Res Part I 55:1364–1374. https://doi.org/10.1016/j.dsr.2008.05.014

Guidi L, Legendre L, Reygondeau G, et al (2015) A new look at ocean carbon remineralization for estimating deepwater sequestration. Global Biogeochem Cycles 29:1044–1059. https://doi.org/10.1002/2014gb005063

Guo B, Nyman L, Nayak AR, et al (2021) Automated plankton classification from holographic imagery with deep convolutional neural networks. Limnol Oceanogr Methods 19:21–36. https://doi.org/10.1002/lom3.10402

Haëntjens N, Della Penna A, Briggs N, et al (2020) Detecting mesopelagic organisms using Biogeochemical-Argo floats. Geophys Res Lett 47:e2019GL086088. https://doi.org/10.1029/2019GL086088

Hartigan JA, Wong MA (1979) Algorithm AS 136: A K-Means clustering algorithm. J R Stat Soc Ser C Appl Stat 28:100–108. https://doi.org/10.2307/2346830

Hartmann J, Suitner N, Lim C, et al (2023) Stability of alkalinity in ocean alkalinity enhancement (OAE) approaches – consequences for durability of CO_2 storage. Biogeosciences 20:781–802. https://doi.org/10.5194/bg-20-781-2023

Hayes CT, Costa KM, Anderson RF, et al (2021) Global ocean sediment composition and burial flux in the deep sea. Global Biogeochem Cycles 35: https://doi.org/10.1029/2020gb006769

Henson SA, Laufkötter C, Leung S, et al (2022) Uncertain response of ocean biological carbon export in a changing world. Nat Geosci 15:248–254. https://doi.org/10.1038/s41561-022-00927-0

Henson SA, Sanders R, Madsen E (2012) Global patterns in efficiency of particulate organic carbon export and transfer to the deep ocean. Global Biogeochem Cycles 26: https://doi.org/10.1029/2011gb004099

Henson SA, Sanders R, Madsen E, et al (2011) A reduced estimate of the strength of the ocean's biological carbon pump. Geophys Res Lett 38: https://doi.org/10.1029/2011gl046735

Honjo S, Manganini SJ, Krishfield RA, Francois R (2008) Particulate organic carbon fluxes to the ocean interior and factors controlling the biological pump: A synthesis of global sediment trap programs since 1983. Prog Oceanogr 76:217–285. https://doi.org/10.1016/j.pocean.2007.11.003

IPCC (2019) IPCC special report on the ocean and cryosphere in a changing climate. Cambridge University Press, Cambridge, UK; New York, NY, USA

Iversen MH (2023) Carbon export in the ocean: A biologist's perspective. Ann Rev Mar Sci 15: https://doi.org/10.1146/annurev-marine-032122-035153

Iversen MH, Lampitt RS (2020) Size does not matter after all: No evidence for a size-sinking relationship for marine snow. Prog Oceanogr 189:102445. https://doi.org/10.1016/j.pocean.2020.102445

Iversen MH, Nowald N, Ploug H, et al (2010) High resolution profiles of vertical particulate organic matter export off cape blanc, mauritania: Degradation processes and ballasting effects. Deep Sea Res Part I 57:771–784. https://doi.org/10.1016/j.dsr.2010.03.007

Jerlov NG (1976) Marine optics. Elsevier

Jiao N, Herndl GJ, Hansell DA, et al (2010) Microbial production of recalcitrant dissolved organic matter: Long-term carbon storage in the global ocean. Nat Rev Microbiol 8:593–599. https://doi.org/10.1038/nrmicro2386

Johnson K, Berelson W, Boss E, et al (2009) Observing biogeochemical cycles at global scales with profiling floats and gliders: Prospects for a global array. Oceanography 22:216–225. https://doi.org/10.5670/oceanog.2009.81

Jónasdóttir SH, Visser AW, Richardson K, Heath MR (2015) Seasonal copepod lipid pump promotes carbon sequestration in the deep north atlantic. Proc Natl Acad Sci U S A 112:12122–12126. https://doi.org/10.1073/pnas.1512110112

Jouandet M-P, Trull TW, Guidi L, et al (2011) Optical imaging of mesopelagic particles indicates deep carbon flux beneath a natural iron-fertilized bloom in the southern ocean. Limnol Oceanogr 56:1130–1140. https://doi.org/10.4319/lo.2011.56.3.1130

Kelley D, Richards C (2021) Oce: Analysis of oceanographic data

Khabbazan B, Mirzakuchaki S (2019) Design and implementation of a Low-Power, embedded CNN accelerator on a low-end FPGA. In: 2019 22nd euromicro conference on digital system design (DSD). pp 647–650

Kiko R, Biastoch A, Brandt P, et al (2017) Biological and physical influences on marine snowfall at the equator. Nat Geosci 10:852–858. https://doi.org/10.1038/ngeo3042

Kiko R, Picheral M, Antoine D, et al (2022) A global marine particle size distribution dataset obtained with the underwater vision profiler 5. Earth System Science Data Discussions

Klaas C, Archer DE (2002) Association of sinking organic matter with various types of mineral ballast in the deep sea: Implications for the rain ratio. Global Biogeochem Cycles 16:63-1-63-14. https://doi.org/10.1029/2001gb001765

Kostadinov TS, Siegel DA, Maritorena S (2010) Global variability of phytoplankton functional types from space: Assessment via the particle size distribution. Biogeosciences 7:3239–3257. https://doi.org/10.5194/bg-7-3239-2010

Kostadinov TS, Siegel DA, Maritorena S (2009) Retrieval of the particle size distribution from satellite ocean color observations. J Geophys Res 114: https://doi.org/10.1029/2009jc005303

Kriest I (2002) Different parameterizations of marine snow in a 1D-model and their influence on representation of marine snow, nitrogen budget and sedimentation. Deep Sea Res Part I 49:2133–2162. https://doi.org/10.1016/S0967-0637(02)00127-9

Krumhansl KA, Head EJH, Pepin P, et al (2018) Environmental drivers of vertical distribution in diapausing calanus copepods in the northwest atlantic. Prog Oceanogr 162:202–222. https://doi.org/10.1016/j.pocean.2018.02.018

Kwon E, Primeau F, Sarmiento J (2009) The impact of remineralization depth on the air–sea carbon balance. Nature Geoscience 2:630–635. https://doi.org/10.1038/NGEO612

Kyathanahally SP, Hardeman T, Reyes M, et al (2022) Ensembles of data-efficient vision transformers as a new paradigm for automated classification in ecology. Sci Rep 12:18590. https://doi.org/10.1038/s41598-022-21910-0

Lacour L, Ardyna M, Stec KF, et al (2017) Unexpected winter phytoplankton blooms in the north atlantic subpolar gyre. Nat Geosci 10:836–839. https://doi.org/10.1038/ngeo3035

Lacour L, Briggs N, Claustre H, et al (2019) The intraseasonal dynamics of the mixed layer pump in the subpolar north atlantic ocean: A biogeochemical-argo float approach. Global Biogeochem Cycles 33:266–281. https://doi.org/10.1029/2018gb005997

Lacour L, Claustre H, Prieur L, D'Ortenzio F (2015) Phytoplankton biomass cycles in the north atlantic subpolar gyre: A similar mechanism for two different blooms in the labrador sea. Geophys Res Lett 42:5403–5410. https://doi.org/10.1002/2015gl064540

Lampitt RS, Achterberg EP, Anderson TR, et al (2008) Ocean fertilization: A potential means of geoengineering? Philos Trans A Math Phys Eng Sci 366:3919–3945. https://doi.org/10.1098/rsta.2008.0139

Laurenceau-Cornec EC, Le Moigne FAC, Gallinari M, et al (2020) New guidelines for the application of stokes' models to the sinking velocity of marine aggregates. Limnol Oceanogr 65:1264–1285. https://doi.org/10.1002/lno.11388

Laurenceau-Cornec EC, Trull TW, Davies DM, et al (2015) Phytoplankton morphology controls on marine snow sinking velocity. Mar Ecol Prog Ser 520:35–56. https://doi.org/10.3354/meps11116

Laws EA, D'Sa E, Naik P (2011) Simple equations to estimate ratios of new or export production to total production from satellite-derived estimates of sea surface temperature and primary production. Limnol Oceanogr Methods 9:593–601. https://doi.org/10.4319/lom.2011.9.593

Laws EA, Falkowski PG, Smith WO Jr, et al (2000) Temperature effects on export production in the open ocean. Global Biogeochem Cycles 14:1231–1246. https://doi.org/10.1029/1999gb001229

Lee H, Park M, Kim J (2016) Plankton classification on imbalanced large scale database via convolutional neural networks with transfer. In: 2016 IEEE international conference on image processing (ICIP). unknown, pp 3713–3717

Legendre L, Rivkin RB, Weinbauer MG, et al (2015) The microbial carbon pump concept: Potential biogeochemical significance in the globally changing ocean. Prog Oceanogr 134:432–450. https://doi.org/10.1016/j.pocean.2015.01.008

Levy M, Bopp L, Karleskind P, et al (2013) Physical pathways for carbon transfers between the surface mixed layer and the ocean interior. Global Biogeochem Cycles 27:1001–1012. https://doi.org/10.1002/gbc.20092

Leys C, Ley C, Klein O, et al (2013) Detecting outliers: Do not use standard deviation around the mean, use absolute deviation around the median. J Exp Soc Psychol 49:764–766. https://doi.org/10.1016/j.jesp.2013.03.013

Li X, Li S (2022) Transformer help CNN see better: A lightweight hybrid apple disease identification model based on transformers. Collect FAO Agric 12:884. https://doi.org/10.3390/agriculture12060884

Liu FT, Ting KM, Zhou Z-H (2012) Isolation-Based anomaly detection. ACM Trans Knowl Discov Data 6:1–39. https://doi.org/10.1145/2133360.2133363

Liu Z, Lin Y, Cao Y, et al (2021) Swin transformer: Hierarchical vision transformer using shifted windows. 10012–10022

Llort J, Langlais C, Matear R, et al (2018) Evaluating southern ocean carbon eddy-pump from biogeochemical-argo floats. J Geophys Res Oceans 123:971–984. https://doi.org/10.1002/2017jc012861

Logan BE, Kilps JR (1995) Fractal dimensions of aggregates formed in different fluid mechanical environments. Water Res 29:443–453. https://doi.org/10.1016/0043-1354(94)00186-B

Logan BE, Wilkinson DB (1990) Fractal geometry of marine snow and other biological aggregates. Limnol Oceanogr 35:130–136. https://doi.org/10.4319/lo.1990.35.1.0130

Lombard F, Boss E, Waite AM, et al (2019) Globally consistent quantitative observations of planktonic ecosystems. Frontiers in Marine Science 6:196. https://doi.org/10.3389/fmars.2019.00196

Lovelock CE, Duarte CM (2019) Dimensions of blue carbon and emerging perspectives. Biol Lett 15:20180781. https://doi.org/10.1098/rsbl.2018.0781

Luo JY, Irisson J-O, Graham B, et al (2018) Automated plankton image analysis using convolutional neural networks. Limnol Oceanogr Methods 16:814–827. https://doi.org/10.1002/lom3.10285

Macreadie PI, Costa MDP, Atwood TB, et al (2021) Blue carbon as a natural climate solution. Nature Reviews Earth & Environment 2:826–839. https://doi.org/10.1038/s43017-021-00224-1

Marshall GJ, Dowdeswell JA, Rees WG (1994) The spatial and temporal effect of cloud cover on the acquisition of high quality landsat imagery in the european arctic sector. Remote Sens Environ 50:149–160. https://doi.org/10.1016/0034-4257(94)90041-8

Martin A, Boyd P, Buesseler K, et al (2020) The oceans' twilight zone must be studied now, before it is too late. Nature 580:26–28. https://doi.org/10.1038/d41586-020-00915-7

Martin JH, Knauer GA, Karl D, Broenkow WW (1987) VERTEX: Carbon cycling in the northeast pacific. Deep Sea Research Part A Oceanographic Research Papers 34:267–285. https://doi.org/10.1016/0198-0149(87)90086-0

McDonnell AMP, Buesseler KO (2012) A new method for the estimation of sinking particle fluxes from measurements of the particle size distribution, average sinking velocity, and carbon content. Limnol Oceanogr Methods 10:329–346. https://doi.org/10.4319/lom.2012.

10.329

McDonnell AMP, Buesseler KO (2010) Variability in the average sinking velocity of marine particles. Limnol Oceanogr 55:2085–2096. https://doi.org/10.4319/lo.2010.55.5.2085

Mignot A, Ferrari R, Claustre H (2018) Floats with bio-optical sensors reveal what processes trigger the north atlantic bloom. Nat Commun 9:190. https://doi.org/10.1038/s41467-017-02143-6

Mobley C (2022) The oceanic optics book

Moreno-Torres JG, Raeder T, Alaiz-Rodríguez R, et al (2012) A unifying view on dataset shift in classification. Pattern Recognit 45:521–530. https://doi.org/10.1016/j.patcog.2011.06.019

National Academies of Sciences (2022) A research strategy for ocean-based carbon dioxide removal and sequestration. National Academies Press (US), Washington (DC)

Neukermans G, Bach LT, Butterley A, et al (2023) Quantitative and mechanistic understanding of the open ocean carbonate pump - perspectives for remote sensing and autonomous in situ observation. Earth-Sci Rev 104359. https://doi.org/10.1016/j.earscirev.2023.104359

Nowicki M, DeVries T, Siegel DA (2022) Quantifying the carbon export and sequestration pathways of the ocean's biological carbon pump. Global Biogeochem Cycles 36: https://doi.org/10.1029/2021gb007083

Oh S, Kim M, Kim D, et al (2017) Investigation on performance and energy efficiency of CNN-based object detection on embedded device. In: 2017 4th international conference on computer applications and information processing technology (CAIPT). pp 1–4

Omand MM, D'Asaro EA, Lee CM, et al (2015) Eddy-driven subduction exports particulate organic carbon from the spring bloom. Science 348:222–225. https://doi.org/10.1126/science.1260062

Orenstein EC, Beijbom O (2017) Transfer learning and deep feature extraction for planktonic image data sets. In: 2017 IEEE winter conference on applications of computer vision (WACV). pp 1082–1088

Orenstein EC, Kenitz KM, Roberts PLD, et al (2020) Semi- and fully supervised quantification techniques to improve population estimates from machine classifiers. Limnol Oceanogr Methods 18:739–753. https://doi.org/10.1002/lom3.10399

Passow U (2004) Switching perspectives: Do mineral fluxes determine particulate organic carbon fluxes or vice versa? Geochem Geophys Geosyst 5: https://doi.org/10.1029/2003gc000670

Passow U, Carlson CA (2012) The biological pump in a high CO world. Mar Ecol Prog Ser 470:249–272

Passow U, De La Rocha CL (2006) Accumulation of mineral ballast on organic aggregates. Global Biogeochem Cycles 20: https://doi.org/10.1029/2005gb002579

Petit F, Uitz J, Schmechtig C, et al (2022) Influence of the phytoplankton community composition on the in situ fluorescence signal: Implication for an improved estimation of the chlorophyll-a concentration from BioGeoChemical-Argo profiling floats. Frontiers in Marine Science 9: https://doi.org/10.3389/fmars.2022.959131

Picheral M, Catalano C, Brousseau D, et al (2021) The underwater vision profiler 6: An imaging sensor of particle size spectra and plankton, for autonomous and cabled platforms.

Limnol Oceanogr Methods. https://doi.org/10.1002/lom3.10475

Picheral M, Guidi L, Stemmann L, et al (2010) The underwater vision profiler 5: An advanced instrument for high spatial resolution studies of particle size spectra and zooplankton. Limnol Oceanogr Methods 8:462–473. https://doi.org/10.4319/lom.2010.8.462

Pinti J, DeVries T, Norin T, et al (2023) Model estimates of metazoans' contributions to the biological carbon pump. Biogeosciences 20:997–1009. https://doi.org/10.5194/bg-20-997-2023

Ploug H, Iversen MH, Koski M, Buitenhuis ET (2008) Production, oxygen respiration rates, and sinking velocity of copepod fecal pellets: Direct measurements of ballasting by opal and calcite. Limnol Oceanogr 53:469–476. https://doi.org/10.4319/lo.2008.53.2.0469

Ramondenc S, Madeleine G, Lombard F, et al (2016) An initial carbon export assessment in the mediterranean sea based on drifting sediment traps and the underwater vision profiler data sets. Deep Sea Res Part I 117:107–119. https://doi.org/10.1016/j.dsr.2016.08.015

Rasse R, Dall'Olmo G, Graff J, et al (2017) Evaluating optical proxies of particulate organic carbon across the surface atlantic ocean. Frontiers in Marine Science 4: https://doi.org/10.3389/fmars.2017.00367

Reiss CS, Cossio AM, Walsh J, et al (2021) Glider-Based estimates of Meso-Zooplankton biomass density: A fisheries case study on antarctic krill (euphausia superba) around the northern antarctic peninsula. Frontiers in Marine Science 8: https://doi.org/10.3389/fmars.2021.604043

Resplandy L, Lévy M, McGillicuddy DJ Jr (2019) Effects of eddy-driven subduction on ocean biological carbon pump. Global Biogeochem Cycles 33:1071–1084. https://doi.org/10.1029/2018gb006125

Riebesell U, Körtzinger A, Oschlies A (2009) Sensitivities of marine carbon fluxes to ocean change. Proc Natl Acad Sci U S A 106:20602–20609. https://doi.org/10.1073/pnas.0813291106

Robinson IS (2004) Measuring the oceans from space: The principles and methods of satellite oceanography. Springer Science & Business Media

Roemmich D, Alford MH, Claustre H, et al (2019) On the future of argo: A global, Full-Depth, Multi-Disciplinary array. Frontiers in Marine Science 6: https://doi.org/10.3389/fmars.2019.00439

Roesler C, Uitz J, Claustre H, et al (2017) Recommendations for obtaining unbiased chlorophyll estimates from in situ chlorophyll fluorometers: A global analysis of WET labs ECO sensors. Limnol Oceanogr Methods 15:572–585. https://doi.org/10.1002/lom3.10185

Roullier F, Berline L, Guidi L, et al (2014) Particle size distribution and estimated carbon flux across the arabian sea oxygen minimum zone. Biogeosciences 11:4541–4557. https://doi.org/10.5194/bg-11-4541-2014

Saba GK, Burd AB, Dunne JP, et al (2021) Toward a better understanding of fish-based contribution to ocean carbon flux. Limnol Oceanogr 66:1639–1664. https://doi.org/10.1002/lno.11709

Sarmiento JL (2006) Ocean biogeochemical dynamics. Princeton University Press

Savoye N, Benitez-Nelson C, Burd AB, et al (2006) 234Th sorption and export models in the water column: A review. Mar Chem 100:234–249. https://doi.org/10.1016/j.marchem.

2005.10.014

Schröder S-M, Kiko R, Irisson J-O, Koch R (2019) Low-Shot learning of plankton categories. In: Pattern recognition. Springer International Publishing, pp 391–404

Schubert E, Sander J, Ester M, et al (2017) DBSCAN revisited, revisited: Why and how you should (still) use DBSCAN. ACM Trans Database Syst 42:1–21. https://doi.org/10.1145/3068335

Sharqawy MH, Lienhard JH, Zubair SM (2010) Thermophysical properties of seawater: A review of existing correlations and data. Desalination Water Treat 16:354–380. https://doi.org/10.5004/dwt.2010.1079

Siegel DA, DeVries T, Cetinić I, Bisson KM (2022) Quantifying the ocean's biological pump and its carbon cycle impacts on global scales. Ann Rev Mar Sci 15: https://doi.org/10.1146/annurev-marine-040722-115226

Siegel DA, DeVries T, Doney S, Bell T (2021) Assessing the sequestration time scales of some ocean-based carbon dioxide reduction strategies. Environ Res Lett. https://doi.org/10.1088/1748-9326/ac0be0

Siegel DA, Doney SC, Yoder JA (2002) The north atlantic spring phytoplankton bloom and sverdrup's critical depth hypothesis. Science 296:730–733. https://doi.org/10.1126/science.1069174

Siegel D, Buesseler K, Doney S, et al (2014) Global assessment of ocean carbon export by combining satellite observations and food-web models. Global Biogeochemical Cycles. https://doi.org/10.1002/2013GB004743

Soetaert K, Herman PMJ (2008) A practical guide to ecological modelling: Using R as a simulation platform, 2009th edn. Springer, New York, NY

Solow A, Davis C, Hu Q (2001) Estimating the taxonomic composition of a sample when individuals are classified with error. Mar Ecol Prog Ser 216:309–311. https://doi.org/10.3354/meps216309

Sosik HM, Olson RJ (2007) Automated taxonomic classification of phytoplankton sampled with imaging-in-flow cytometry. Limnol Oceanogr Methods 5:204–216. https://doi.org/10.4319/lom.2007.5.204

Steinberg DK, Landry MR (2017) Zooplankton and the ocean carbon cycle. Ann Rev Mar Sci 9:413–444. https://doi.org/10.1146/annurev-marine-010814-015924

Stemmann L, Jackson GA, Ianson D (2004) A vertical model of particle size distributions and fluxes in the midwater column that includes biological and physical processes—part i: Model formulation. Deep Sea Res Part I 51:865–884. https://doi.org/10.1016/j.dsr.2004.03.001

Stukel MR, Aluwihare LI, Barbeau KA, et al (2017) Mesoscale ocean fronts enhance carbon export due to gravitational sinking and subduction. Proc Natl Acad Sci U S A 114:1252–1257. https://doi.org/10.1073/pnas.1609435114

Sverdrup HU (1953) On conditions for the vernal blooming of phytoplankton. ICES J Mar Sci 18:287–295. https://doi.org/10.1093/icesjms/18.3.287

Takahashi T, Sutherland SC, Wanninkhof R, et al (2009) Climatological mean and decadal change in surface ocean pCO2, and net sea–air CO2 flux over the global oceans. Deep Sea Res Part 2 Top Stud Oceanogr 56:554–577. https://doi.org/10.1016/j.dsr2.2008.12.009

Terrats L, Claustre H, Cornec M, et al (2020) Detection of coccolithophore blooms with BioGeoChemical-Argo floats. Geophys Res Lett 47:e2020GL090559. https://doi.org/10.1029/2020GL090559

Trudnowska E, Lacour L, Ardyna M, et al (2021) Marine snow morphology illuminates the evolution of phytoplankton blooms and determines their subsequent vertical export. Nat Commun 12:2816. https://doi.org/10.1038/s41467-021-22994-4

Turner JT (2015) Zooplankton fecal pellets, marine snow, phytodetritus and the ocean's biological pump. Prog Oceanogr 130:205–248. https://doi.org/10.1016/j.pocean.2014.08.005

Uitz J, Stramski D, Reynolds RA, Dubranna J (2015) Assessing phytoplankton community composition from hyperspectral measurements of phytoplankton absorption coefficient and remote-sensing reflectance in open-ocean environments. Remote Sens Environ 171:58–74. https://doi.org/10.1016/j.rse.2015.09.027

Våge K, Pickart RS, Thierry V, et al (2008) Surprising return of deep convection to the subpolar north atlantic ocean in winter 2007–2008. Nat Geosci 2:67–72. https://doi.org/10.1038/ngeo382

Vaswani A, Shazeer N, Parmar N, et al (2017) Attention is all you need. Adv Neural Inf Process Syst 30:

Volk T, Hoffert MI (1985) Ocean carbon pumps: Analysis of relative strengths and efficiencies in Ocean-Driven atmospheric CO2 changes. The Carbon Cycle and Atmospheric CO2: Natural Variations Archean to Present 99–110. https://doi.org/10.1029/GM032p0099

Wang B, Fennel K (2022) Biogeochemical-Argo data suggest significant contributions of small particles to the vertical carbon flux in the subpolar north atlantic. Limnol Oceanogr 67:2405–2417. https://doi.org/10.1002/lno.12209

Westberry TK, Siegel DA (2006) Spatial and temporal distribution ofTrichodesmium-blooms in the world's oceans. Global Biogeochem Cycles 20: https://doi.org/10.1029/2005gb002673

Williams JR, Giering SLC (2022) In situ particle measurements deemphasize the role of size in governing the sinking velocity of marine particles. Geophys Res Lett 49:e2022GL099563. https://doi.org/10.1029/2022GL099563

Williamson P, Gattuso J-P (2022) Carbon removal using coastal blue carbon ecosystems is uncertain and unreliable, with questionable climatic Cost-Effectiveness. Frontiers in Climate 4: https://doi.org/10.3389/fclim.2022.853666

Wilson JD, Andrews O, Katavouta A, et al (2022) The biological carbon pump in CMIP6 models: 21st century trends and uncertainties. Proc Natl Acad Sci U S A 119:e2204369119. https://doi.org/10.1073/pnas.2204369119

Wolpert DH (1996) The lack of a priori distinctions between learning algorithms. Neural Comput 8:1341–1390. https://doi.org/10.1162/neco.1996.8.7.1341

Wong A, Keeley R, Carval T, Others (2022) Argo quality control manual for CTD and trajectory data

Wu Y, Platt T, Tang CCL, Sathyendranath S (2008) Regional differences in the timing of the spring bloom in the labrador sea. Mar Ecol Prog Ser 355:9–20. https://doi.org/10.3354/meps07233

Xing X, Briggs N, Boss E, Claustre H (2018a) Improved correction for non-photochemical quenching of in situ chlorophyll fluorescence based on a synchronous irradiance profile. Opt Express 26:24734–24751. https://doi.org/10.1364/OE.26.024734

Xing X-G, Claustre H, Boss E, Chai F (2018b) Toward deeper development of Biogeochemical-Argo floats. Atmospheric and Oceanic Science Letters 11:287–290. https://doi.org/10.1080/16742834.2018.1457932

Yang B, Boss ES, Haëntjens N, et al (2020) Phytoplankton phenology in the north atlantic: Insights from profiling float measurements. Front Mar Sci 7: https://doi.org/10.3389/fmars.2020.00139

Yang B, Fox J, Behrenfeld MJ, et al (2021) In situ estimates of net primary production in the western north atlantic with argo profiling floats. J Geophys Res Biogeosci 126:e2020JG006116. https://doi.org/10.1029/2020JG006116

Yashayaev I, Loder JW (2017) Further intensification of deep convection in the labrador sea in 2016. Geophys Res Lett 44:1429–1438. https://doi.org/10.1002/2016gl071668

Yashayaev I, Loder JW (2009) Enhanced production of labrador sea water in 2008. Geophys Res Lett. https://doi.org/10.1029/2008GL036162

Zaneveld JRV (1994) Optical closure: From theory to measurement. Ocean Optics. https://doi.org/10.1093/oso/9780195068436.001.0001/isbn-9780195068436-book-part-7

Zeebe RE (2012) History of seawater carbonate chemistry, atmospheric CO2, and ocean acidification. Annu Rev Earth Planet Sci 40:141–165. https://doi.org/10.1146/annurev-earth-042711-105521